Three Dimensional Nonlinear Statistical Modeling Framework for Morphological Analysis

A Dissertation Presented for
the Doctor of Philosophy
Degree
The University of Tennessee, Knoxville

Emam ElHak Abdel Fatah
December 2012

Copyright © 2012 by Emam ElHak Abdel Fatah
All rights reserved.

"The trouble with the world is that the stupid are cocksure and the intelligent are full of doubt."
Bertrand Russell

DEDICATION

This dissertation is dedicated to my father Ali ElDin and mother Nagwa Saleh, for their continuous lifelong support, love and friendship and for instilling in me the confidence and passion to lead a successful life.

ACKNOWLEDGMENTS

I would like to thank my advisor and mentor, Dr. Mohamed Mahfouz, through this lengthy course of knowledge acquisition, as well as for his continued support of my research and career goals. He granted me the opportunity to not only pursue my advanced education in the field in which I excelled, but also conferred upon me the ability to pursue those aspirations in the United States. As Dr. Mahfouz's graduate research assistant, I have not only been able to gain valuable insight into how science and engineering are played out day-to-day both in academia and industry, but have also discovered what it takes to be prosperous in these fields. Having had these experiences, I am confident that I can apply lessons learned and examples observed during my time at the Center for Musculoskeletal Research (CMR) in my future academic career.

I would like to extend my gratitude to CMR as a whole, including Dr. Richard Komistek, for providing occasions to travel and gain insight into the workings of academia and research groups around the Globe. The support of Research Coordinator, Rebecca Robertson, provided me the opportunity to focus on my progress in research and the scientific field. I would also like to extend my gratitude to Research Associate, Lyndsay Bowers, for her gracious collaboration on many issues and situations, including grants and teaching.

I am also very appreciative of the assistance extended to me by my CMR colleagues, current doctoral candidates, Mr. Gary To, Mr. Sumesh Zingde, Mr. Hatem El Dakhakhni, Mr. Michael Johnson, Mr. Chris Carr, Mr. Joseph Mitchell; as well as Dr. Michael Kuhn, Dr. Brandon

Merkl, Dr. Filip Leszko, Dr. John Kyle Patrick Mueller, and Dr. Boyd Evans; and Mr. Wesley Underwood and Mr. Nicholas Battaglia.

From the Anthropology Department, I would like to thank Dr. Natalie Shirley for both her professional collaboration on different aspects of research and her friendship. I would also like to thank Dr. Richard Jantz for all of his helpful insight into various research elements.

I am particularly grateful for all my committee members' willingness to participate in acquiring this honored degree, including Dr. William Hamel and Dr. Ali Fathy.

After all of these recognitions, my endeavors were unquestionably encouraged by my brother, Ahmed, and sisters, Iman and Asmaa, and I will be forever thankful for their commitment to me.

Abstract

This dissertation describes a novel three-dimensional (3D) morphometric analysis framework for building statistical shape models and identifying shape differences between populations. This research generalizes the use of anatomical atlases on more complex anatomy as in case of irregular, flat bones, and bones with deformity and irregular bone growth. The foundations for this framework are: 1) **Anatomical atlases** which allow the creation of homologues anatomical models across populations; 2) **Statistical representation** for output models in a compact form to capture both local and global shape variation across populations; 3) **Shape Analysis** using automated 3D landmarking and surface matching. The proposed framework has various applications in clinical, forensic and physical anthropology fields. Extensive research has been published in peer-reviewed image processing, forensic anthropology, physical anthropology, biomedical engineering, and clinical orthopedics conferences and journals.

The forthcoming discussion of existing methods for morphometric analysis, including manual and semi-automatic methods, addresses the need for automation of morphometric analysis and statistical atlases. Explanations of these existing methods for the construction of statistical shape models, including benefits and limitations of each method, provide evidence of the necessity for such a novel algorithm. A novel approach was taken to achieve accurate point correspondence in case of irregular and deformed anatomy. This was achieved using a scale space approach to detect prominent scale invariant features. These features were then matched and registered using a novel multi-scale method, utilizing both coordinate data as well as shape

descriptors, followed by an overall surface deformation using a new constrained free-form deformation.

Applications of output statistical atlases are discussed, including forensic applications for the skull sexing, as well as physical anthropology applications, such as asymmetry in clavicles. Clinical applications in pelvis reconstruction and studying of lumbar kinematics and studying thickness of bone and soft tissue are also discussed.

Table of Contents

DEDICATION iv

ACKNOWLEDGMENTS v

Abstract vii

Table of Contents ix

List of Tables xv

List of Figures xviii

ABREVIATIONS AND SYMBOLS xxviii

1. INTRODUCTION 1

1.1 Motivation 1

1.2 Background 2

1.2.1 Statistical Atlases for Segmentation 4

1.2.1.1 Reconstruction 6

1.2.2 Statistical Atlases in Morphometric 7

1.3 Contributions 8

1.4 Organization 9

2. MORPHOMETERIC 13

2.1 Traditional Morphometric 14

2.1.1 Landmarks Classification 14

2.2 Geometric Morphometric 17

2.2.1 Shape Coordinates Method 18

2.2.2 Superimposition Method 18
2.2.3 Thin-Plate Spline Method 19
2.2.4 Outline Method 19
2.2.5 Voxel Based Method 19
2.2.6 Surface Based Method 20
2.2.7 Deformation Based Method 20
3. STATISTICAL SHAPE MODELS 21
3.1 Components of Valid Shape Model 21
3.1.1 Shape Representation 21
3.1.2 Alignment 22
3.1.3 Dimensionality Reduction 22
3.2 Generating Shape Correspondence 23
3.2.1 Mesh-to-Volume Registration 23
3.2.2 Volume-to-Volume Registration 25
3.2.3 Parameterization-to-Parameterization Registration 26
3.2.4 Population-Based Optimization 29
3.2.5 Mesh-to-Mesh Registration 31
3.3 Evaluation 33
3.3.1 Generalization: 33
3.3.2 Specificity: 33
3.3.3 Compactness: 34
4. DEVELOPMENT OF MORPHOMETRIC FRAMEWORK USING STATISTICAL ATLASES 35

4.1 Atlas Creation 35
4.1.1 Mesh Representation 36
4.1.2 Mesh Constraints 39
4.1.3 Template Mesh Quality 41
4.2 Mesh Segmentation 43
4.2.1 Algorithm 1: Calculating mesh 1st and 2nd differential properties: 45
5. STATISTICAL SHAPE ATLASES CREATION 49
5.1 Normalization 51
5.1.1 Bounding Box 51
5.1.2 Centroid Size 51
5.1.3 Area 52
5.1.4 Average Centroid Size 52
5.2 Scale Space Mapping 55
5.3 Features Extraction 61
5.3.1 Algorithm 2: Calculating mesh 1st and 2nd differential properties: 68
5.3.2 Algorithm 3: Mesh Features Extraction: 73
5.3.2.1 Normal Scale Features: 73
5.3.2.2 Scale Space Features: 74
5.4 Multi Resolution 3D Registration 83
5.4.1 Algorithm 4: Multi resolution 3D registration: 86
5.4.1.1 Rigid Registration: 87
5.4.1.2 Similarity Registration: 89

5.4.1.3 Articulated Registration: 97
5.4.1.4 Non-rigid Registration: 104
5.4.1.5 Relaxation: 116
5.5 Free Form Deformation 119
5.5.1 Algorithm 5: Free form deformation: 119
5.6 Calculating Correspondence 124
5.6.1 Algorithm 6: Calculating Final Correspondence: 124
5.7 Results 127
5.7.1 Evaluating Deformation 127
5.7.2 Evaluating Correspondence 136
5.7.2.1 Validation study design: 137
6. STATISTICAL SHAPE MODEL CREATION 142
6.1 Construction of SSM ..... **Error! Bookmark not defined.**135
6.1.1 Algorithm 7: SSM Construction: 142
6.2 Results 145
7. BONE SEXING ..... **Error! Bookmark not defined.**147
7.1 Skull ..... **Error! Bookmark not defined.**147
7.1.1 Introduction ..... **Error! Bookmark not defined.**147
7.1.2 Methods ..... **Error! Bookmark not defined.**151
7.1.2.1 Sample and Data Acquisition ..... **Error! Bookmark not defined.**151
7.1.2.2 Computer Automated Analyses: Global and Local 162
7.1.2.3 Statistical Analysis and Validation 167

7.1.3 Results 168
7.1.3.1 Global Analysis 168
7.1.3.2 Local Analysis 169
7.1.3.3 Linear Discriminant Analysis 172
7.1.3.4 Validation 173
8. DIRECTIONAL ASSYMETERY 175
8.1 Clavicle 175
8.1.1 Introduction 175
8.1.2 Methods ..... **Error! Bookmark not defined.**169
8.1.2.1 Landmarking and cross-sectional analyses 179
8.1.2.2 3D surface analysis. 183
8.1.3 Results 185
8.1.3.1 Cross-sectional analyses 185
8.1.3.2 3D surface analysis 194
9. RECONSTRUCTION OF PARTIAL OR DEFORMED ANATOMY 201
9.1 Introduction 201
9.2 Methods ..... **Error! Bookmark not defined.**193
9.3 Results 205
10. KINEMATIC ANALYSIS 209
10.1 Lumbar 209
10.1.1 Introduction 209
10.1.2 Methods ..... **Error! Bookmark not defined.**202

10.1.2.1 X-ray Fluroscopy ..... **Error! Bookmark not defined.**203
10.1.2.2 Model Creation ..... **Error! Bookmark not defined.**203
10.1.2.3 3D-to-2D Registration 214
10.1.2.4 Statistical atlas and automatic landmarking.. **Error! Bookmark not defined.**205
10.1.3 Results 219
11. BONE and SOFT TISSUE THICKNESS MODELING 223
11.1 Skull Vault Thickness Modeling ..... **Error! Bookmark not defined.**213
11.1.1 Introduction ..... **Error! Bookmark not defined.**213
11.1.2 Methods ..... **Error! Bookmark not defined.**213
11.1.3 Results 226
11.2 Cartilage Thickness Modeling 230
11.2.1 Introduction 230
11.2.2 Methods ..... **Error! Bookmark not defined.**220
11.2.2.1 Dataset 231
11.2.2.2 Modeling BCI ..... **Error! Bookmark not defined.**221
11.2.3 Results 234
12. FUTURE WORK 237
12.1 Cartilage Prediction 237
12.2 Facial Reconstruction 238
12.3 Fragmentary Remains Reconstruction 240
BIBLIOGRAPHY 242
VITA 261

List of Tables

Table 4-1 Empirically determined template mesh quality 42

Table 5-1 Scale for different bones. 59

Table 5-2 Statistics of final RMS error between atlas model and original model in mm (population is the number of sample in each training set) 129

Table 5-3 Landmarks used in validation study 137

Table 5-4 Definition of measurements used for evaluation correspondence and intra-observer variability 138

Table 5-5 Correspondence validation study results for pelvis 140

Table 5-6 Correspondence validation study results for scapula 141

Table 6-1 Mean and standard deviation for the RMS error across population 145

Table 6-2 Mean and standard deviation for the RMS error across population 147

Table 6-3 Mean and standard deviation for the RMS error across population 149

Table 6-4 Mean and standard deviation for the RMS error across population 153

Table 6-5 Mean and standard deviation for the RMS error across population 154

Table 7-1 Landmarks used in skull sexing and their definitions 162

Table 7-2 Measurements definitions 165

Table 7-3 Descriptive statistics for angular measurements 170

Table 7-4 Descriptive statistics for linear measurements 171

Table 7-5 Descriptive statistics for skull vault thickness measurements. 172

Table 7-6 Results for the linear discriminant analysis. 172

Table 7-7 Measurement validation results (% error) 174

Table 7-8 Measurement validation results (t-tests) 174

Table 8-1 Contour measurements at each cross-section for males (M) and females (F) 191

Table 8-2 Asymmetry of contour measurements at each muscle attachment site for males (M) and females (F). See Table 1 for abbreviations 192

Table 8-3 Mean, standard deviation, and p-value for average medial axis angle and length asymmetry 193

Table 8-4 Significant differences between males and females in absolute asymmetry 193

Table 8-5 RMS, mean, and standard deviation for the 3D normalized and un-normalized surface analysis 195

Table 9-1 Descriptive statistics for the RMS error between reconstructed and original model in mm 205

Table 10-1 Average difference in disc height (mm) relative to the supine position during flexion-extension..... 219

Table 10-2 Average difference in disc height (mm) relative to the supine position during axial rotation 219

Table 10-3 Average difference in disc height (mm) relative to the supine position during lateral bending..... 219

Table 10-4 Average difference in disc height (mm) relative to the supine position in the left anterior quadrant 220

Table 10-5 Average difference in disc height (mm) relative to the supine position in the left posterior quadrant 220

Table 10-6 Average difference in disc height (mm) relative to the supine position in the middle anterior quadrant 220

Table 10-7 Average difference in disc height (mm) relative to the supine position in the middle posterior quadrant 220

Table 10-8 Average difference in disc height (mm) relative to the supine position in the right anterior quadrant 221

Table 10-9 Average difference in disc height (mm) relative to the supine position in the right posterior quadrant 221

Table 10-10 Average left intertransverse ligament length (mm) relative to the supine position221

Table 10-11 Average right intertransverse ligament length (mm) relative to the supine position 221

Table 10-12 Average supraspinous ligament length (mm) relative to the supine position.....222

Table 11-1 Descriptive statistics for femoral and tibial cartilage.....234

List of Figures

Figure 1-1 Proposed modeling framework 2

Figure 1-2 Manual segmentation process 3

Figure 2-1. Same shape under different transformations. 13

Figure 2-2 Landmark digitizer 15

Figure 2-3 Example of object shadowing in-Xray 16

Figure 2-4 Comparison of femoral neck angle measured in 3D and from 2D x-ray 17

Figure 3-1 Example of pelvis stastistical shape model 21

Figure 3-2 Different representation of same physical object 22

Figure 3-3 Mesh-to-volume registration 24

Figure 3-4 Bootstrap approach for mesh to volume registration 25

Figure 3-5 Volume to volume registration 26

Figure 3-6 Multi resolution B-Splines and normalized mutual information metric for registration 27

Figure 3-7 Parameterization to parameterization registration approach 28

Figure 3-8 Use of mutual information over curvature features for registration 28

Figure 3-9 Fourier descriptor statistical atlas 28

Figure 3-10 Population based optimization registration approach 30

Figure 3-11 Building optimal 2D SSMs 30

Figure 3-12 Mesh to mesh registration approach 31

Figure 3-13 Creation of statistical atlas using free form deformation 32

Figure 4-1 Atlas creation steps 35

Figure 4-2 Polygonal mesh representation 37
Figure 4-3 Indexed face set structure 38
Figure 4-4 Winged-edge list 38
Figure 4-5 Half-edge structure 38
Figure 4-6 Fixing mesh degeneracy 40
Figure 4-7 Input mesh, detected degeneracy and output mesh 40
Figure 4-8 Mesh Quality as a measure of different triangle resolution 41
Figure 4-9 Effect of mesh quality on landmarks 42
Figure 4-10 Inconsistency in internal surface 44
Figure 4-11 Process of adding skull to atlas 44
Figure 4-12 Example of mesh segmentation 44
Figure 4-13 Mesh segmentation algorithm 47
Figure 4-14 Feature generation algorithm 47
Figure 4-15 Evolution of ecto & endo cranial surface during segmentation process 48
Figure 4-16 Final segmented surfaces 48
Figure 5-1 Different types of noise 50
Figure 5-2 High-level algorithm of adding new bone to atlas 50
Figure 5-3 Scaling using bounding box dimensions 53
Figure 5-4 Scaling using centroid size 53
Figure 5-5 Comparing registration errors for vertebra using each of the normalization methods 53
Figure 5-6 Comparing registration errors for pelvis using each of the normalization methods 54

Figure 5-7 Distance map showing registration error using each of normalization method 54
Figure 5-8 Image at different scale space 59
Figure 5-9 Scale space and normal space skull 59
Figure 5-10 Scale space and normal space scapula 60
Figure 5-11 Scale space and normal space lumbar 60
Figure 5-12 Scale space and normal space pelvis 61
Figure 5-13 Osculating circle 63
Figure 5-14 Principal curvature 66
Figure 5-15 Neighborhood notations for gauess-bonett schema 68
Figure 5-16 Shape classes based on values of shape index (S) 72
Figure 5-17 Extracting features in normal scale 74
Figure 5-18 Calculating mesh shape descriptors in scale space 75
Figure 5-19 Extracting features in scale space 75
Figure 5-20 Feature extraction in scale space (lumbar) 77
Figure 5-21 Feature extraction in normal scale (lumbar) 77
Figure 5-22 Feature extraction in scale space (pelvis) 78
Figure 5-23 Feature extraction in normal scale (pelvis) 79
Figure 5-24 Feature extraction in scale space (scapula) 80
Figure 5-25 Feature extraction in normal scale (scapula) 81
Figure 5-26 Feature extraction in scale space (skull) 82
Figure 5-27 Feature extraction in normal scale (skull) 82
Figure 5-28 Multi resolution 3D registration algorithm overview 86

Figure 5-29 Rigid registration 88

Figure 5-30 Rigid alignment (TM-Pink) and (NM-Purple) 89

Figure 5-31 Similarity registration 90

Figure 5-32 Similarity registration on L1 lumbar (green represents$\boldsymbol{TMridges}$. , Red $\boldsymbol{TMridges}$ after registration, yellow $\boldsymbol{NMridges}$) (cm) 94

Figure 5-33 Similarity registration on pelvis (green represents$\boldsymbol{TMridges}$. , Red $\boldsymbol{TMridges}$ after registration, yellow $\boldsymbol{NMridges}$) (cm) 95

Figure 5-34 Similarity Registration on scapula (green represents$\boldsymbol{TMridges}$. , Red $\boldsymbol{TMridges}$ after registration, yellow $\boldsymbol{NMridges}$) (cm) 96

Figure 5-35 Articulated registration algorithm overview 98

Figure 5-36 Matching features pair 101

Figure 5-37 Matching feature pairs (L5 lumbar) 101

Figure 5-38 Articulating registration on lumbar L1 102

Figure 5-39 Articulating registration on pelvis 102

Figure 5-40 Articulating registration on scapula 103

Figure 5-41 Articulating registration on skull 103

Figure 5-42 Overview of non-rigid registration step 104

Figure 5-43 Scale Invariant Weighted Matching registration algorithm 106

Figure 5-44 Comparison of SIWM performance against ICP on lumbar in scale space 108

Figure 5-45 Comparison of SWIM performance against ICP on lumbar in original space 109

Figure 5-46 Results of feature points registration on lumbar spines process in scale space 109

Figure 5-47 Registration of feature points using SIWM in original space 110

Figure 5-48 Comparing registration results for pelvis in scale space 110

Figure 5-49 Comparing registration results for pelvis in original space 111
Figure 5-50 Registration using SIWM for pelvis in scale space 111
Figure 5-51 Registration using SIWM for pelvis in original space 112
Figure 5-52 Registration results on scapula in scale space 112
Figure 5-53 Results of non-rigid registration on pelvis 114
Figure 5-54 Results of non-rigid registration on skull 114
Figure 5-55 Results of non-rigid registration on lumbar L1 115
Figure 5-56 Results of non-rigid registration on scapula 115
Figure 5-57 Overview of relaxation step 117
Figure 5-58 Results of relaxation on pelvis 117
Figure 5-59 Results of relaxation on skull 118
Figure 5-60 Results of relaxation on lumbar L1 118
Figure 5-61 Results of relaxation on scapula 119
Figure 5-62 Overview of the free form deformation step 120
Figure 5-63 Results of free form deformation on scapula 122
Figure 5-64 Results of free form deformation on pelvis 122
Figure 5-65 Results of free form deformation on skull 123
Figure 5-66 Results of free form deformation on lumbar L1 123
Figure 5-67 Overview of correspondence calculation step 125
Figure 5-68 Results after correspondence on pelvis 125
Figure 5-69 Results after correspondence on skull 126
Figure 5-70 Results after correspondence on lumbar L1 126

Figure 5-71 Results after correspondence on scapula 127

Figure 5-72 RMSE map between atlas model and original model for skull 130

Figure 5-73 RMSE map between atlas model and original model for pelvis 131

Figure 5-74 average RMSE map between atlas model and original model for clavicle 131

Figure 5-75 RMSE map between atlas model and original model for scapula 132

Figure 5-76 RMSE map between atlas model and original model for L1 132

Figure 5-77 RMSE map between atlas model and original model for L2 133

Figure 5-78 RMSE map between atlas model and original model for L3 133

Figure 5-79 RMSE map between atlas model and original model for L4 134

Figure 5-80 RMSE map between atlas model and original model for L5 134

Figure 5-81 Atlas output for a pelvis with Severe deformity (case 1) 135

Figure 5-82 Atlas output for a pelvis with Severe deformity (case 2) 135

Figure 5-83 Atlas output for a L1 lumbar with Severe deformity (case 1) 136

Figure 5-84Comparison of landmarks used for validation of correspondence on pelvis 139

Figure 5-85 Comparison of landmarks used for validation of correspondence on scapula 139

Figure 6-1 Constructing SSM from training set 143

Figure 6-2 RMS vs. % accumulated variance for scale normalized and non-normalized female and male pelvis SSM 145

Figure 6-3 Average distance map for reconstructed models using leave one out test 146

Figure 6-4 Accumulated variance vs. number of coefficients of the overall normalized and non-normalized pelvis SS 146

Figure 6-5 RMS vs. % accumulated variance for scale normalized and non-normalized pelvis SSM 147

Figure 6-6 Average distance map for reconstructed models using leave one out test.....148

Figure 6-7 Accumulated variance vs. number of coefficients of the overall normalized and non-normalized scapula SSM.....148

Figure 6-8 RMS vs. % accumulated variance for scale normalized and non-normalized female and male skull SSM.....149

Figure 6-9 Average distance map for reconstructed models using leave one out test.....150

Figure 6-10 Accumulated variance vs. number of coefficients of the overall normalized and non-normalized skull SSM.....150

Figure 6-11 RMS vs. % accumulated variance for scale normalized and non-normalized L1 to L5 SSM.....151

Figure 6-12 Average distance map for reconstructed models using leave one out test.....152

Figure 6-13 Accumulated variance vs. number of coefficients of the overall normalized and non-normalized skull SSM.....153

Figure 6-14 RMS vs. % accumulated variance for scale normalized and non-normalized male and female clavicle SSM.....154

Figure 6-15 Average distance map for reconstructed models using leave one out test.....155

Figure 6-16 Accumulated variance vs. number of coefficients of the overall normalized and non-normalized clavicle SSM.....155

Figure 7-1 Flow chart outlining the design of the skull sexing analysis.....161

Figure 7-2 Flow chart outlining methodology of calculating automated measurements.....166

Figure 7-3 Sequence of automatic landmark calculations.....166

Figure 7-4 Results of global 3D surface analysis (principal components 1 through 5).....168

Figure 7-5 Results of global 3D surface analysis for combined principal components 1 through 40.....170

Figure 8-1 The two-step feature extraction methodology used to identify asymmetry within and between the sexes.....180

Figure 8-2 Calculating landmarks, cross-sectional contours, and the medial axis 181

Figure 8-3 Flow chart showing the identification of the muscle attachment sites and contour calculations at these sites 182

Figure 8-4 3D surface analysis performed to identify asymmetry 184

Figure 8-5 Histogram of maximum length and cross-sectional contours at 10% increments and maximum length. Asymmetry is presented as a count variable, where values >50 are right-biased and <50 are left-biased 187

Figure 8-6 Contour differences at 10% increments, where 10% = lateral end and 90% = medial end. The vertical direction is anterior-posterior, and the horizontal direction is superior-inferior 189

Figure 8-7 Histogram of cross-sectional contours at muscle attachment sites. Asymmetry is presented as a count variable, where values >50 are right-biased and <50 are left-biased. See Table 1 for abbreviations 190

Figure 8-8 Contour differences at muscle attachment sites. The vertical direction is anterior-posterior, and the horizontal direction is superior-inferior 190

Figure 8-9 . Morphological differences between a left and right clavicle from an individual male and female in this study sample (pink=right, blue=left) 195

Figure 8-10 Un-normalized distance map showing the average distance between homologous points on the left and right clavicles for the entire population 196

Figure 8-11 Normalized distance map showing the average distance between homologous points on the left and right clavicles for the entire population 197

Figure 8-12 Surface map showing significant differences between the left and right clavicles based on the p-values from paired sign tests 199

Figure 8-13 Surface map of thresholded p-values (p>0.1=red and p<0.1=blue) with super-imposed muscle attachment sites (green) 200

Figure 9-1 An example of pelvis discontinuity 204

Figure 9-2 Process of reconstructing full bone from partial anatomy 204

Figure 9-3 Simulating three different types of complexities 205

Figure 9-4 Average RMS distance map between reconstructed surface and original surface for the three complexities 206

Figure 9-5 Volume render for real test patient with pelvis discontinuity 207

Figure 9-6 surface model for real test patient with pelvis discontinuity 207

Figure 9-7 Real bone (yellow) vs. reconstructed bone (purple) and right innominate flipped 208

Figure 9-8 Distance map showing different between real anatomy vs. Right bone and vs. reconstructed bone 208

Figure 10-1 Fluoroscopic image captured during flexion-extension activity for a healthy lumbar spine captured (from left to right) at full extension, neutral, mid-flexion, and maximum flexion 213

Figure 10-2 The process of overlaying: starting to fit (left) and finished spinal frame (right) 214

Figure 10-3 Flow chart for the analysis 215

Figure 10-4 Propagation of contact points using statistical atlas 216

Figure 10-5 Division of the contact area on the vertebral surface into six defined parts 217

Figure 10-6 Automatic calculation of the supraspinous and intertransverse ligament attachment sites 218

Figure 10-7 Tracking of the ligament length across the full range-of-motion during flexion-extension 218

Figure 11-1 algorithm for soft tissue and bone thickness modeling 224

Figure 11-2 Localizing point on base mesh for vault thickness calculation 225

Figure 11-3 Calculation of vault thickness 225

Figure 11-4 Skull vault thickness mean map (mm) 227

Figure 11-5 Skull vault thickness standard deviation map (mm) 228

Figure 11-6 Areas of high variation (right), thickness bias (Left) 229

Figure 11-7 Cartilage modeling algorithm 230

Figure 11-8 Bone cartilage distance calculation 232

Figure 11-9 Femur vertices BCI histogram count and probability density estimate 232

Figure 11-10 Tibia vertices BCI histogram count and probability density estimate 233

Figure 11-11 Calculated bone cartilage interface 233

Figure 11-12 Femoral cartilage mean and stand deviation map (mm) 235

Figure 11-13 Tibial cartilage mean and stand deviation map (mm) 236

Figure 12-1 Cartilage prediction using non-parametric kernel regression 238

Figure 12-2 Facial reconstruction using SSM of bone and soft tissue thickness 239

Figure 12-3 Proposed method for facial reconstruction using soft tissue and bone thickness SSM 239

Figure 12-4 Rendered facial reconstruction 240

Figure 12-5 Overview of proposed method for fragmentary remain reconstruction 241

ABREVIATIONS AND SYMBOLS

2D	Two Dimensional
3D	Three Dimensional
CADX	Computer Aided Diagnosis
CAD	Computer Aided Design
TM	Template Model
NM	New Model
NS	Normal Scale
SS	Scale Space
MRI	Magnetic Resonance Imaging
CT	Computed Tomography
SSM	Statistical Shape Model
CAS	Computer Aided Surgery
PCA	Principal Component Analysis
PDF	Point Distribution Model
ASM	Active Shape Model
GA	Genetic Algorithm
SSA	Statistical Shape Atlas
MDL	Minimum Description Length
ICP	Iterative Closest Point
GPA	Generalized Procrustes Analysis
DXA	Dual-energy X-ray Absorptiometry
QCT	Quantitative Computed Tomography
BMI	Body Mass Index
HFI	Hyperostosis Frontalis Interna
PDM	Point Distribution Method
FCM	Fuzzy C Means
RANSAC	Random Sample Consensus
RMSE	Root Mean Square Error
RRMSE	Relative Root Mean Square Error
SVD	Singular Value Decomposition
SIWM	Size Invariant Weighted Matching
DICOM	Digital Imaging and Communications in Medicine
LDA	Linear Discriminant Analysis
MSM	Muscle Stress Markers
%DA	Percent Directional Asymmetry
%AA	Percent Absolute Asymmetry

MNI	Minimum Number of Individuals
MLNI	Most likely Number of Individuals
MNE	Minimum Number of Elements
OIS	Osteological Information System
GIS	Geographic Information System
THA	Total Hip Arthroplasty
HLBP	Healthy with Low Back Pain Group
LBP	Low Back Pain
ROM	Range of Motion
BCI	Bone Cartilage Interface

1. INTRODUCTION

1.1 Motivation

Advances in the field of medical imaging in recent years have transformed medical care in regards to both research and commercial aspects. Acquiring information about patient anatomy from either magnetic resonance imaging (MRI), computer tomography (CT), ultrasound (US) and x-ray has become an essential part in computer aided diagnosis (CADx), treatment planning, surgical preplanning, as well as prosthetics design. Morphometric analyses are currently being used in the fields of biomedical engineering and anthropology for identifying shape differences and capture variations in populations. However, the majority of these methods lack automation in the process of defining landmarks. Additionally, none of these methods address cases with degenerative bone or deformed anatomy. Generating accurate correspondence is a key component in automating landmark calculation and building of a statistical shape model (SSM). The core of proposed framework is a novel 3D to 3D registration technique and deformation method (Atlas Creation) which allow for the accurate generation of dense surface correspondence across populations, even in the presence of bone deformity or irregular bone growth. Figure 1-1 highlights the proposed framework where a set of training models is added to the atlas to generate correspondence; the resultant models can then be used to either build SSMs by capturing modes of variation or to propagate landmarks loci for automatic landmark calculation. These landmarks can then be used to perform a traditional morphometric by calculating measurements or a surface-based morphometric. This

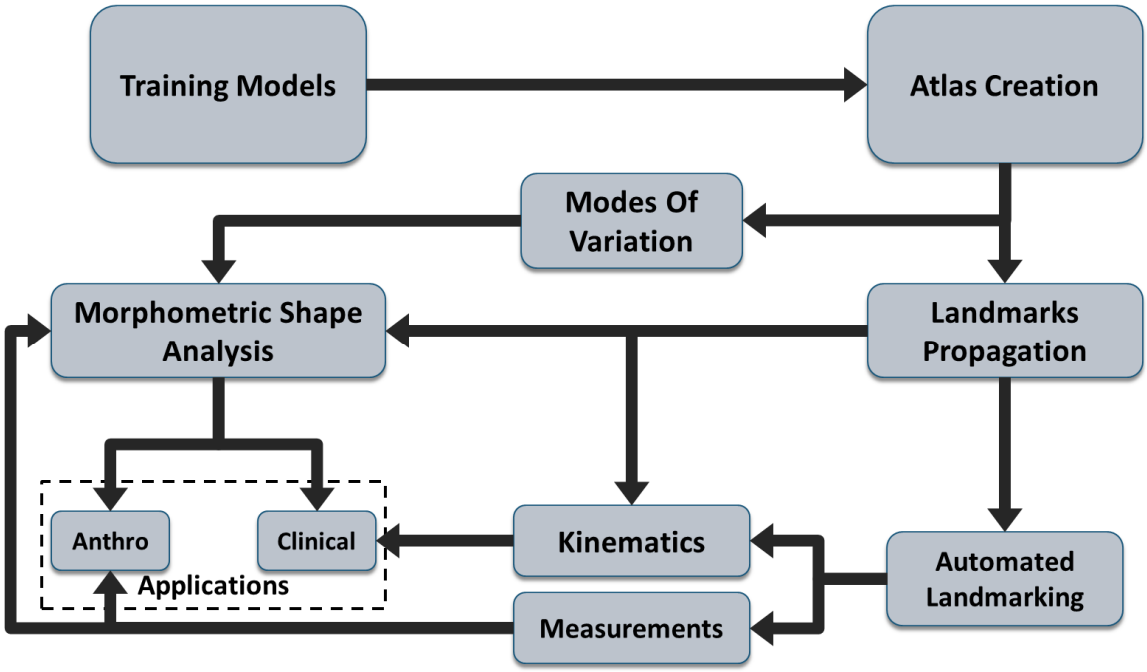


Figure 1-1 Proposed modeling framework

has various applications in anthropology for demographic estimation or partial bone reconstruction. Likewise, applications within the medical field could potentially be utilized in prosthetic design or kinematic tracking.

1.2 Background

The far reaching potential for CADx and medical imaging, especially in the area of Computer Aided Surgery (CAS), is becoming increasingly prevalent as doctors continue to access high technology equipment and advanced 3D graphics systems in the medical field. Availability of such new tools to doctors is bringing an unprecedented accuracy and reliability to patient treatment. Recently, use of medical imaging has expanded even further, and morphometric data from different populations are used to design more anatomical prosthetic

devices. Outside the medical field, imaging is being actively used in forensics to extract biological profiles of recovered deceased individuals. Availability of digital images from various skeletal collections has enabled computers to determine morphometric differences across populations by tracking secular changes or identifying evolutionary traits.

In all these applications, the fundamental step is the extraction of anatomical structures from the images using segmentation. This can be a time consuming step, especially in cases where manual segmentation is required, wherein an expert segments the regions or structures in a given set of images by hand. Figure 1-2 shows the overall process for segmentation of a radius from a CT scan. Interpolation is performed between each slice in the set of segmented images to create a 3D model. The resulting surface is a triangular representation of the interfaces of the segmented bone. Initially, the generated model is rough, but smoothing can reduce the number of triangles, or faces, along the surface of the bone.

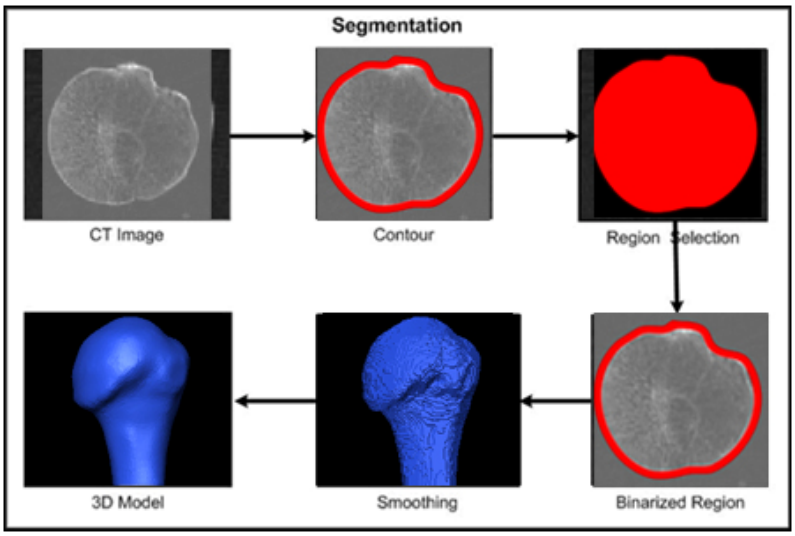


Figure 1-2 Manual segmentation process

1.2.1 Statistical Atlases for Segmentation

As previously described, manual segmentation is a time consuming and labor intensive process, especially in cases of volumetric data, such as CT or MRI. Aside from these disadvantages, in cases of structures with low contrast, it is also prone to inter- and intra-observer error. In order to enhance and speed up the segmentation process, different automatic and semi-automatic algorithms have been developed. Segmentation can be divided into two main categories: image or model-based.

In image-based segmentation, also known as "top-down," local structures from images like edges, corners and ridges are extracted using either gray scale or gradient information. This is then used as input in a generic segmentation scheme which labels the structures found in the image. Different segmentation methods can be classified under this category, such as thresholding which creates binary partitions of image intensity s[1] and region growing [2, 3] [4]. The classifier method of segmentation utilizes features extracted from an image to partition data with known labels during a training phase and then uses the output trained classifier to partition unknown data[5]. Clustering performs the same functionality as the classifier method, but for data with unknown prior labels [6-8]. The most significant drawbacks for these methods are the sensitivity to initialization or image quality occasionally yielding non meaningful information especially in the presence of noise.

Since active shape models were first introduced by Cootes and Taylor[9] as a means to incorporate a priori shape information, their use in the segmentation of medical images has

drastically increased. A SSM is constructed by considering the canonical representation of a set of similar shape instances, or training shapes. Performing a principal component analysis (PCA) on these shapes highlights the statistical modes of variation in the shape, allowing for a possible reduction in the dimension of the model shape space. A well-constructed statistical model will provide a shape constraint on subsequent segmentations of new images.

Different active shape model (ASM) schemes were introduced for segmentation. Duta[10] utilized point distribution models (PDMs) to segment and interpret deep neuroanatomic structures. such as thalamus, putamen, ventricular system in magnetic resonance (MR) brain images. Ginneken [11] utilized a nonlinear, k nearest neighbor classifier to find the optimal displacements for landmarks using a multi-resolution scheme. He determined a set of optimal features at each resolution level during the optimization procedure of segmentation. Features were then selected using sequential forward and backward feature selection. Bruijne [12]utilized both shape and active appearance models for segmentation of tubular objects. He adapted the original formulation of an ASM by modeling the axis deformation independent of the cross-sectional deformation, and by adding supplementary cylindrical deformation model. He also used a non-parametric estimation method for determining probability of boundary and non-boundary points. Van Assen [13] utilized 3D ASM for segmentation of the left ventricle from both CT and MRI. In his approach, he utilized a fuzzy c-means inference system guided by ASM. McIntosh [14] utilized a shape model with genetic algorithms (GA) for a segmentation of corpus callosum from MRI brain images. Berg,

et.al [15] utilized active contours driven by a shape model generated from Fourier descriptors of training database to segment images of the knee from MRI and CT. Merkl et.al[16] used a 3D ASM to guide bones' edges extracted from gray scale gradients from CT images.

1.2.1.1 Reconstruction

While use of ASM started in segmentation, its capabilities are well beyond just segmentation. With the ability of ASM to capture anatomical variation across populations while expressing such variation in smaller numbers of principal components, it may also be used as a mean for interpolating missing information and reconstructing patient-specific bones from sparse data. For example, sparse data could be a point cloud acquired intra-operatively using optical or electromagnetic trackers or in a case of bone morphing[17] or ultrasound signal with ecomorphing [18, 19].

Reconstruction of 3D patient-specific, anatomical models from 2D data, such as still x-ray or fluoroscopic images, is one of the current active research areas. In its essence, this method optimizes a similarity measure assessing the difference between projections of the shape model and the x-ray images[20]. Mahfouz et.al[21] utilized a 3D ASM to optimize a deformable model to match information extracted from two x-ray views. A GA was used to minimize a cost function for both edge and area of the generated shape. Kadoury [22] adopted a similar approach where he utilized 3D database of scoliotic patients to reconstruct a training set that was used to reconstruct 3D models from two biplanar x-ray images of patient spine. Humbert [23] proposed a new method for 3D reconstruction of both shape and bone mineral

density distribution for the proximal femur from dual-energy x-ray absorptiometry (DXA) images. In his algorithm he utilized an active appearance model that was reconstructed from database of quantitative computed tomography (QCT). Chaibi et.al [24] proposed the use of parametric models and statistical inferences from biplanar x-rays with clinical measurements as a way to asses patient anatomy in the standing position in a clinical setting.

1.2.2 Statistical Atlases in Morphometric

Aside from their use in segmentation and reconstruction, ASM models play an important role in capturing morphological variations among populations. This has direct applications in anthropology as well as the medical field. By applying strong statistical techniques, such as PCA, certain 3D morphological variations of anatomical features can be quantified across various populations. Mahfouz et. al pioneered this field wherein SSA was utilized to study sexual dimorphism in adult femora [25], which was used in design of gender-specific knee prosthetics. ASM, along with nonlinear classifiers, were used to detect sex from patella [26]. Recently SSA were also used to study morphological variation in the femur and the tibia across multiple ethnicities [27]. Mahfouz et. al utilized correspondence generated during the reconstruction of ASM as a method for propagating landmark loci; thus, automating calculation of boney landmarks, which has an advantage of removing intra and inter-observer error. Such automation of landmarks has direct applications in both prosthetic device[28] design , preplanning for surgical navigation, [29]and studying variations across populations with large number of samples [30].

1.3 Contributions

Theoretical elements of several principal disciplines have been integrated into the development of the statistical atlas and generation of correspondence presented here, including differential geometry, computer vision, pattern recognition, signal processing and image processing. This research has produced extensive fundamental contributions in both theory and application, such as the development of a new algorithm for mesh segmentation and partitioning. This includes the use of this algorithm for separating the skull into ecto- and endo-cranial surfaces, where output from the ecto-cranial model was used as input for the SSA to examine the external cranial morphology. Endo-cranial models are used to investigate internal cranial structures, as well as to assess brain imprints used for tracking secular changes.

A novel method for creating an SSA and generating dense correspondence across populations for complex anatomical structures in presence of severe bone deformity was also developed. This method utilizes scale space and multi-resolution registration to ensure accurate correspondence between anatomical features even in circumstances where anatomy is deformed or missing. The output of the method is validated on different anatomical structures, including the skull, pelvis, scapula, and the lumbar. The results were evaluated on three levels: 1) deformation and shape matching, 2) accurate anatomical correspondence, and 3) the validation of generalization and compactness of the output. These SSMs were generated using correspondence from the developed SSA mentioned earlier.

Accurate SSMs for the skull and clavicle and corresponding automated landmarking were developed for each of these. The applications for these in the assessment of ecto- and endocranial morphology and investigation of 3D asymmetry for the clavicle were conducted. Using this analysis, 97.3% accuracy was achieved in skull sexing, which exhibits improved classification rates over those currently published. This method for the clavicle adds to existing literature as the first complete 3D surface analysis for studying asymmetry.

Accurate pelvis and vertebrae SSMs were also developed and resultant applications were revealed. For the pelvis, full anatomical structure from deformed and partial anatomy was reconstructed and the methods were validated on partial data that simulated various bone conditions, as well as on actual patient-specific data with pelvis discontinuity. The vertebrae SSM generated correspondence to study morphology, disc spacing, and ligaments and their relation to kinematics between different groups of patients (normal, low back pain, degenerative and fusion). For the development of the bone and soft tissue 3D SSM, its application in modeling the skull vault's thickness for sexual dimorphism and its relation to Hyperostosis Frontalis Interna (HFI) was also discussed. Additionally, this 3D SSM for bone and soft tissue was applied to well articulating cartilage thickness in knee.

1.4 Organization

Chapter 2 introduces the concept of morphometrics and shapes, as well as traditional morphometric and various kinds of landmarks and their classification. A discussion of geometric, morphometric and other methods that fall under this category also follow. These

methods include: shape coordinates, superimposition method, thin-plate spline, outline method, voxel based, surface based, and deformation based.

Chapter 3 introduces statistical shape models (SSMs) and components needed to reconstruct a valid shape model. This includes shape representation, alignment, and generating shape correspondence. Next, different methods for generating shape correspondence, including Mesh-to-Volume, Volume-to-Volume, Parameterization-to-Parameterization, Population-based Optimization, and Mesh-to-Mesh Registration are discussed. This chapter ends with a discussion of criterions used for evaluation of SSM, such as generalization, specificity, and compactness.

Chapter 4 outlines the building blocks in the development of the proposed framework for morphological analysis using SSA, their creation, mesh representation, mesh constraints, and template mesh quality. Details of the newly developed method for mesh segmentation to manage irregular and inconsistent anatomy, including that of the skull, are then related, followed by an introduction to the concept of automatic landmarking.

Chapter 5 discusses the method for the creation of SSA in detail, including the various methods used for testing initial alignment. The concepts of multiscale and scale space are introduced, followed by discussion of the algorithm developed for feature extraction, matching and registration. The constrained deformation algorithm and generation of correspondence across shapes is disclosed. Finally, results of the atlas creation algorithm for the lumbar, clavicle, skull, pelvis and scapula and the evaluation of correspondence are likewise revealed.

Chapter 6 presents the use of generated models after correspondence in the creation of SSMs, including feature reduction and PCA. Discussions of the results of generated SSMs for the skull, pelvis, vertebrae, and clavicle, are disclosed, as well as evaluation of generalization, compactness and specificity.

Chapter 7 focuses on the application of SSM in bone sexing for the skull sexing. This chapter discusses the relevant literature and existing research, methods used for analysis followed by results and findings.

Chapter 8 concentrates on the application of SSM in studying directional asymmetry in the clavicle by introducing relevant literature and background for the problem, followed by methods used, outline of the results and discussion.

Chapter 9 depicts the application of SSM in restoration of partial or deformed anatomy, specifically in the area of pelvis reconstruction. There is a discussion of relevant clinical literature and existing systems, followed by an outline of the methods, concluded by results and discussion.

Chapter 10 focuses on the application of SSM in the modeling lumbar bones, intervertebral disc,as well as locations of tendons and ligaments. It first introduces relevant literature to lumbar kinematics and the limitations of existing methods. It then discusses details of the method implemented for lumbar tracking and contact analysis. Next, it outlines the results of analysis and discusses these results.

Chapter 11 focuses on the use of SSM for modeling of bone and soft tissue thickness and its application for skull vault thickness and cartilage modeling.

Chapter 12 discusses future work and applications for statistical atlases .

2. MORPHOMETERIC

The term "Morphology" comes from the Greek word μορφή or morphé = form and λόγος or lógos = study, which is the qualitative analysis of shape differences (i.e., study of form and structure) using images and detailed description. On the other hand, morphometrics deals with the quantitative analysis of shapes using measurements and numbers[31]. Although there are differences in definition between morphology and morphometrics, they both attempt to identify the differences in shapes across different populations or extract the statistical variations of shapes around average shapes of certain populations [32]. The most adapted definition for shape is one by Kendall [33]: "Shape is all the geometrical information that remains when location, scale, and rotational effects are filtered out from an object." This defines shape independent from its scale, orientation and location in space depicted in Figure 2-1.

By adopting this general definition of shape, shapes can have multiple descriptions depending on the encoding and embedding of the object.

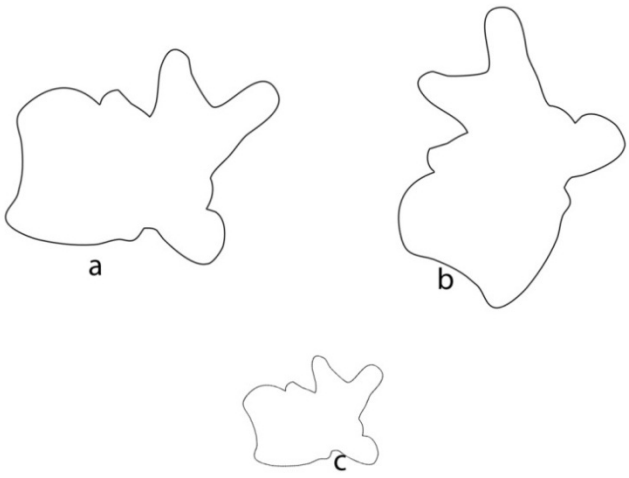


Figure 2-1. Same shape under different transformations.

2.1 Traditional Morphometric

In traditional morphometrics, shapes are described using measurements: length, width, mass, angles, ratios, or areas. In order to perform some of these measurements (length, width, or ratios), a set of landmarks must be defined on the object to measure. A landmark is a point of correspondence on each object that matches between and within populations[33]. Currently, there are two systems for landmark classification [33].

2.1.1 Landmarks Classification

Landmark Classification I:

- ***Anatomical Landmark:*** a point assigned by an expert that corresponds between organisms in some biologically meaningful way (e.g., the corner of an eye). Anatomical landmarks designate parts of an organism that correspond in terms of biological derivation and these parts are known as homologous.
- ***Mathematical Landmark:*** a point located on an object according to some mathematical or geometrical property (e.g., point of high curvature, extreme point, etc.).
- ***Pseudo-Landmark:*** a constructed point on an organism located either around the outline or in between anatomical or mathematical landmarks.

Landmark Classification II:

- ***Type I Landmark:*** a point that occurs at joints of tissues/bones.

- ***Type II Landmark:*** a point defined by local properties (e.g., maximum curvature).
- ***Type III Landmark:*** a point that occurs at an extreme point or a point that represents a constructed landmark (e.g., centroids).

These two systems can be related to each other in the following manner:

- Anatomical Landmark - Type I or Type II Landmark.
- Mathematical Landmark - Type II or Type III Landmark.
- Pseudo-Landmark - Type III Landmark.

These landmarks and measurements were traditionally taken using calibers, but recent use of digitizers has increased as a means to collect landmarks (Figure 2-2). The use of calibers and digitizers is vulnerable to intra- and inter-observer error. This method also has limited access to anatomical features, especially internal features, unless an autopsy is performed. Collecting large numbers of measurements and landmarks is also time consuming.



Figure 2-2 Landmark digitizer

X-ray has also been used as a method for capturing shape geometry and calculating measurements directly from radiographs. This approach possesses a significant limitation: x-ray is a 2D projection of 3D structures, and thus, a dense object can shadow structures behind it, as shown in Figure 2-3. Projection of objects in x-ray depends on the relative rotation angle between the object and the imaging plane which can affect the measurements. Figure 2-4 depicts a previous analysis [28] that investigated the effect of object rotation relative to the x-ray plane on measuring the femoral neck angle.

The use of traditional morphometrics is restricted in that two different shapes can result in the same measurements. Additionally, it is not possible to reconstruct a full graphical representation of the shape from measurements acquired by traditional morphometrics. This method is also only capable in capturing size while using normalized ratios.

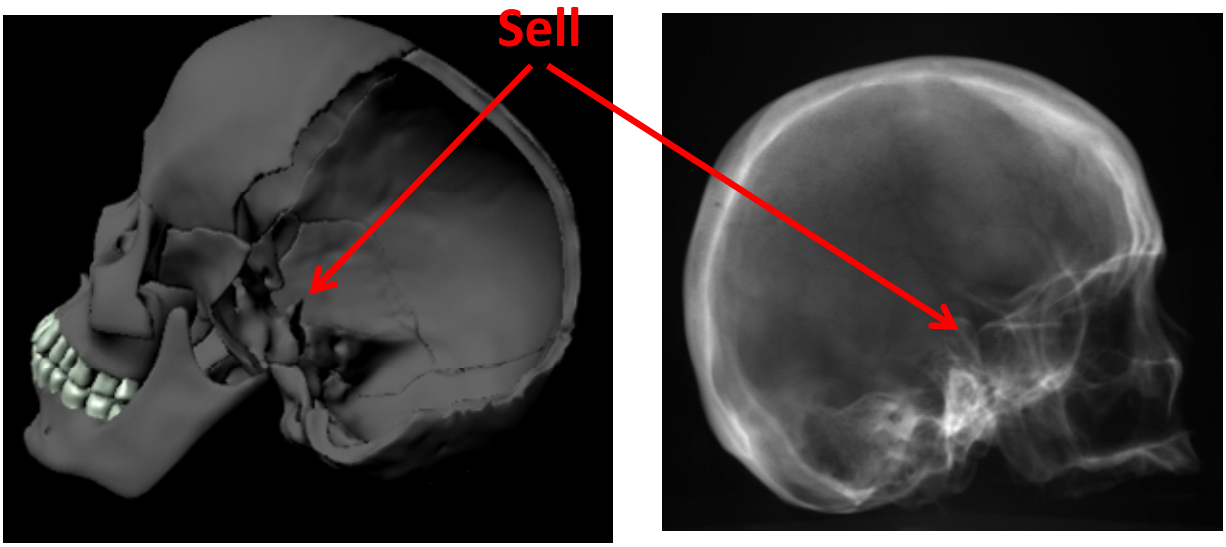


Figure 2-3 Example of object shadowing in x-ray

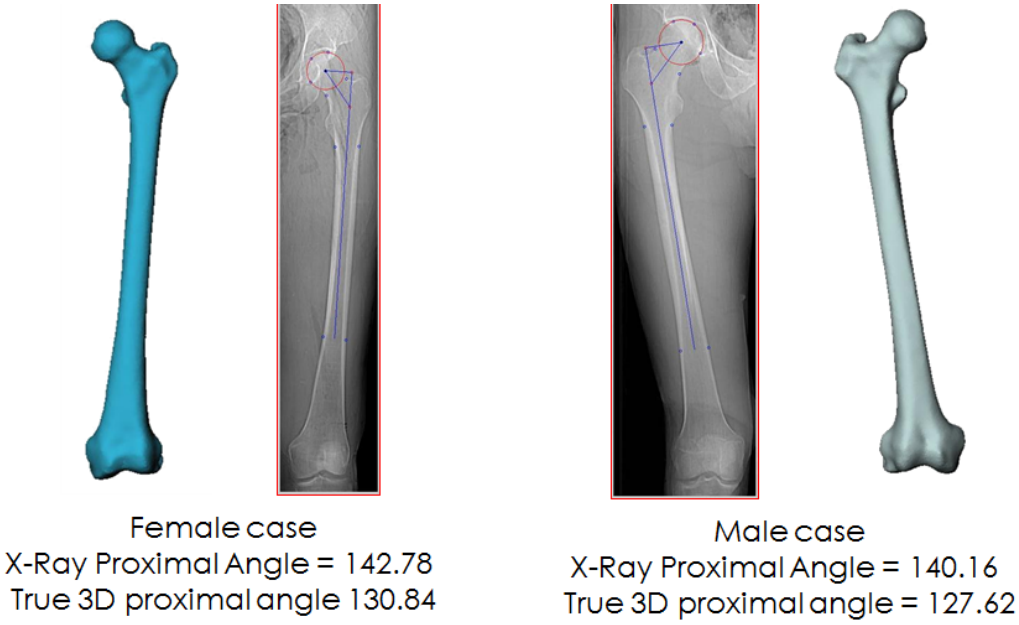


Figure 2-4 Comparison of femoral neck angle measured in 3D and from 2D x-ray

2.2 Geometric Morphometric

Since the early 1980s, the modern field of geometric morphometrics has emerged as a fusion of geometry and biology as a means to analyze biological forms in a way that preserves the physical integrity of this form in 2D or 3D. The most popular form of geometric morphometrics is analyzing landmark coordinates by acquiring a set of homologues landmarks acquired from each shape. Theses landmarks' coordinates are then normalized to scale and used to calculate the mean and the variation of landmarks around it. A summary of different methodologies that have emerged for geometric morphometrics is provided below.

2.2.1 Shape Coordinates Method

Analysis based on standardizing positions of all landmarks relative to a baseline defined by two landmarks with coordinates set to (0,0 and 0,1) [34]. Shape coordinates are also referred to as Bookstein coordinates. For *k* landmarks, *k*-2 coordinates can be derived for a given baseline.

2.2.2 Superimposition Method

The most commonly adopted method to align landmark coordinates utilizes generalized procrustes analysis (GPA) [35, 36] by fitting all *k* landmark points for *n* specimens using various fitting procedures (e.g., least squares, resistant fit). The resulting superimposed data represent shape information free of scale, rotation, and position. GPA iteratively aligns specimens and estimates the mean until convergence; the detailed steps are provided below:

1) Choose an initial estimate of the mean shape.
2) Align all the remaining shapes to the mean shape.
    a. Align centroid shapes to origin.
    b. Normalize scale to eliminate effect of size (a common approach is to normalize centroid size to unit length [3]).

$$S = \sum_{j=1}^{n} \sqrt{(x_j - \bar{x})^2 + (y_j - \bar{y})^2}$$

    c. Calculate rotation using least square fit that best align each shape with mean.
3) Re-calculate the estimate of the mean from the aligned shapes.
4) Check change in mean shape for convergence.

2.2.3 Thin-Plate Spline Method

This method was first adopted to analyze deformations of metal sheets. It is suitable for transforming one coordinate system into another and visualizes the variation[37]. The parameters of the thin-plate spline transformation can be used to explore shape changes between objects (relative warp analysis).

2.2.4 Outline Method

This method is analysis based on multivariate analyses of landmarks and pseudo-landmarks defined by physical boundaries of objects (Cartesian coordinate points of outlines) [38, 39]. Fourier transform is then calculated for each of these boundaries and multivariate analysis is performed on the Fourier coefficients. The foremost limitation of this approach is the absence of internal shape data.

2.2.5 Voxel Based Method

This approach is primarily utilized in neuroimaging to capture variations of brain anatomy using statistical parametric mapping [40]. A preprocessing step maybe performed on the MRIs of the brain; the input, fitted to a template removes most of the significant differences in brain anatomy among people. The brain images are then smoothed so that each voxel represents the average of itself and its neighbors. Finally, the image volume is compared across brains at every voxel.

2.2.6 Surface Based Method

Widely used in identifying changes in brain anatomy, the surface based method first segments brain structures to generate a surface model. A group of brain morphometrics techniques are then used to construct and analyze theses surfaces which represent structural boundaries within the brain [41].

2.2.7 Deformation Based Method

Non-linear registration algorithms are used to register volumes of brain images in the deformation based method; statistical analyses are then performed on the deformation fields used to register them [42].

3. STATISTICAL SHAPE MODELS

Initially used as a basis for guiding image segmentation, SSMs are a means to capture prior knowledge about the shape being segmented [43]. The prime objective in SSMs is the establishment of point's correspondence across a set of n training shapes. This correspondence is used to generate a mean model and then calculate the models of variation around this mean model as shown in Figure 3-1

3.1 Components of Valid Shape Model

3.1.1 Shape Representation

A physical object can have more than one representation in shape space. Shapes can be represented by discrete landmarks PDM, volume, and parametric or polygonal surface, as is shown in Figure 3-2.

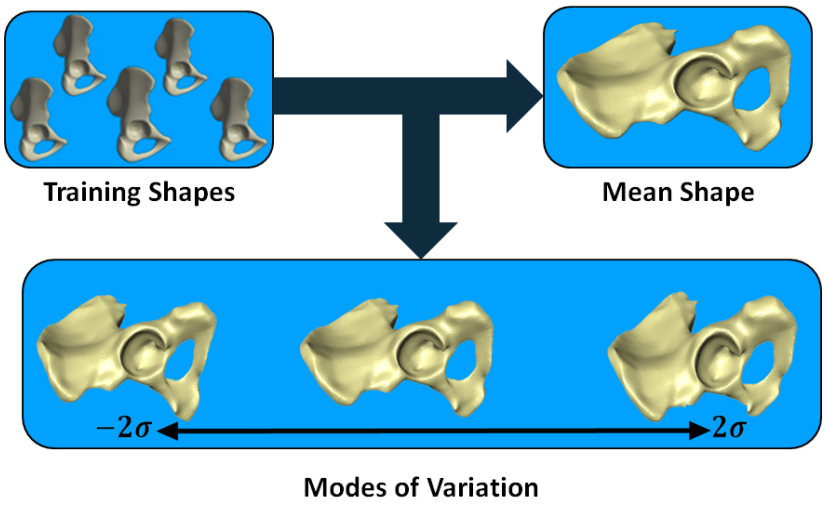


Figure 3-1 Example of pelvis stastistical shape model

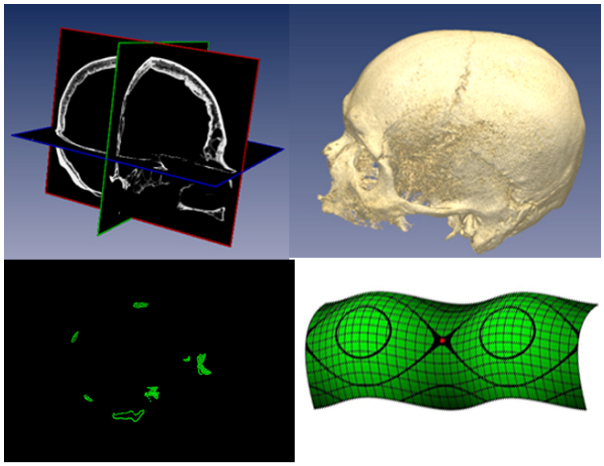


Figure 3-2 Different representation of same physical object

3.1.2 Alignment

As noted earlier, shapes should not change with rotation, translation or uniform scale. In order to build a compact and valid, general SSM, it should be ensure that these incidents do not occur and all shapes are thus aligned; occasionally, changes in sizes are treated as anatomical variations[25, 44], otherwise shapes have to be normalized in size. Usually, GPA[35] is used as a method for alignment by minimizing the mean squared distance between shapes. Another method used is the minimum description length optimization for shape alignment [45].

3.1.3 Dimensionality Reduction

In order to efficiently capture statistics across a training set, a dimensionality reduction step is required. This involves finding a set of modes that best represents the variation in the training dataset. PCA [46] has been the main method to capture such variation. So, given a set of n training shapes, the mean shape is calculated, followed by calculation of the covariance matrix

S. Calculating the Eign values of S gives PCs which will be a maximum of (n-1); each of these components capture variation in certain area of shape. Usually, a variance threshold is set to determine the number of principal components needed to achieve this variance.

3.2 Generating Shape Correspondence

Shape correspondence is an important factor in the production of a valid SSM. Importance of correspondence, however, expands beyond SSM as it can be used as a method for propagating landmarks for automated measurements [25, 26], as well as kinematic tracking.

The task of generating correspondence is the most challenging part of building the SSM. The first attempts were made by manually picking points on 2D shapes. However, due to lack of reproducibility and high intra- and inter-observer error, this approach was no longer used [47]; when it comes to three dimensions, this task is very time-consuming with many contributing factors affecting selection. To automatically calculate correspondence, a registration step is required between training shapes. The main categories of registration are found, and each of them uses a different representation of shape space to minimize the registration error.

3.2.1 Mesh-to-Volume Registration

In this approach, the training sets are volumetric data (CT or MRI). In the original approach, binary volumes were created from the input training sets. The template mesh are then aligned with each volume and deformed to match the object of interest. Upon conversion,

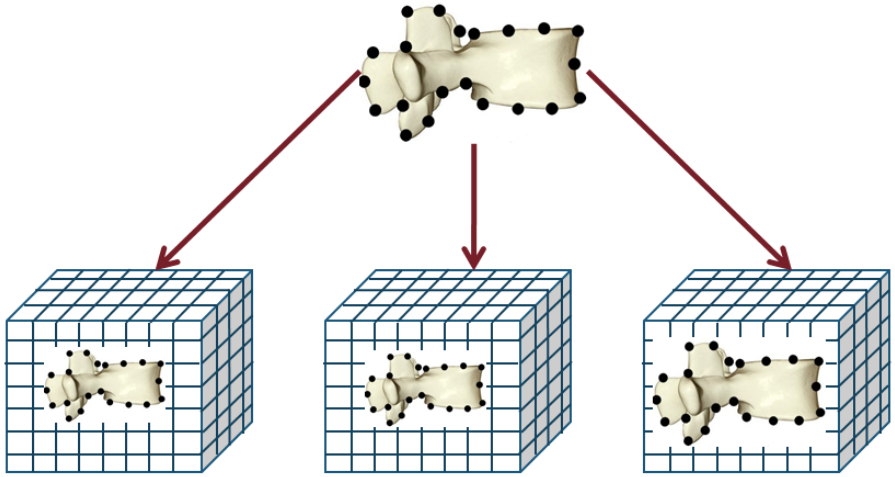


Figure 3-3 Mesh-to-volume registration

the template mesh should closely match the training set. The correspondence is then defined by the vertices location on the deformed template mesh, as shown in Figure 3-3.

Later attempts utilized the original volumetric data instead of binaries, segmenting the object of interest while generating correspondence[48]. Bootstrapping is another approach used [49], in which an SSM was used to segment training data and iteratively refine correspondences. A flow chart of this approach is shown in Figure 3-4.

The guarantee of homeomorphic mapping without the occurrence of self-folding is a significant advantage of this correspondence approach [47]. No correspondence is generated during segmentation so it is not necessary to pre-segment models. The results are also considerably influenced by the object's type, as well as the quality of input images, and are sensitive to the initial alignment of the template with volume. There must also be volumetric data.

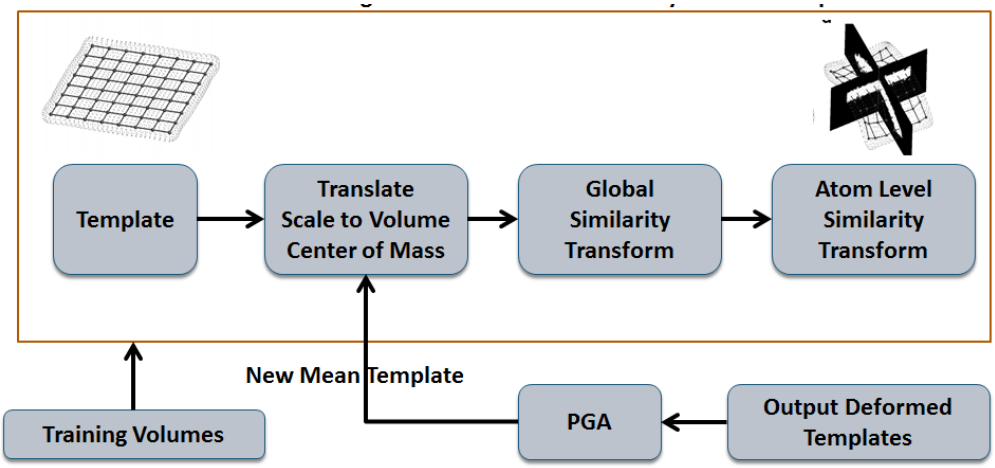


Figure 3-4 Bootstrap approach for mesh to volume registration

3.2.2 Volume-to-Volume Registration

In the volume-to-volume registration approach, both the training set and the template consist of volumetric data. In this method, intensity information is used to register the template volume with the training set. Resulting deformation fields are then used to move landmarks that were previously defined on the template mesh. The new location of landmarks after applying the deformation fields are considered to be the new corresponding landmarks that belong to the training set, see Figure 3-5.

Another approach was developed [50] where a multi-resolution B-spline and a normalized mutual information metric were used to register the template volume to the training volume. Although SSMs were not constructed using landmarks in this approach, the deformation fields were used in their place.

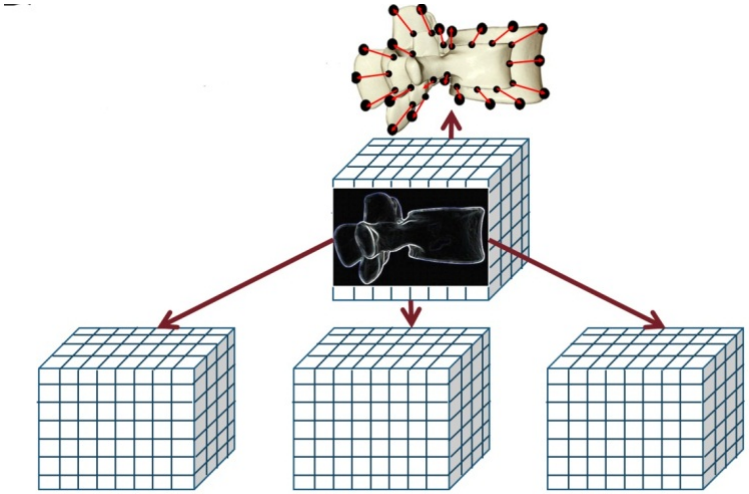


Figure 3-5 Volume to volume registration

The most significant benefit of this approach is that it contains volumetric information (i.e., internal surface structure) and no segmentation is required. However, there are substantial disadvantages as well, including large errors, especially when shapes are not similar. This approach requires ample processing time and more computing power. Altering the lattice resolution was attempted to remedy this, but this adjustment affects the resolution of deformation, reflecting even poorer registration quality [47].

3.2.3 Parameterization-to-Parameterization Registration

In this approach, shapes are mapped to the base domain using a bi-jective function. In 2D, the most common domain is a circle, and correspondence can be generated by determining points of similar arc-length. In 3D, this process becomes more complex and dependent upon the topology of the surface. This raises a significant limitation for this approach as most of the methods are limited to objects that are orientated with spherical common base domain [47].

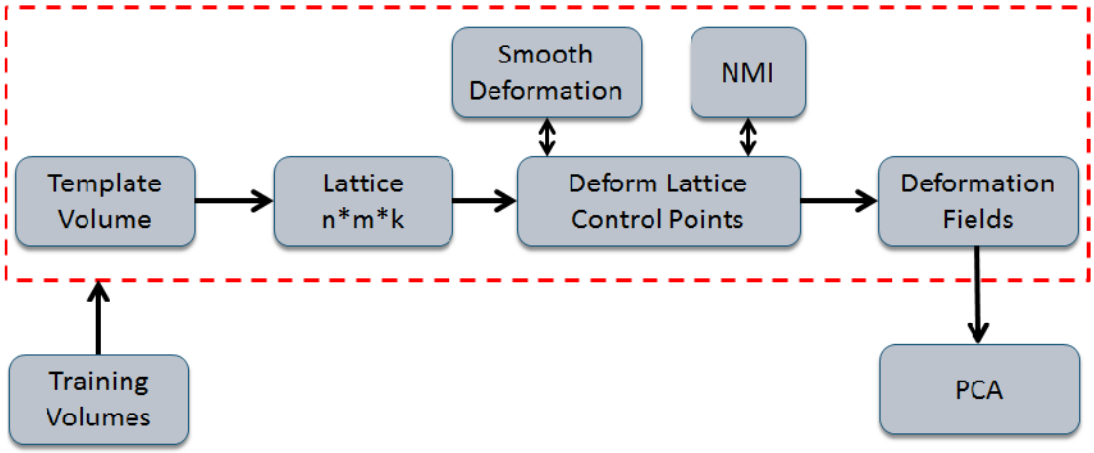


Figure 3-6 Multi resolution B-Splines and normalized mutual information metric for registration

First, shapes are parameterized, landmarks are defined and matching in the base domain is performed. Landmarks are then transferred back to the surface using an inverse mapping function. See Figure 3-7.

In order to make the method independent of topological genus, Wang, et.al calculated curvature features over all training surfaces and optimized a mutual information metric on the corresponding parameterizations. In this approach, all shapes are automatically divided into the required number of patches, making the method independent of the topological genus[51], as shown in Figure 3-8. Berg et.al conducted a different approach where Fourier descriptors were calculated on a set of 2D contours for the distal femur. PCA was then performed on the Fourier coefficients, see Figure 3-9 [15].

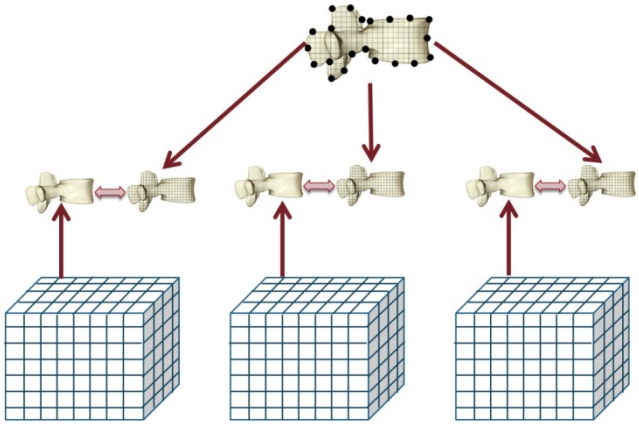


Figure 3-7 Parameterization to parameterization registration approach

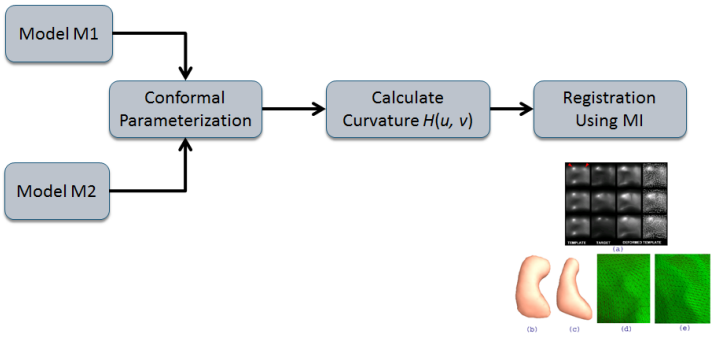


Figure 3-8 Use of mutual information over curvature features for registration

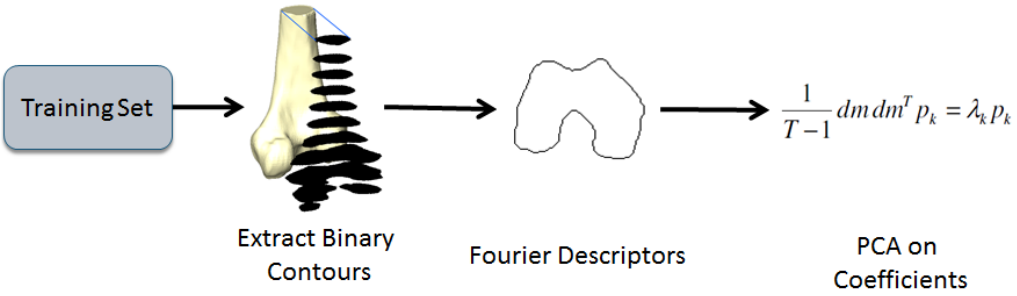


Figure 3-9 Fourier descriptor statistical atlas

This approach is independent of the topological genus when surface is divided into small batches and results are guaranteed to be homeomorphic. Selecting the right parameterization function proved to be difficult, and required initial landmark selection on parametric template. However, the most significant disadvantages of this approach are its limitations to objects with spherical mapping in cases of spherical harmonics and that it requires smooth, orientable surfaces as input.

3.2.4 Population-Based Optimization

The population-based optimization approach originated from the hypothesis that the best correspondence is the one that generates the most compact SSM (i.e., fewer modes). It involves the same initial steps as parameterization-to-parameterization, which includes mapping of all shapes into a common base domain and defining landmarks in that base domain. However, it differs by iteratively changing correspondence by optimizing the re-parameterization function using a cost function that describes the quality of SSM. See Figure 3-10.

Taylor, et.al [52] were the first to develop a method to optimize correspondence by minimizing an objective function based on the determinant of the covariance matrix S. This approach, however, had no theoretical sounding and did not converge in all the cases. To resolve this, Davis, et.al developed an optimization function based on minimum description length (MDL) which originates from information theory. Information theory states the best model is the one that describes training data as efficiently as possible [47] see Figure 3-11.

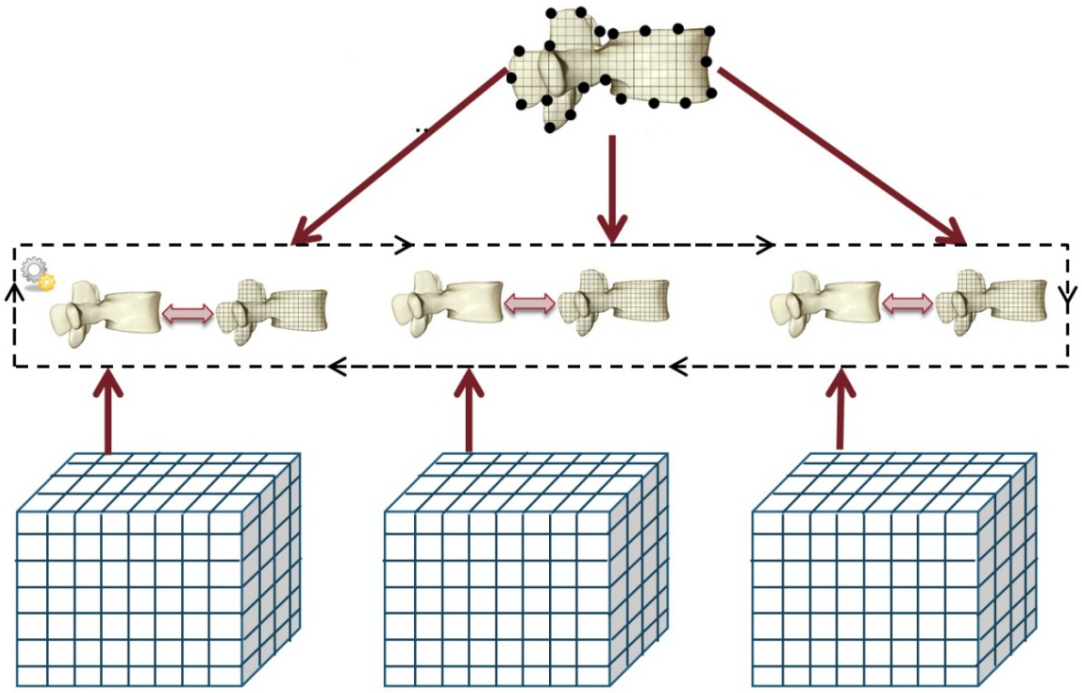


Figure 3-10 Population based optimization registration approach

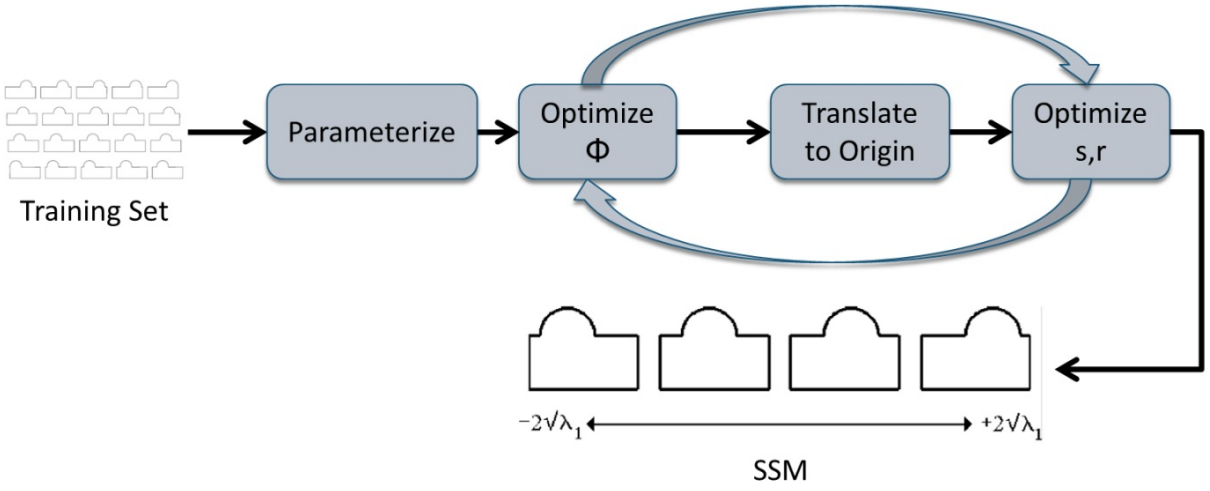


Figure 3-11 Building optimal 2D SSMs

This approach makes the best use of training data, as it not only considers only pairs of shapes, but also samples them simultaneously. However, it shares some of the same disadvantages as the parameterization-to-parameterization approach: choosing the right parameterization function; limitation to objects with spherical mapping; and requiring smooth orientable surfaces as input. Other drawbacks of this approach are that re-parameterization is calculated with each new model added and significant processing time and power are required since it utilizes optimization.

3.2.5 Mesh-to-Mesh Registration

In this approach, surface models are first extracted from training sets, a template model is then fitted to all the training surfaces, propagating landmarks and defining correspondence see Figure 3-12.

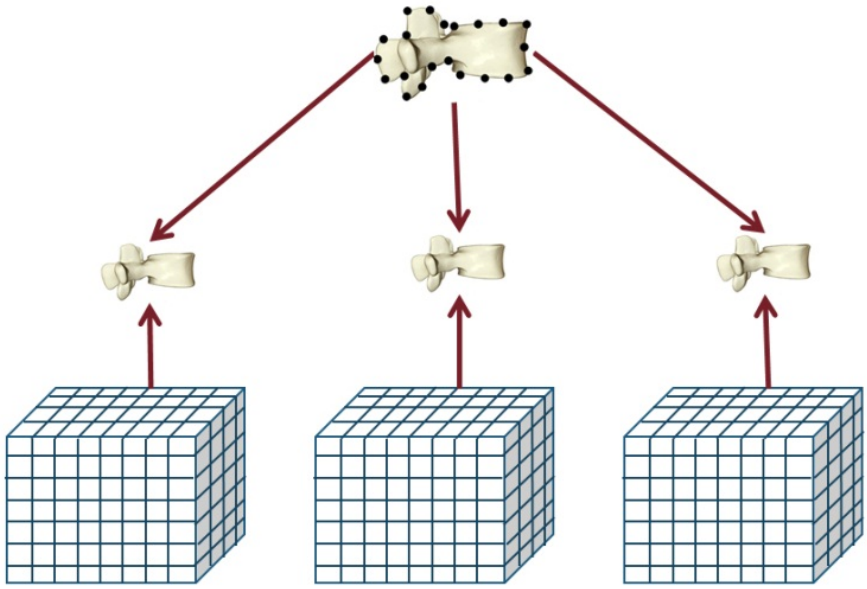


Figure 3-12 Mesh to mesh registration approach

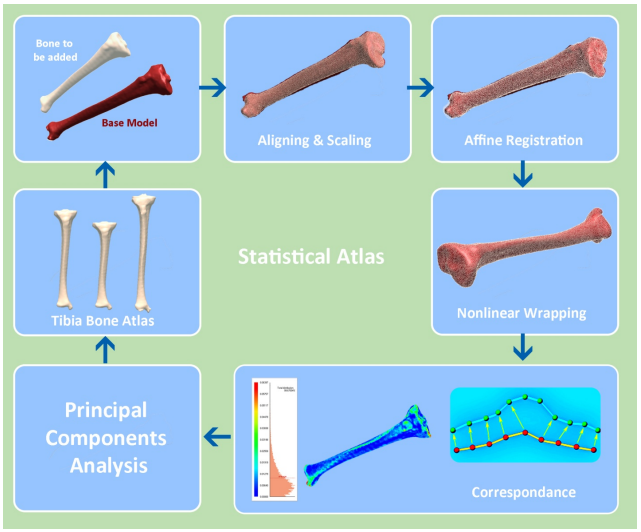


Figure 3-13 Creation of statistical atlas using free form deformation

The simplest form of this approach starts with surface registration techniques as iterative closest point (ICP) [53], which requires two surfaces with a different number of points and outputs - the transformation that best registers the two sets together. However, this simple approach does not offer accurate correspondence and suffers from bias error based on the selection of the template model. Mahfouz et.al developed a method for generating correspondence which involves deforming a template surface model to match the training sets by projecting back and forth between the template model and the training model[25]. This approach achieved good results in long bones, see Figure 3-13.

This approach is the fastest compared to the previous approaches, and also it performs pair wise matching whereby no retraining must be done for each additional new model. It also does not require a constraint on the nature of the training shape. Disadvantages are its production of non-homeomorphic mappings and degenerative triangles in certain situations.

Likewise bias can be introduced by choosing the template model. Also standard point matching algorithms restricted to similarity transform isnot adequate for population with large variations.

3.3 Evaluation

The next step in building a SSM is evaluation of the model's performance. There are three criteria used to evaluate performance of any SSM.

3.3.1 Generalization:

Generalization evaluates the capability of the model to represent new shapes. The model should be able to describe all shapes of the class, not only those of the training set.

$$G(n_m) = \frac{1}{n_s}\sum_{j=1}^{n_s} \left\| x_j - x'_j\ (n_m) \right\|^2$$

Where:

n_m : Number of modes used to construct the shape

n_s : $Number\ of\ samples\ in\ the\ SSM$

x_j : Model left out

x'_j : Reconstructed Model from SSM

3.3.2 Specificity:

Specificity evaluates the validity of the shapes produced by the model. The model can only represent shapes from the shape class for valid parameter values.

$$S(n_m) = \frac{1}{N}\sum_{j=1}^{n_s} \left\| y_j - y'_j\ (n_m) \right\|^2$$

Where:

y'_j : Shape example generated by the model

y_j : Nearest model in the training data to

n_m : Number of modes used to construct the shape

N : Number of generated models

3.3.3 Compactness:

Compactness evaluates the accumulative variance of the model. The model should represent all shapes of the class with as little variance as possible in the shape variation modes and preferably with few modes.

$$C(n_m) = \sum_{j=1}^{n_m} \lambda_j$$

a. Where:

b. λ_j : Variance in shape mode j

c. n_m : Number of modes

4. DEVELOPMENT OF MORPHOMETRIC FRAMEWORK USING STATISTICAL ATLASES

Most of the various, previously introduced methods for morphometric analysis lack automation in the process of defining landmarks. None of these methods address cases with degenerative bone or deformed anatomy. Generating accurate correspondence is a key component in automating landmark calculation and in building SSMs. The core of the proposed framework is a novel 3D to 3D registration and deformation method (Atlas Creation) which allow for the accurate generation of dense surface correspondence across populations, even in the presence of bone deformity or irregular bone growth.

4.1 Atlas Creation

The atlas creation process involves adaptation of a template mesh to accurately match an input training model to be added to atlas. This adaptation will generate accurate dense points and surface correspondence, as shown in Figure 4-1. Chapter 5 will reveal additional details about atlas creation.

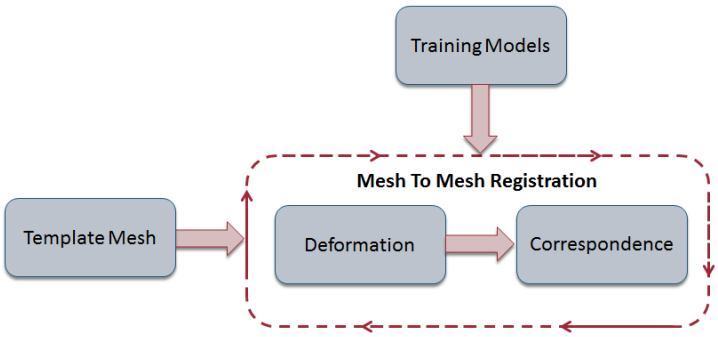


Figure 4-1 Atlas creation steps

4.1.1 Mesh Representation

Template and training shapes are triangular mesh models, as shown in Figure 4-2. A mesh is a Pair of (P,K) where P is a set of points (Mesh Geometry).

In this case p_i is embedded in 3D Euclidian space R^3. K is a simplicial complex that contains topological information (Mesh Connectivity)

K is a set of:

- Vertices $v = \{i\} \in V$
- Faces $f = \{i_1, \dots\dots, i_{nf}\} \in F$
  - In our case triangular mesh $f = \{i_1, i_2, i_3\}$
- Edges $e = \{i, j\} \in E$
- $K = V \cup F \cup E$

Satisfying that:

- Each edge must belong to at least one face:

$$e = \{i, j\} \in E \; iff \; \exists \; f = \{i_1, \dots., j, k, \dots., i_{nf}\} \in F$$

- Each vertex must belong to at least one edge:

$$V = \{j\} \in V \; iff \; \exists \; e = \{i, j\}$$

Different data structures have been developed over the years to represent meshes and wall into two main categories: Face-Based, as indexed face sets, and Edge-Based, as winged-edge list and half edge (Figure 4-5). In indexed face sets, two lists are structured and stored one contains face information and the other contains point coordinates.

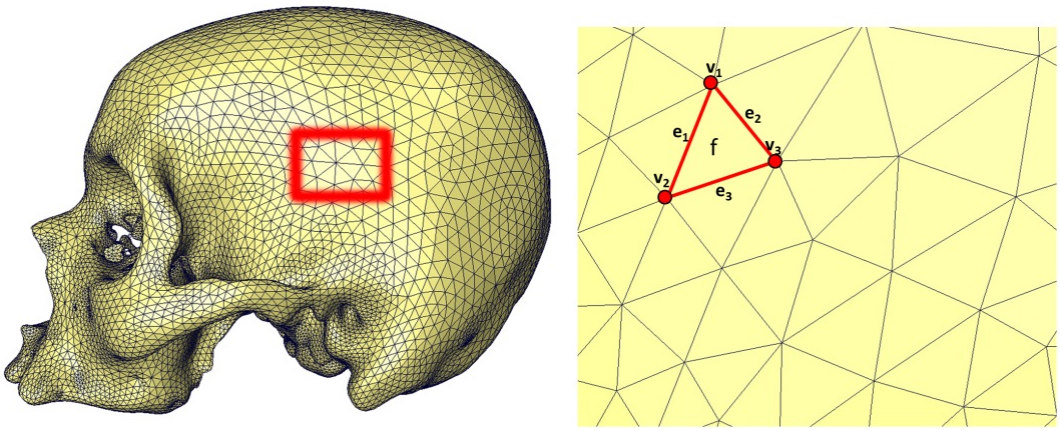


Figure 4-2 Polygonal mesh representation

It is a compact representation, but there is no topological information (Figure 4-3). Winged-edge was introduced by Baumgart in 1975, and it explicitly represents the vertices, faces, and edges of a mesh (Figure 4-4), whereby split and merge operations can be conducted quickly. Their primary drawback is the large storage requirement. There is also increased complexity due to the maintenance of many indices; fixed orientation has to be assumed before navigating. The half-edge structure splits each edge into a pair of half edges [54] , see Figure 4-5. The half-edge data structure overcomes the problem of search speed in case of neighborhood operations; it can represent different topological structures (triangles and quadrangles). It also solves the orientation problem, assuming an orientation before navigation, associated with winged-list. Since the 3D/3D registration and mesh deformation requires heavily neighborhood queries, half-edge structure was the structure of choice for both speed and compactness.

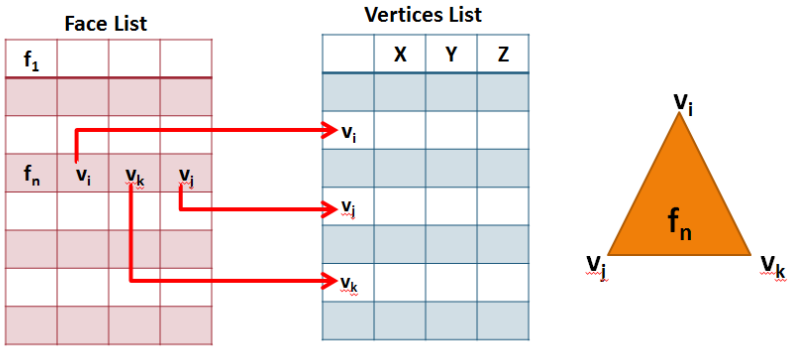
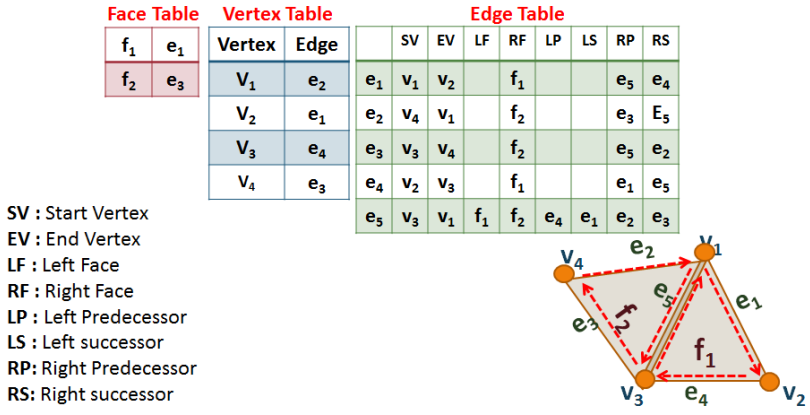


Figure 4-3 Indexed face set structure

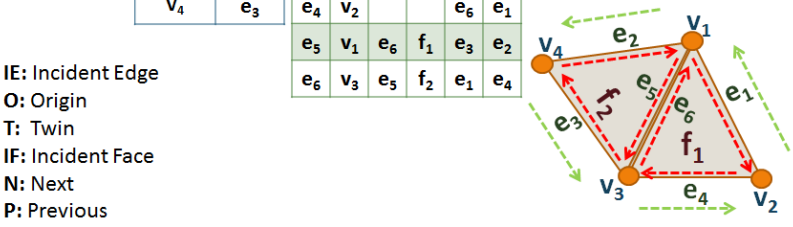


f_1	e_1
f_2	e_3

Vertex	Edge
V_1	e_2
V_2	e_1
V_3	e_4
V_4	e_3

	SV	EV	LF	RF	LP	LS	RP	RS
e_1	v_1	v_2		f_1			e_5	e_4
e_2	v_4	v_1		f_2			e_3	E_5
e_3	v_3	v_4		f_2			e_5	e_2
e_4	v_2	v_3		f_1			e_1	e_5
e_5	v_3	v_1	f_1	f_2	e_4	e_1	e_2	e_3

Figure 4-4 Winged-edge list



f_1	e_1
f_2	e_3

Vertex	IE
V_1	e_2
V_2	e_1
V_3	e_4
V_4	e_3

	O	T	IF	N	P
e_1	v_1			e_4	e_6
e_2	v_4			e_5	e_3
e_3	v_3			e_2	e_5
e_4	v_2			e_6	e_1
e_5	v_1	e_6	f_1	e_3	e_2
e_6	v_3	e_5	f_2	e_1	e_4

Figure 4-5 Half-edge structure

4.1.2 Mesh Constraints

A mesh can be generated from different sources, as each source generates a different type of mesh. A mesh can be any of the following type:

A. Registered Range Scans
B. Fused Range Scans
C. Triangle Soups
D. Triangulated NURBS Patches
E. Contoured Meshes
F. Badly Meshed Manifolds

In this application the only applicable two types are:

Contoured Meshes: Extracted from volumetric data segmentation and are usually manifold. Associated artifacts are spurious handles, disconnected components, duplicate vertices, and cavities.[55]

Badly Meshed Manifolds: Generated by tessellation of computer aided design (CAD) models, or as output models of marching cube like algorithms enhanced by edge preserving techniques. Artifacts associated with it are triangles with zero area, needles, caps, triangle flips, and duplicate vertices [55].

These artifacts can affect the quality of registration algorithm, and thus, a preprocessing step is required to fix any model degeneracy. Figure 4-6 depicts a flow chart of detecting artifacts and fixing model degeneracy. Figure 4-7 shows an example of input skull mesh and detected degeneracy and output fixed mesh.

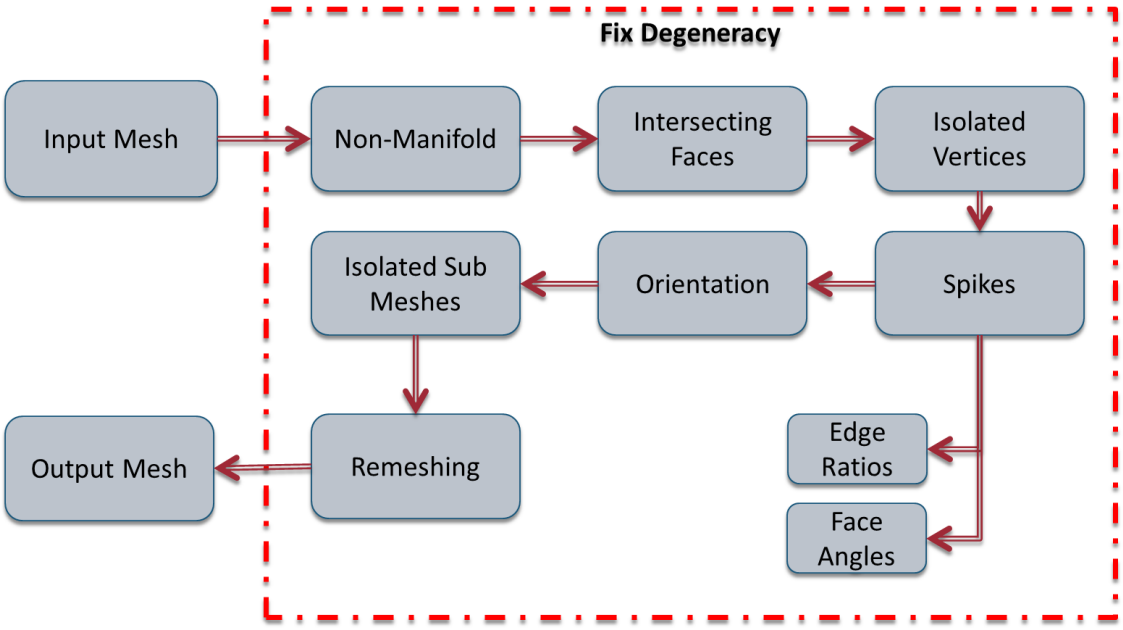


Figure 4-6 Fixing mesh degeneracy

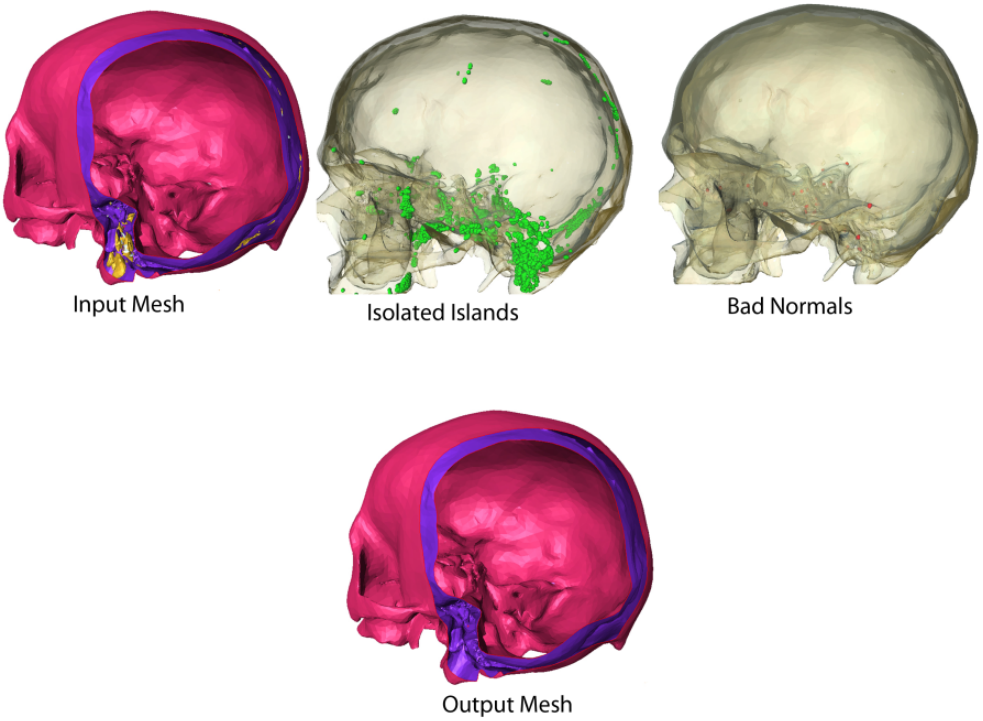


Figure 4-7 Input mesh, detected degeneracy and output mesh

4.1.3 Template Mesh Quality

Mesh quality includes the resolution of the mesh (number of faces and vertices) see Figure 4-8, as well as the smoothness of the surface. The quality of the template mesh can affect the landmark distribution in the atlas and can also cause washing out of the landmarks. Figure 4-9 shows the effect of mesh quality on the accuracy of calculated landmarks.

The mesh quality can have a considerable impact on the computational analysis in terms of the quality of the solution and the time needed to obtain it. This aspect becomes especially important if poorly conditioned problems, non-linear, and/or transient analysis are considered. From this point of view, the evaluation of the quality of the mesh is very useful because it provides some indication of how suitable a particular discretization is for the analysis type . Different experiments were conducted to find the best mesh quality that guarantees smooth, high resolution surface. Mesh quality for different bones are shown in Table 4-1 Empirically determined template mesh quality.

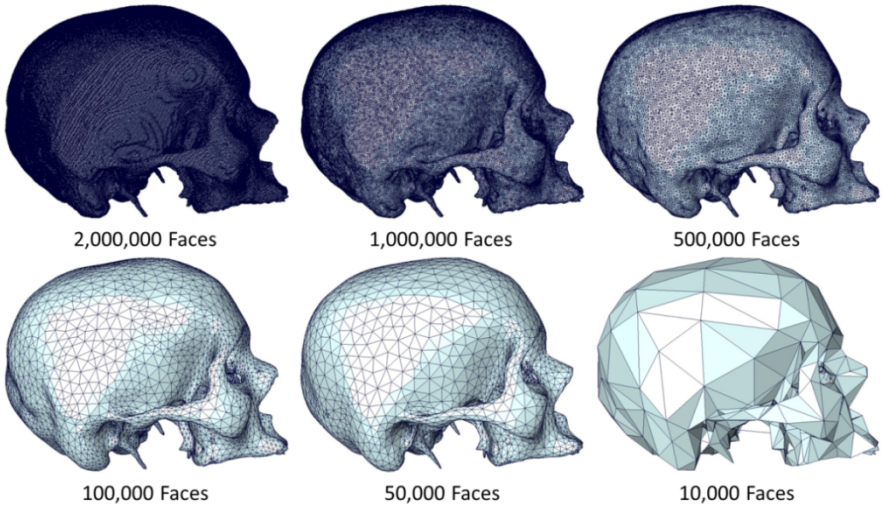


Figure 4-8 Mesh Quality as a measure of different triangle resolution

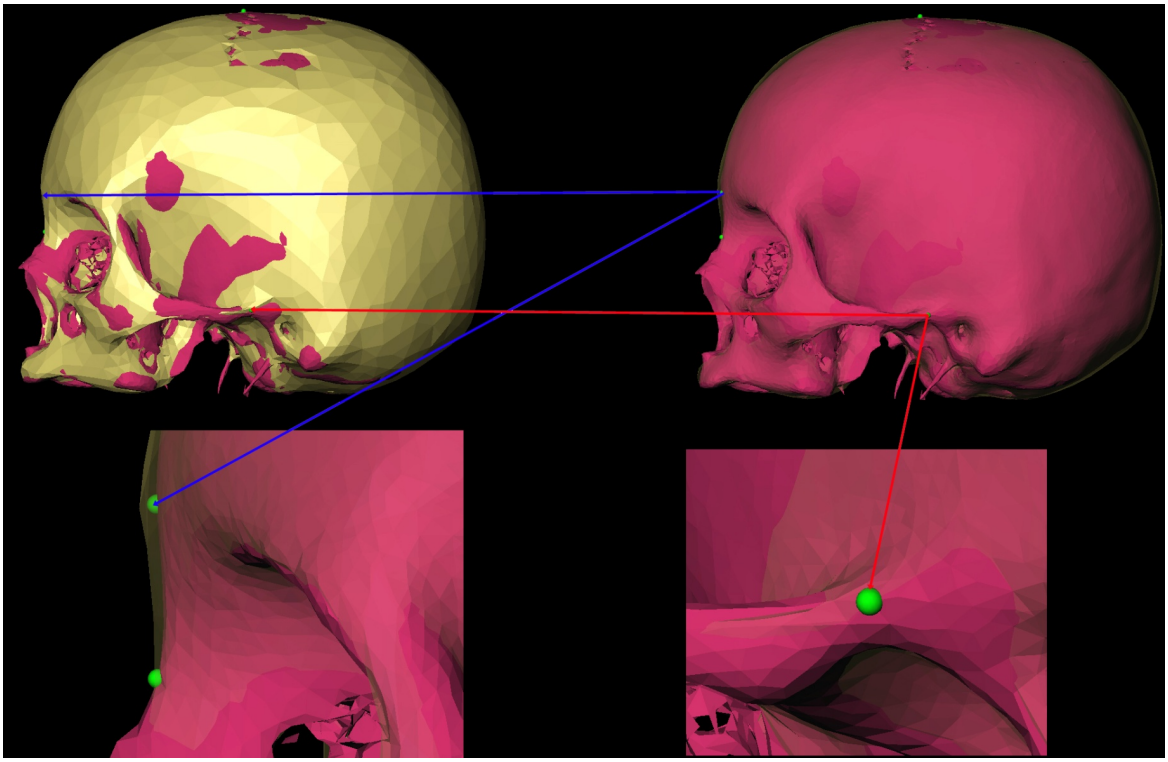


Figure 4-9 Effect of mesh quality on landmarks

Table 4-1 Empirically determined template mesh quality

Bone	Number of Vertices
Skull	25,000
Lumbar	15,000
Pelvis	15,000
Scapula	7500
Clavicle	15,000

4.2 Mesh Segmentation

The cranium is a complex bone with many ecto-cranial and endo-cranial features. However, these endo-cranial features can be inconsistent due to the quality of bone, which deteriorates post-mortem, see Figure 4-10; Error also occurs during the segmentation process. These inconsistencies can introduce error in the atlas creation process where the focus is to separate the cranial surface into two components, ecto-cranial and endo-cranial. Adding the ectocranial surface to the atlas and using it to generate correspondence is used as a reference for the endocranial surface see Figure 4-11. This increases the necessity for a mesh segmentation technique to perform this task efficiently and consistently.

Mesh segmentation is the process of partitioning mesh into different components; it has become a key element in many geometric modeling and computer graphics applications. It aids

in the parameterization, deformation, editing, and shape matching [56]. Methods developed for mesh segmentation include image processing and unsupervised machine learning. Different algorithms have been developed to perform mesh segmentation into meaningful constituent parts [57], see Figure 4-12. These algorithms are all general, in that features on the mesh are used for partitioning with no regard to the semantic each segment.

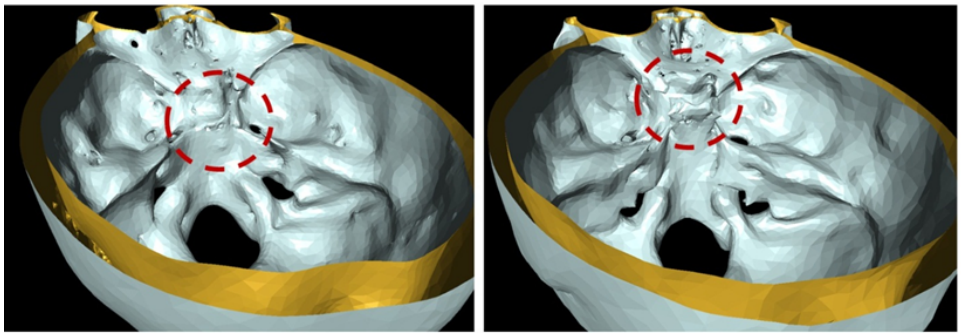


Figure 4-10 Inconsistency in internal surface

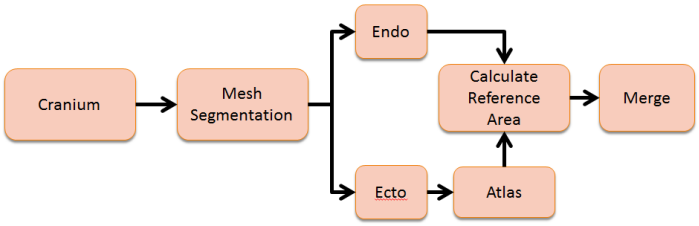


Figure 4-11 Process of adding skull to atlas



Figure 4-12 Example of mesh segmentation

4.2.1 Algorithm 1: Calculating mesh 1st and 2nd differential properties:

A novel technique was developed to segment skull mesh into ecto- and endo- cranial surface, details of this algorithm are outlined in Figure 4-13. Input to this algorithm is a full skull model, five sets of features are computed (F1 to F5) for each vertex on the input model. Fuzzy c means clustering (FCM) is then used to create two initial clusters of ecto- and endo - vertices. K nearest neighbor voting is then used to refine the initial set of ecto- and endo- vertices. Output ecto-vertices are then dilated. Island vertices are then computed and added to the endo- vertices list. Final step of the algorithm is detecting and filling any holes in the computed ecto-cranial model.

1. Calculate a set of features from the input skull model, see Figure 4-14. These features are the following:

   F1: Angle between centroid-Vertex vector and normal vector

F2: Angle between centroid-Vertex vector and smoothed normal vector

F3: F1 of the first intersection point

F4: Number of Intersection points

F5: Ratio between (first intersection point-Vertex) distance and (last intersection point-Vertex)

2. Cluster features using Fuzzy c-means clustering [58].

Minimize function: $E(U,V)=\sum_{i=1}^{k}\sum_{j=1}^{n}\left(u_{ij}\right)^{m}\left\|\bar{x}_j-\bar{v}_i\right\|^2$

Subject to $\sum_{i=1}^{k}u_{ij}=1 \qquad \forall j=1,\ldots,n$

Fuzzy partition matrix $U=\left[u_{ij}\right]_{k\times n} \qquad u_{ij}\in[0,1]$

Fuzzification parameter $m\in[1,\infty]$

Output from FCM clustering is initial guess of the two clusters, see Figure 4-15.

3. Calculate confidence score for each point.
4. Remove outliers from each cluster.
5. Dilate the ecto-cranial points using 1 ring neighbors.
6. Calculate isolated vertices in ecto-cranial surface and added to the list of endo-cranial.

7. Detect holes in the ecto-cranial surface.

8. Fill holes with closest points from endo-cranial surface.

Figure 4-16 shows final segmented surfaces.

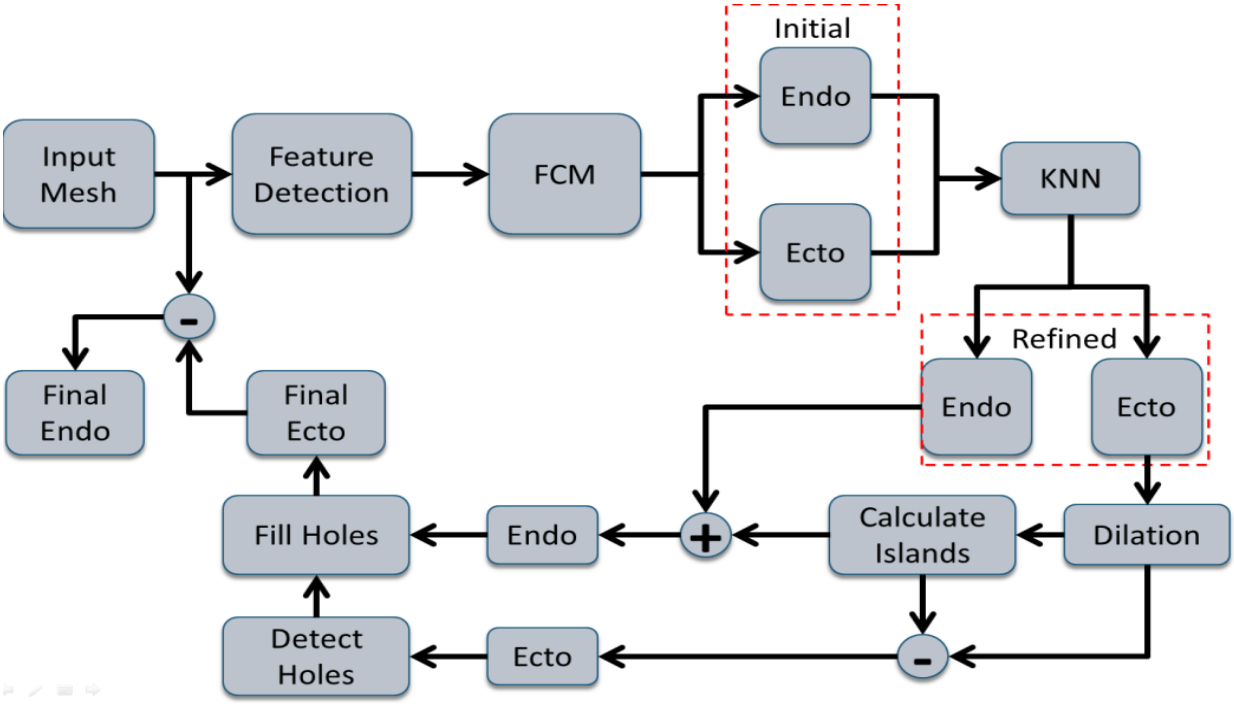


Figure 4-13 Mesh segmentation algorithm

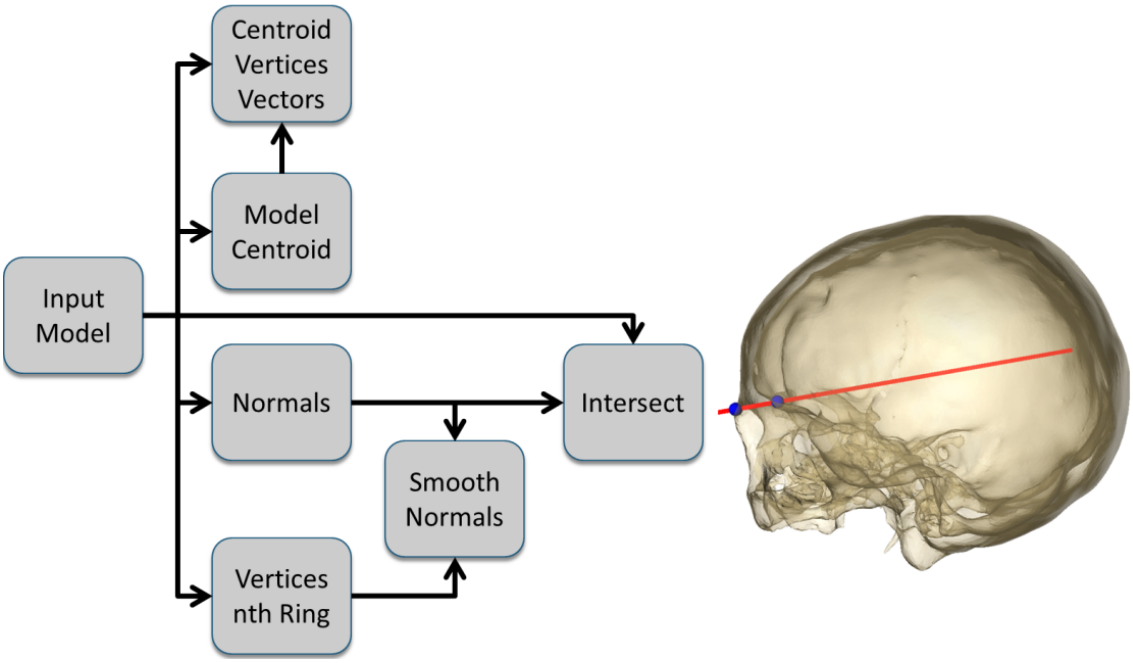


Figure 4-14 Feature generation algorithm

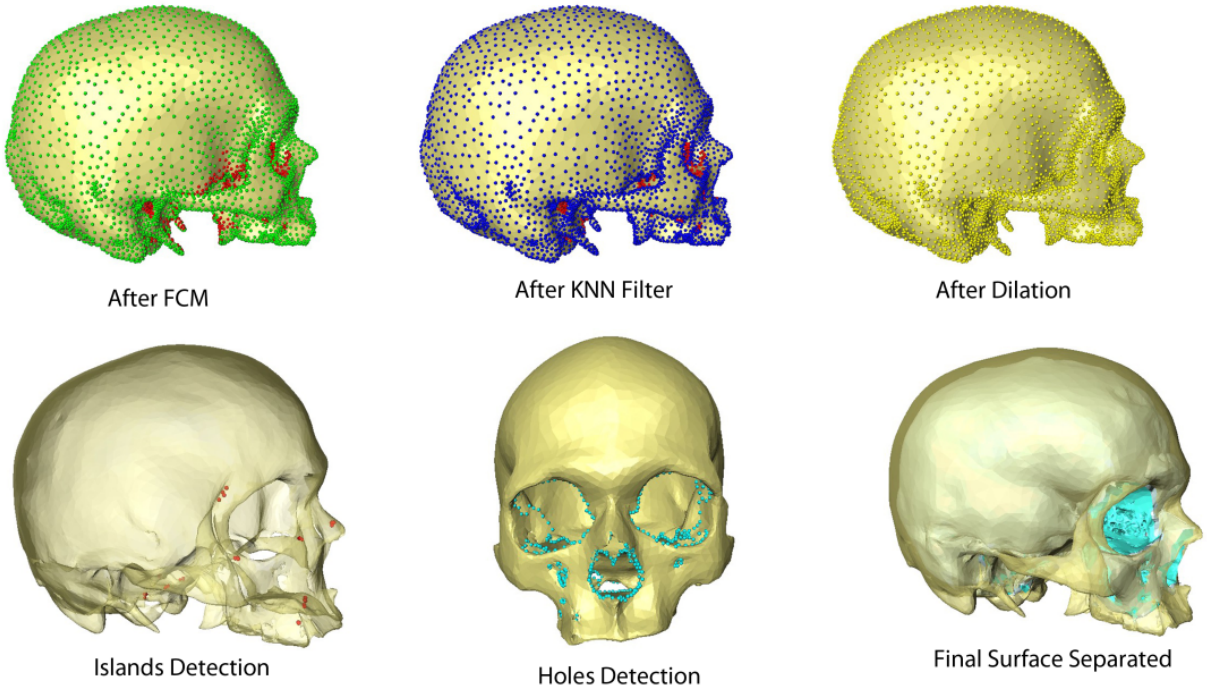


Figure 4-15 Evolution of ecto & endo cranial surface during segmentation process

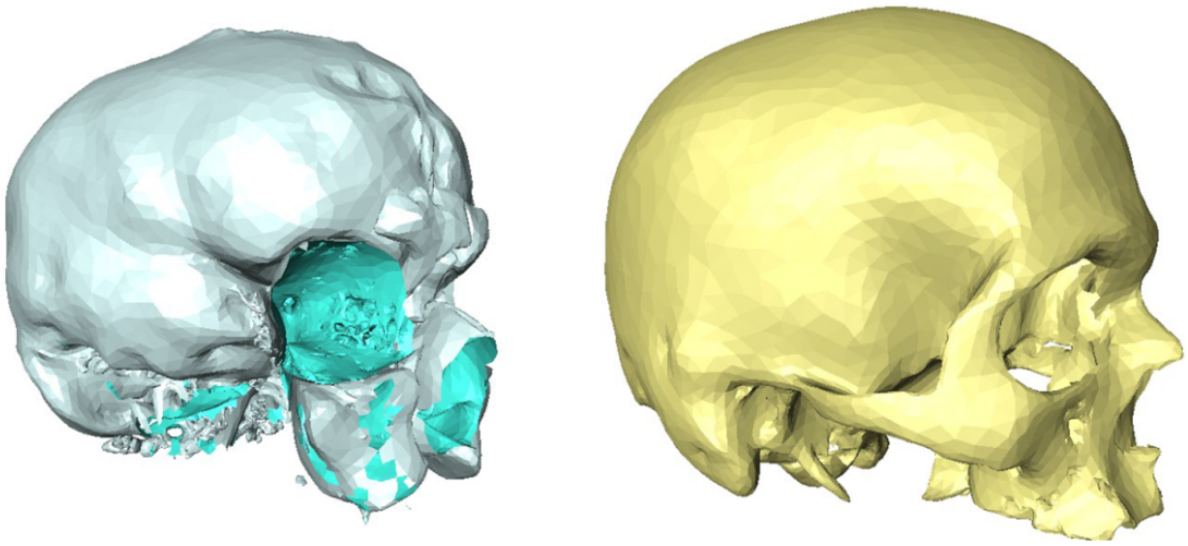


Figure 4-16 Final segmented surfaces

5. STATISTICAL SHAPE ATLASES CREATION

Atlas creation is the process of morphing the template model to match the training models. This process determines the accuracy of correspondence, and blind deformation can lead to incorrect registration and point correspondence. In order to perform an accurate deformation an initial registration step is required. During this step, feature points on the surface are matched based on shape descriptor. Due to the nature of the problem, noise can be present which can bias or affect the accuracy of the registration process. In the perspective of this application noise is defined as undesired components generated from segmentation, the model generation process, deformed anatomy or irregular bone gross, as shown in Figure 5-1 Different types of noise. In order to overcome the effect of this problem, prominent surface features must first be detected. Then using these features initial registration and matching steps are performed followed by a free form deformation and correspondence calculation. Figure 5-2 outlines the high level algorithm of adding new bone to the atlas. For abbreviation purposes during description of the algorithm (TM) will be used to reference template model and (NM) will be used to reference the new model to be added, (NS) will be used indicate normal scale, and (SS) to indicated scale space.

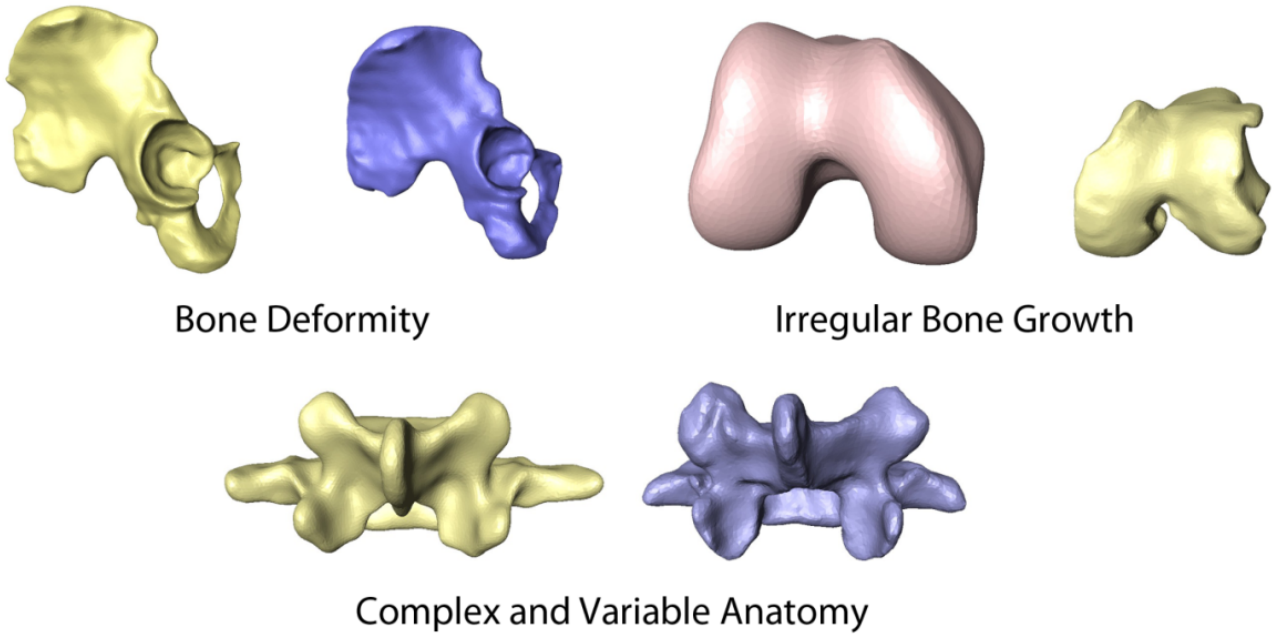


Figure 5-1 Different types of noise

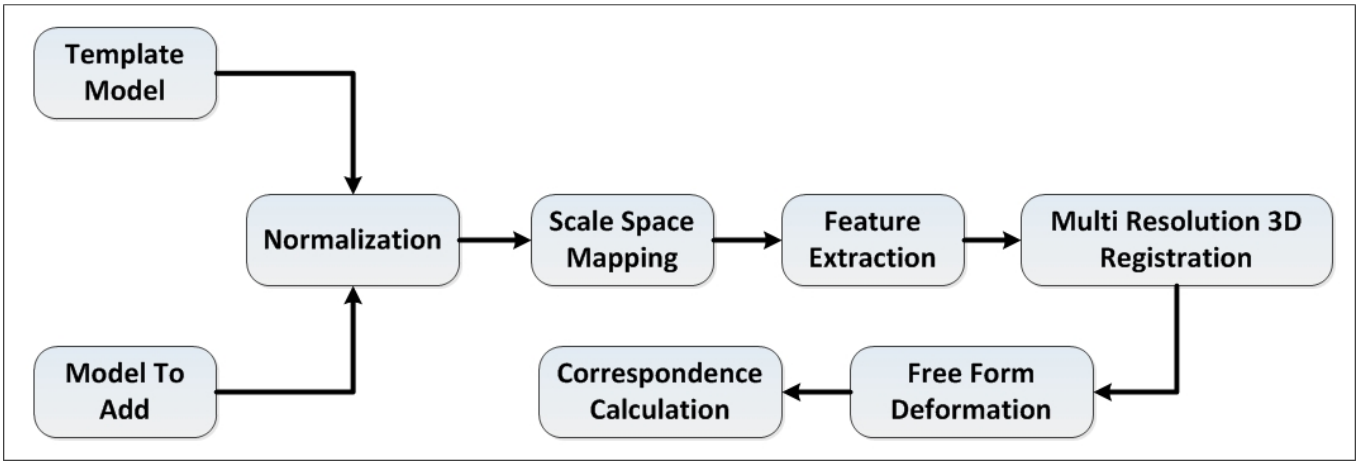


Figure 5-2 High-level algorithm of adding new bone to atlas

5.1 Normalization

The first step in the process of adding bone to atlas is scale normalization (i.e scaling template mesh to the same size as the training mesh). Different methods for scale normalization were investigated and the best results were found using average centroid size normalization.

5.1.1 Bounding Box

The bounding box of the template is scaled to match the same bounding box dimension of training model see Figure 5-3. This method is limited by the dependency on the orientation of the models in space, and since it calculates the bounding box, it is sensitive to any noise outside the model. In general this method tends to enlarge the model. One advantage of this method is its insensitivity to triangulation noise.

5.1.2 Centroid Size

Scale is calculated as a ratio between the centroid size of the template and training meshes see Figure 5-4. This method is sensitive to the number of vertices in each model since the centroid size is the summation of distances between all vertices and the centroid. Advantages of this method are its insensitivity to triangulation noise, is independence of orientation of the model in space, and its correlation to shape geometry.

$$S = \sqrt{\sum_{i=0}^{n-1} (v_i - COG)^2} \quad (1)$$

5.1.3 Area

Scale is calculated as a ratio of the template mesh and training mesh areas. This method is limited in that it is very sensitive to triangulation noise. It is, however, insensitive to orientation and it does correlate to model topology.

$$A = \sum_{j=0}^{f-1} a_j \quad (2)$$

5.1.4 Average Centroid Size

Scale is calculated as a ratio of the average centroid size of the template and training meshes. This method solves the problem of sensitivity to the number of vertices. Using the average of the vertices makes it more robust and less affected by noisy points.

$$S(avg) = \frac{1}{n} \sqrt{\sum_{i=0}^{n-1} (v_i - COG)^2} \quad (3)$$

Comparing the registration error with each of the normalization methods shows the robustness of the average centroid method. As a result, this was the method utilized through the deformation algorithm.

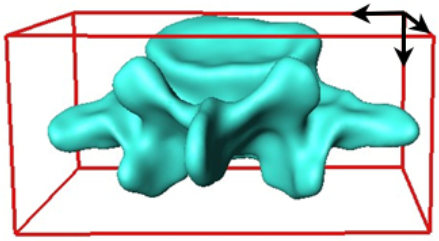


Figure 5-3 Scaling using bounding box dimensions

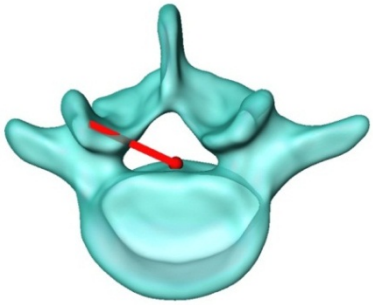


Figure 5-4 Scaling using centroid size

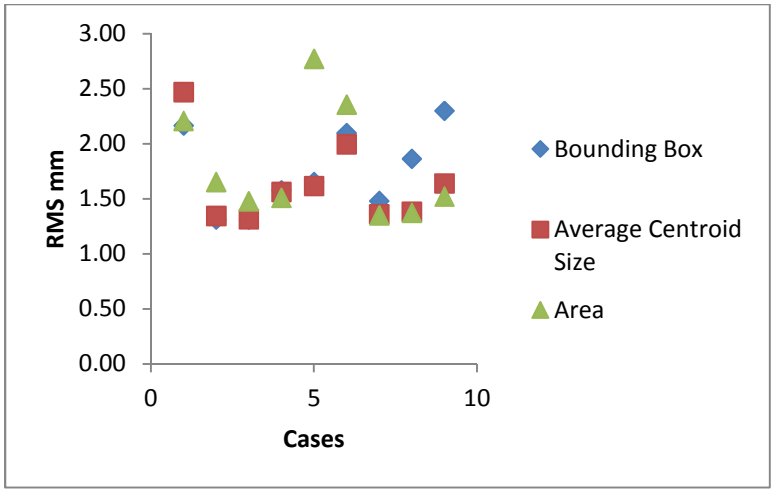


Figure 5-5 Comparing registration errors for vertebra using each of the normalization methods

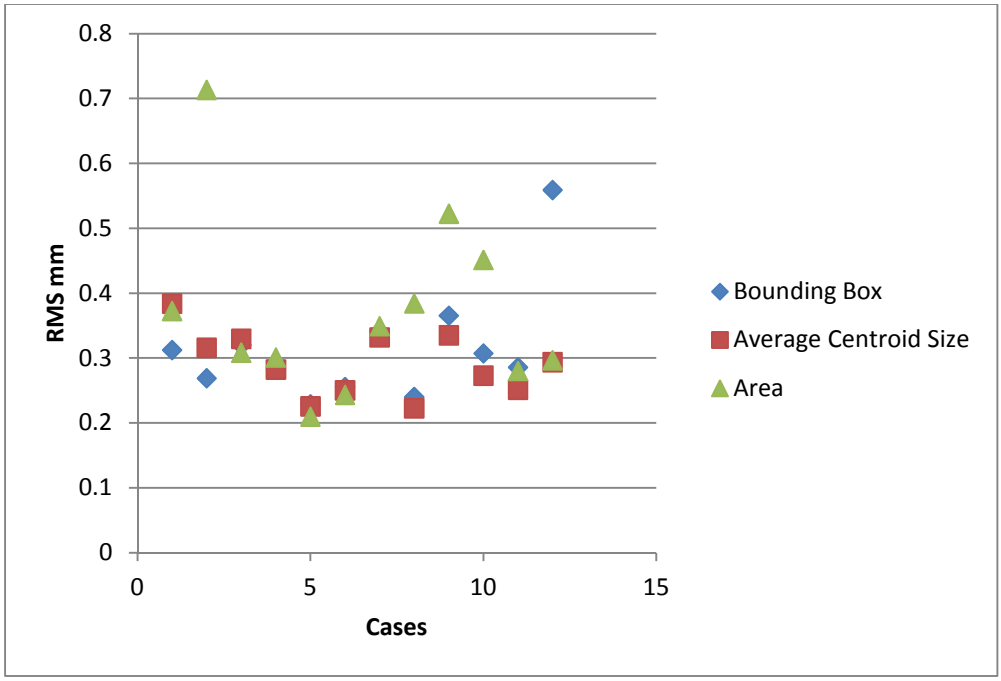


Figure 5-6 Comparing registration errors for pelvis using each of the normalization methods

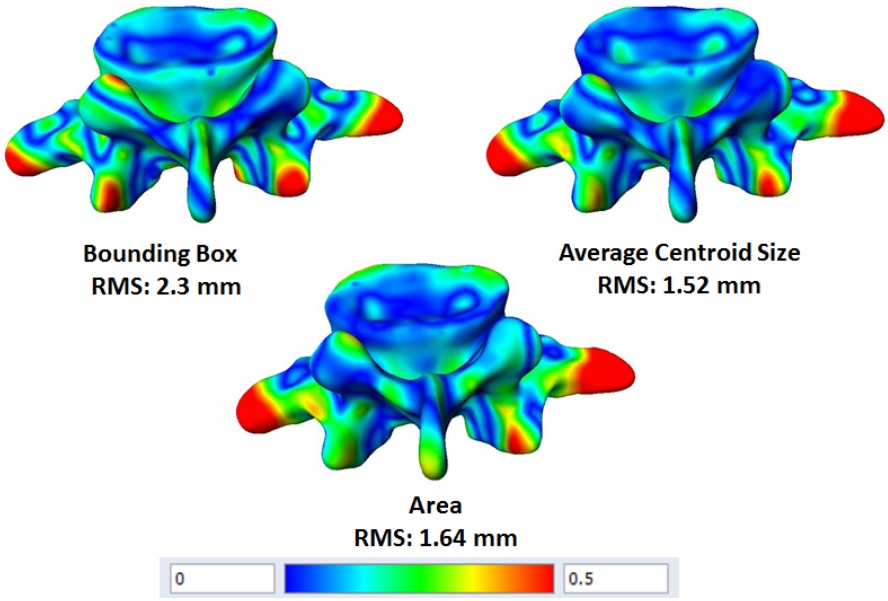


Figure 5-7 Distance map showing registration error using each of normalization method

5.2 Scale Space Mapping

In order to achieve accurate registration most prominent features have to be detected consistently with minimal sensitivity to noise. Such problem can be casted as a SS problem by finding features points that are consistent and prominent through different scales.

Lindeberg[59] related SS theory and biological vision. Many SS operations show a high degree of similarity with receptive field profiles recorded from the mammalian retina and the first stages in the visual cortex. In these respects, the SS framework can be seen as a theoretically well-founded paradigm for early vision, as it has been thoroughly tested by algorithms and experiments. In contrast to ideal mathematical entities like points and lines that appear the same way in all scales of observation, objects in the real world and details in their images only exist as meaningful entities over limited ranges of scale. A basic example to outline the concept is observing the human arm. Observing the human arm at the nanometer scale does not convey a true sense of the structure. The more logical scale on which to view such an object would be on a scale from centimeter to meter.

Witkin [60] first introduced the concept of SS in 1983 from a signal processing point of view on 1D signal. He observed that the number of zero crossings decreased monotonically when convolving a signal with a Laplacian filter. Koenderink [61] extended the same concept on 2D signals and introduced the notion of causality, which states that new level surfaces cannot be created when increasing scale parameter. Details at different scales must also be traced across all scales. Using such definition, SS must satisfy a diffusion equation, continuous in both

space and time, discretizing time (corresponds to taking time slices of the continuous system), and no new phenomena should arise. In discretizing space, the green function becomes a discrete Gaussian kernel rather than a continuous kernel.

SS was widely adopted in the detection of features in 2D images [62-64]. The basic idea behind SS is embedding a signal into one parameter of derived signals, where SS, t, is a scale parameter. Given a signal, f, a function, L, is defined by convoluting f with the Gaussian Kernel g.

$$L(x;t) = \int_{\varepsilon=-\infty}^{\infty} \frac{1}{\sqrt{2\pi t}} e^{\frac{\varepsilon^2}{2t}} f(x-\varepsilon)d\varepsilon \tag{4}$$

Koenderink obtained connection between the Gaussian SS and the diffusion equation, see Figure 5-8[61]

$$\frac{\partial L(x,t)}{\partial t} = \Delta L(x,t) = \sum_{i}^{d} \frac{\partial^2 L(x,t)}{\partial x_i^2} \tag{5}$$

Where Δ is Laplacian operator

The same concept was extended from 2D-to-3D shapes. Yuen, et.al [65] utilized SS to achieve smooth surface properties by convolving local parameterization of the surface with a 2D Gaussian filter. Parameterization was achieved by constructing semi-geodesic coordinates around each vertex. Mokhtarian [66] used the same approach for curvature calculation on different SS by convolving a 2D Gaussian with surface parameterization. Hua [67] utilized a similar approach where he uniquely mapped a 3D surface to a canonical rectangular domain

and encoded the shape properties, such as mean curvature of the surface, in the 2D domain to construct a geodesic distance-weighted shape vector image. Kimmel utilized the level set method to construct a geometric SS for images embedded on surfaces [68]. Novatnack constructed a SS representation to extract scale-dependent features for corner and edge detection [69]. In case of point-based representation (i.e., point clouds), Pauly [70, 71] proposed using geometric low-pass filters to achieve a multi-scale representation from fine to coarse. Li [66] used SS to detect salient feature points that are invariant under rigid transformation as a mean to align point based surfaces. Laga extended 2D SS to 3D as a means to analyze and classify features at different scales. By applying PCA on a neighborhood with different sizes, he computed surface curvature distribution for each point, modeling the 4D vector for curvature and position as a mixture of Gaussian using expectation maximization [72]. Zou generated geometric SS by diffusing surface intrinsic geometry using Ricci flow [73].

Given the different types of noise outlined in Figure 5-1, we can solve the problem of achieving correspondence by deforming the template model to match the new model to be added as the need to attenuate noise and generalize both surfaces, allowing an accurate matching of prominent anatomical features. Scale-dependent Laplacian (Diffusion) is commonly used as a method for noise attenuation.

$$\frac{\partial \mathrm{x}}{\partial \mathrm{t}} = \mu \mathrm{L}(\mathrm{x}) \tag{6}$$

where $\boldsymbol{\mu}$: Diffusion Constant $\mathbf{L}(\mathbf{x})$: Laplacian Operator

By integrating diffusion equation over time minimal noise will vanish within a neighborhood, achieving an overall high-frequency smoothing effect. It must be noted that the main shape will suffer from slight degradation. Taubian [74] presented explicit integration of diffusion using the explicit Euler scheme which yields:

$$x^{n+1} = (I + \mu dtL)x^n \tag{7}$$

For 3D mesh L(x) can be approximated at each vertex by Umbrella operator:

$$L(x_i) = \sum_{j \in N_1(i)} w_{ij}(x_j - x_i) \tag{8}$$

Where weight w_{ij} represents the fujiwara weights.

$$w_{ij} = \frac{1}{|e_{ij}|} \tag{9}$$

In this case n is the Scale parameter is the iteration numbers of smoothing.

Choice of n differs for each bone to satisfy two criteria:

A. Maintain overall surface structure without collapsing
B. Enough to generalize surface

Table 5-1 shows values of n for different bones that fulfill above outlined criterions. Figure 5-9, Figure 5-10, Figure 5-11, and Figure 5-12 show SS for the skull, scapula, lumbar and pelvis, respectively.



Figure 5-8 Image at different scale space

Table 5-1 Scale for different bones.

Bone	Scale
Clavicle	200
Lumbar	600
Pelvis	400
Scapula	200
Skull	100
Sacrum	200

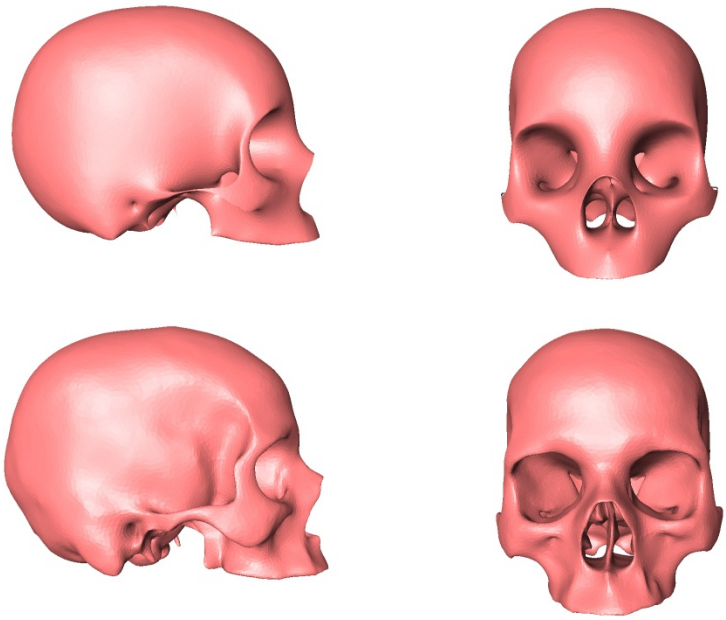


Figure 5-9 Scale space and normal space skull

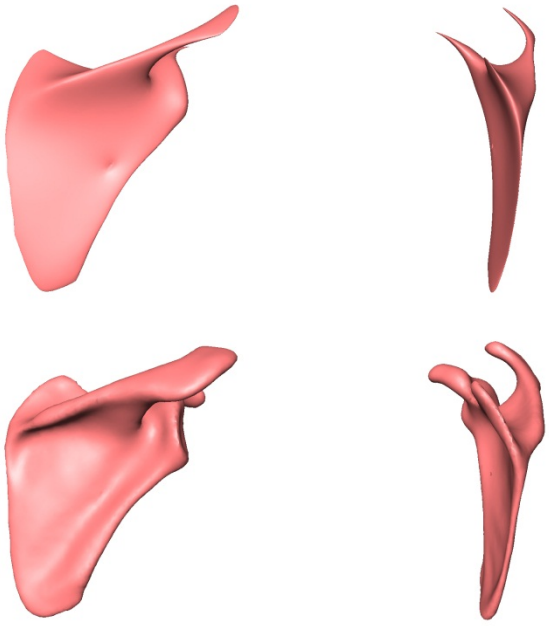


Figure 5-10 Scale space and normal space scapula

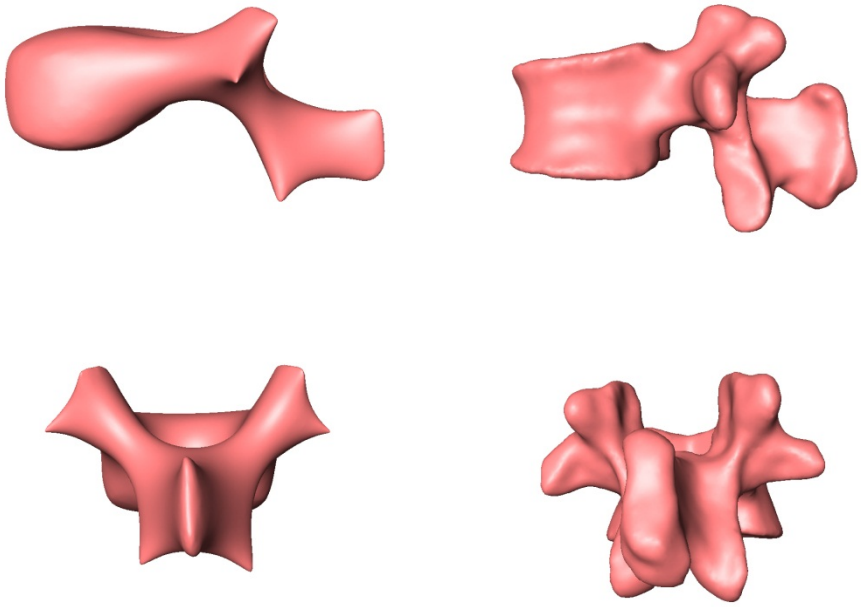


Figure 5-11 Scale space and normal space lumbar

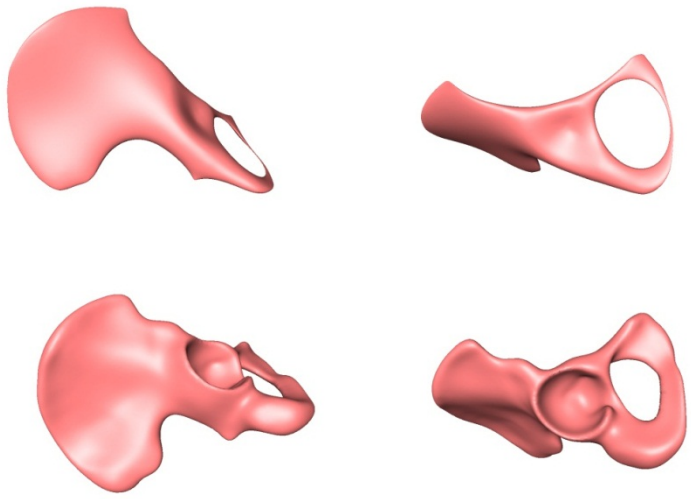


Figure 5-12 Scale space and normal space pelvis

5.3 Features Extraction

By definition, "features" are parts that are more prominent or have distinct characteristics when compared to neighbors. Feature points are used intensively in both 2D and 3D for shape retrieval and classification. Hoffman [75] first introduced the theory of salience visual parts in 1997 which built on the minima rule for defining part boundaries. This rule states that human vision defines part boundaries at negative minima of curvature on silhouettes and along negative minima of the principal curvatures on surfaces. He stated that the salience of a part depends on three factors: size relative to the whole object, the degree of protrusion, and the strength of boundaries. Boyer [76] presented a recognition system for free form objects based on attributed graphs constructed from surface segmentation based on the saliency theory where he utilized mean and Gaussian curvatures to segment the surface into four saliency classes based on curvature consistency using a multi-voting scheme.

Different shape encoding methods have been used as a means to calculate feature points or similarity between shapes. Osada [77] calculated dissimilarities between 3D polygonal models by building shape distribution using functions that describe shape signatures that are also invariant under similarity transform. He utilized five shape functions based on angles A3: between random points on surface lengths, D1: the distance between a fixed point and one random point on surface, D2: the distance between random points on surface areas, D3: the square root of the area of the triangle between three random points on the surface and volumes, D4: measures the cube root of the volume of the tetrahedron between four random points on the surface.

Mahmoudi [78] used a different approach where he represented 3D models using a set of characteristic views that were then used to index models. Filali [79] built on the same concept by including a Bayesian framework for model indexing using the characteristic views. Ankerst [80] used a 3D shape histogram as a method to calculate similarity between 3D shapes. He generated histograms by decomposing the model using three techniques: a shell model, a sector model, and a spiderweb model (a combination of both the shell and sector models).

A different approach for mesh encoding and feature point calculation utilizes differential properties of the surfaces. Differential properties can be divided into first order, corresponding to normal or tangent plane, second order, providing the principal curvature, and third order, providing the directional derivative of the principal curvature.

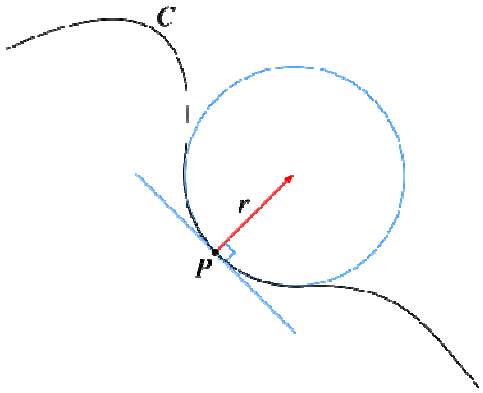


Figure 5-13 Osculating circle

Curvature was first described by Newton in his Principia in 1670 where he introduced a osculating circle as a measure of curvature of curves in Euclidean planes. See Figure 5-13. Curvature is divided into two types:

Extrinsic: dependent upon embedding (i.e., detectable only to the outsider). It is defined as the "change rate" of the normalized normal vector along the hyper-surface E. If E is flatly embedded, then the "change rate" equals zero. An example of this is mean curvature, H, (first introduced in elasticity theory) and torsion

Intrinsic: independent from embedding (i.e., detectable to inhabitants of surface). It is dependent only on how the distances are measured on the surface. An example of this is a Gaussian curvature, K, (introduced in Theorema Egregium by Gauss).

Principal Curvature determines the local shape of a point on a surface. It characterizes the rate of maximum and minimum , bending of the surface, as well as the tangent

directions in which they occur. See Figure 5-14. Euler's Theorem expresses this relationship using equation (10)

$$k_t = k_1 \cos(\psi)^2 + k_2 \sin(\psi)^2 \tag{10}$$

Where:

k_t is the normal curvature at point p with normal t on surface S.

k_1 & k_2 are the maximum and minimum principal curvatures at point p with directions t_1 & t_2

Ψ is the angle between t and t_1

Using the two principal curvatures, the mean (H) and Gaussian (K) curvature can be calculated using equations (11) and (12)

$$K = k_1 k_2 \tag{11}$$

$$H = \frac{1}{2}(k_1 + k_2) \tag{12}$$

Let

$$x = \pm \cos\psi / (|k_t|)^{\frac{1}{2}} \text{ and } y = \pm \sin\psi / (|k_t|)^{\frac{1}{2}} \tag{13}$$

Then

$$k_1 x^2 + k_2 y^2 = \pm 1 \tag{14}$$

Equations (13) and (14) describe a Dupin indicatrix of surface S at point P, a method to characterize local shape of the surface directly related to the Gaussian curvature (K) at this point as follows:

- If K >0 the Dupin indicatrix is an ellipse described by equation (15) .

$$|k_1|x^2 + |k_2|y^2 = 1 \tag{15}$$

- If K<0 the Dupin indicatrix is a set of conjugate hyperbolas described by equation (16).

$$k_1x^2 + k_2y^2 = 1 \text{ , \& } k_1x^2 + k_2y^2 = -1 \tag{16}$$

- If K=0 the Dupin indicatrix is a set of parallel described by equation (17).

$$x^2 = |1/k_1| \text{ or \& } y^2 = |1/k_2| \tag{17}$$

In case of an axis other than principal curvature direction is used Dupin indicatrix takes the form

$$Ax^2 + Cxy + By^2 = \pm 1 \tag{18}$$

Different methods were proposed for approximation of the surface differential properties based on the domain of the problem and whether the input is an unstructured point cloud or structured polyhedral mesh.

One class of methods utilizes surface fitting which is used mainly for an unstructured point cloud sampled on smooth manifolds. Todd [81] suggested use of a Quadratic surface to approximate the sampled areas of the surface to calculate the Dupin indicatrix of surfaces.

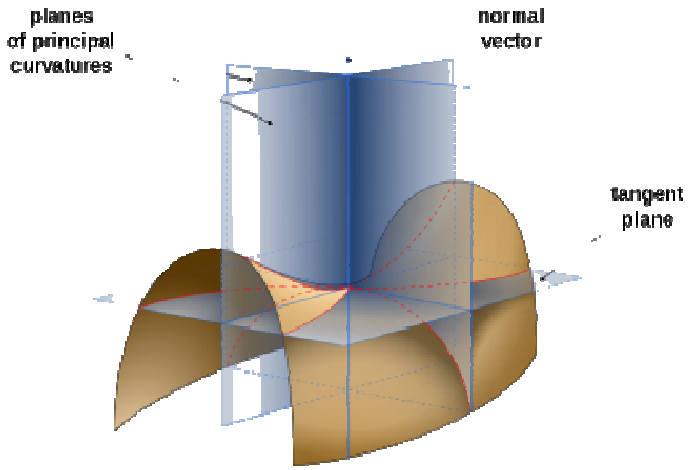


Figure 5-14 Principal curvature

The Quadratic surface passing through the origin is described by equation (19) which can be solved by constructing a system of linear equations using five points. The solution to a unique circumstance of this system of equations for a normal unit with curvature of the quadratic can be calculated using equation (20) [82]. This method has poor accuracy, especially in cases with poorly conditioned systems of equations [83].

—— —— (19)

—= and ————, (20)

Cazals [84] used a truncated taylor expansion, also known as a jets, as a method for fitting the local representation of a surface on point clouds sampled over smooth manifolds. Principal components are then calculated to approximate the first order differential properties, or the normal directions, and second order properties are computed using Eigen values of the Weingarten map of the surface.

Martin [85] used fitting circles as a means to approximate curvature by construction of fitted circles through the vertex v on a mesh and a pair of its neighbor vertices. Such that the angle between two vectors joining the point with the two neighbor points is close to π, values of the principal curvature may then be calculated using both Euler and Meusnier Theorem.

In case of triangular meshes, the first order differential at each vertex can be approximated using the average of faces normal connected to this vertex [82]. Different average schemes were suggested, such as arithmetic mean, area-weighted average, and angle-weighted average [86-89]. Taubian [90] used an area-weighted average normal to compute principal curvatures and principal directions by calculating the Eigenvalues and Eigenvectors of a 3*3 symmetric matrix defined by integral formulas in a closed form, closely related to the matrix representation of the tensor of curvature.

Using the Gauss-Bonett Theorem, a discrete scheme called an angle-deficit scheme, was developed to calculate principal curvature [82, 91, 92]. Surazhsky [93] evaluated the performance of the five methods for curvature estimation, including Paraboloid fitting, circular fitting, and the Gauss-Bonett scheme. His analysis indicated that the Gauss-Bonett scheme did

indeed give the best results for estimation of overall curvature. Additionally, a regular Gauss-Bonett scheme provided estimation with linear convergent rate for the Gaussian curvature [94].

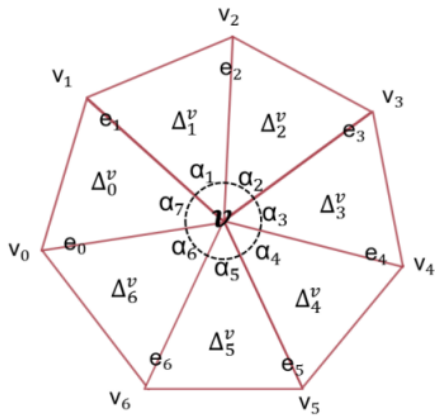


Figure 5-15 Neighborhood notations for gauess-bonett schema

Given the domain of the present problem dealing with smooth structured triangular mesh (where first order differential properties are estimated using faces normal), speed of the calculation and accuracy of the curvature estimation, the Gauss-Bonett scheme was chosen as the method for estimation of surface differential properties. Algorithm 2 outlines details of the calculation of differentials properties using a discrete Gauss-Bonett scheme.

5.3.1 Algorithm 2: Calculating mesh 1st and 2nd differential properties:

9. Calculate Face Normal

$$n_f = e_i \, X \, e_{i+1} \tag{21}$$

10. Calculate Weighted Vertex Normal

$$n_v = \sum_{f=0}^{n} n_f * \alpha_f \tag{22}$$

Where $n_v = \frac{n_v}{|n_v|}$ n: number of neighbors

11. Calculate Gaussian Curvature

$$K = \frac{2\pi - \sum_{i=0}^{n-1} \alpha_i}{\frac{1}{3}A} \tag{23}$$

Where $A = \sum_{i=0}^{n-1} a_i$ and $a_i = \frac{\|e_i \, X \, e_{i+1}\|}{2}$

12. Calculate Mean Curvature

$$H = \frac{0.25 \sum_{i=0}^{n-1} \|e_i\| \beta_i}{\frac{1}{3}A} \tag{24}$$

Where $\|e_i\|$ $norm\ of\ edge\ i$ β_i deviation of $normal\ i$

13. Calculate Maximum Curvature

$$k_1 = H + \sqrt{\max(0, H^2 - K)} \tag{25}$$

14. Calculate Minimum Curvature

$$k_2 = H - \sqrt{\max(0, H^2 - K)} \tag{26}$$

The step after computing the second differential properties for both templates TM and NM involves identification of the features to be used for both rigid and deformable registration.

In context of the current problem, features are defined as vertices that correspond to prominent anatomically consistent features across different scales in SS.

Surface creases (ridges and valleys) are points where a single principal curvature has extrema along its curvature lines. Ridges were used in many applications in computer graphics and modeling [95] as a means to define the segment boundaries for mesh segmentation [96], as well as image and data analysis [97], face recognition [98], and medical image registration [99]. Calculating surface creases involves the calculation of higher order differential properties. They are considered to be third order differential properties of surfaces as differentiation of the principal curvature is involved. Given two principal curvatures (maximum and minimum curvatures k_1 & k_2 $with\ direction\ t_1\ and\ t_2$, respectively), calculating the derivative of principal curvatures along principal directions using equation (27), extrema of curvature along their curvature lines can be found using the zero crossing of e_1 & e_2.

$$e_1 = \frac{\partial k_1}{\partial t_1} \ \& \ e_2 = \frac{\partial k_2}{\partial t_2} \tag{27}$$

These extrema points can be then classified into ridges and valleys based on following criterion [100] .

$$\begin{aligned} &e_1 = 0\ , \quad \frac{\partial e_1}{\partial t_1} < 0\ , \ k_1 > |k_2| \qquad \text{Ridge point} \\ &e_2 = 0\ , \quad \frac{\partial e_2}{\partial t_2} > 0\ , \ k_2 < -|k_1| \quad \text{Valley point} \end{aligned} \tag{28}$$

While ridges give a good description on the overall shape structure and areas where surface normal bends, it does not, however, give a comprehensive picture of the local shape variation and missing anatomical landmarks. The lengths of the ridges are scale variant (i.e., dependent upon the size of the shape). This raises the need for scale (size) invariant shape descriptors that can capture the local shape information and can be used to detect more feature points to be used for registration. Although the Gaussian curvature is independent from shape embedding in Euclidian space (i.e., scale invariant), neither the Gaussian nor the mean curvature capture the intuitive notion of local shape information [101]. In 1992, Koenderink [101] defined two shape descriptors' curvedness and shape index are both driven from second differential properties of the surface and are both scale invariant.

I. Curvedness "Castori Curvature" (C): is a rotation and translation invariant shape descriptor. It measures the intensity of the surface curvature and describes how gently or strongly curved a surface is[101].

$$C = \sqrt{\frac{k_1^2 + k_2^2}{2.0}} \tag{29}$$

II. Shape Index (S): is a quantitative measure of shape of surface. Each unique surface shape correspond to different value of (S) except or planar points which have indeterminate shape index since as $k_1 = k_2 = 0$. Using shape index local shape can be identified into different types[101]. Figure 5-16 shows nine classes of shapes defined using shape index :

A. Umbilical Point: |S|=1

B. Elliptical Point: 0.5<|S|<1

C. Parabolic Point: |S|=0.5

D. Hyperbolic Point: 0<|S|<0.5

$$S = \frac{2}{\pi}\arctan(\frac{k_2 + k_1)}{k_2 - k_1} \tag{30}$$

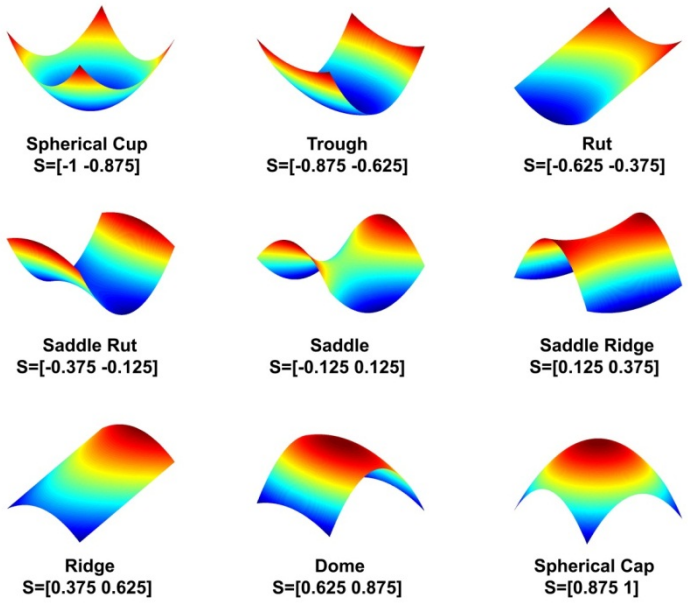


Figure 5-16 Shape classes based on values of shape index (S)

III. Edge Weighted Gaussian Curvature: This is a new descriptor that describes the Gaussian curvature of each vertex in relation to its nth ring neighbors.

$$\nabla_v = \sum_{i=0}^{n-1} \frac{K_v}{K_i} * \frac{e_i}{e_{Total}} \quad (31)$$

Where v: is the current vertex.

e: is the edge length.

n: is the number of n ring neighbors of current vertex.

In order to achieve accurate registration between the template and the model to be added, features are extracted in both normal scale and in SS. Features calculated in normal scale using the ridges, whereas in SS features are calculated using curvedness. Shape index, Gaussian, mean and edge-weighted Gaussian curvatures are also calculated in SS and used during feature matching and the registration phase.

5.3.2 Algorithm 3: Mesh Features Extraction:

An algorithm for a feature point's calculation is divided into two parts: extraction of the feature points in normal scale and extraction of the feature points in SS.

5.3.2.1 Normal Scale Features:

5.3.2.1.1 Calculate features:

a. Calculate mesh ridges using method outlined in [102].
b. Trace ridges and filter ridges into continuous n distinct ridge contours.
c. Filter ridge contours using threshold T(R) (Number of points per contour). Contours with less than 10 points were considered as noise and filtered out.

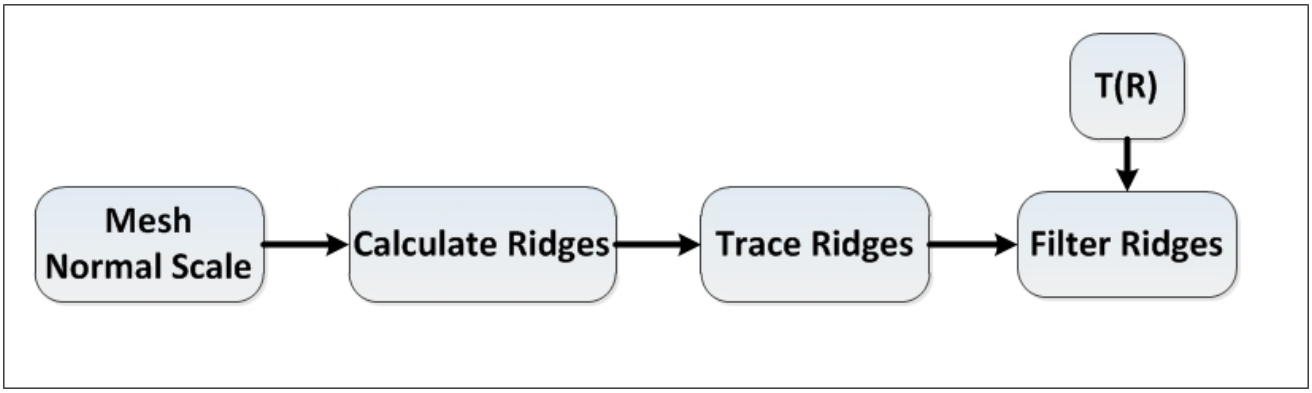


Figure 5-17 Extracting features in normal scale

5.3.2.2 Scale Space Features:

5.3.2.2.1 Calculate shape descriptors:

a. Calculate mesh 1st and 2nd order differential properties using algorithm 1.

b. Calculate shape index using equation (30).

c. Calculate edge weighted Gaussian curvature using equation (31).

- To minimize the effect of any singularities in Gaussian curvature due to SS, in the histogram for the Gaussian curvature all vertices are calculated and outliers are filtered out during calculation of ∇.

d. Calculate curvedness using equation (29).

e. Calculate curvedness histogram$h(C)$.

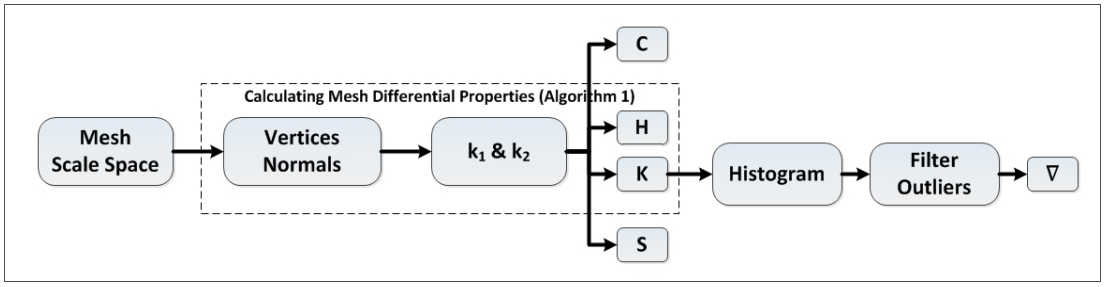


Figure 5-18 Calculating mesh shape descriptors in scale space

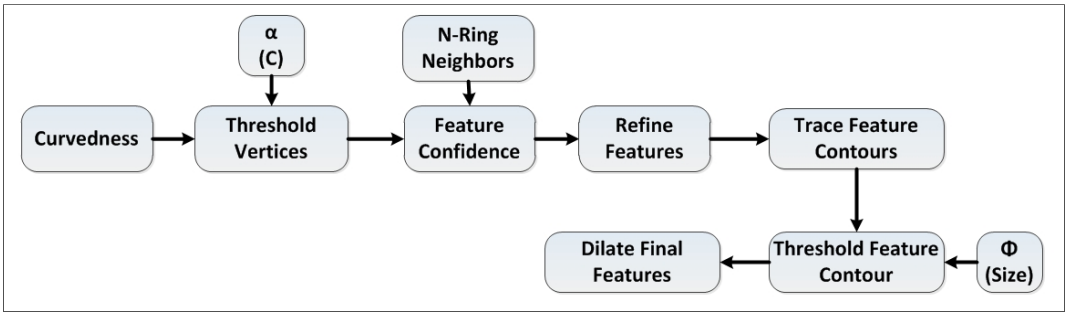


Figure 5-19 Extracting features in scale space

5.3.2.2.2 Calculate features

a. Compute initial feature points by detecting points with extremum curvedness value using threshold α.

$$v \in feature \; iff \; c_v \geq \alpha \tag{32}$$

Where v is current vertex to be tested

$feature$ is the set of feature points.

c_v is the curvedness of current vertex.

b. Compute confidence for detected feature points.

$$conf(v) = \frac{n_f}{n_t} * 100 \tag{33}$$

Where v: is the current feature point.

n_f: is the number of neighbors in the nth ring neighbors that belong to set of feature points.

n_t is the total number of points in the nth ring neighbors .

c. Refine the set of feature points by rejecting the feature points with confidence less than 50%.

d. Trace feature contours by detecting connected feature points.

e. Threshold feature contours by rejecting contours with a number of points less than Φ.

f. Dilate final feature contours using n ring neighbors.

The process of feature extraction is performed on both the TM and NM.

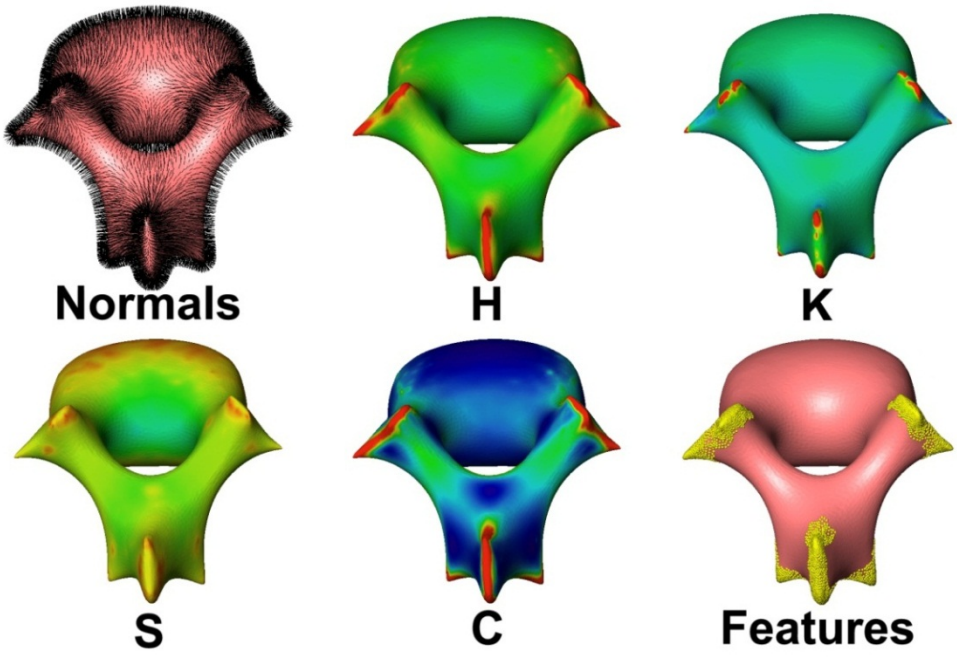


Figure 5-20 Feature extraction in scale space (lumbar)



Figure 5-21 Feature extraction in normal scale (lumbar)

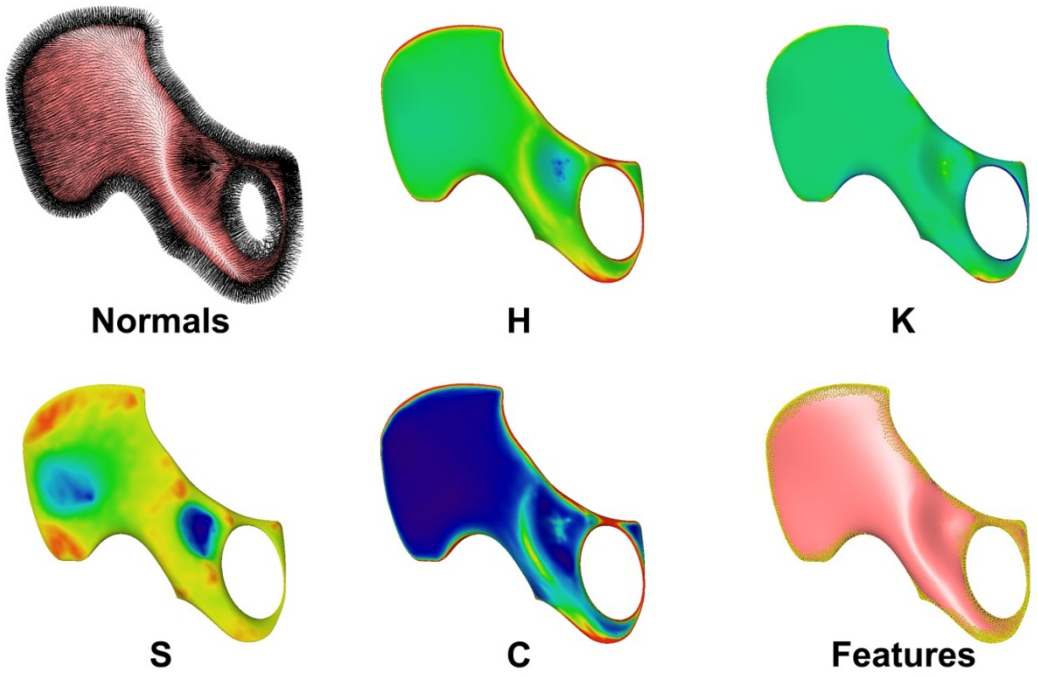


Figure 5-22 Feature extraction in scale space (pelvis)

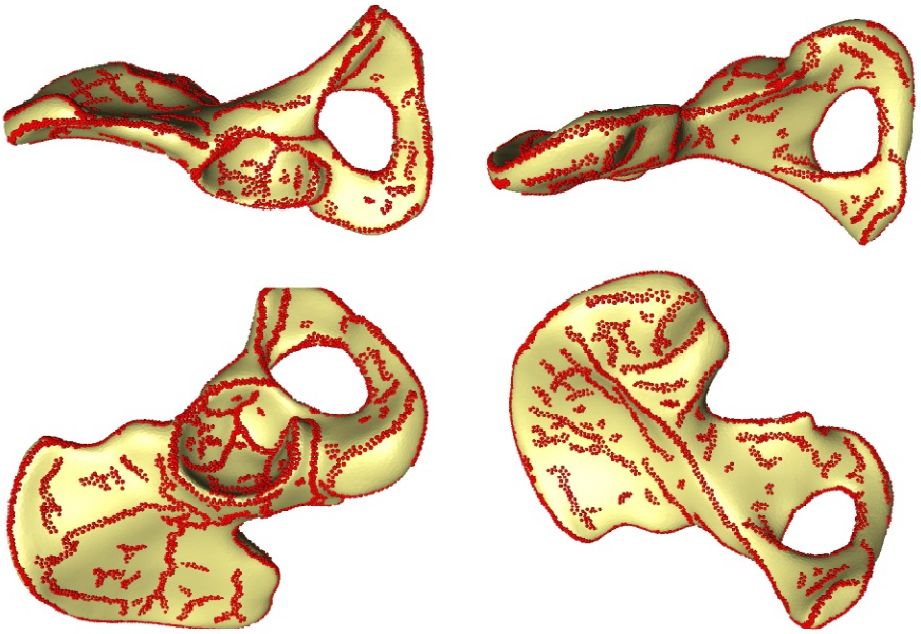


Figure 5-23 Feature extraction in normal scale (pelvis)

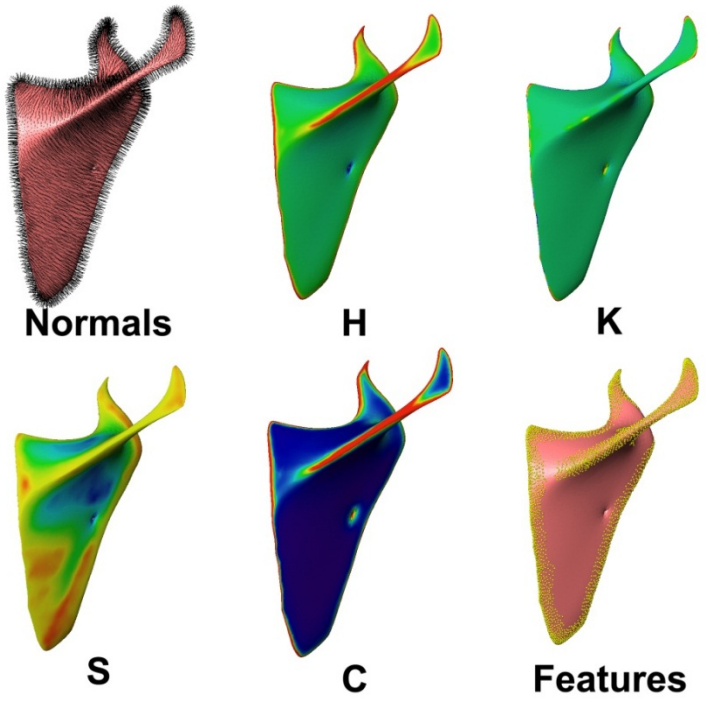


Figure 5-24 Feature extraction in scale space (scapula)

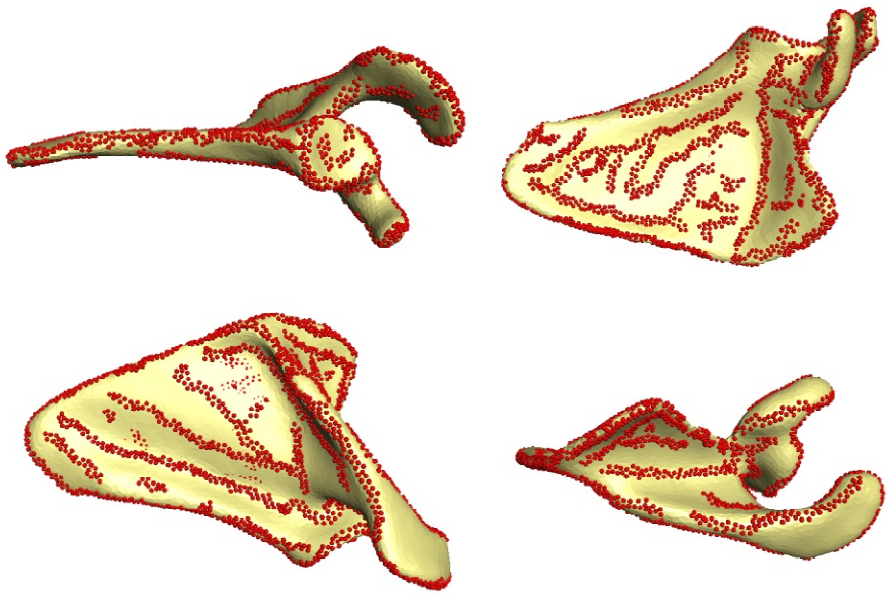


Figure 5-25 Feature extraction in normal scale (scapula)

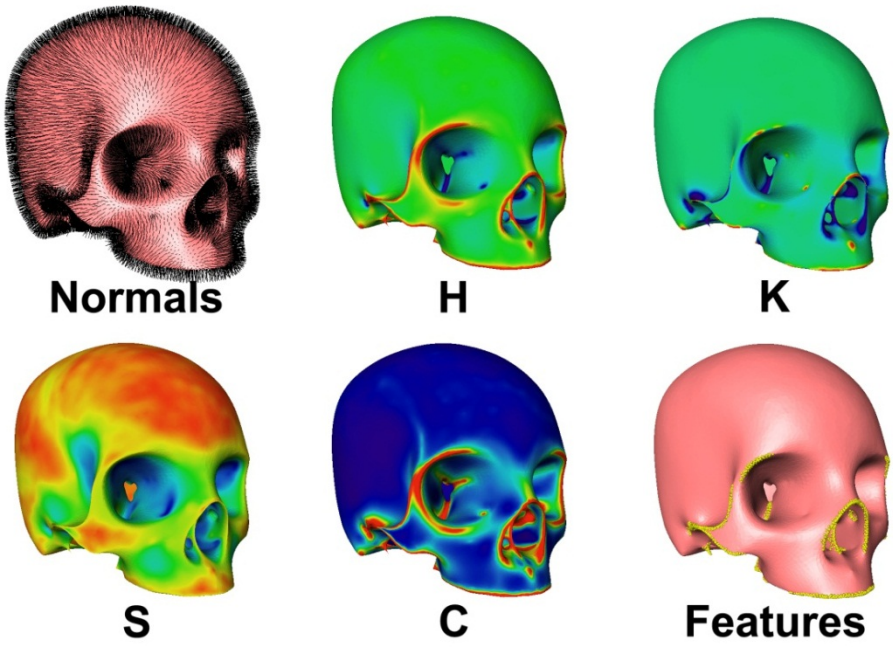


Figure 5-26 Feature extraction in scale space (skull)

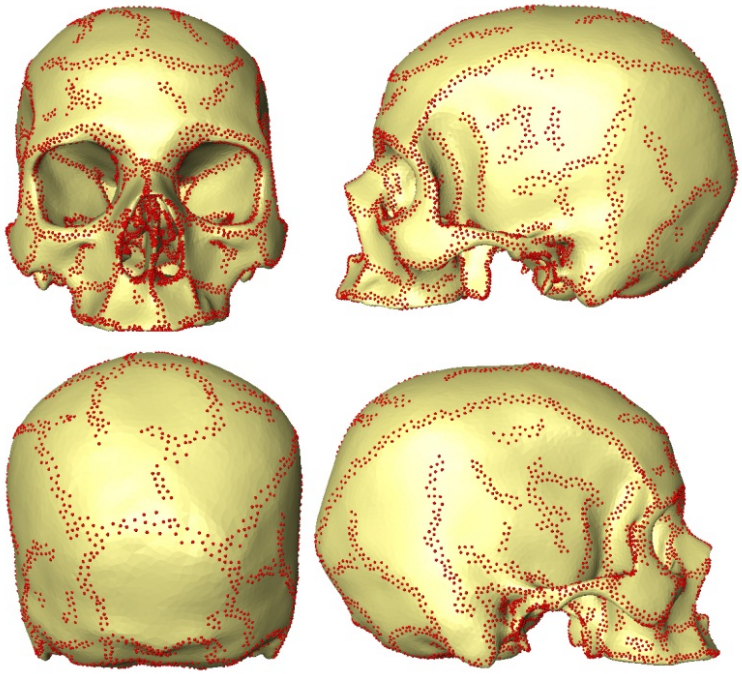


Figure 5-27 Feature extraction in normal scale (skull)

5.4 Multi Resolution 3D Registration

Three-dimensional registration is the process of aligning two set of points by finding the geometric transformation that best superimposes them. Registration is a crucial step in many applications such as biometrics identification [103], facial tracking and animation [104], registration of range scans [105, 106], 3D watermarking [107], registration of anatomical structures [108], and surgical navigation [109]. 3D registration can be classified into: **rigid** which involves only translation and rotation [110], and **affine** which involves translation, rotation, and shear [111, 112]. Articulating registration involves dividing the models into patches and performing registration of each patch separately [113], and finally **non-rigid,** which involves moving each point separately by obtaining deformation fields [108, 114]. Different techniques were used to solve the registration problem such as RANdom SAmple Consensus (RANSAC) [115], absolute orientation [116], and ICP, introduced in 1992 by Besl [117]. ICP is the most commonly used technique in registration, as it is generically applicable to any two objects represented by point clouds and can be proven to converge to an at least local minimum with respect to a given root mean square error (RMSE) [110]. ICP align two sets of moving and reference points by minimizing the sum of the distance error between them. It iteratively establishes correspondence between the moving and reference points, It then solves for the rigid transformation that aligns these two sets, apply transformation to the moving points then recalculate correspondence until convergence . In its original variant, correspondence is established using the closest point, and rigid transformation is found in a least square sense

using closed form solution. Many variants have been introduced to enhance the performance of the algorithm. Rusinkiewicz [118] in a survey paper identified six points in which these variants differs:

a. Sampling:

   This affects what points to be picked for matching. In the original variant, Besl [117] suggested using all available points, where Turk [119] suggested a uniform subsampling strategy. Masuda [120] took a different approach where he performed random sampling, ensuring different points are picked in each iteration.

b. Correspondence (Points Pair Matching):

   This is the step of matching points between the two point sets. Feldmar [121] and Sharp [106] suggested the use of curvature as an invariant feature. Pulli [122] used angles between normals for matching. Granger [123] and Horaud [113] explored points matching in an expectation maximization framework. Maier-Hein accounted for anisotropic localization uncertainty for both input point sets [110].

c. Pairs weighting:

   In the original variant, Besl [117] used constant weights for all matched point pairs, whereas Godin [124] assigned lower weights to points with greater point-to-point distance. Normals compatibility was used for weighting by Rusinkiewicz [118]

d. Outlier detection:

   Similar to weighting, outlier detection rejects pairs that are classified as outliers. Using point-to-point distance, Pulli [122] ranked pairs and rejecting the lowest 10%. While Masuda rejected pairs with distances greater than a multiple standard deviation of distances [120], Turk rejected points on mesh boundaries [119].

e. Error metric and minimization:

   This is the step of computing the error metric and minimizing this metric for conversion. Using the sum of the squared distances between pairs, a closed form solution for rigid transformation can be calculated. Different methods were proposed: Arun [125] used a singular value decomposition; Horn [116] utilized quaternions; Walker [126] used dual quaternions, whereas Horn [127] used orthonormal matrices. Chen [128] utilized the sum of the squared distances from the source points to the plane containing the destination point and the same orientation as the point normal. Blais proposed simulated annealing as a method for enhancing robustness of the algorithm.

Given the context of the current problem, the generation of robust correspondence across anatomical shapes given the three types of noise discussed earlier (Figure 5-1). A multi-resolution approach is used to develop a new registration algorithm, where registration is carried on over three different resolutions' overall mesh, features and vertices in both normal

scale and SS. Matching feature points in SS will generate more accurate registration in original SS. Shape invariant features were also used in calculating correspondence and a new error metric was proposed that combined both spatial information (i.e., coordinate data) and invariant features (e.g., shape index, edge-weighted Gaussian curvature and curvedness).

5.4.1 Algorithm 4: Multi resolution 3D registration:

Figure 5-28 shows the overview of the multi-3D resolution registration algorithm. As can be seen, there are three resolutions considered during this registration algorithm mesh, features and vertices level. Input for this algorithm is the TM and NM in NS and SS, as well as the indices of the detected NS features and SS. Each vertex on both the TM and the NM is classified as either: 1) SS feature vertex, 2) NS feature vertex, or 3) non-feature vertex.

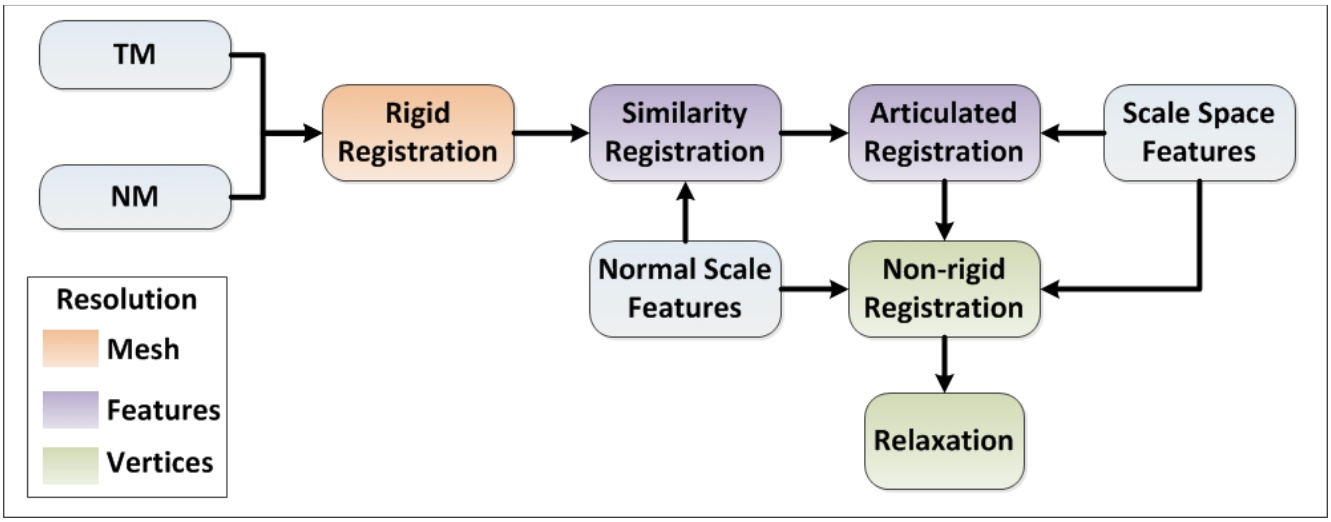


Figure 5-28 Multi resolution 3D registration algorithm overview

5.4.1.1 Rigid Registration:

The purpose of this step of the algorithm is to initially align the TM and the NM to ensure they are in same space and with no pose singularity. Figure 5-29 outlines the steps of the rigid registration process. Results of the rigid registration step on the lumbar are shown in Figure 5-30.

a. Align Centroid:

    a. Calculate centroid of TM and NM.

$$c_m = \frac{1}{n}\left(\sum_{i=1}^{n} v_i\right) \tag{34}$$

Where: n is the number of vertices (v) in the mesh M.

    b. Transform TM using T_c

$$T_c = c_{NM} - c_{TM} \tag{35}$$

b. Align Principal Axes:

    a. Calculate principal axis of TM and NM.

        i. Compute the singular value decomposition (SVD) of vertices centered at origin.

$$[U, S, V] = SVD(v - c) \tag{36}$$

        ii. Sort Eigen values (S) in descending order.

iii. Find two extreme points along both direction of axes that corresponds to $S(0)$ & $S(1)$.

iv. Calculate the distance between the model centroid and each extreme point.

v. Fix axis direction to point toward the point with maximum distance from centroid.

b. Compute rotation that aligns P_1 & P_2 of TM with P_1 & P_2 of NM.

c. Align TM with NM using ICP:

i. Find pair match between TM and NM points pair match

$$\mathrm{Z} = \left\{\mathrm{v_{TM,i}}, \mathrm{v_{NM,j}}\right\} \tag{37}$$

ii. Minimize

$$\sum_{1}^{\mathrm{n}} \|\mathrm{NM} - \mathrm{T} * \mathrm{TM}\| \tag{38}$$

Where T is calculated using method described by Arun [125]

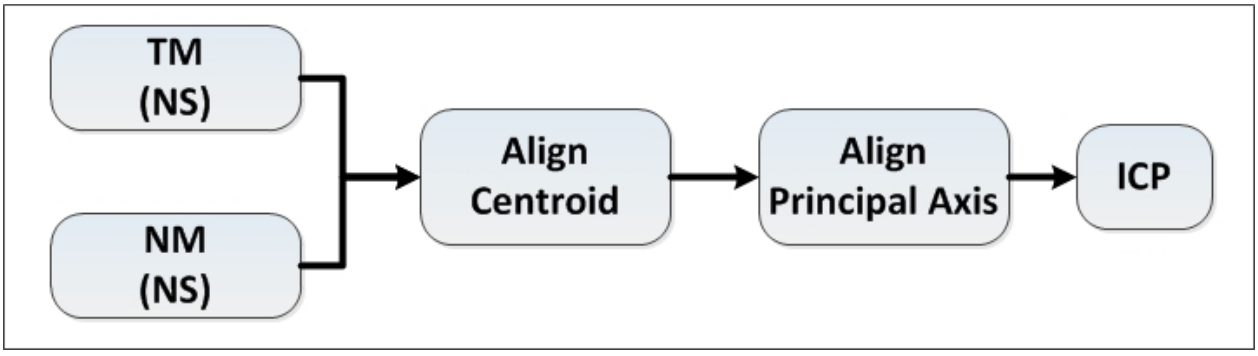


Figure 5-29 Rigid registration

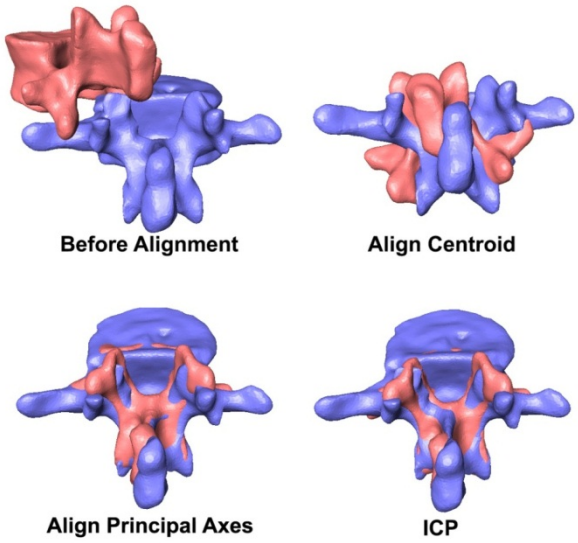


Figure 5-30 Rigid alignment (TM-Pink) and (NM-Purple)

5.4.1.2 Similarity Registration:

This step involves aligning the TM and the NM in NS iteratively by calculating similarity transform that best align the NS features (ridges) for both the TM and the NM. Figure 5-31outlines the algorithm for similarity registration. The iterative similarity alignment algorithm is a variant of ICP within each iteration rotation, translation and scale are calculated between point pairs until convergence. Pair matching or correspondence between the two set of points is evaluated using distance query calculated using Kd-tree.

Kd-tree: Is a binary search tree for storing n set of points sampled from a k dimensional space that allow a fast nearest neighbor and range search [129]; this was first introduced by Bentley in 1975[130]. Since then it has been widely used in many computer graphics

applications including ray tracing [131] . Given set of a n points, a kd-tree is reconstructed recursively.

The space is subdivided into set or rectangular cells by applying a certain splitting rule. Choosing a splitting rule is crucial in the reconstruction of kd-tree, as it dictates the shape of the cells and structure of the tree, thus affecting the efficiency of the search. Friedman and Bentley [132] proposed the standard splitting rule, where a splitting dimension was proven to have the maximum variation (i.e., maximum difference between minimum and maximum values in this dimension). The splitting value was then defined using the median of the points in this dimension. They showed that in using such a rule, a nearest neighbor query can be performed in $O(\log n)$ expected case time for any d-dimension data given uniformly distributed points. The mid-point splitting rule, chooses the hyper-plane to pass through the center of the cell and bisect the longest side of the cell.

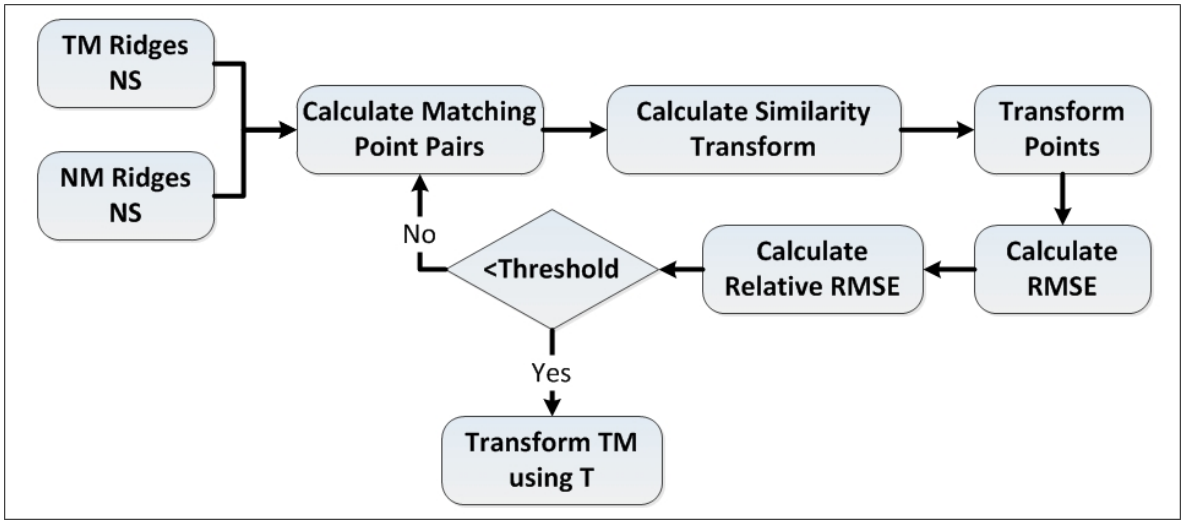


Figure 5-31 Similarity registration

In case a root cell is a hypercube , it is considered a binary version of an octree [133]. Maneewongvatana introduced a variation of the rule named sliding-midpoint, where the center of the cell is only used in case there are points on both sides of the split; otherwise, it splits on the nearest point to the center [133]. Using this variant, the query can be answered in $O\left(\frac{1}{\epsilon^d}\log n\right)$. In a recent study, Elseberg [134] benchmarked the performance of standard ICP using different neighbor search algorithms. In his results, a kd-tree outperformed the rest of algorithms, including an octree, r-tree and k-nn.

Given two set of points, set NM ridges NM_{ridges} with m points and TM ridges TM_{ridges} with n points, the goal is to find the similarity transform (R, T, S) that best aligns TM_{ridges} to the reference point NM_{ridges}. Results for similarity registration on the lumbar L1, pelvis and scapula are shown in Figure 5-32 Similarity registration on L1 lumbar (green represents$\boldsymbol{TM_{ridges}}$. , Red $\boldsymbol{TM_{ridges}}$ after registration, yellow $\boldsymbol{NM_{ridges}}$)are depicted in Figure 5-32 , Figure 5-33, and Figure 5-34, respectively.

a. Calculate Point Correspondence (Matching point pairs):

$$z = \{(i, j), \dots \dots \dots \dots .\}$$

I. Construct kd-tree $tree_{NM}$ using sliding midpoint splitting rules on theNM_{ridges}.

II. For each point i in TM_{ridges} find closest neighbor point j in NM_{ridges} using $tree_{NM}$.

b. Using z calculate similarity transform T:

I. Center both point sets around origin.

$$C_{TM_{ridges}} = \frac{1}{n}\left(\sum_{i=1}^{n} p_i\right)$$

$$TM_{ridges_Centered} = TM_{ridges} - C_{TM_{ridges}} \tag{39}$$

Where: $TM_{ridges_Normalized}$ is a n*3 matrix.

II. Normalize both point clouds to have unit norm:

$$TM_{ridges_Normalized} = \frac{TM_{ridges_Centered}}{\left\|TM_{ridges_Centered}\right\|} \tag{40}$$

Where: $TM_{ridges_Normalized}$ is a n*3 matrix.

III. Calculate Matrix a:

$$a = Transpose\left(NM_{ridges_{Normalized}}\right) * TM_{ridges_Normalized} \tag{41}$$

Where: a 3*3 matrix

IV. Calculate singular value decomposition of matrix a:

$$[m, d, l] = SVD(a) \tag{42}$$

V. Calculate Scale S:

$$S = trace(d) \tag{43}$$

VI. Calculate matrix t:

$$t = m * Transpose(l) \tag{44}$$

VII. Calculate translation T:

$$T = C_{NM_{ridges}} - \left(C_{TM_{ridges}} * s\right) * t \tag{45}$$

VIII. Calculate rotation R:

$$R = Transpose(t) \tag{46}$$

c. Transform TM_{ridges} using (R,T,S).

d. Calculate RMSE:

$$RMSE = SQRT(\sum_{i=0}^{n} \left\| NM_{ridges}(j) - TM_{ridges}(i) \right\| \tag{47}$$

Where j is the index in NM_{ridges} for the corresponding point to ith TM_{ridges} point.

e. Calculate RRMSE:

$$RRMSE(k) = (RMSE(k) - RMSE(k-1))/RMSE(k-1) \tag{48}$$

Where k is the current iteration count.

f. Check convergence:

$$k > maximuim\ number\ of\ iterations$$
$$OR \tag{49}$$

$$RRMSE \leq minimuim\ error\ threshold$$

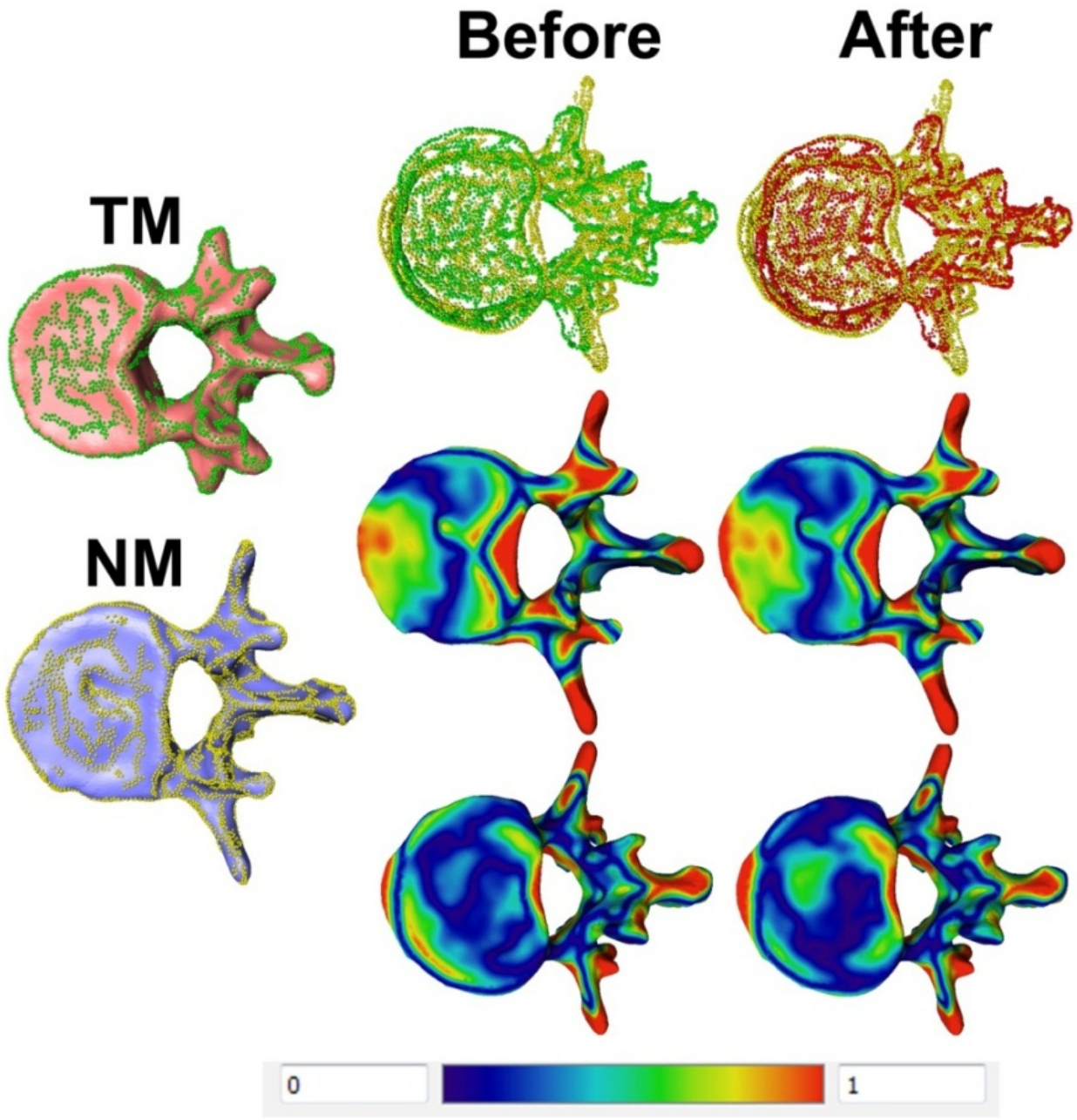


Figure 5-32 Similarity registration on L1 lumbar (green representsTM_{ridges}. , Red TM_{ridges} after registration, yellow NM_{ridges}) (cm)

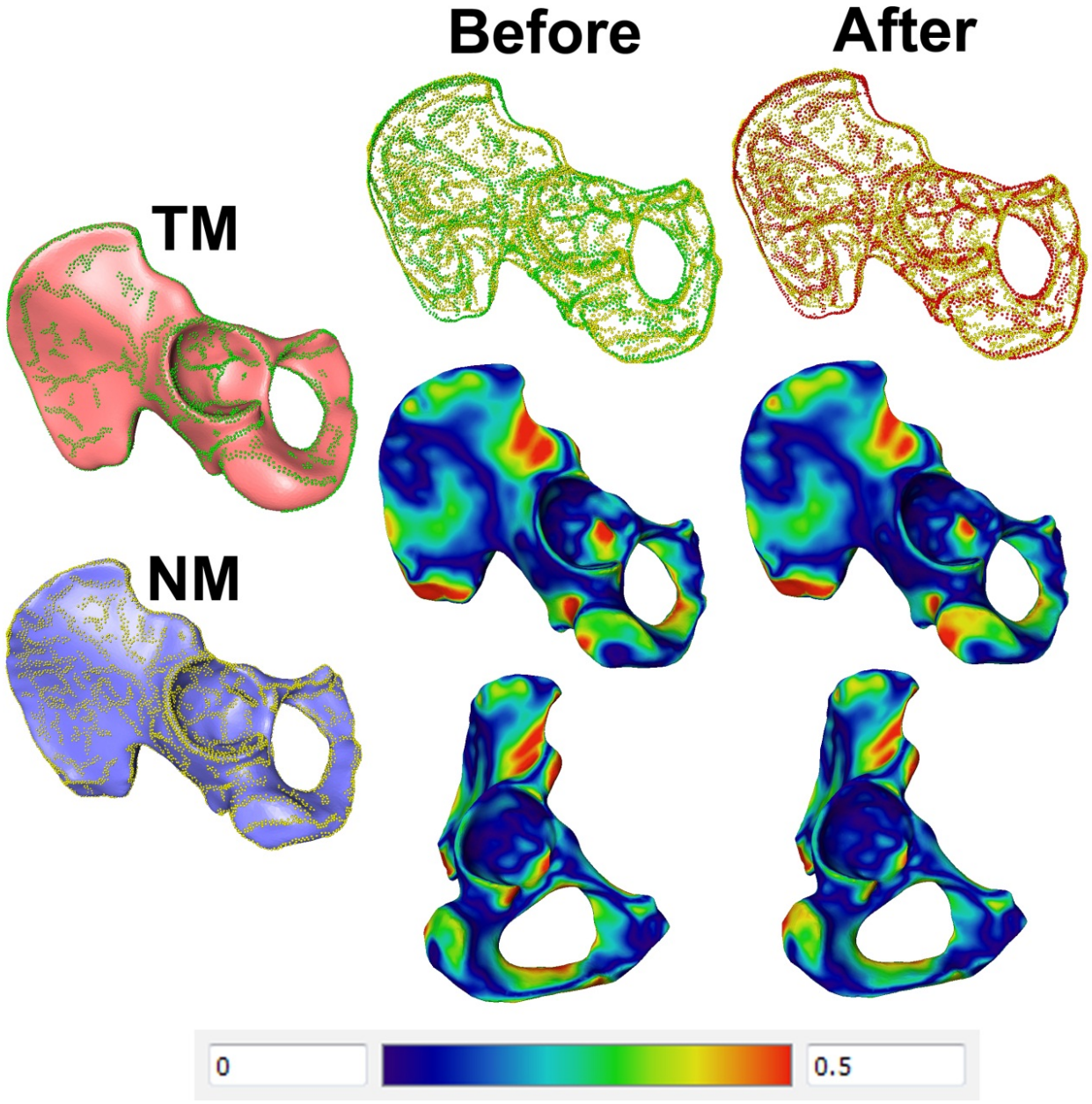


Figure 5-33 Similarity registration on pelvis (green representsTM_{ridges}. , Red TM_{ridges} after registration, yellow NM_{ridges}) (cm)

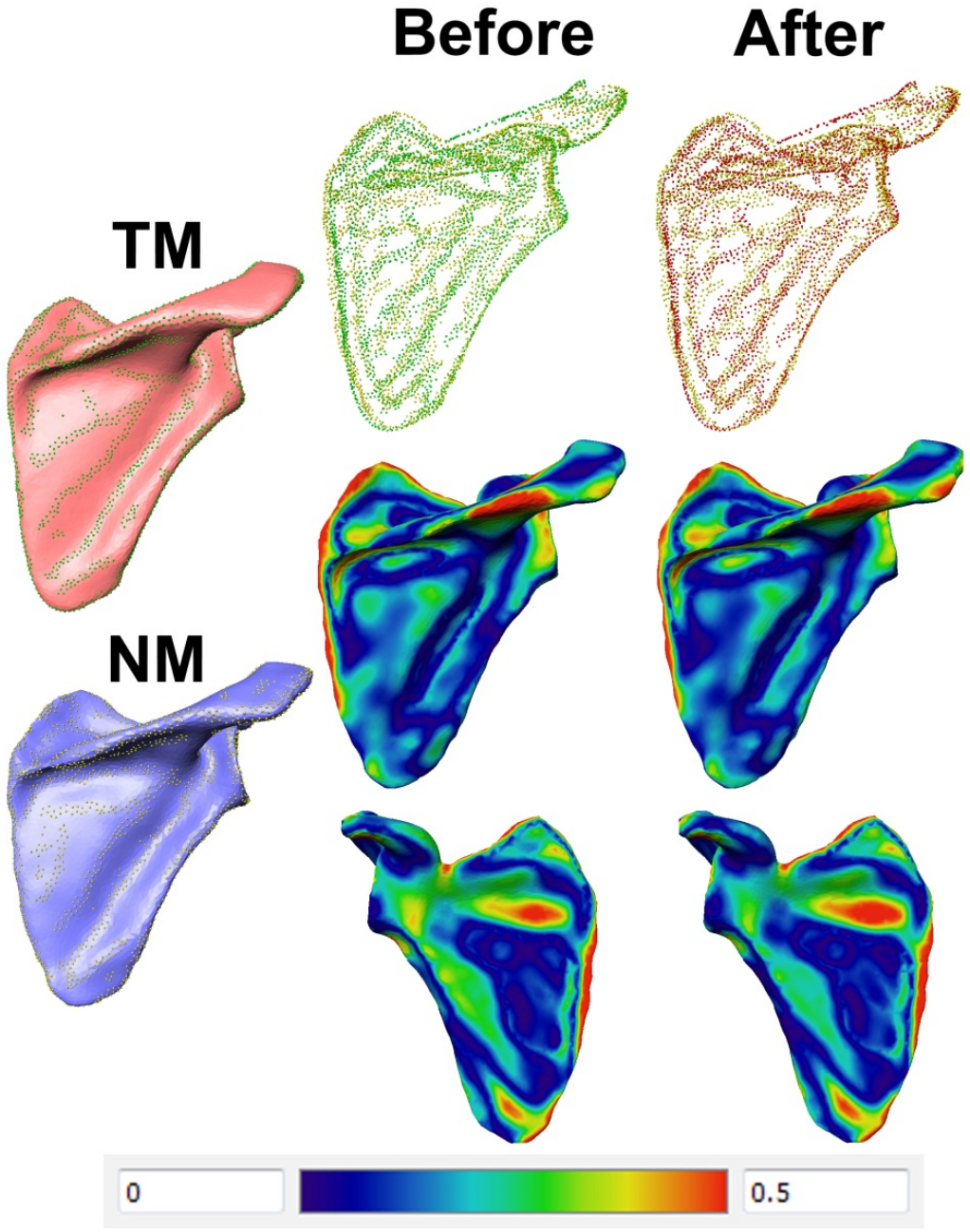


Figure 5-34 Similarity Registration on scapula (green representsTM_{ridges}. , Red TM_{ridges} after registration, yellow NM_{ridges}) (cm)

5.4.1.3 Articulated Registration:

The purpose of this step of the algorithm is to match n ss features of TM (TM_{SSF}) with m ss features calculated on the NM(NM_{SSF}). The difference between the number of detected features on TM and NM is due to anatomical variation. This difference in a number of detected features can result in a many relationships between TM_{SSF} andNM_{SSF}. Therefore, a two-way, mutual feature matching is performed to accommodate such variation and achieve accurate matching between all mutual features. First, all n features from TM_{SSF} are matched to NM_{SSF} (TM_{SSF}"To Match", NM_{SSF} "$Reference$") and output is a feature correspondence map z_1 the same size as TM_{SSF} and can have (1-r) relationship. Secondly, all features from NM_{SSF} are matched to TM_{SSF} (TM_{SSF}"Reference", TM_{SSF} "$To\ Match$") output is a feature correspondence map z_2 same size as TM_{SSF} and can have (q-1) relationship. Matched features from z_1 and z_2 are then merged together to form a new set of feature pairs $NM_{SSF_{Merged}}$ and $TM_{SSF_{Merged}}$ and new correspondence map z_3 with (1-1) relationship. Correspondence between each point in a feature pair is then calculated and used to calculate affine transformation between the combined set of feature points. This affine transformation is used to transform$TM_{SSF_{Merged}}$. The final step involves aligning each individual feature in $TM_{SSF_{Merged}}$ with the corresponding feature in $NM_{SSF_{Merged}}$. An overview of the articulated registration algorithm is outlined in Figure 5-35. Results of articulating registration step on the lumbar, pelvis, scapula and skull are shown in Figure 5-38, Figure 5-39, Figure 5-40 , andFigure 5-41 Articulating registration on skull

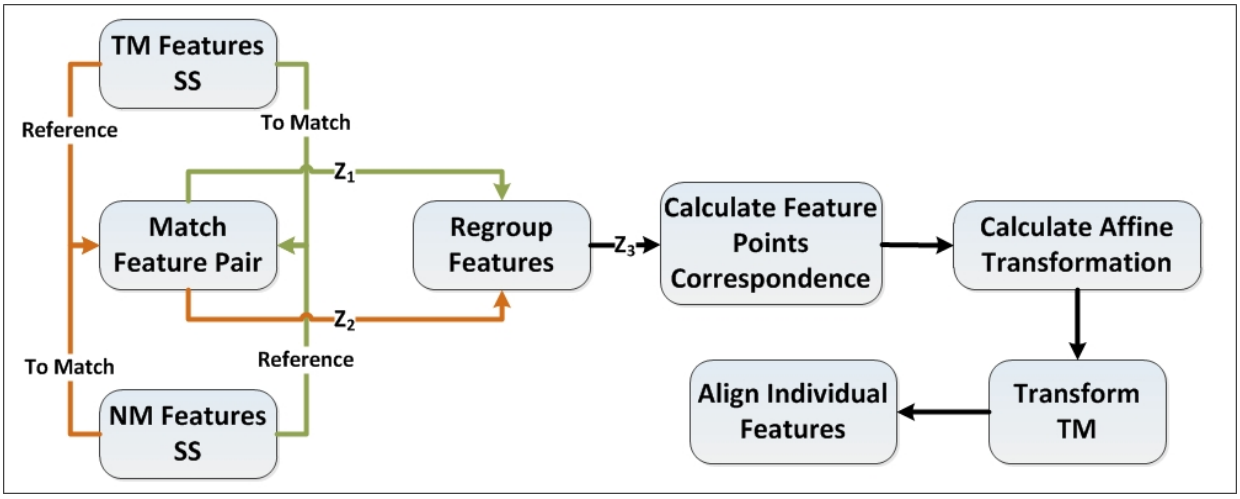


Figure 5-35 Articulated registration algorithm overview

a. Match feature pair using NM features as reference and TM features as to match and calculate correspondence map z_1 :

b. Feature pair matching involves creation of a correspondence map between features with minimum dissimilarity measure. Figure 5-36 details the feature matching step, and Figure 5-36 shows the results of the pair matching algorithm on L5 lumbar.

I. Construct feature correspondence map z by finding the index j of the feature in the reference features (REF_F) that minimize the dissimilarity measure current feature to match (TOM_F) .

$$d = sqrt\left(\sum_{f=1}^{g}(\|p_f - q_f\| + \|S_{pf} - Sq_f\|)\right) \quad (50)$$

Where

g: is the number of points in the i^{th} feature in TOM_F

p_f: is the f^{th} point in the i^{th} feature in TOM_F

q_f: is the closest point in the j^{th} feature in REF_F to the f^{th} point in the i^{th} feature in TOM_F

Sp_f: is the shape index of the point p_f .

Sq_f: is the shape index of the point q_f .

II. For every matched feature pairs compute correspondence vector y_i that contains indices of the closest point on the j^{th} REF_F feature to every point on the i^{th} TOM_F.

III. Compute histogram for indices in all y_i.

IV. Reject matches with the histogram containing pins with frequency larger than 50% of total point's number. (This step is done to remove outliers from the matching step).

c. Repeat step a using TM as reference features and NM to match features and calculate correspondence map z_2.

d. Regroup features.

I. Using correspondence map z_1 merge features in TM_{SSF} with multiple matches in NM_{SSF} and generate new feature vector $TM_{SSF_{Merged}}$.

II. Using correspondence map z_2 merge features in NM_{SSF} with multiple matches in TM_{SSF} and generate new feature vector$NM_{SSF_{Merged}}$.

III. Generate correspondence map z_3 with new feature indices from $NM_{SSF_{Merged}}$ and $TM_{SSF_{Merged}}$.

e. Calculate feature points correspondence.

I. For all points for features in $TM_{SSF_{Merged}}$ construct point's vector u_{TM}

II. For all points in u_{TM} find closest points in corresponding feature in $NM_{SSF_{Merged}}$ and construct point's vector u_{NM}.

f. Calculate affine transformation T_{Affine} that aligns u_{TM} with u_{NM}.

$$T_{Affine} = Inv(U_{TM}) * U_{NM} \tag{51}$$

g. Apply transformation T_{Affine} to both TM in scale space and in normal space.

h. Realign individual features.

I. For every feature in $TM_{SSF_{Merged}}$ align with corresponding feature in $NM_{SSF_{Merged}}$ Using similarity registration algorithm outlined in 5.4.1.2.

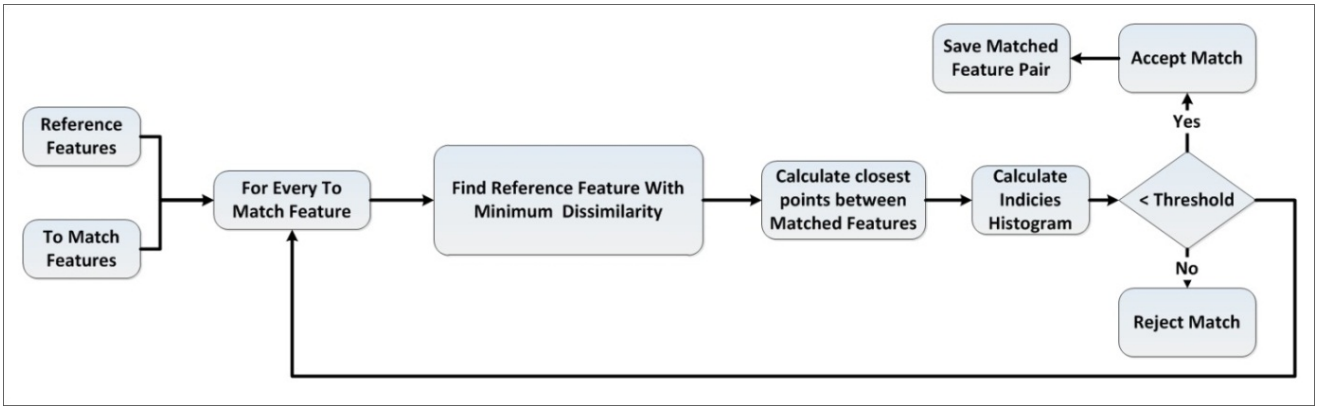


Figure 5-36 Matching features pair

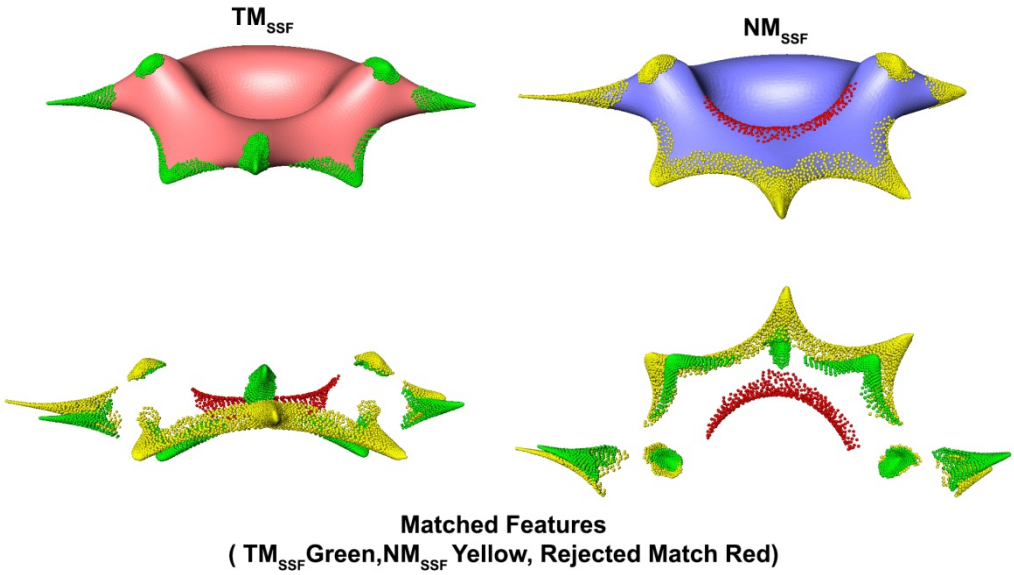


Figure 5-37 Matching feature pairs (L5 lumbar)

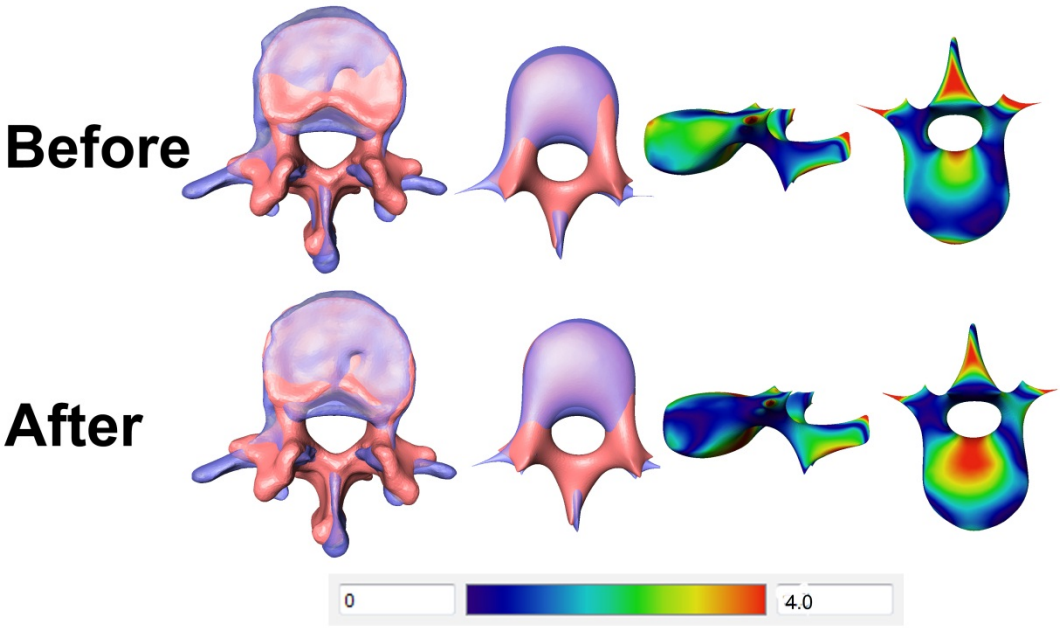


Figure 5-38 Articulating registration on lumbar L1

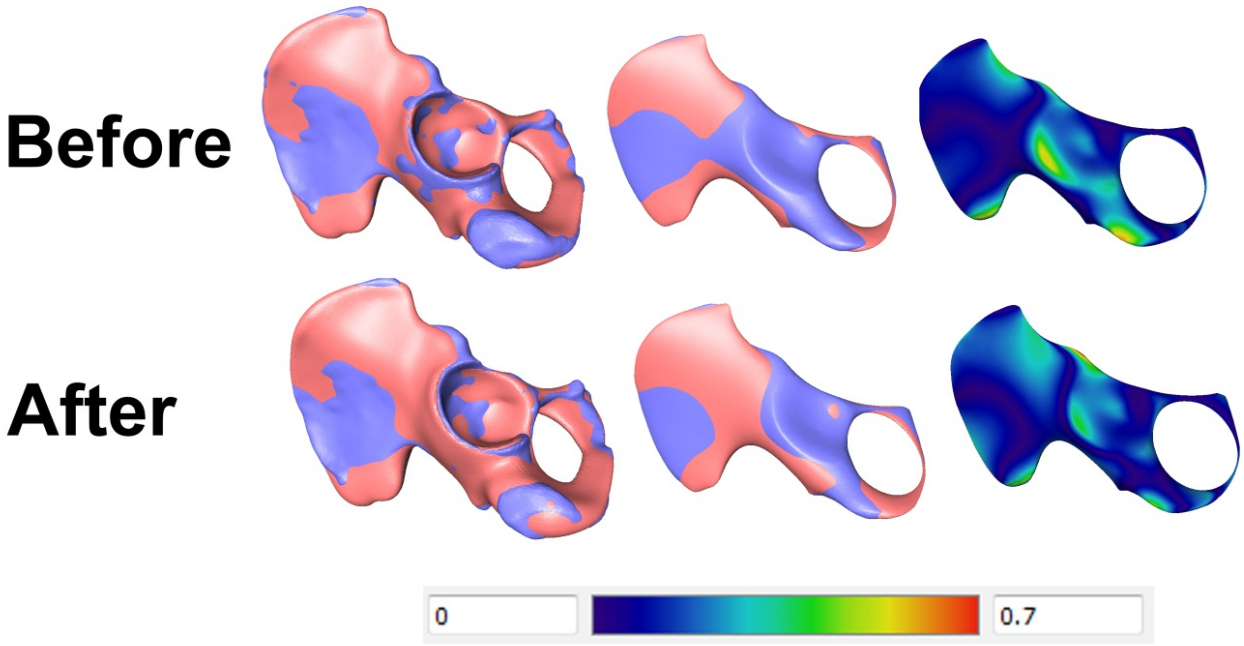


Figure 5-39 Articulating registration on pelvis

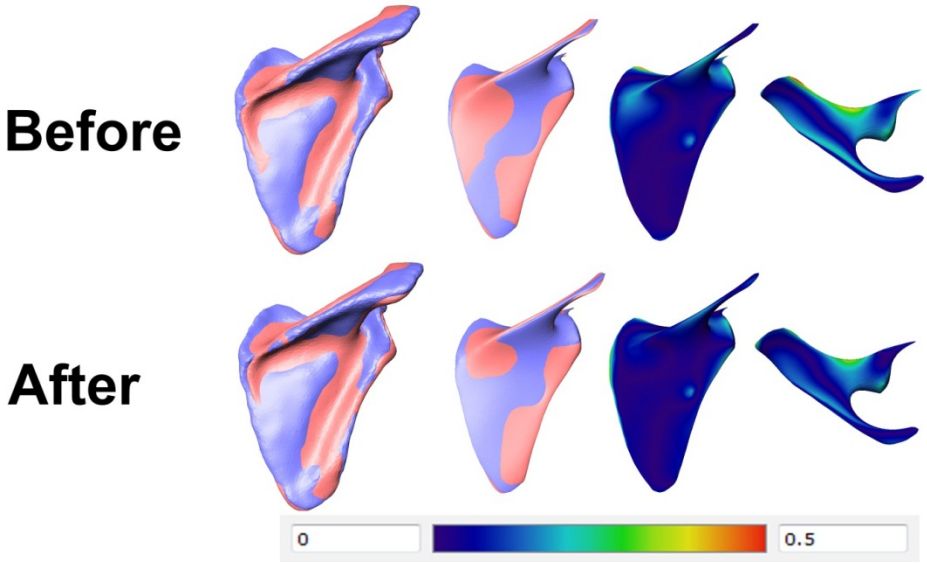


Figure 5-40 Articulating registration on scapula

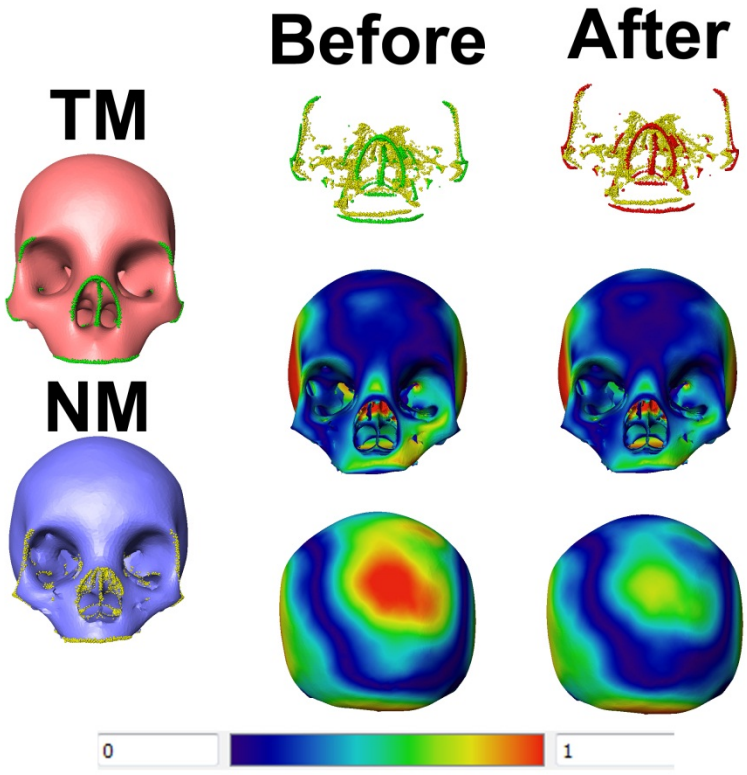


Figure 5-41 Articulating registration on skull

5.4.1.4 Non-Rigid Registration:

This step involves matching all surface vertices on the TM to vertices on NM and calculates initial correspondence. This correspondence is then used to calculate deformation fields that move each vertex on TM to the matched point on NM. Matching is done between vertices within the same class (i.e., SS feature vertex; NS feature vertex, or non-feature vertex).

5.4.1.4.1 Calculate SS features correspondence:

a. Dilate TM_{ssf} & NM_{ssf} using n rings neighbors:

$$n = \frac{V_{total}}{V_{ffs}} \tag{52}$$

Where V_{total} is total number of vertices in the mesh

V_{ffs} is the total number of SS features.

b. Align feature using SWIM (Size Invariant Weighted Matching):

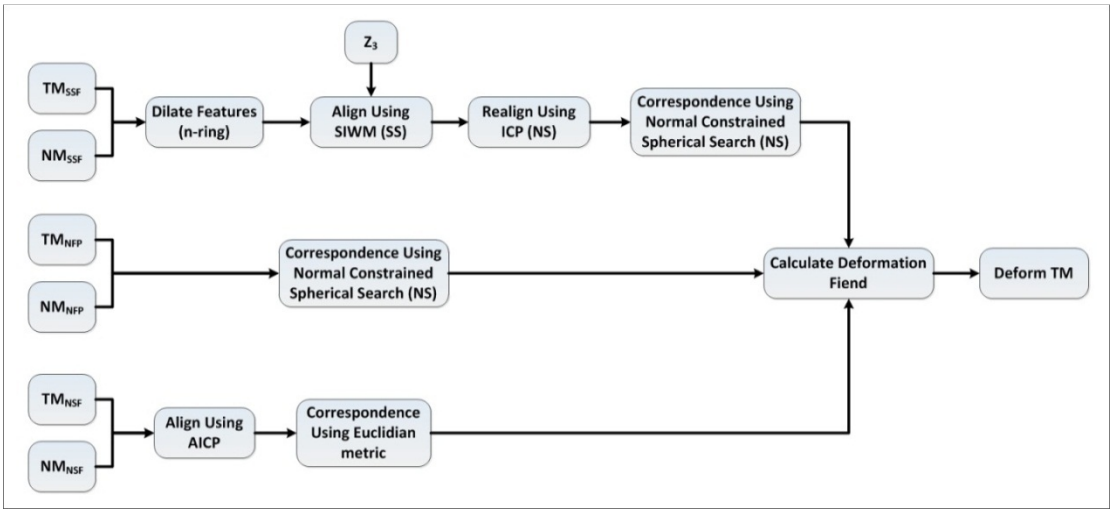


Figure 5-42 Overview of non-rigid registration step

Size Invariant Weighted Matching: ICP in many of its variants. Both algorithms utilize only spatial information [103, 111, 113, 117, 118, 123, 135, 136] and, thus, the solution converges by minimizing the overall point's spatial registration error. Given the nature of the present problem of matching features in SS, both local and global shape information are crucial for correctly matching corresponding feature points. Sharp suggested the use of Gaussian curvature with ICP as a way to capture local shape information and enhance the registration [106]. Dorai [137] suggested the use of shape index and curvedness to encode local shape information in a new shape representation scheme called COSMOS. However, in his approach, surface was divided into patches, and the shape index of overall patches was encoded. SIWM uses a similar approach to both Dorai and Sharp where point sets in each matched pair of SS features are registered not only using spatial information (i.e., coordinate data), but also using scale invariant features like shape index and curvedness. Details of the algorithm are outlined in Figure 5-43.

Given two point clouds, reference (X) and moving (Y), the goal is to iteratively align them to minimize overall error metric, under constraint of a minimum RRMSE, and maximum angle threshold.

I. Compute mean of both X and Y.

II. Calculate vector V_1 joining the two mean points.

III. For every point in X, find the matching point in Y and compute correspondence vector z_1:

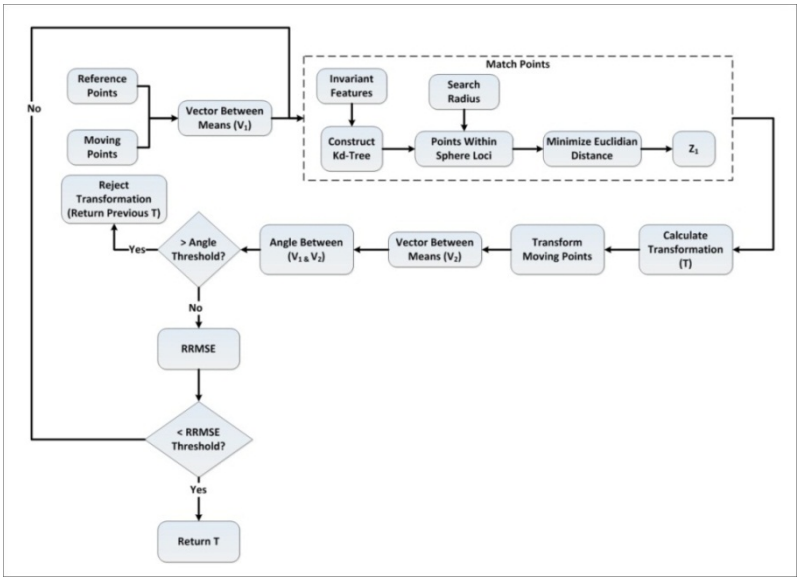


Figure 5-43 Scale Invariant Weighted Matching registration algorithm

1. Construct kd-tree k_1 using size invariant features (C,S,∇) of Y.
2. Define initial search radius r:

$$r = \mu_{distance} + 1.5\sigma_{distance} \tag{53}$$

   Where $\mu_{distance}$ & $\sigma_{distance}$ are the mean and standard deviation of the Euclidian distance between X and closest points in Y.

3. Using k1 find points in Y with values of invariant features that lies within sphere of radius r from the current search point in X.
4. Using the search results of the sphere loci, find the point in Y with minimum Euclidian distance to coordinate data of current search point in X.

5. Repeat step 4 and 5 for all points in X.

IV. Using matched point pairs compute transformation T [125] that transforms X to matched points in Y.

V. Compute new mean for points in X.

VI. Compute vector V_2 between new mean for X and mean for point Y.

VII. Compute angle ω between V_1 and V_2.

VIII. If ω is greater than the angle threshold, exit the algorithm and return to previously calculated T.

IX. If ω is less than the angle threshold, compute RRMS.

X. If RRMS is less than the threshold, exit the algorithm and return to current T.

XI. If RRMS is less than the threshold, repeat the algorithm until conversion.

Figure 5-44 shows a comparison of the registration error between ICP and SIWM on the lumbar in ss. Figure 5-45 shows the comparison of the registration error between ICP and SIWM on the lumbar in original space. Figure 5-46 compares the alignment of ICP versus SIWM: SIWM aligned feature points more closely, and ICP distributed error on overall points. Figure 5-47 shows registration after mapping the lumbar back to original space.

Figure 5-48 shows a comparison of registration error between ICP and SIWM on the pelvis in ss. Figure 5-49 shows a comparison of registration error between ICP and SIWM on the pelvis in original space. Figure 5-50 compares the alignment of ICP versus SIWM. Figure 5-51

shows the registration after mapping the pelvis back to original space. Figure 5-52 shows results of registration of features using SIWM.

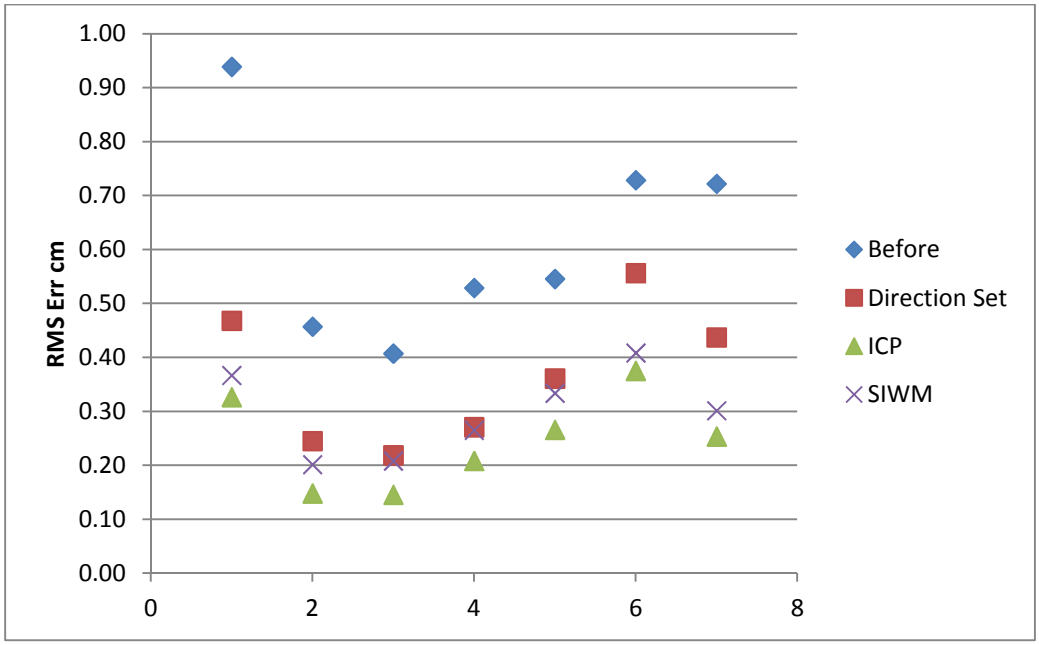


Figure 5-44 Comparison of SIWM performance against ICP on lumbar in scale space

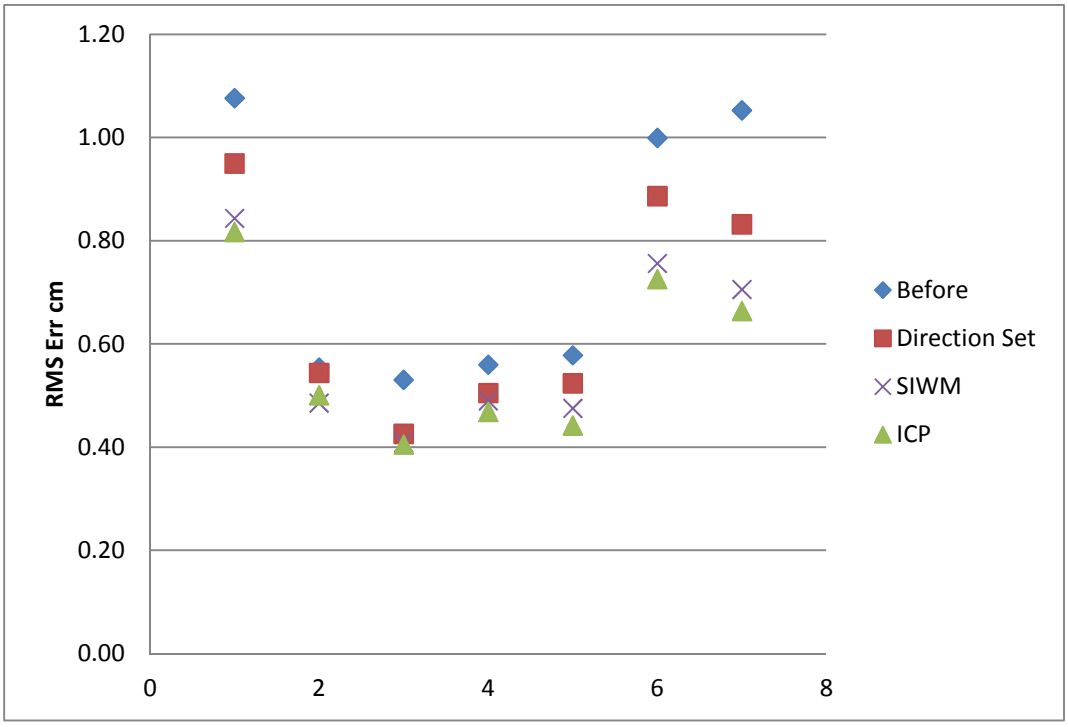


Figure 5-45 Comparison of SIWM performance against ICP on lumbar in original space

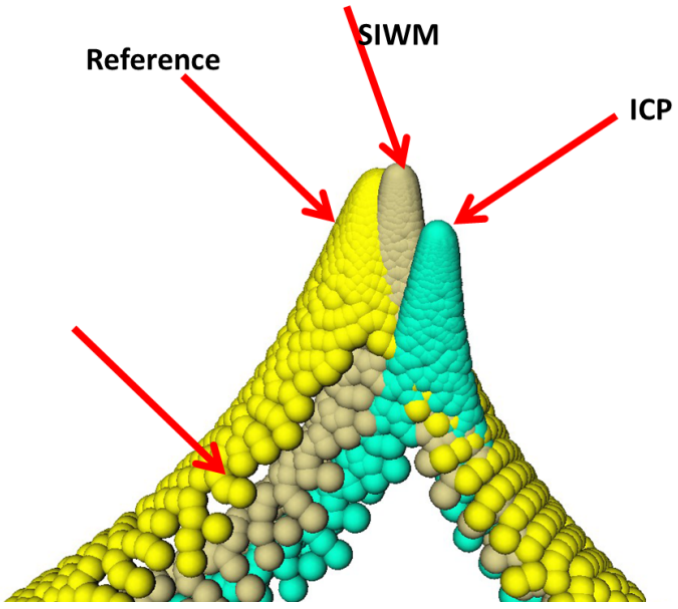


Figure 5-46 Results of feature points registration on lumbar spines process in scale space

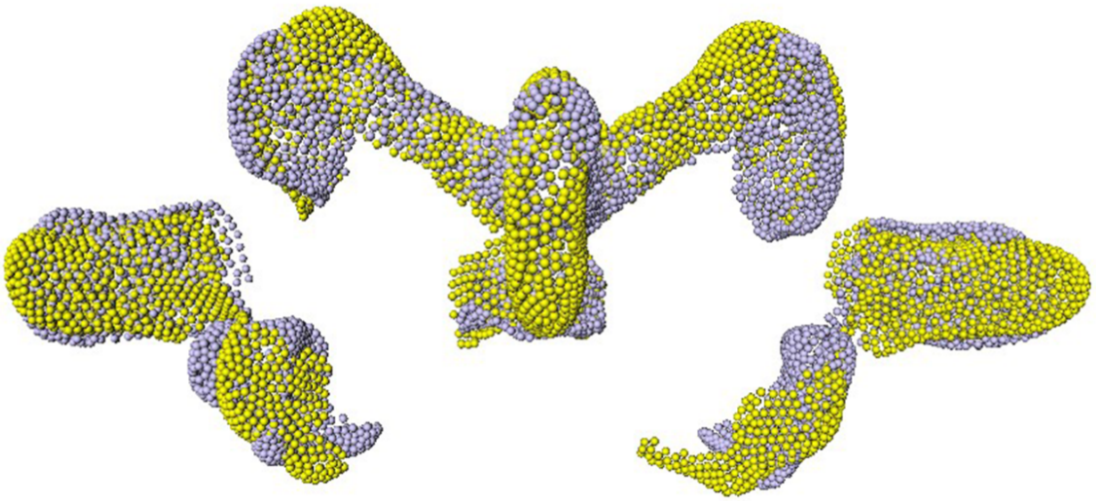


Figure 5-47 Registration of feature points using SIWM in original space

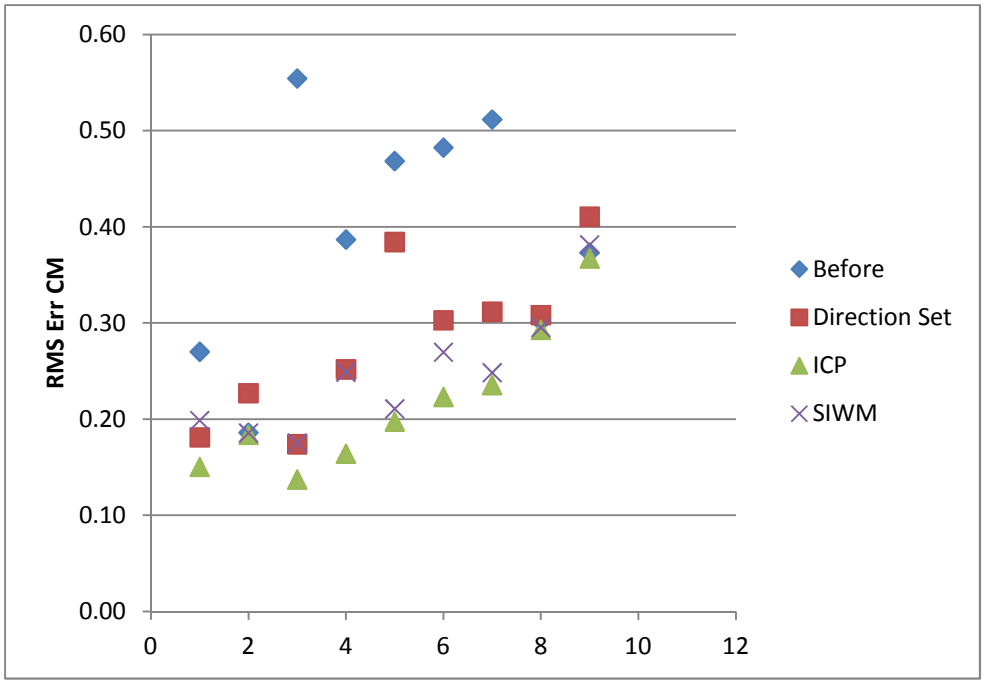


Figure 5-48 Comparing registration results for pelvis in scale space

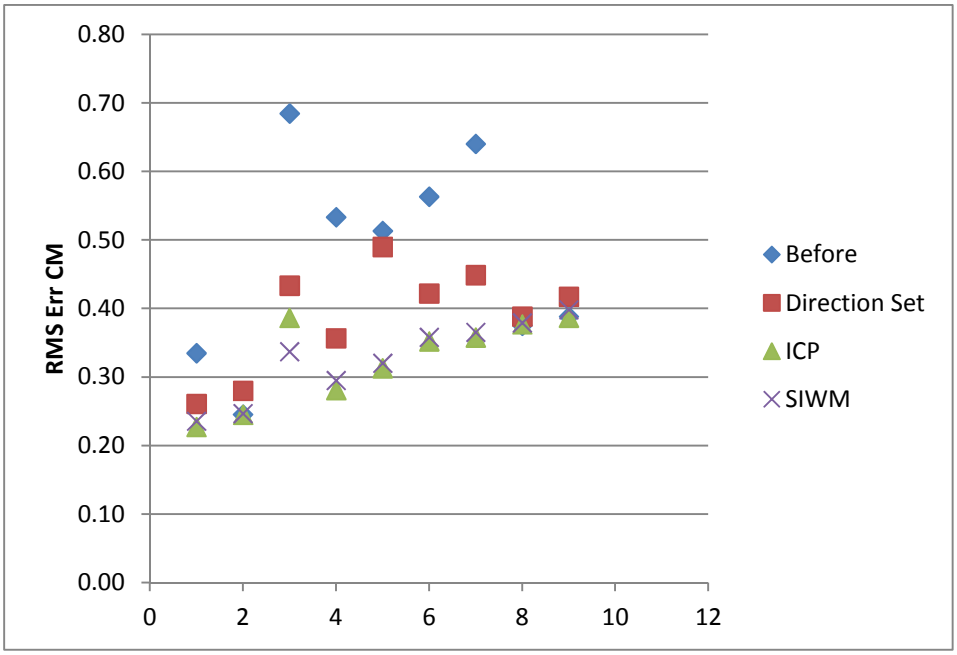


Figure 5-49 Comparing registration results for pelvis in original space

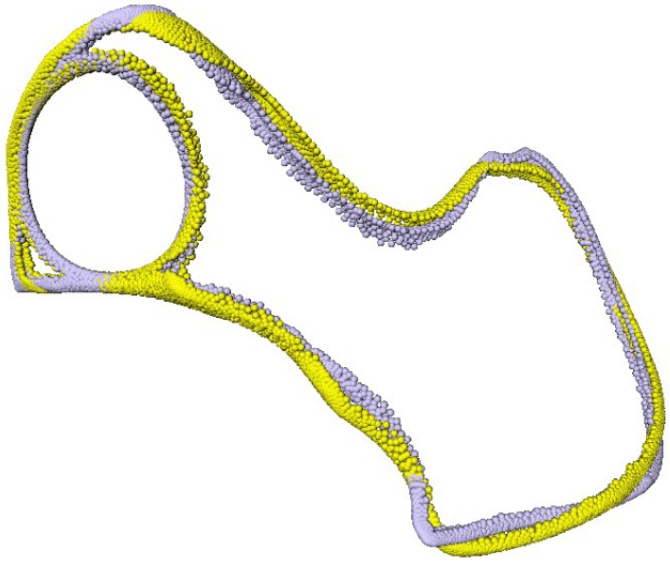


Figure 5-50 Registration using SIWM for pelvis in scale space

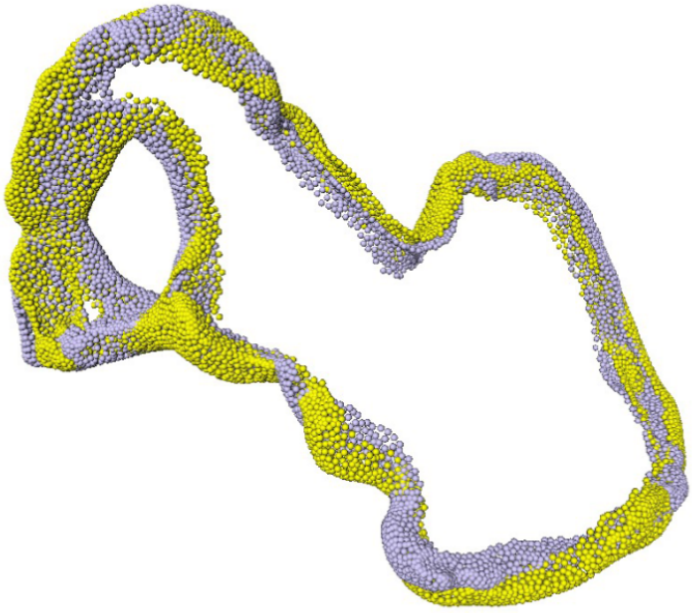


Figure 5-51 Registration using SIWM for pelvis in original space

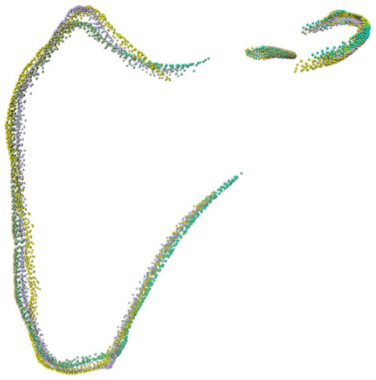


Figure 5-52 Registration results on scapula in scale space

c. Realign feature pairs in normal scale using ICP.

d. Compute correspondence between points in feature pairs (TM_{ssf_i} and NM_{ssf_j}) using a normal constrained, spherical search:

   I. Construct kd-tree k_2 using coordinate data of NM_{ssf_j}.

II. For every point in $TM_{ssf_i,}$ find the point in NM_{ssf_i} that minimizes the Euclidian distance and satisfies the following two constraints:

1. Lies in spherical loci of radius r from current point in TM_{ssf_i}.
2. Angle between normal at this point and the normal at the reference point in TM_{ssf_i} is less than the normal angle threshold criterion.

5.4.1.4.2 Calculate non feature points' correspondence:

a. For every point in $TM_{NFP,}$ find the closest points in NM_{NFP} using normal constrained, spherical search outlined above.

5.4.1.4.3 Calculate normal scale features' correspondence:

a. Align points in TMNSF to points in NMNFP using affine ICP.
b. For every point in TMNSF, find the closet point in NMNSF that minimize the Euclidian distance.

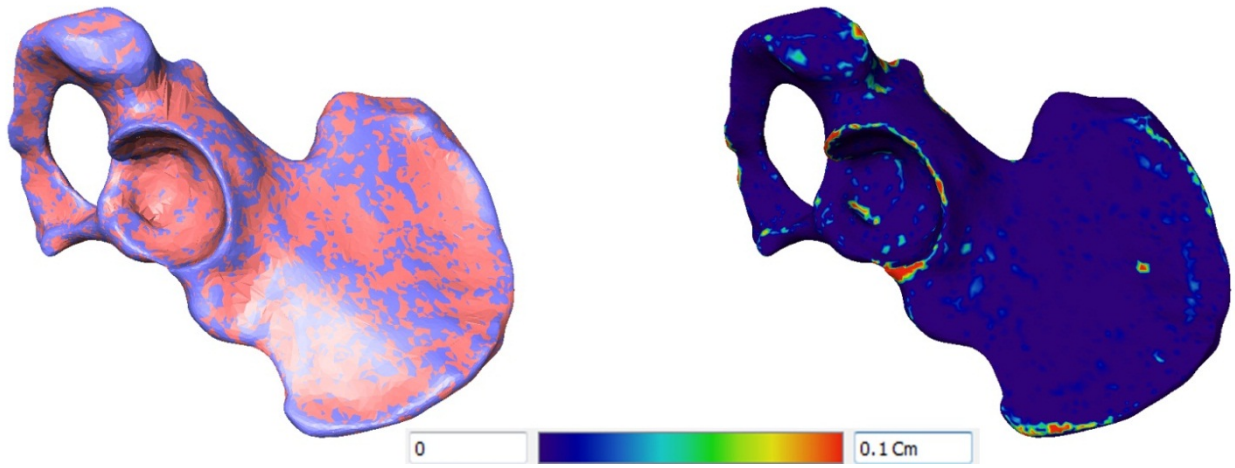


Figure 5-53 Results of non-rigid registration on pelvis

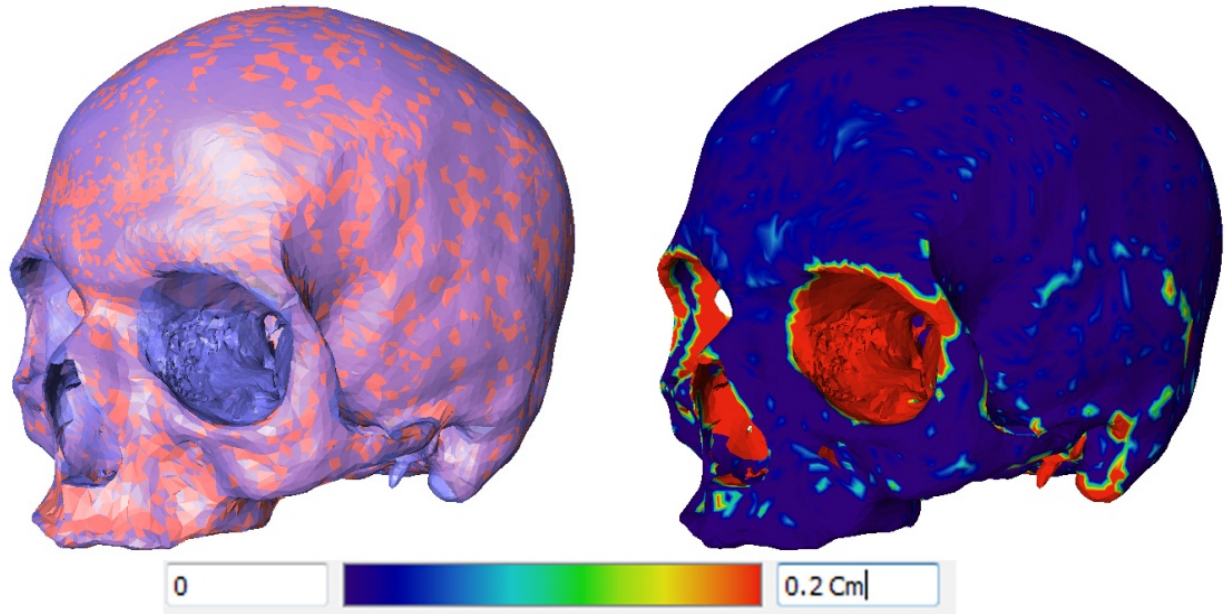


Figure 5-54 Results of non-rigid registration on skull

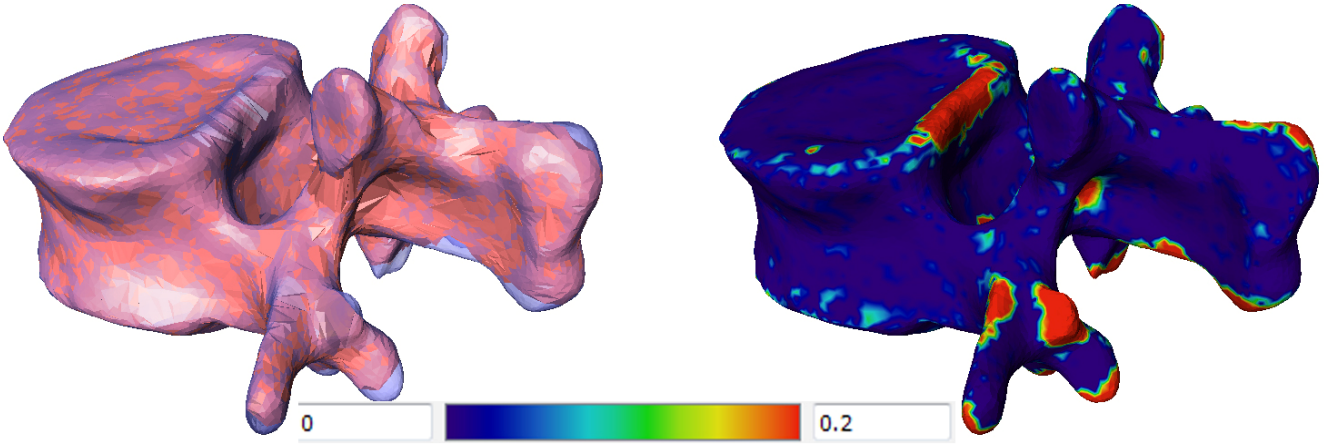


Figure 5-55 Results of non-rigid registration on lumbar L1

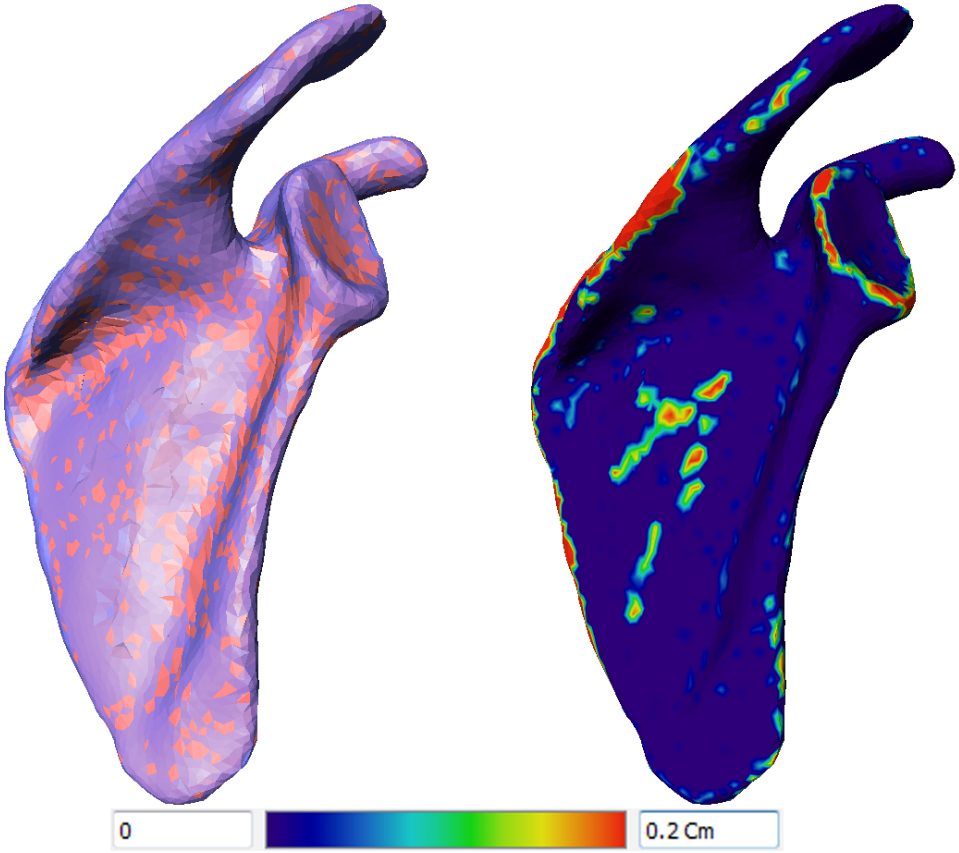


Figure 5-56 Results of non-rigid registration on scapula

5.4.1.5 Relaxation:

The purpose of the relaxation step is to move the vertices of the TM mesh closer to surface of NM after the multi-resolution registration step and smooth the output model. Figure 5-57 Overview of relaxation step.

a. Relax TM vertices using weighted match.

b. Relax TM vertices using weighted match.

   I. Compute closet vertices on TM to NM using normal constrained spherical search algorithm outlined previously.

   II. Using closest vertices generate a correspondence vector from each vertex in TM and it's matched vertices in NM (this can results in more than one match point from NM).

   III. Using matched points for each vertex on TM compute the weighted mean of the matched points on NM (weights based on the Euclidian distance from the point and matched points).

$$w_{ij} = \frac{\left\| v_{TM_i} - v_{NM_j} \right\|}{\sum_{k=1}^{m} \left\| v_{TM_i} - v_{NM_k} \right\|} \tag{54}$$

Where

v_{TM_i} is the current vertex to be moved from TM

v_{NM_j} is the j[th] matched NM vertex to v_{TM_i}.

m is the total number of matched vertices from NM to v_{TM_i}

c. Move every vertex on TM to closest point on NM surface.

d. Smooth output model.

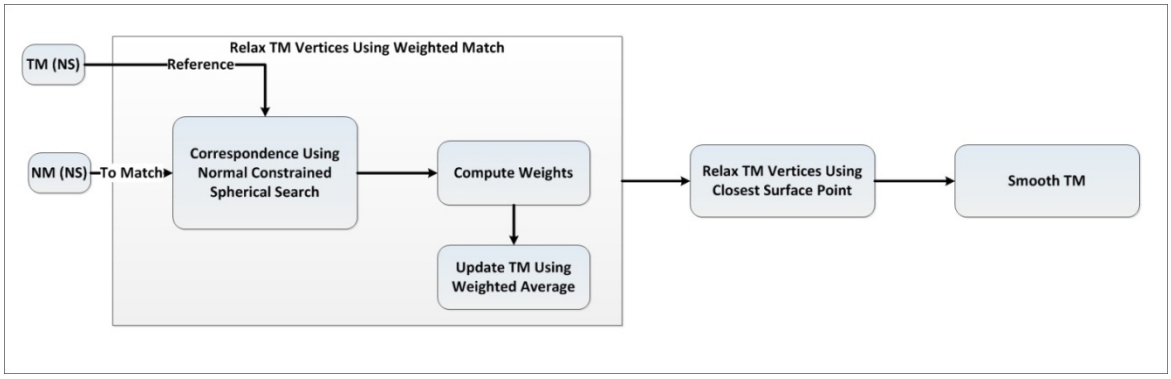


Figure 5-57 Overview of relaxation step

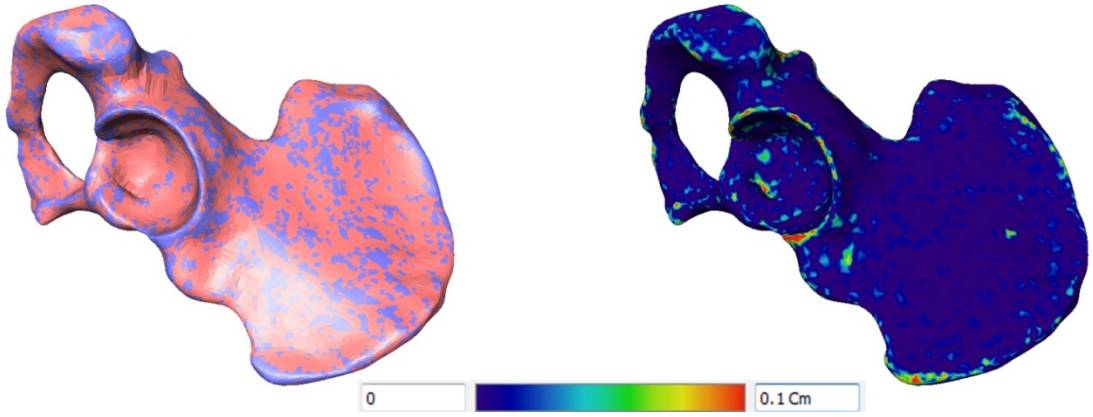


Figure 5-58 Results of relaxation on pelvis

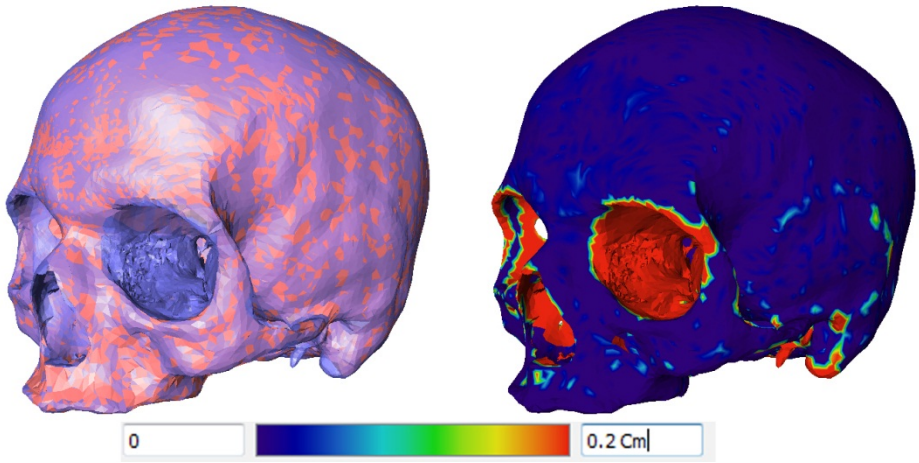


Figure 5-59 Results of relaxation on skull

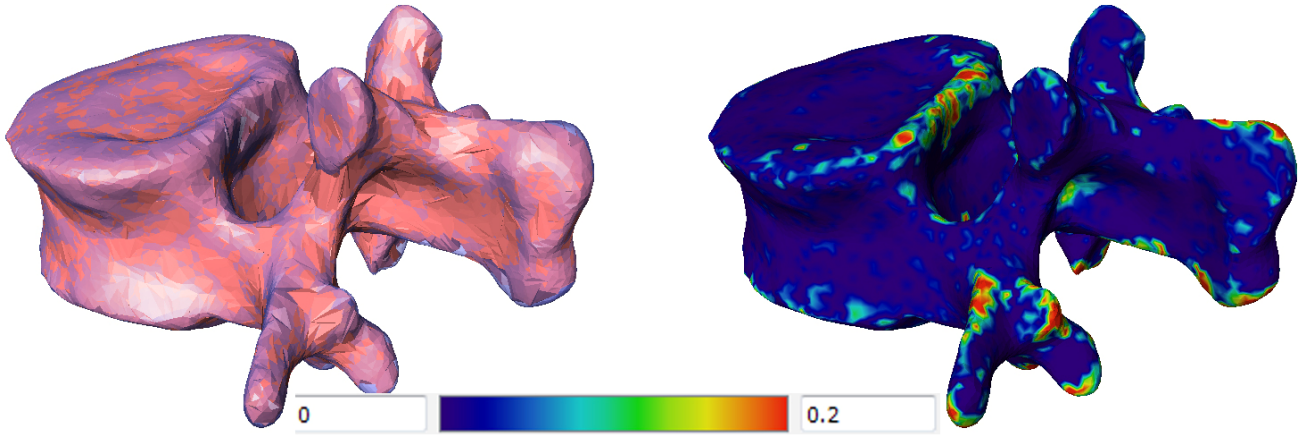


Figure 5-60 Results of relaxation on lumbar L1

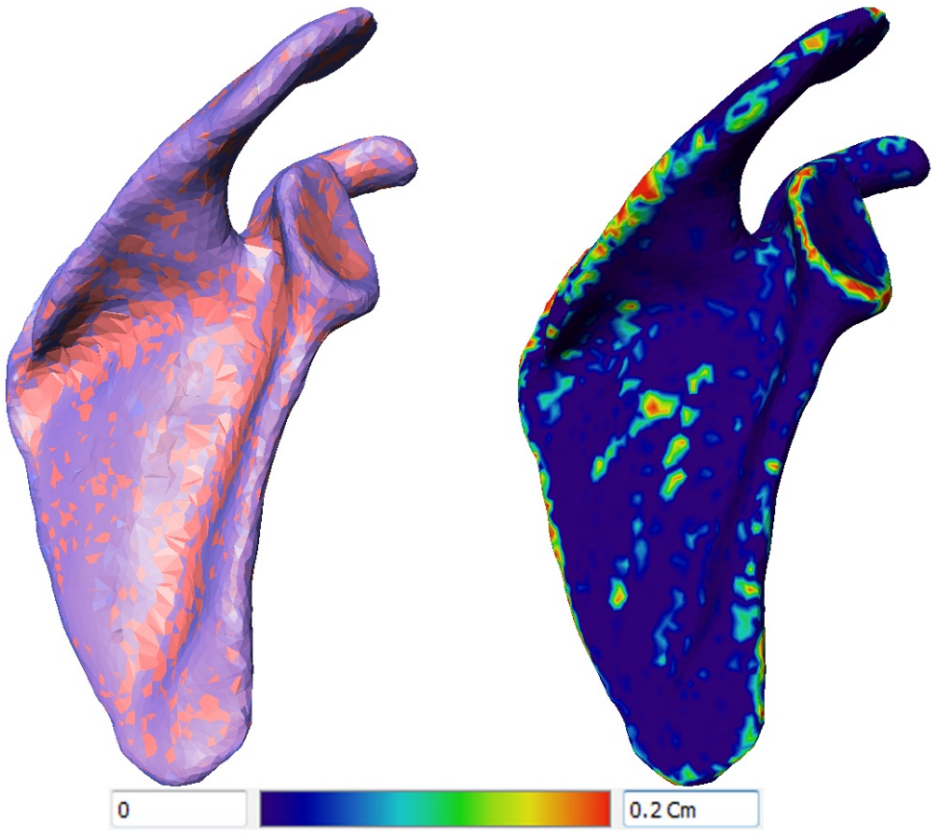


Figure 5-61 Results of relaxation on scapula

5.5 Free Form Deformation

This is the final step in the atlas before calculating correspondence. During this step, the surface of TM is iteratively moved closer to NM using a weighted ratio between mutually matched points on both surfaces. After this step, TM surface matches the surface of NM.

5.5.1 Algorithm 5: Free Form Deformation:

a. Smooth the vertices normal of TM and NM using two ring neighbors.

b. For all TM vertices, find the closest vertices on NM and generate correspondence map M_1.

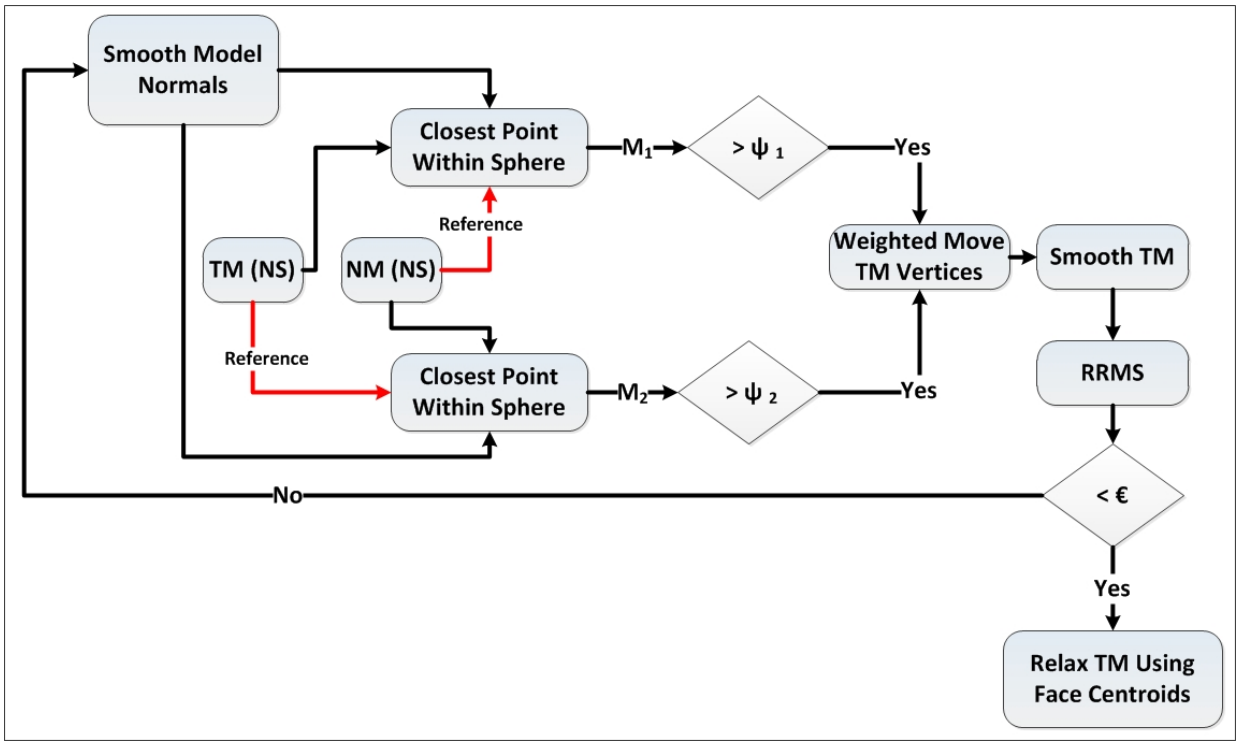


Figure 5-62 Overview of the free form deformation step

c. For all NM vertices, find the closest vertices on TM and generate correspondence map M_2.

d. Compute Euclidian distances for all points in M_1 and M_2.

e. Compute threshold ψ_1

$$\psi_1 = \mu_{M1} + 2 * \sigma_{M1} \quad (55)$$

Where

μ_{M1} and σ_{M1} are the mean and standard deviation of the Euclidian distances of points in M_1.

f. Compute threshold ψ_2 using equation (55).

g. Refine points in M_1 by deleting points with distances less than ψ_1.

h. Refine points in M_2 by deleting points with distances less than ψ_2.

i. Move TM vertices using weighted average of matched points in refined M_1 and M_2.

j. Smooth TM.

k. Compute RRMS.

l. If RRMS is greater than the RRMS threshold, repeat the algorithm.

m. If RRMS is less than the threshold, relax TM using faces centroids of NM.

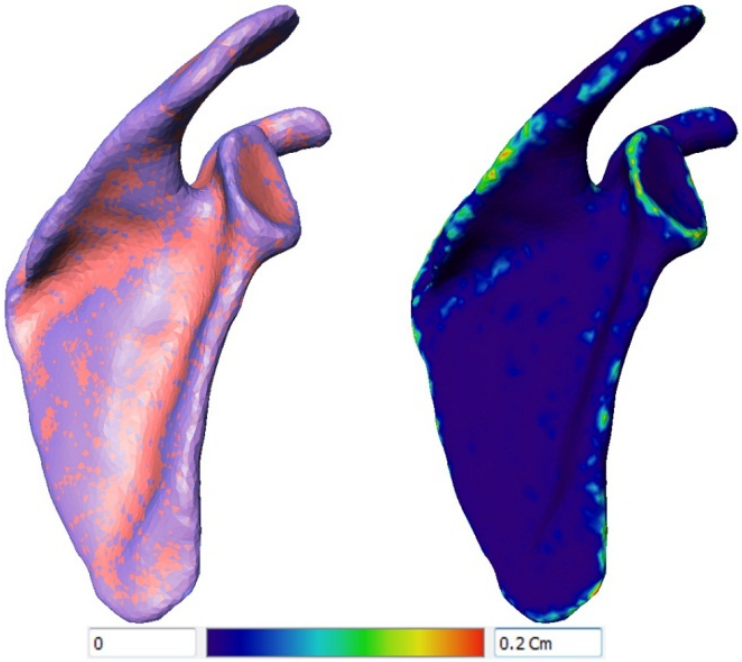


Figure 5-63 Results of free form deformation on scapula

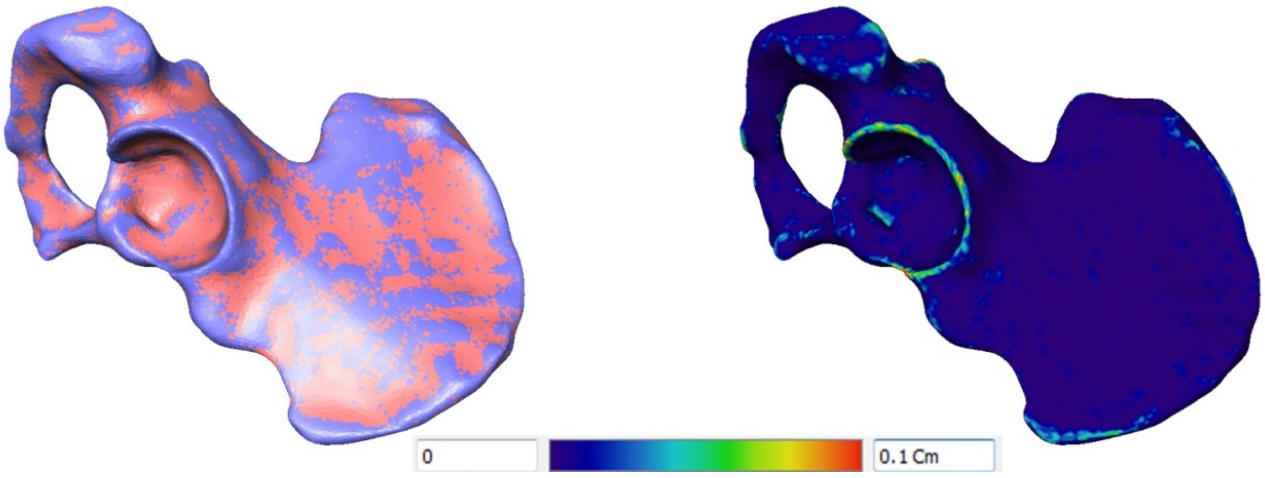


Figure 5-64 Results of free form deformation on pelvis

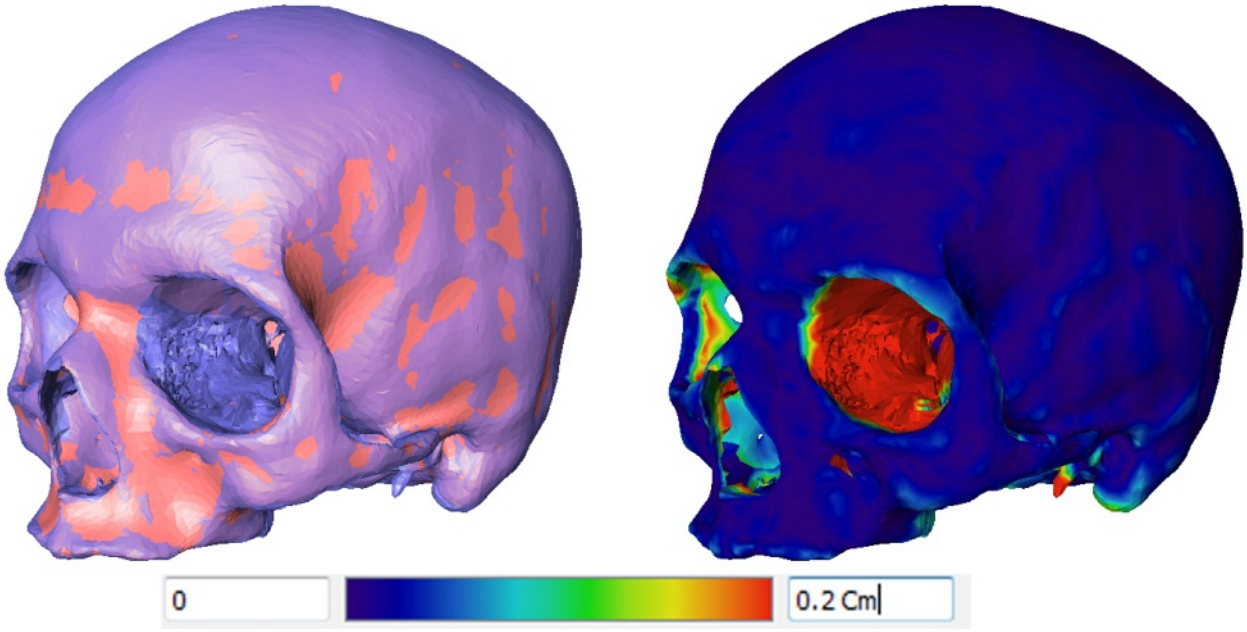


Figure 5-65 Results of free form deformation on skull

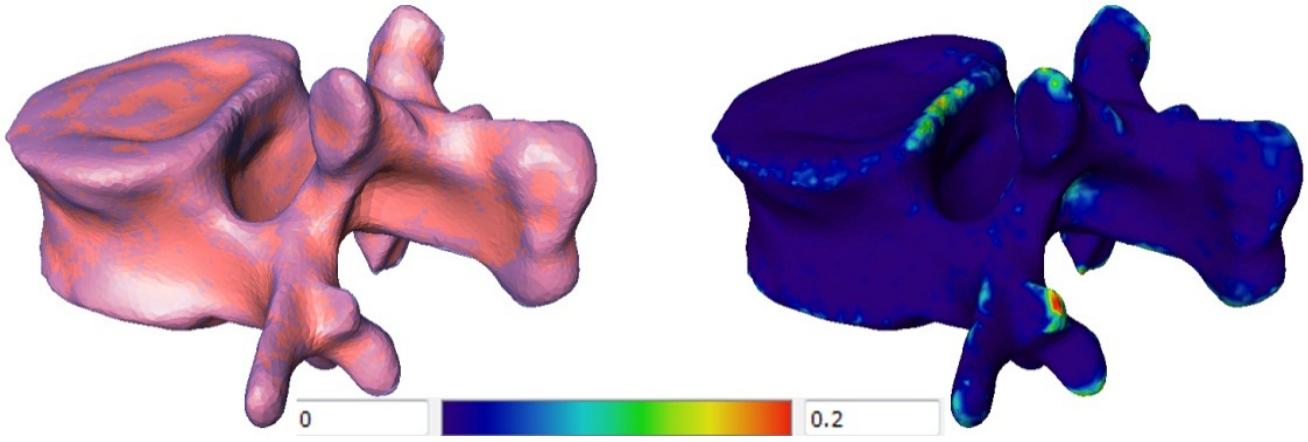


Figure 5-66 Results of free form deformation on lumbar L1

5.6 Calculating Correspondence

The purpose of this step is to refine the output from the free form deformation step and perform a final match between vertices' location on TM and surface of NM to ensure accurate final correspondence. Likewise, it is performed to ensure the TM has completely deformed to match the surface of the model to be added.

5.6.1 Algorithm 6: Calculating Final Correspondence:

a. Form a set of rays $Rays_{TM}$, where the rays points are the vertices of TM and direction is the vertices normal.

b. Intersect NM surface with $Rays_{TM}$ using AABB trees.

c. Filter intersection points for every vertex.

    I. By selecting the closest intersection point.

    II. Rejecting closest intersection point with distance > 3mm vertex on TM.

d. Interpolate location of rejected points using knn interpolation.

e. Update TM using the calculated new points location.

f. Relax TM using closest surface point.

g. Compute final RMS value between deformed TM and NM.

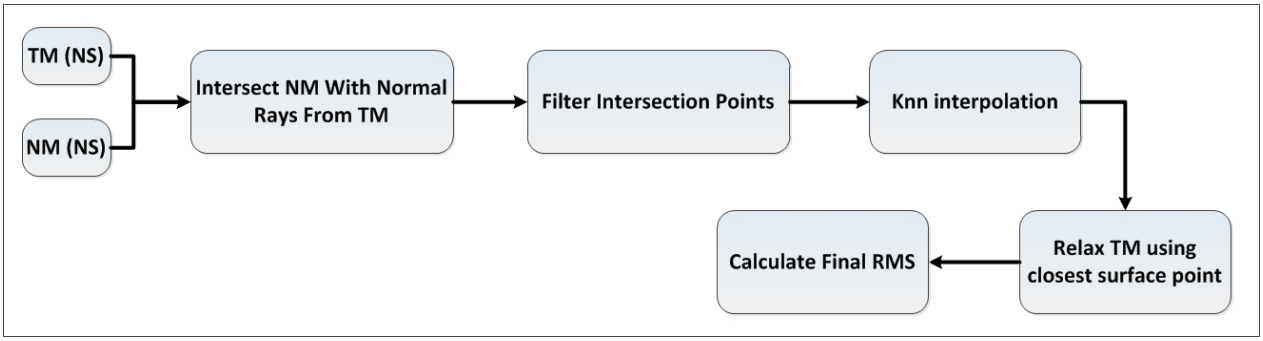


Figure 5-67 Overview of correspondence calculation step

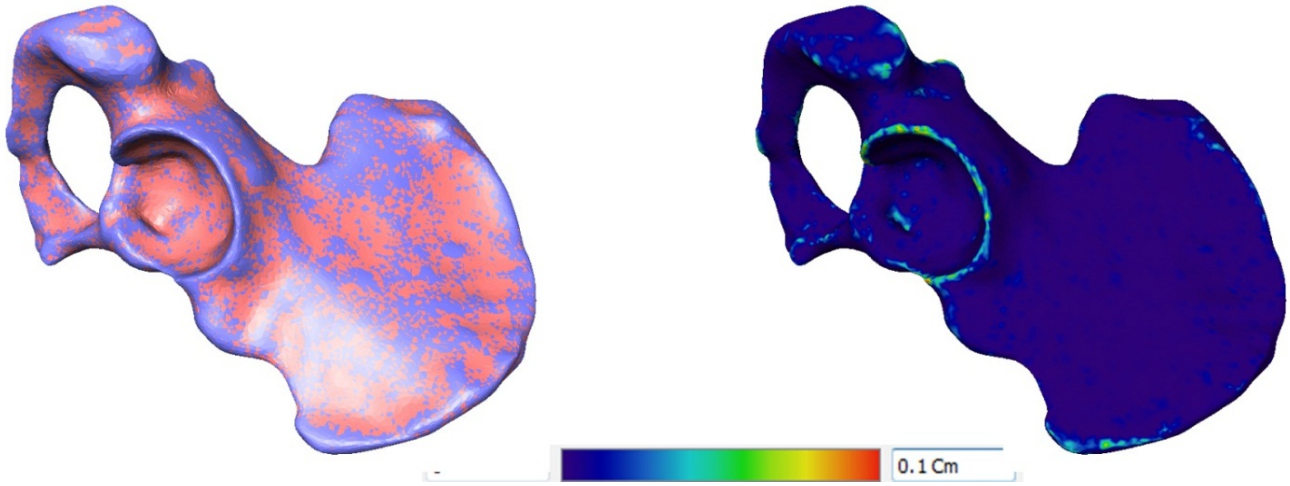


Figure 5-68 Results after correspondence on pelvis

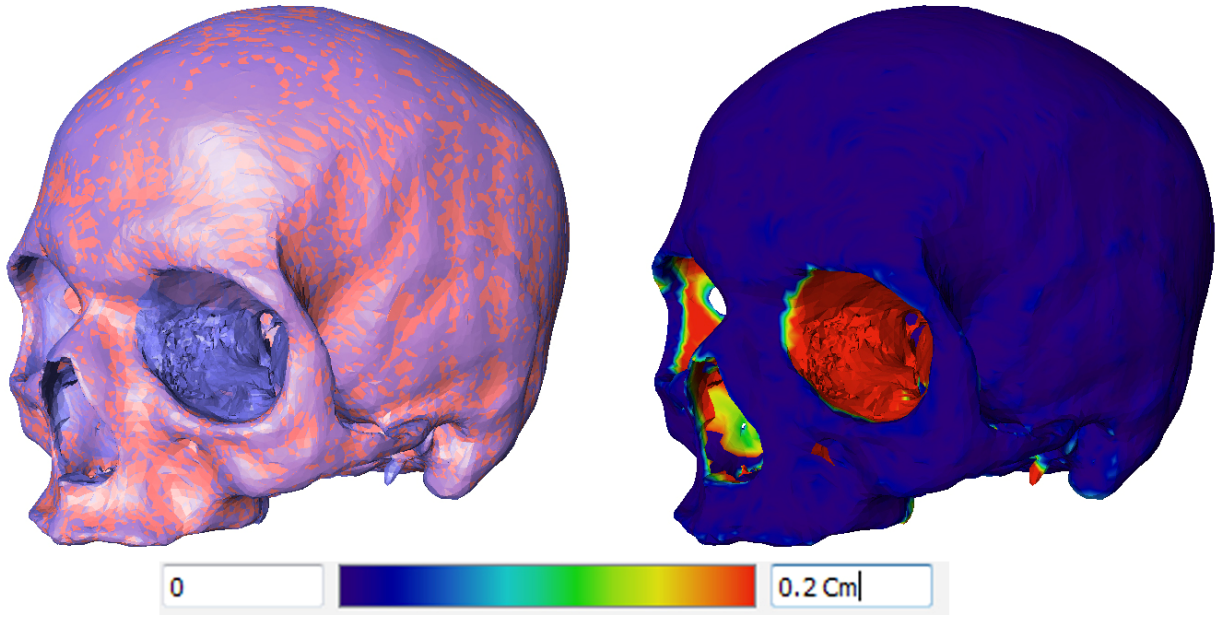


Figure 5-69 Results after correspondence on skull

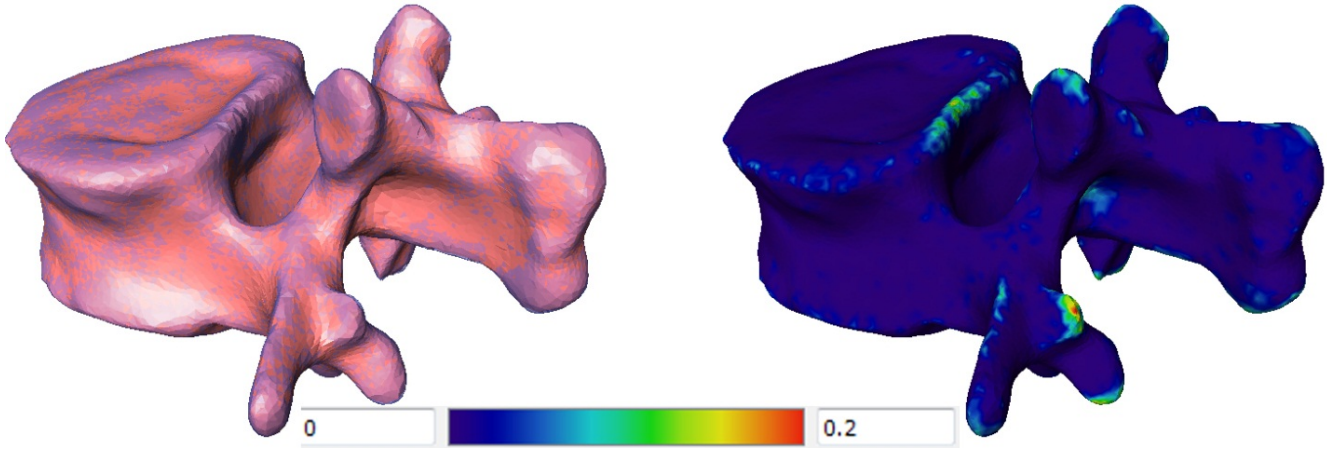


Figure 5-70 Results after correspondence on lumbar L1

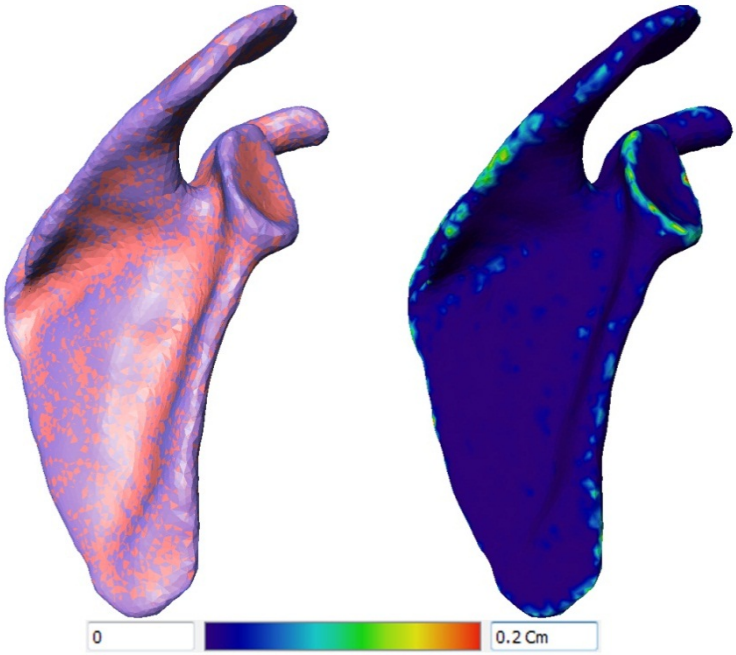


Figure 5-71 Results after correspondence on scapula

5.7 Results

The goal of the atlas creation process is generation of correspondence between the vertices of all the training shapes, wherein every anatomical point on a shape is matched to the same anatomical point in all training shapes. This task is achieved as described above by deforming a TM to match each shape in the training set. Upon generation of correspondence across all training shapes, output can then be used to build SSM, or to propagate anatomical landmarks for measurement calculation.

The output of the atlas creation step can be evaluated in the context of the method used to achieve correspondence, which in this case, is the ability of the registration and deformation algorithm to fully deform the TM correctly to match the surface of the training shape and

achieve the correct correspondence between landmarks. Output of the atlas creation can also be evaluated in the context of the generated SSM [138, 139], which will be explored in the next chapter. Due to different approaches used in correspondence generation (as outlined earlier in section 3.2) primarily used for building SSM, there was a lack of data to be directly compared to results within existing literature; authors usually refer to end results for which the SSM application was used, not in evaluating the method of generation itself [140-143].

The results of this chapter will focus on the evaluation of the atlas creation method through evaluating the deformation.

5.7.1 Evaluating Deformation

Input for the deformation algorithm is a TM and a NM to be added to the atlas and the output is TM deformed to match the surface of NM (TD). Performance of the deformation algorithm was evaluated by measuring the RMS error between the surface of the TD model and NM.

$$RMS = \sqrt{\frac{\sum_{i=1}^{n} \left\| V_{NM_i} - V_{TD_i} \right\|}{n}} \tag{56}$$

Where

n is the number of vertices in the template mesh.

V_{TD_i} is the ith vertex in the output deformed model TD.

V_{NM_i} is the closet point on NM to V_{TD_i}.

Descriptive statistics of the measured RMS for the output atlas models across all training sets for lumbar (L1-L5), pelvis, scapula, skull, and clavicle are shown in Table 5-2.

Table 5-2 Statistics of final RMS error between atlas model and original model in mm (population is the number of sample in each training set)

	Minimum	Maximum	Mean	StdDev	Population
L1	2.19E-06	0.044624	0.0012657	0.0027407	44
L2	2.13E-06	0.065143	0.0013231	0.0028249	44
L3	2.38E-06	0.06031	0.0017859	0.0031257	44
L4	5.40E-04	0.16591	0.0091526	0.0070666	44
L5	0	0.064516	0.0039999	0.0038473	44
Skull	0	0.12194	0.0025243	0.0053059	326
Scapula	0	0.45057	0.0076082	0.03089	7
Clavicle	1.31E-04	0.024728	0.0025779	0.0020091	530
Pelvis	1.36E-06	0.11333	0.0015118	0.0042853	106

It is evident that the average RMS for all bones was less than 0.009 mm, and maximum error was less than 0.1 mm, except for the scapula where the maximum error was 0.4 mm, due to segmentation error in the reference NM model. However, due to limited number of training instances, this model was still included in the analysis. Figure 5-72Figure 5-73Figure 5-74Figure 5-75Figure 5-76Figure 5-77Figure 5-78Figure 5-79Figure 5-80 show the average map for RMS error for all vertices of training instances for the skull, pelvis, clavicle, scapula, lumbar (L1-L5), respectively. The algorithms were evaluated on cases where severe deformity and osteophytes were present, and the algorithms were able to capture the anatomy of these cases with a mean RMS error <0.2 mm. Figure 5-81Figure 5-82 show two sample cases for the pelvis with severe

deformity and the ouput of the atlas. Figure 5-83 shows a sample case for L1 lumbar with severe deformity.

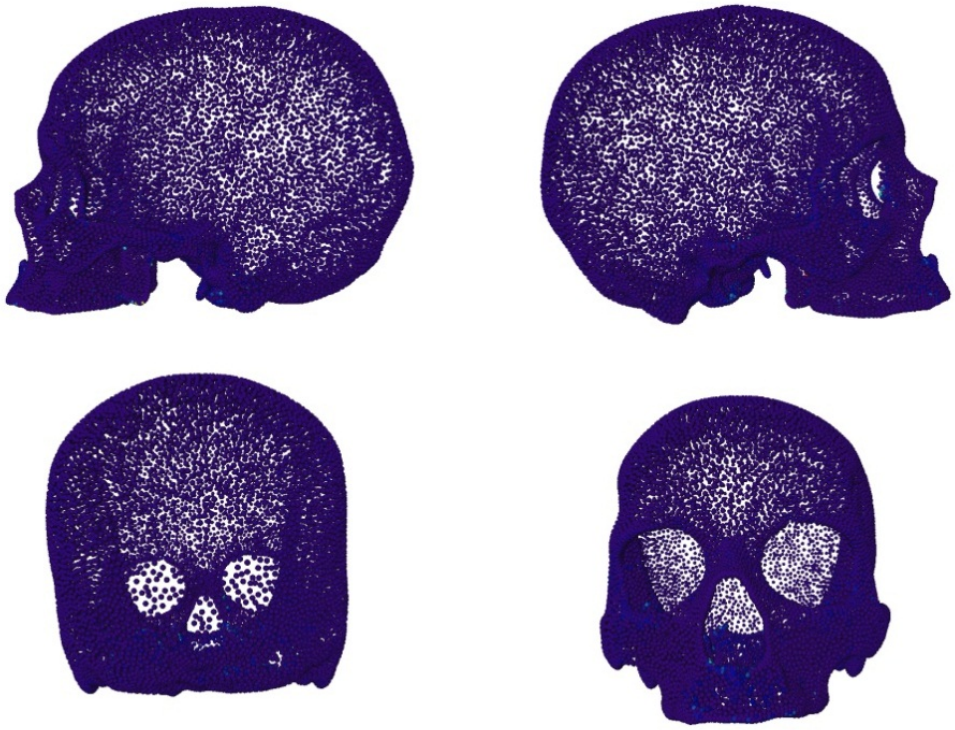


Figure 5-72 RMSE map between atlas model and original model for skull

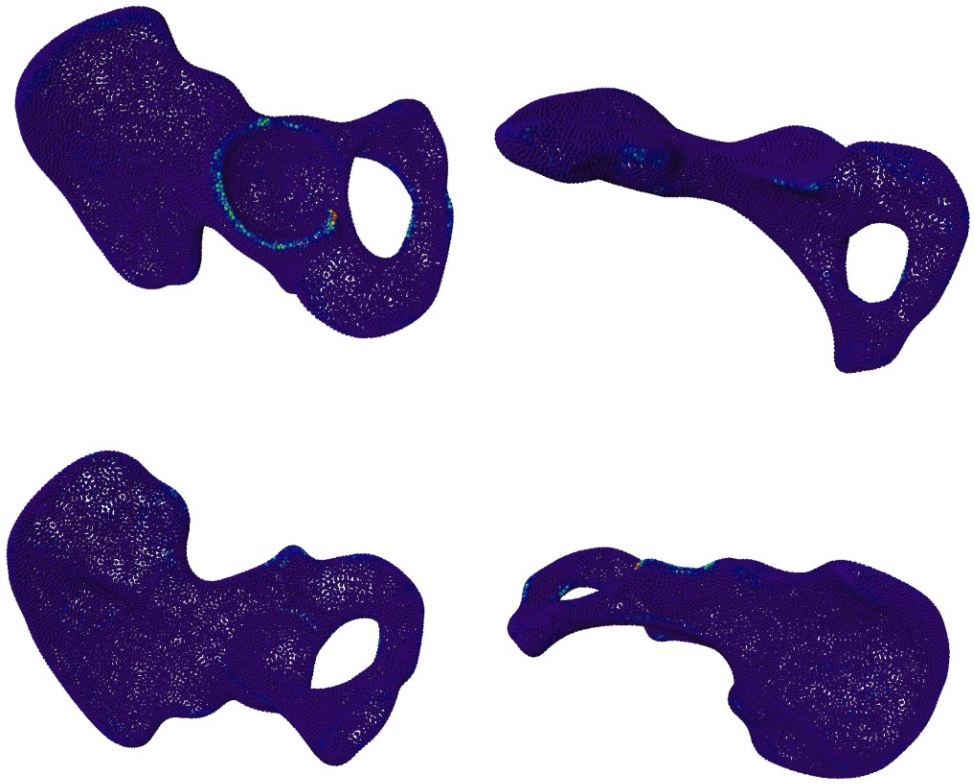


Figure 5-73 RMSE map between atlas model and original model for pelvis

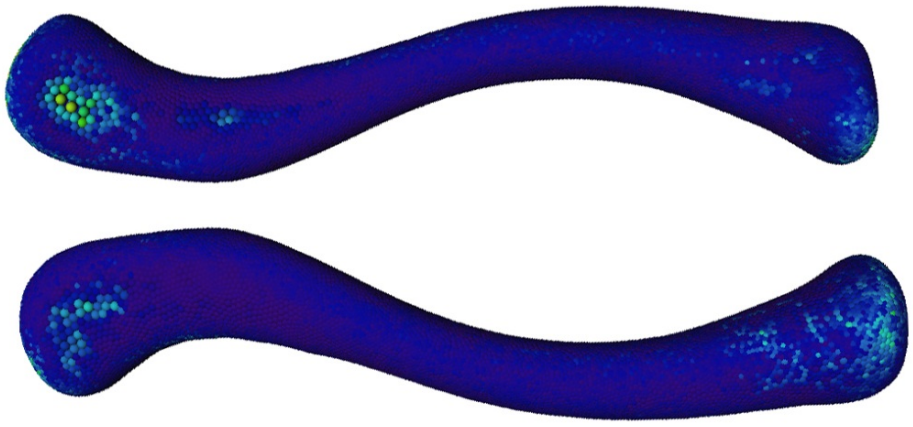


Figure 5-74 average RMSE map between atlas model and original model for clavicle

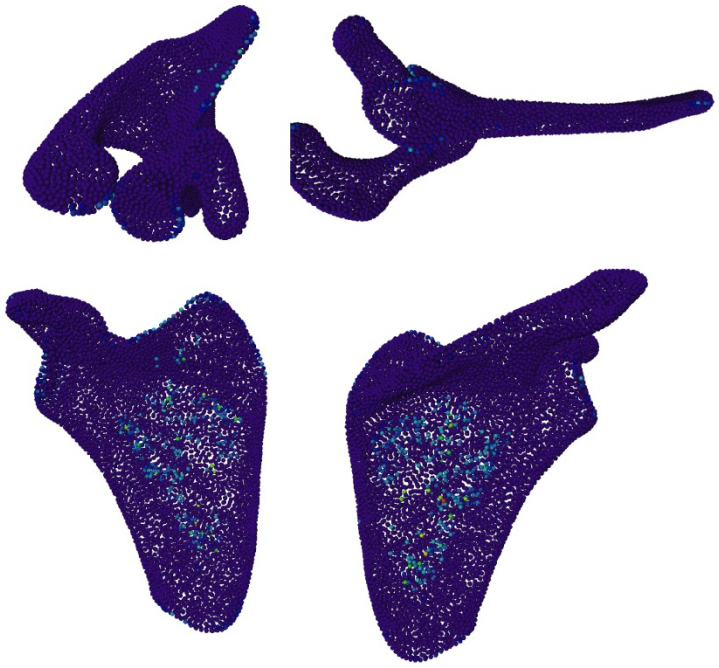


Figure 5-75 RMSE map between atlas model and original model for scapula

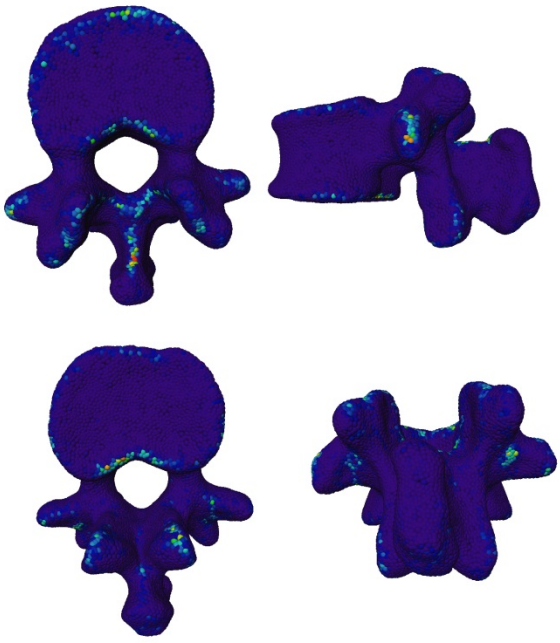


Figure 5-76 RMSE map between atlas model and original model for L1

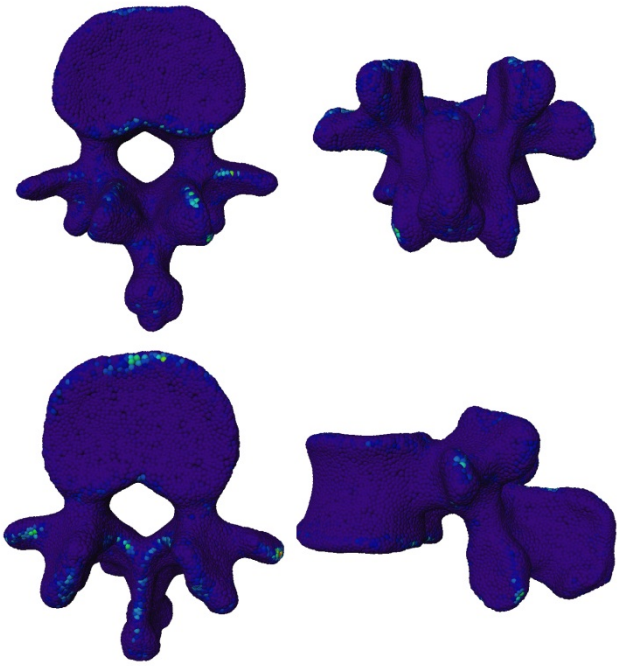


Figure 5-77 RMSE map between atlas model and original model for L2

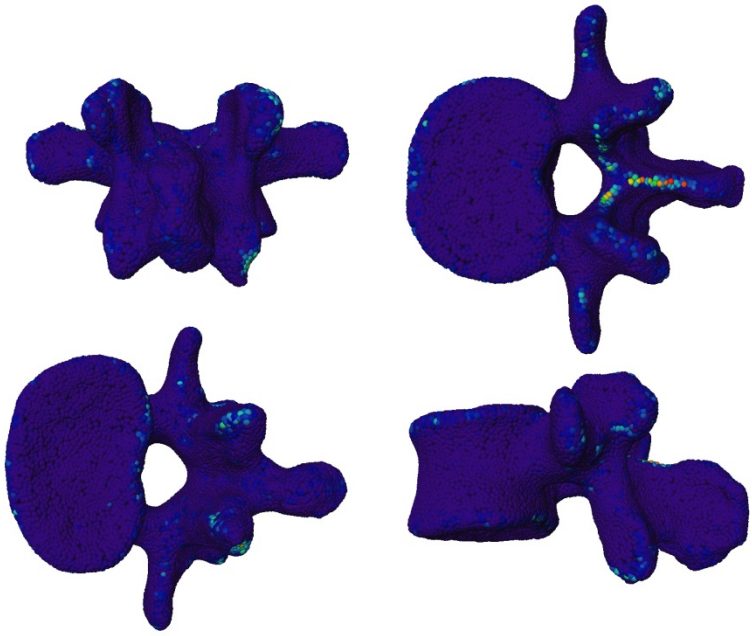


Figure 5-78 RMSE map between atlas model and original model for L3

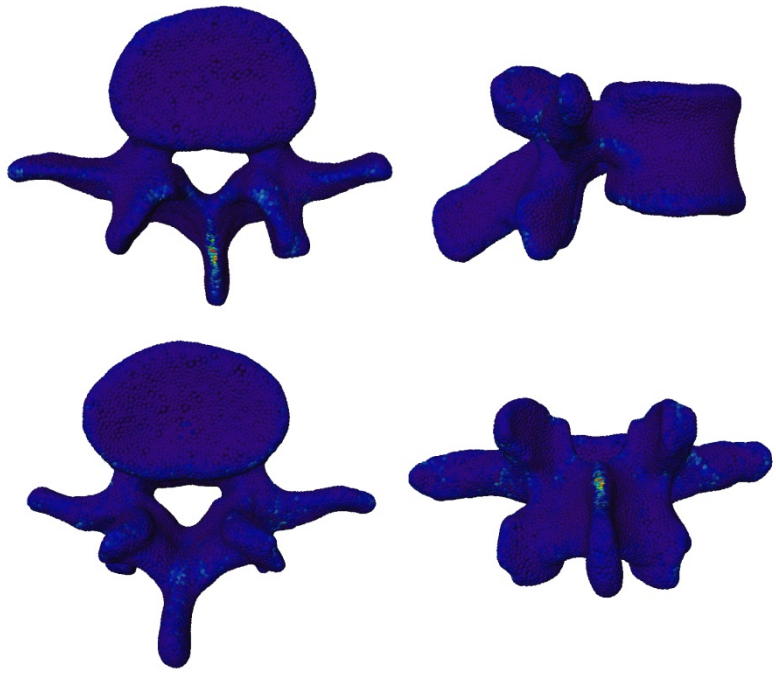


Figure 5-79 RMSE map between atlas model and original model for L4

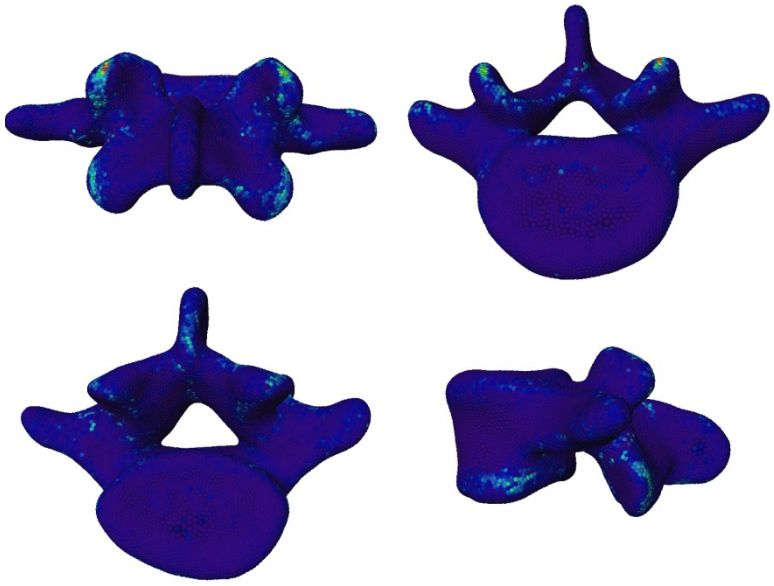


Figure 5-80 RMSE map between atlas model and original model for L5

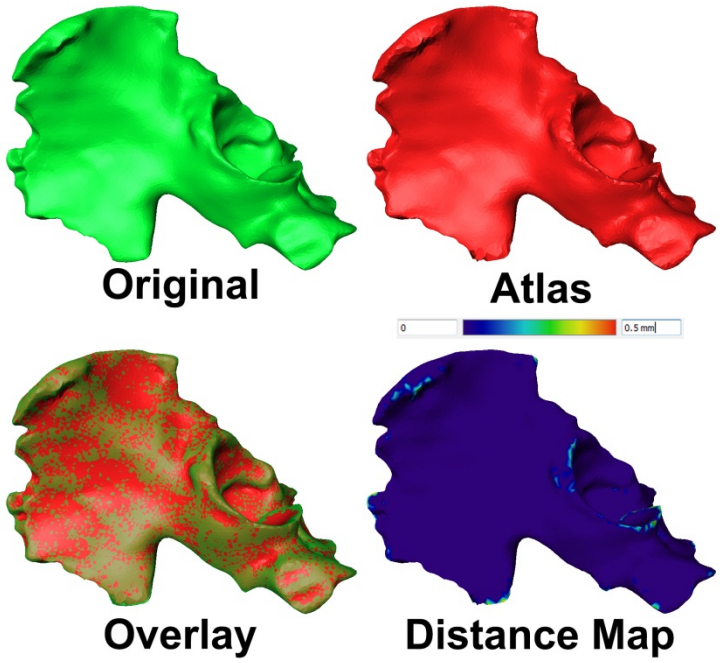


Figure 5-81 Atlas output for a pelvis with Severe deformity (case 1)

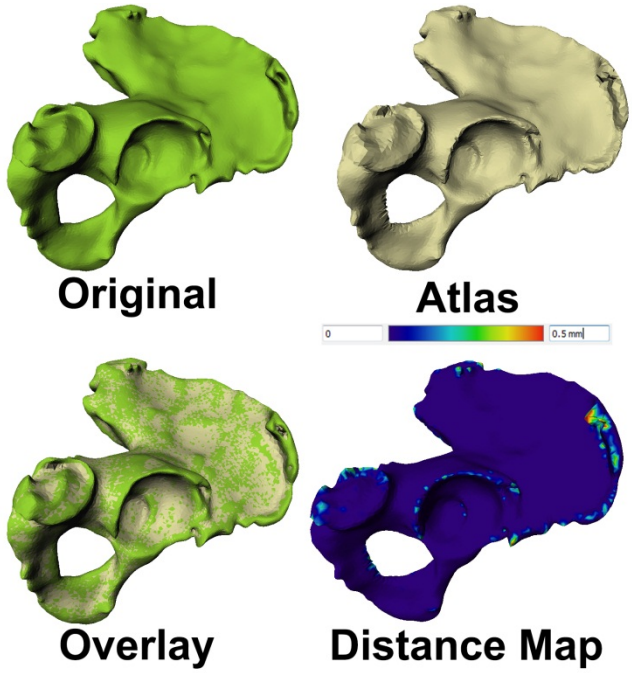


Figure 5-82 Atlas output for a pelvis with Severe deformity (case 2)

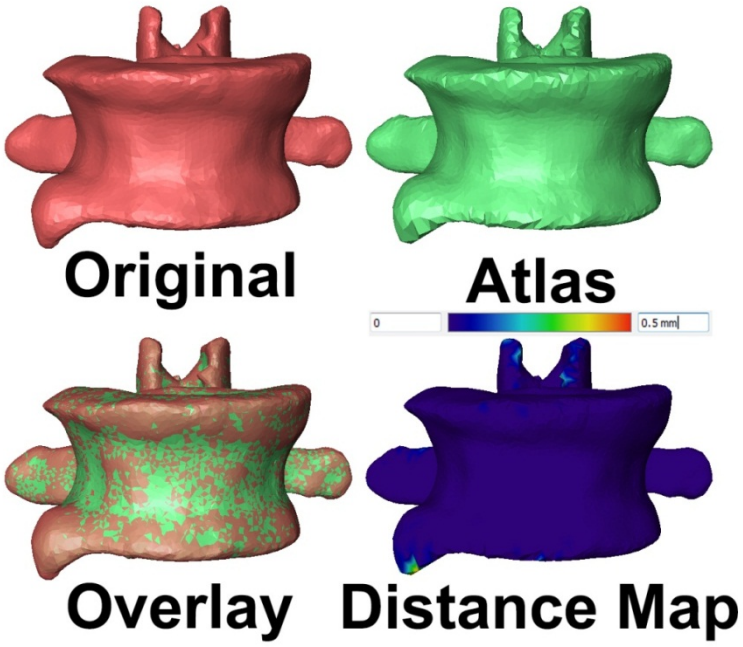


Figure 5-83 Atlas output for a L1 lumbar with Severe deformity (case 1)

5.7.2 Evaluating Correspondence

In evaluation of automatic algorithms, such as segmentation or deformation, the knowledge of a human expert is considered to be the gold standard used to compare to the output of the automated algorithm. In segmentation, this task is easier, as contours of the anatomical objects are less ambiguous to localize and therefore, do not permit much variation [25]. However, in evaluating correspondence, one of the most challenging tasks is the defining landmarks to be used for analysis. Andres [139] suggested the measure of correspondence by defining a set of landmarks and then calculating the corresponding parameter values that generate these landmarks, using parameter values that regenerate the landmarks and compare these manually defined landmarks (57). However, this approach is tailored to correspondence

generated by optimizing a parameterization function – not by mesh-to-mesh deformation. Styner [144] suggested the use of a small set of anatomical landmarks selected manually by a human expert on each object, calculating the mean absolute distance between each manual landmark and each point corresponding to the same landmarks on the output model.

$$gcm = \frac{1}{n_s(n_s-1)n_g}\sum_{i=1}^{n_s}\sum_{j=1}^{n_g}\sum_{k\in K} d\left(x_k\left(\gamma_k(t_{ij})\right), g_{kj}\right) \quad (57)$$

Where

γ_k is the parameterization of the shape x_k.

g_{kj} is the j[th] ground truth point of the shape x_k.

5.7.2.1 Validation study design:

A similar approach to Styner was used to design a validation study for evaluating correspondence where three expert anthropologists were asked to quantify a set of landmarks on the scapula and pelvis. One of the challenges was to find a set of type 1 landmarks to minimize the intra-observer error. The pelvis and scapula were selected due to the more prominent landmarks, decreasing intra-obvserver variation.

Table 5-3 Landmarks used in validation study

Pelvis	Scapula
Anterior Inferior Illiac Spine	Suprascapular Notch
Anterior Superior Illiac spine	Supraglenoid Tubercle
Acetabular Cup Rim	
Ischial Spine	
Posterior Superior Illiac Spine	
Sciatic Notch	

Experts were given 20 pelvis models (10 females and 10 males) and seven scapula models. Participants were then asked to localize six landmarks on pelvis and two on the scapula, outlined in Table 4-1. The average bone models for the pelvis and scapula population were then calculated and the same landmarks were then localized on these mean models. Indices of the vertices corresponding to landmarks were then used to propagate these landmarks on the same models experts used to localize landmarks, as shown in Figure 5-84 and Figure 5-85. For abbreviation purposes, P_C will refer to the landmark propagated automatically using atlas correspondence; P_{P1}, P_{P2}, and P_{P3} will refer to landmarks defined by Participants P1, P2 and P3, respectively, and P_{MP} will refer to the mean point of the three participant landmarks. A set of measurements were then computed to assess the accuracy of the correspondence and the intra-observer variability between participants in localizing the landmarks, as shown in **Error! Not a valid bookmark self-reference.**Table 5-4.

Table 5-4 Definition of measurements used for evaluation correspondence and intra-observer variability

Measurement	Definition
$P_{C_}P_{MP}$	Distance between P_C and P_{MP}
$P_{P1_}P_C$	Distance between P_{P1} and P_C
$P_{P2_}P_C$	Distance between P_2 and P_C
$P_{P3_}P_C$	Distance between P_3 and P_C
$P_{P1_}P_{P2}$	Distance between P_{P1} and P_{P2}
$P_{P1_}P_{P3}$	Distance between P_{P1} and P_{P3}
$P_{P2_}P_{P3}$	Distance between P_{P2} and P_{P3}
μ_P	Mean of the Absolute Distance between P_{MP} and (P_{P1}, P_{P2}, and P_{P3})

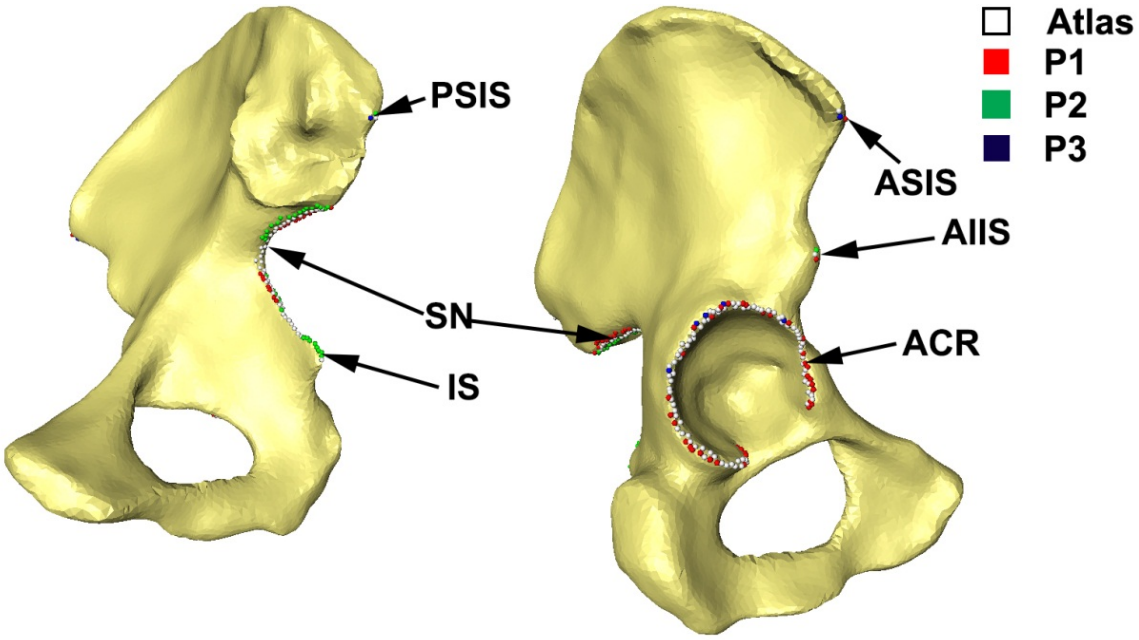


Figure 5-84Comparison of landmarks used for validation of correspondence on pelvis

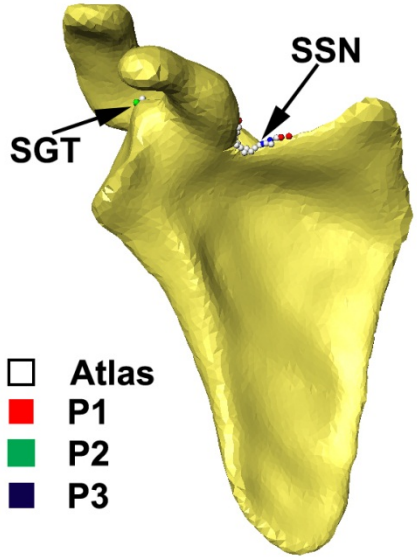


Figure 5-85 Comparison of landmarks used for validation of correspondence on scapula

Table 5-5 Correspondence validation study results for pelvis. An average error of 3.4 mm was found between the automatically propagated landmarks and the average of the landmarks of the three participants. The smallest mean error between participants was 1.27 mm between P1 and P3. The maximum error was between P2 and P3 at 2.48 mm. The scapula landmarks exhibited less error compared to the pelvis with an average error of 2.71 mm between the automatically propagated landmark and the mean landmark of the three participants. The error between P2 and P3 was 1.55 mm, while the highest error was 2.22 mm between P1 and P2, as shown in Table 5-6.

Table 5-5 Correspondence validation study results for pelvis

	Landmark											
Measurement	**AIIS**		**ASIS**		**CR**		**IS**		**PSIS**		**SN**	
	μ	**σ**	**μ**	**σ**	**μ**	**σ**	**μ**	**σ**	**μ**	**σ**	**μ**	**σ**
μP	1.32	1.22	0.82	0.73	1.08	1.21	0.80	0.71	1.60	1.14	1.31	1.03
$P_{C_}\ P_{MP}$	3.00	2.87	3.08	2.34	2.27	1.85	2.51	1.51	5.96	3.26	3.73	2.46
$P_{P1_}\ P_{C}$	3.56	2.97	3.42	2.57	1.97	1.61	2.74	1.53	6.33	3.57	3.75	2.86
$P_{P2_}\ P_{C}$	3.31	2.90	2.75	2.49	2.09	1.84	2.56	1.74	5.54	3.58	4.82	2.64
$P_{P3_}\ P_{C}$	3.43	3.15	3.27	2.52	3.53	3.23	2.77	1.53	6.50	3.57	3.85	2.66
$P_{P1_}\ P_{P2}$	2.68	2.81	1.62	1.75	1.16	1.36	1.78	1.58	2.89	2.67	2.40	2.14
$P_{P1_}\ P_{P3}$	0.75	1.26	0.84	1.28	2.82	2.96	0.06	0.27	1.26	1.79	1.87	1.77
$P_{P2_}\ P_{P3}$	2.85	2.74	1.51	1.51	2.44	2.87	1.79	1.58	3.45	2.52	2.82	2.55

Table 5-6 Correspondence validation study results for scapula

	Landmark			
Measurment	SN		SGT	
	μ	**σ**	**μ**	**σ**
μP	1.12	0.47	1.13	0.61
$P_{C_}\ P_{MP}$	3.73	1.82	1.69	0.71
$P_{P1_}\ P_{C}$	3.48	1.18	2.13	1.55
$P_{P2_}\ P_{C}$	3.97	2.41	1.72	1.20
$P_{P3_}\ P_{C}$	4.11	2.21	1.55	1.46
$P_{P1_}\ P_{P2}$	2.15	1.00	2.30	1.23
$P_{P1_}\ P_{P3}$	1.88	1.11	1.86	1.48
$P_{P2_}\ P_{P3}$	1.71	1.20	1.38	1.32

6. STATISTICAL SHAPE MODEL CREATION

The goal of SSM is to capture the variation in a set of training shapes that represent certain populations. Each of these shapes is represented by n points which can be in any dimension, although it should be noted that for a given shape, its points are invariant under similarity transformation (translation, rotation and scaling). Capturing variation of a shape across populations allows for the creation of the new synthetic data or analysis of existing data. A correct correspondence between shapes' points is an essence for an accurate SSM, and this is one of the main applications of the statistical atlas creation algorithm defined in Chapter 5. Upon adding a bone to the corresponding statistical atlas, a dense point correspondence is established between the vertices of the template mesh and those of the new model. Correspondence is carried by the vertices' indices, the i^{th} vertex on all training shapes is guaranteed to have accurate anatomical correspondence.

Given the large number of vertices per template model, as shown in Table 4-1, a compact SSM is essential, especially in cases where it is used in conjunction with optimization for shape reconstruction. SSM fulfills this task by expressing the variation as delta changes from the mean along the direction of a set of axes. These axes are defined to capture the directions of the biggest variations in vertices, instead of capturing variation along each vertex of the mean mode. The most commonly used way to accomplish this task is using PCA. Cootes and Taylor [145] first introduced the use of PCA for construction of SSM in the early 1990s. Since then, it has become the standard for building SSM in computer vision and medical imaging.

6.1 Construction of SSM

Given set of n training shapes $X = \{x_1, x_2, \ldots \ldots x_n\}$ with point correspondence established using mesh vertices indices, the goal is to construct a SSM that captures variation in these sets of shapes. SSM can be established either directly using training models without any scale normalization; in this case, the variation captured will include size difference information. Shapes may also be normalized to have the same scale first, and in this case, captured variations are mainly pure shape variation independent of size. An overview of the process of SSM construction is shown in Figure 6-1.

6.1.1 Algorithm 7: SSM Construction:

a. Compute training set X mean shape:

$$\bar{x} = \frac{1}{n}\sum_{1}^{n} x_i \tag{58}$$

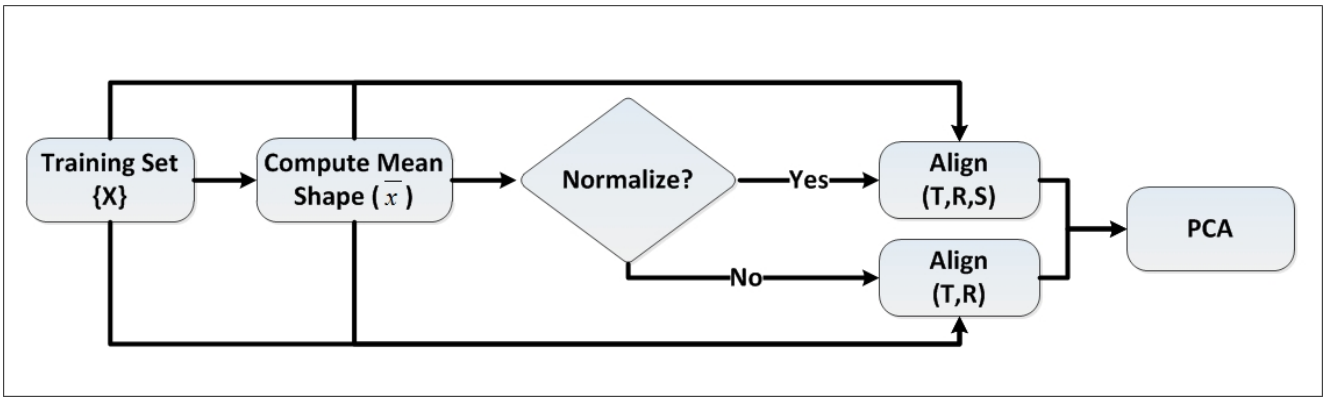


Figure 6-1 Constructing SSM from training set

b. Align all shapes in X with $\bar{x}$:

   I. In such a case where a scale-independent SSM is required, compute the rotation, translation , and scale that best align x_i with $\bar{x}$ using Procrustes [146].

   II. In such a case where a scale-dependent SSM is required, compute the rotation and translation that best align x_i with $\bar{x}$ using Arun [125].

c. Compute covariance matrix S using aligned shapes:

$$S = \frac{1}{n-1}\sum_{n1}^{n}(x_i - \bar{x})(x_i - \bar{x})^T \tag{59}$$

d. Compute Eigen values λ_i and corresponding vectors p_i of S using economy singular value decomposition SVD :

$$[P, \lambda, V] = \mathrm{SVD}(S) \tag{60}$$

e. Sort λ_i in descending order.

f. Compute computed accumulated variance V_{λ_i} for each component :

$$V_{\lambda_i} = \sum_{j=1}^{i}\lambda_j \tag{61}$$

6.2 Results

This section will describe the results of the SSM for skull, pelvis, lumbar and clavicle. Scapula was excluded due to the limited number of samples in the training set. For each bone, both normalized and non-normalized SSM were evaluated using criteria outlined in section 3.3. The results for the SSM validation are detailed by bone type and below:

Table 6-1 Mean and standard deviation for the RMS error across population

% Variance	70		75		80		85		90		95		100	
RMS	μ	σ	μ	σ	μ	σ	μ	σ	μ	σ	μ	σ	μ	σ
Female NN	2.11	0.35	2.12	0.38	2.00	0.36	1.89	0.30	1.81	0.29	1.68	0.27	1.56	0.24
Female N	1.87	0.34	1.80	0.34	1.79	0.33	1.72	0.33	1.67	0.31	1.59	0.28	1.55	0.27
Male NN	2.05	0.34	1.98	0.33	1.89	0.33	1.83	0.31	1.64	0.27	1.50	0.22	1.38	0.21
Male N	1.77	0.29	1.71	0.31	1.67	0.29	1.50	0.22	1.44	0.22	1.39	0.20	1.30	0.21

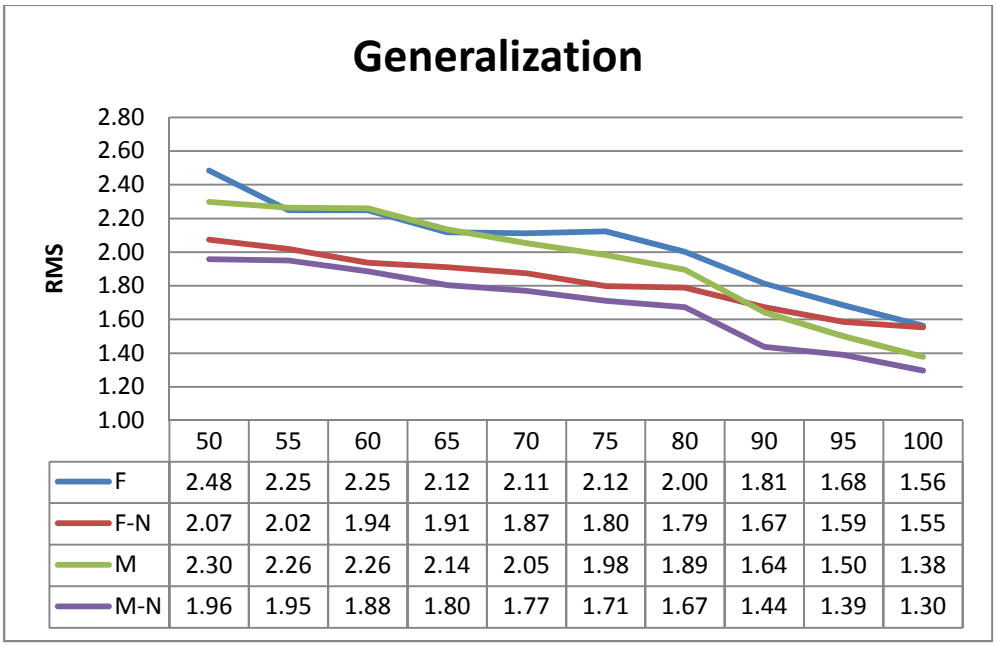


Figure 6-2 RMS vs. percentage accumulated variance for scale normalized and non-normalized female and male pelvis SSM

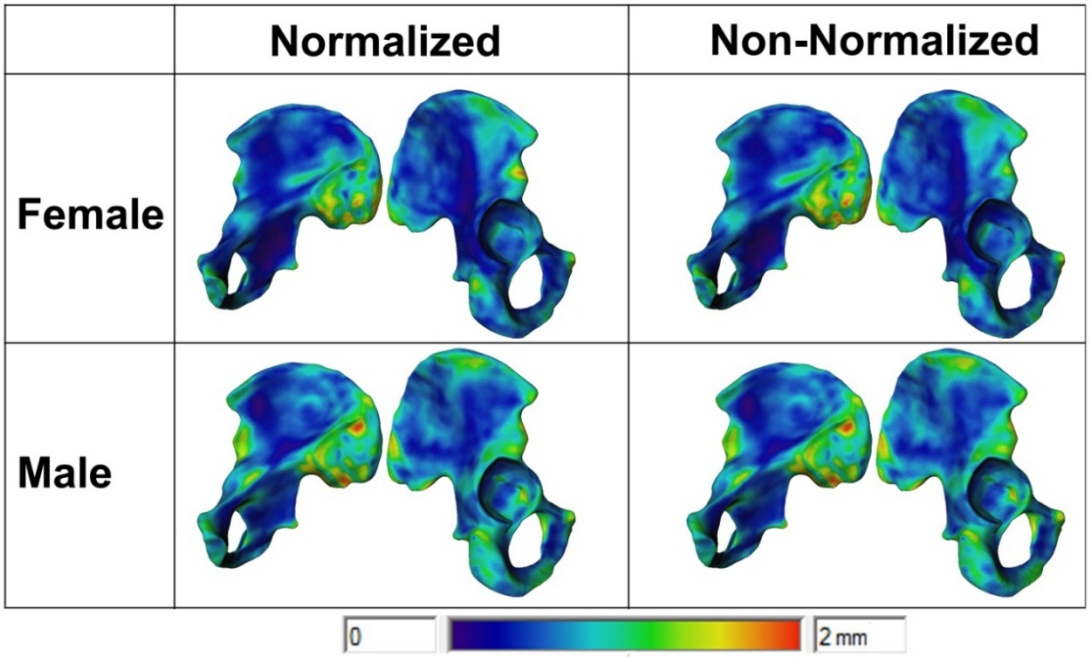


Figure 6-3 Average distance map for reconstructed models using leave one out test

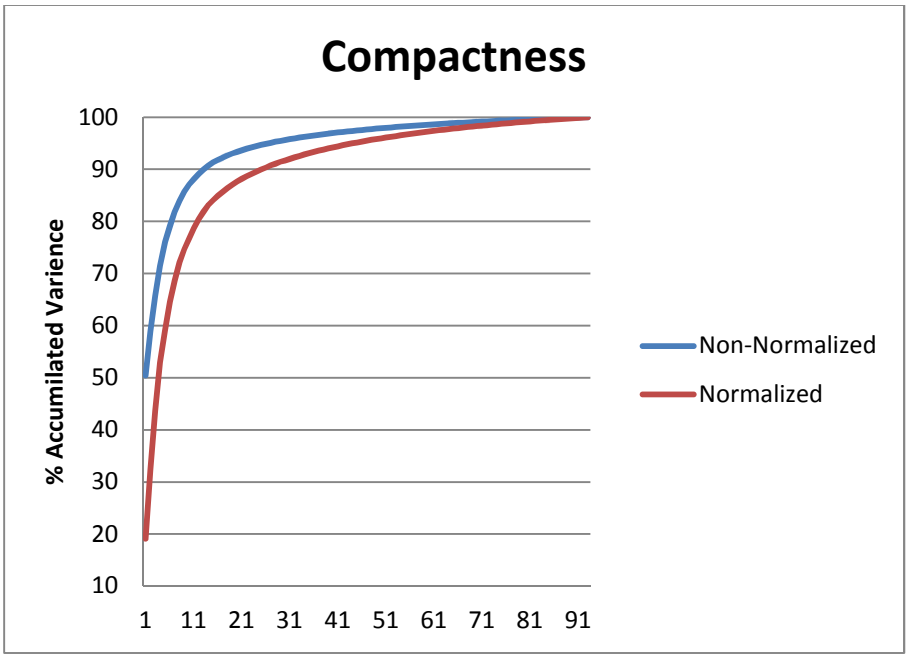


Figure 6-4 Accumulated variance vs. number of coefficients of the overall normalized and non-normalized pelvis SS

Table 6-2 Mean and standard deviation for the RMS error across population

% Variance	70		75		80		85		90		95		100	
RMS	μ	σ	μ	σ	μ	σ	μ	σ	μ	σ	μ	σ	μ	σ
NN	2.02	0.27	2.01	0.27	1.61	0.31	1.61	0.31	1.61	0.31	1.59	0.30	1.54	0.30
N	1.60	0.17	1.60	0.17	1.61	0.16	1.62	0.20	1.62	0.20	1.59	0.21	1.59	0.21

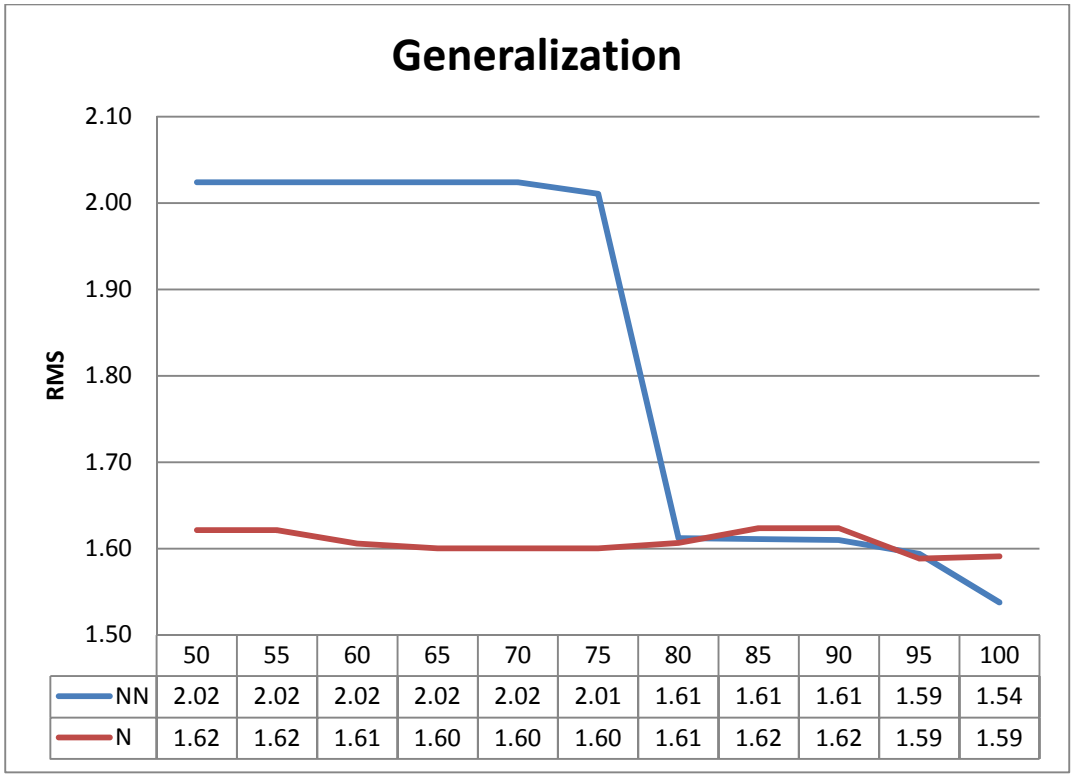


Figure 6-5 RMS vs. percentage accumulated variance for scale normalized and non-normalized scapula SSM

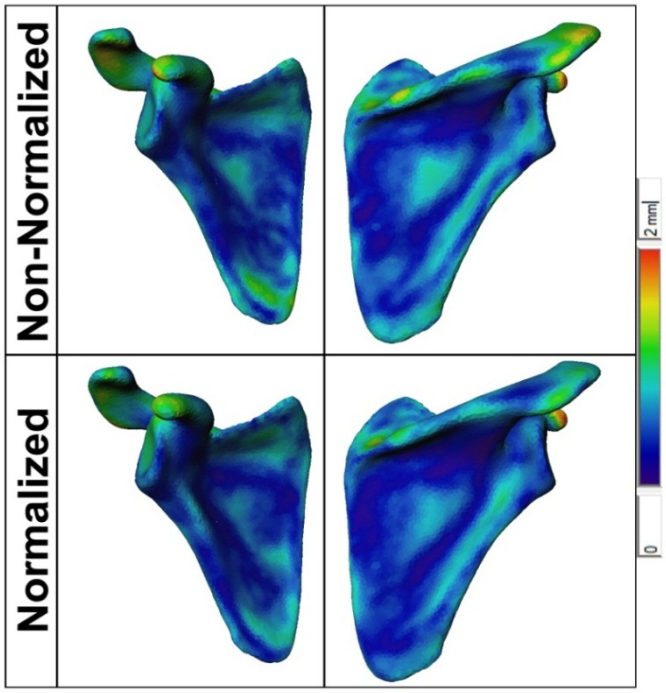


Figure 6-6 Average distance map for reconstructed models using leave one out test

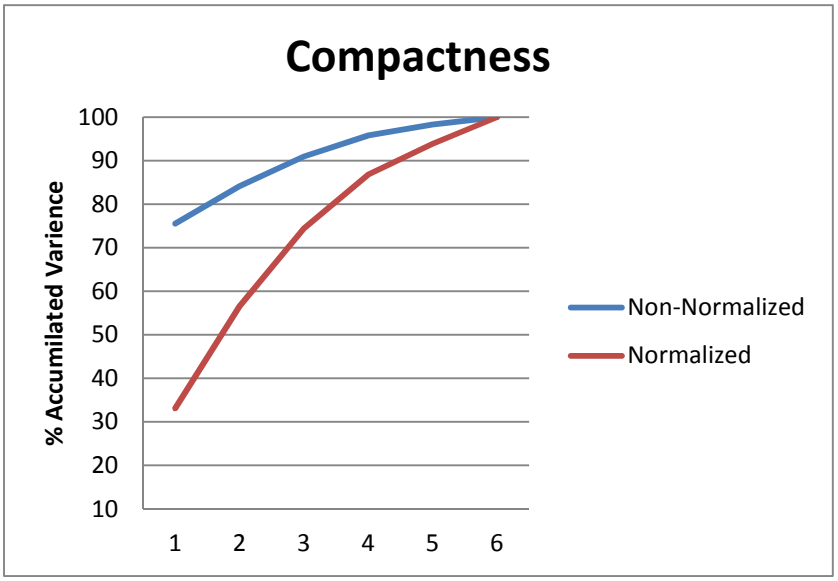


Figure 6-7 Accumulated variance vs. number of coefficients of the overall normalized and non-normalized scapula SSM

Table 6-3 Mean and standard deviation for the RMS error across population

	μ	σ	μ	σ	μ	σ	μ	σ	μ	σ	μ	σ	μ	σ
% Variance	**70**		**75**		**80**		**85**		**90**		**95**		**100**	
RMS	**μ**	**σ**	**μ**	**σ**	**μ**	**σ**	**μ**	**σ**	**μ**	**σ**	**μ**	**σ**	**μ**	**σ**
FNN	1.96	0.36	1.93	0.37	1.82	0.32	1.76	0.29	1.60	0.27	1.50	0.22	1.40	0.22
FN	1.80	0.28	1.74	0.27	1.64	0.24	1.62	0.25	1.52	0.20	1.47	0.21	1.41	0.20
MNN	2.00	0.32	1.88	0.27	1.84	0.26	1.73	0.23	1.54	0.18	1.35	0.16	1.16	0.13
MN	1.71	0.23	1.62	0.21	1.57	0.20	1.45	0.17	1.33	0.15	1.23	0.14	1.13	0.14

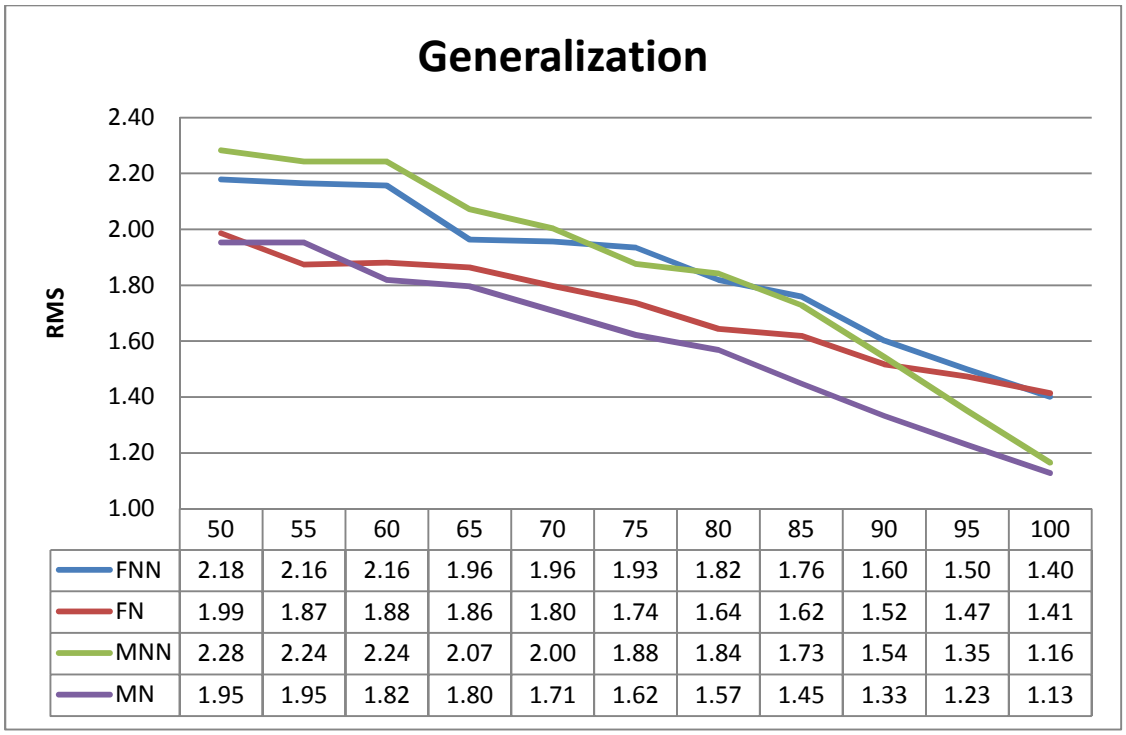


Figure 6-8 RMS vs. percentage accumulated variance for scale normalized and non-normalized female and male skull SSM

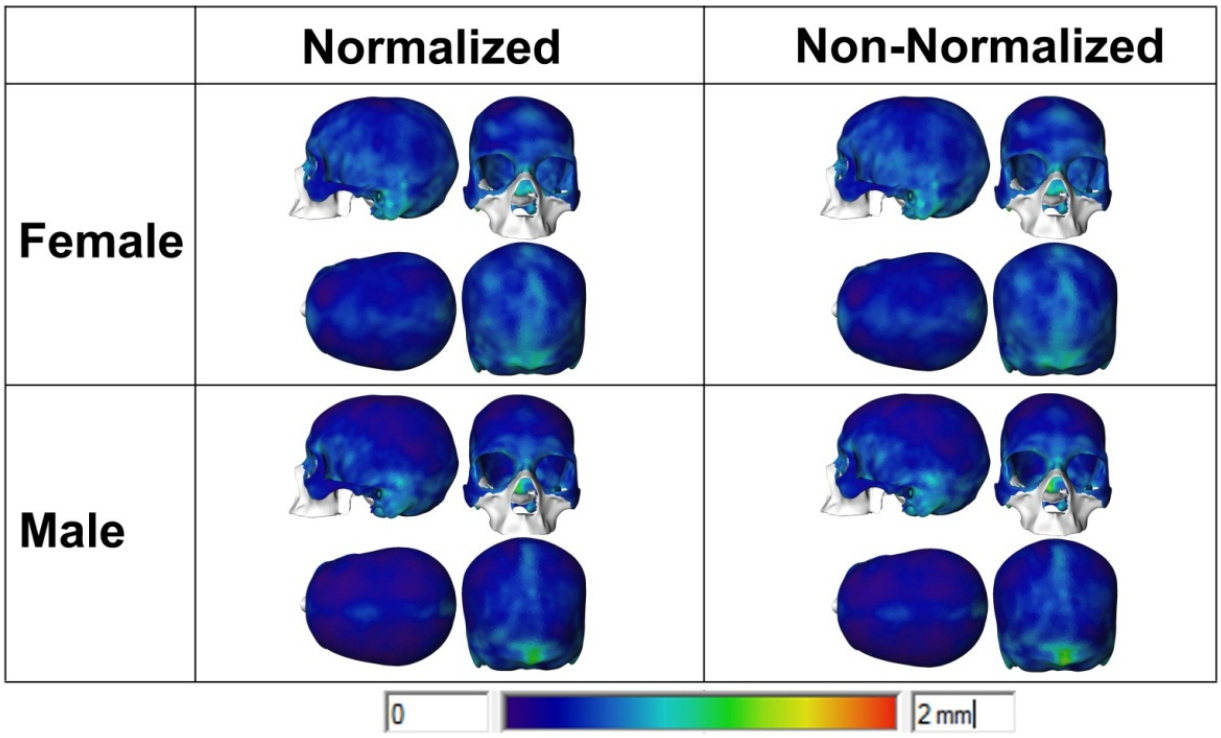


Figure 6-9 Average distance map for reconstructed models using leave one out test

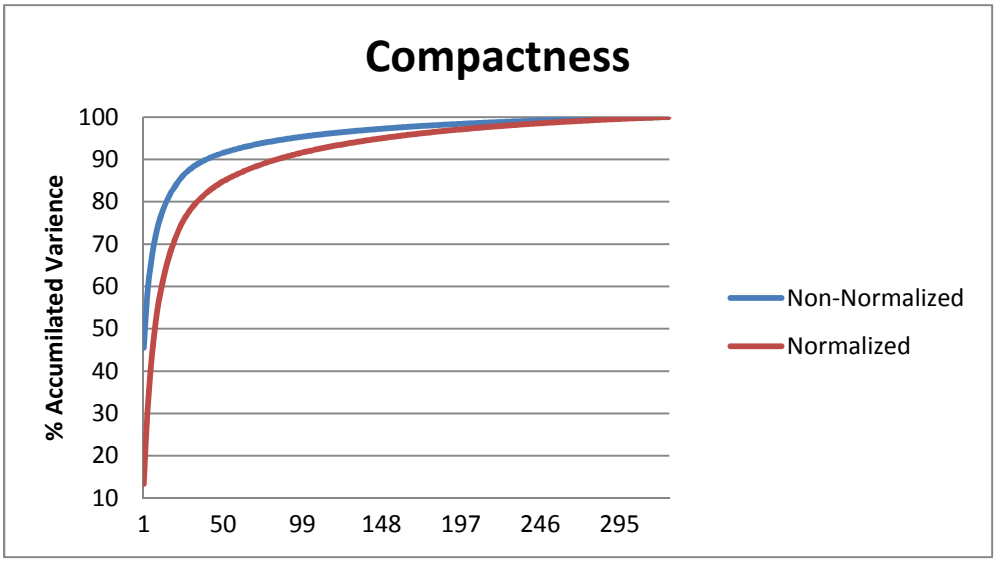
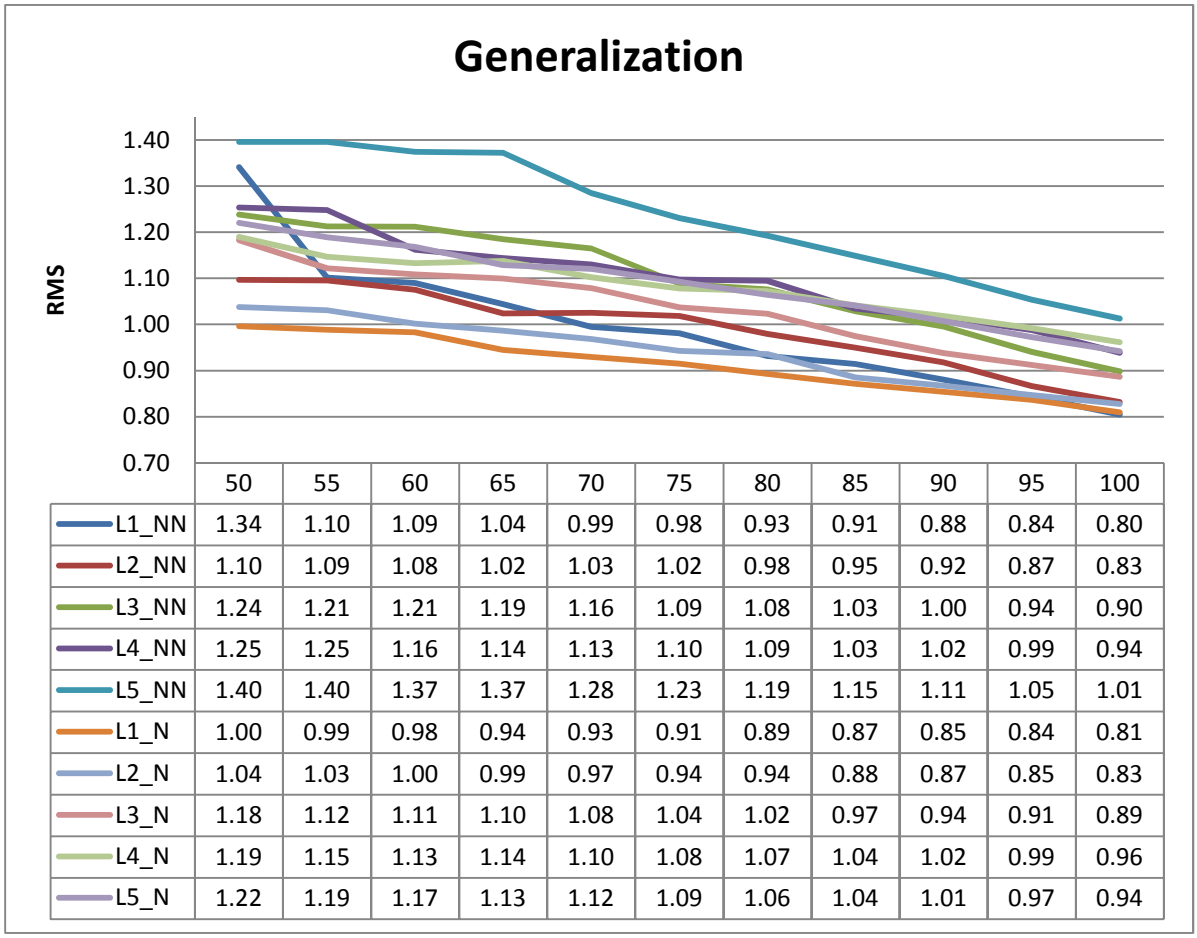


Figure 6-10 Accumulated variance vs. number of coefficients of the overall normalized and non-normalized skull SSM



	50	55	60	65	70	75	80	85	90	95	100
L1_NN	1.34	1.10	1.09	1.04	0.99	0.98	0.93	0.91	0.88	0.84	0.80
L2_NN	1.10	1.09	1.08	1.02	1.03	1.02	0.98	0.95	0.92	0.87	0.83
L3_NN	1.24	1.21	1.21	1.19	1.16	1.09	1.08	1.03	1.00	0.94	0.90
L4_NN	1.25	1.25	1.16	1.14	1.13	1.10	1.09	1.03	1.02	0.99	0.94
L5_NN	1.40	1.40	1.37	1.37	1.28	1.23	1.19	1.15	1.11	1.05	1.01
L1_N	1.00	0.99	0.98	0.94	0.93	0.91	0.89	0.87	0.85	0.84	0.81
L2_N	1.04	1.03	1.00	0.99	0.97	0.94	0.94	0.88	0.87	0.85	0.83
L3_N	1.18	1.12	1.11	1.10	1.08	1.04	1.02	0.97	0.94	0.91	0.89
L4_N	1.19	1.15	1.13	1.14	1.10	1.08	1.07	1.04	1.02	0.99	0.96
L5_N	1.22	1.19	1.17	1.13	1.12	1.09	1.06	1.04	1.01	0.97	0.94

Figure 6-11 RMS vs. percentage accumulated variance for scale normalized and non-normalized L1 to L5 SSM

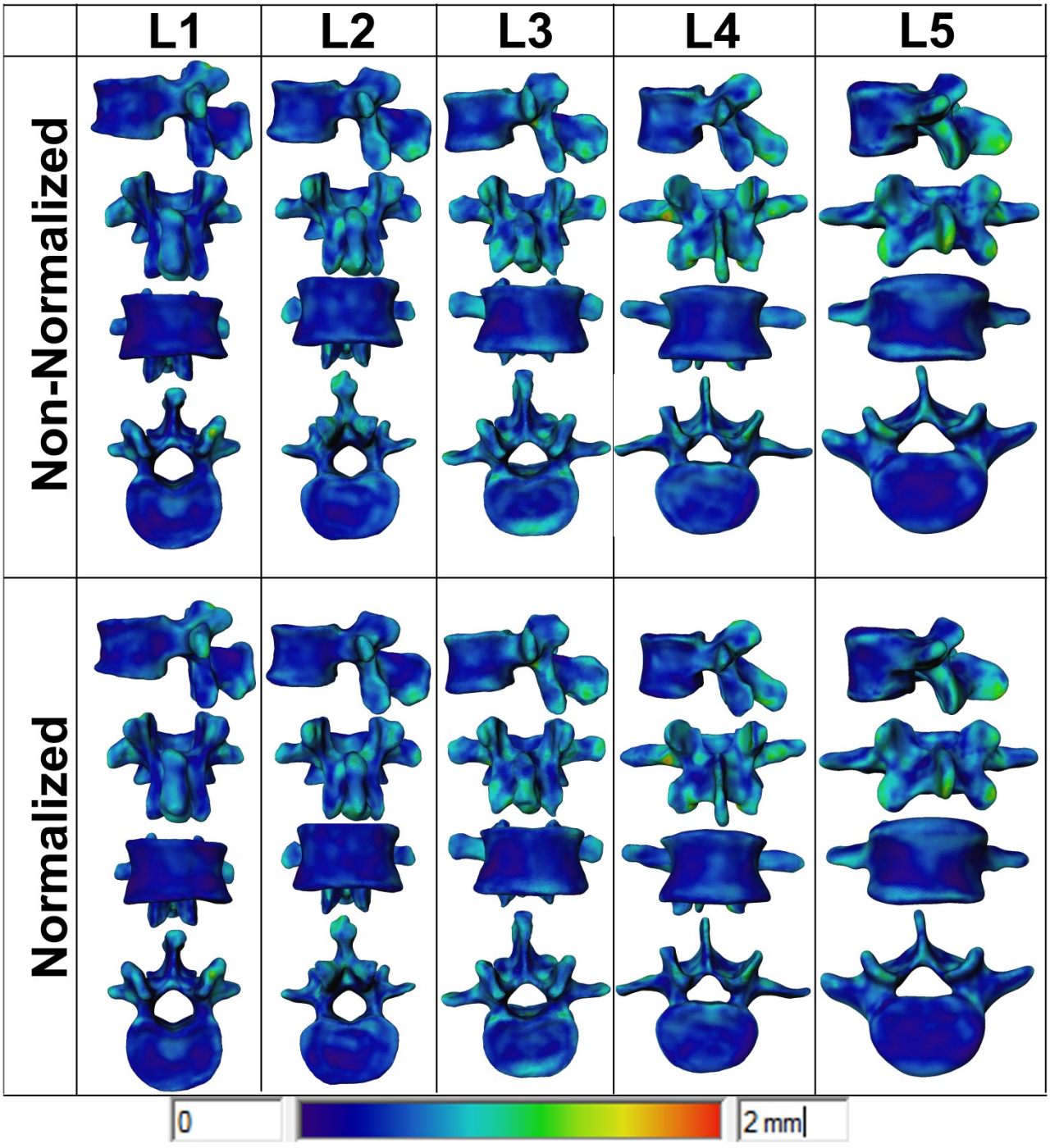


Figure 6-12 Average distance map for reconstructed models using leave one out test

Table 6-4 Mean and standard deviation for the RMS error across population

	μ	σ	μ	σ	μ	σ	μ	σ	μ	σ	μ	σ	μ	σ
% Variance	70		75		80		85		90		95		100	
RMS	μ	σ	μ	σ	μ	σ	μ	σ	μ	σ	μ	σ	μ	σ
L1_NN	0.99	0.22	0.98	0.22	0.93	0.18	0.91	0.18	0.88	0.16	0.84	0.16	0.80	0.15
L2_NN	1.03	0.18	1.02	0.18	0.98	0.16	0.95	0.15	0.92	0.16	0.87	0.12	0.83	0.12
L3_NN	1.16	0.17	1.09	0.14	1.08	0.15	1.03	0.13	1.00	0.13	0.94	0.12	0.90	0.13
L4_NN	1.13	0.15	1.10	0.13	1.09	0.13	1.03	0.13	1.02	0.13	0.99	0.12	0.94	0.11
L5_NN	1.28	0.31	1.23	0.29	1.19	0.28	1.15	0.27	1.11	0.27	1.05	0.27	1.01	0.27
L1_N	0.93	0.17	0.91	0.17	0.89	0.16	0.87	0.16	0.85	0.16	0.84	0.15	0.81	0.15
L2_N	0.97	0.16	0.94	0.15	0.94	0.15	0.88	0.13	0.87	0.12	0.85	0.12	0.83	0.12
L3_N	1.08	0.17	1.04	0.16	1.02	0.16	0.97	0.14	0.94	0.14	0.91	0.13	0.89	0.14
L4_N	1.10	0.14	1.08	0.14	1.07	0.14	1.04	0.13	1.02	0.13	0.99	0.12	0.96	0.11
L5_N	1.12	0.26	1.09	0.26	1.06	0.25	1.04	0.27	1.01	0.28	0.97	0.26	0.94	0.26

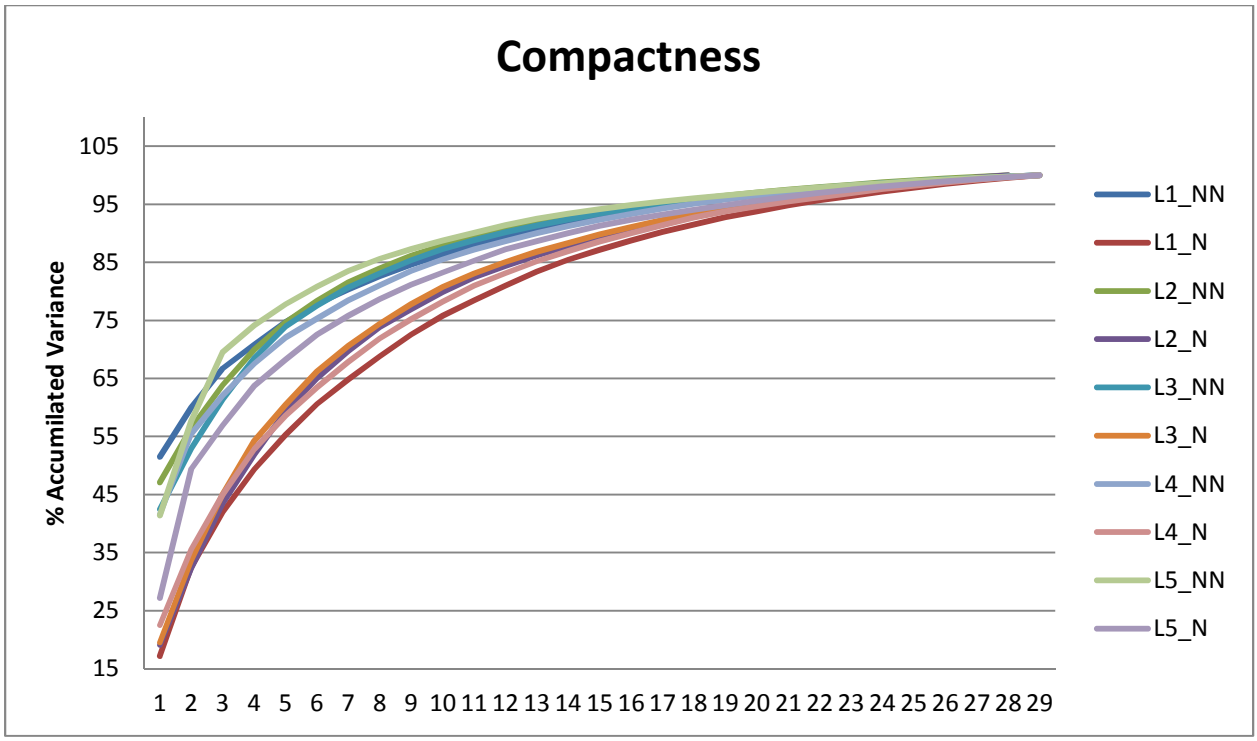
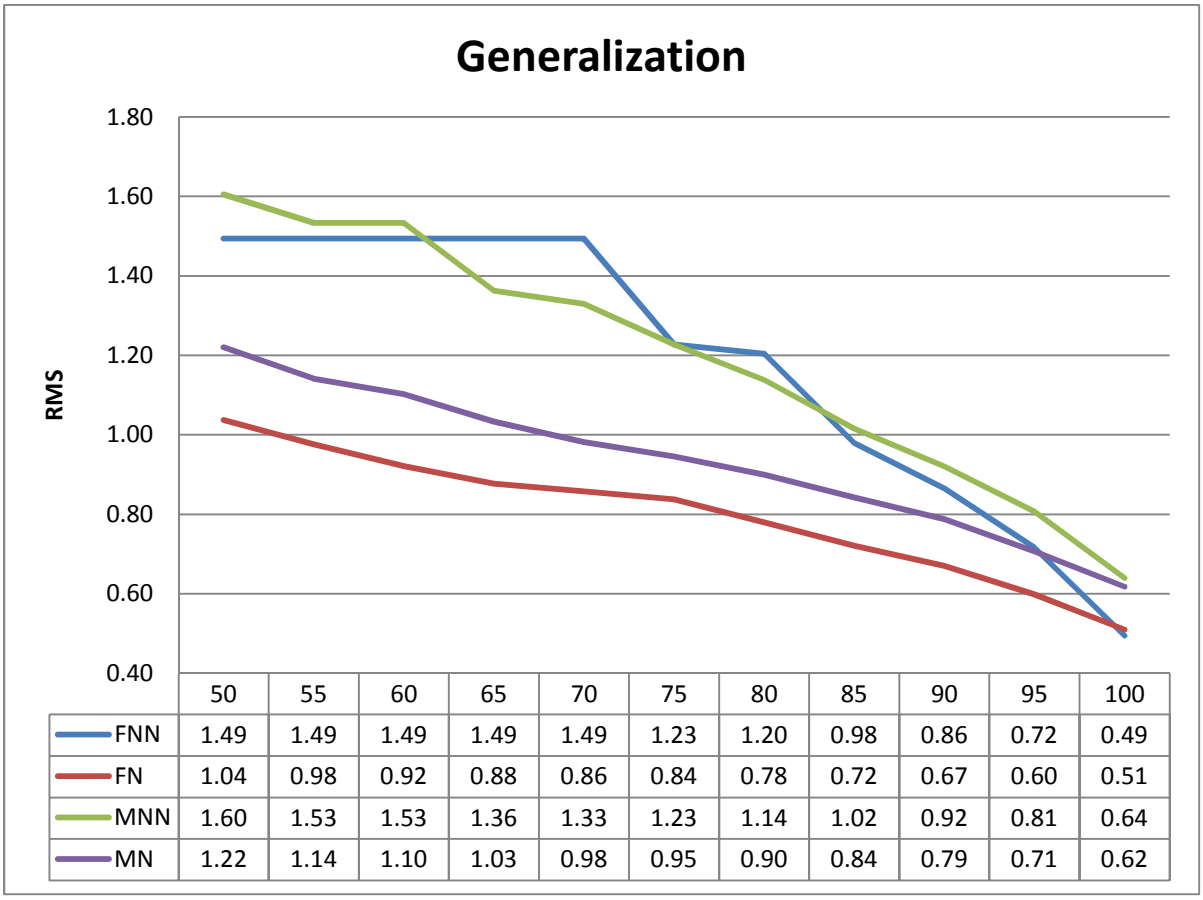


Figure 6-13 Accumulated variance vs. number of coefficients of the overall normalized and non-normalized skull SSM



	50	55	60	65	70	75	80	85	90	95	100
FNN	1.49	1.49	1.49	1.49	1.49	1.23	1.20	0.98	0.86	0.72	0.49
FN	1.04	0.98	0.92	0.88	0.86	0.84	0.78	0.72	0.67	0.60	0.51
MNN	1.60	1.53	1.53	1.36	1.33	1.23	1.14	1.02	0.92	0.81	0.64
MN	1.22	1.14	1.10	1.03	0.98	0.95	0.90	0.84	0.79	0.71	0.62

Figure 6-14 RMS vs. percentage accumulated variance for scale normalized and non-normalized male and female clavicle SSM

Table 6-5 Mean and standard deviation for the RMS error across population

	μ	σ	μ	σ	μ	σ	μ	σ	μ	σ	μ	σ	μ	σ
% Variance	**70**		**75**		**80**		**85**		**90**		**95**		**100**	
RMS	**μ**	**σ**	**μ**	**σ**	**μ**	**σ**	**μ**	**σ**	**μ**	**σ**	**μ**	**σ**	**μ**	**σ**
FNN	1.49	0.31	1.23	0.16	1.20	0.14	0.98	0.10	0.86	0.09	0.72	0.09	0.49	0.08
FN	0.86	0.13	0.84	0.14	0.78	0.14	0.72	0.13	0.67	0.13	0.60	0.12	0.51	0.08
MNN	1.33	0.32	1.23	0.31	1.14	0.29	1.02	0.25	0.92	0.21	0.81	0.18	0.64	0.15
MN	0.98	0.22	0.95	0.20	0.90	0.20	0.84	0.18	0.79	0.17	0.71	0.16	0.62	0.14

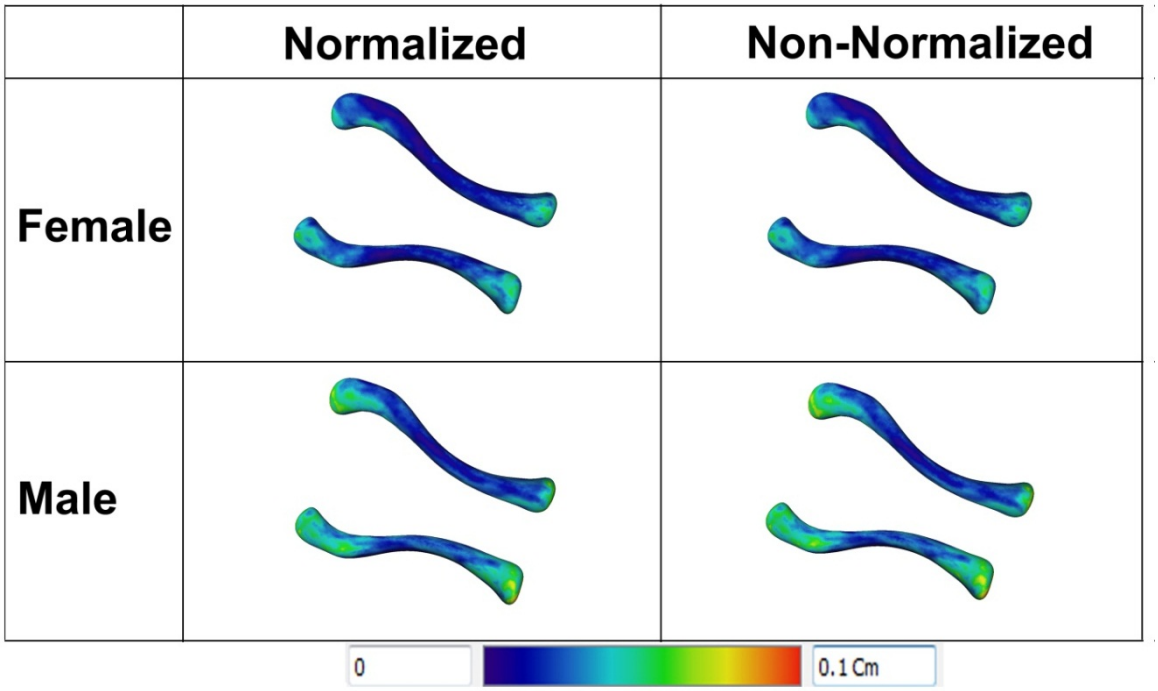


Figure 6-15 Average distance map for reconstructed models using leave one out test

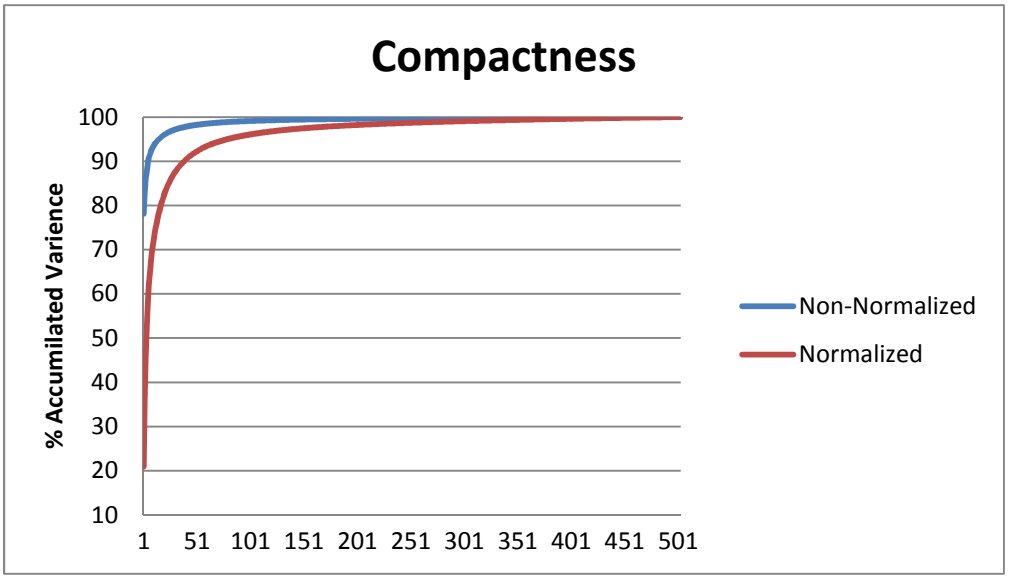


Figure 6-16 Accumulated variance vs. number of coefficients of the overall normalized and non-normalized clavicle SSM

7. BONE SEXING

Direct application for statistical atlases is studying morphometrics and identifying differences between populations [147], which can be broken down further by group demographics. Achieving accurate point correspondence between shapes in populations allows for both global shape analysis using principal components [25, 27] and local analysis using automatically calculated landmarks and measurements [25-27, 29]. In this chapter, the focus will be on the use of morphometrics for bone sexing and exploring sexual dimorphism in the skull.

7.1 Skull

The analysis in this section was funded by National Institute of Justice grant 2008-DN-BX-K182, and the results were submitted for the grant's fulfillment. A final copy of grant report can be found under [148].

7.1.1 Introduction

Estimating sex of human crania traditionally has been and remains to be almost exclusively based on measurements or observations of external cranial features. These methods seldom exceed 90% accuracy and are often well below that. Since crania are overly represented in forensic contexts, it is important to improve sexing accuracy because sex is an important component of the biological profile (i.e., sex must be determined before proceeding with the remaining elements of the profile: age, stature, and ancestry). The purpose of the proposed research is to examine cranial sexual dimorphism in a modern American skeletal sample and provide criteria for sexing that will improve success rates of estimating sex of human crania.

The literature concerning sexing of the crania is extensive and spans many disciplines, including biological anthropology, archeology, biomedical engineering, odontology, and the forensic sciences. For sexing the skull, biological anthropologists have relied historically on visual assessment of features exhibiting obvious dimorphism. These features include: brow ridges, mastoid size, supraorbital margins, chin morphology, and nuchal crest size [149]. Evaluation of these traits is subjective and, to a considerable extent, experience-based. Blind tests by experienced observers seldom yield accuracy in excess of 90%. Stewart [150] achieved a success rate of 77% on the Terry collection crania and Krogman [151] managed a success rate of 92% on the Todd collection, although he considered this figure to be an overestimate because males greatly outnumbered females. Recent work using modern samples of white Americans yielded accurate assessments ranging between 89% and 92% [152]. Treating the observations quantitatively reduces subjectivity to a degree, but does not improve accuracy significantly [153]. Walker [154] has provided the most extensive analysis of traditional morphological features, including nuchal crest, mastoid process, orbital margin, glabella supraorbital ridge, and mental eminence. Even with standardized, multi-state scoring of traits and sophisticated statistical analysis, Walker could only achieve an 88% correct classification of sex, falling short of nearly all postcranial elements which routinely provide sexing accuracy in excess of 90% [155]. Garvin [156] developed a method using laser scans for quantifying supraorbital forms, which is superior to the ordinal scoring system, but it did not improve sexing accuracy

significantly. In contrast to the typical methods, Ramsthaler [157] used CT scans to score traditional traits in the absence of actual skeletal collections.

Giles and Elliot [158] introduced metric sexing of the crania using a statistical procedure in 1963. Their success rate was in the high 80%, a rate typical of subsequent cranial sexing analyses. In general, it is rare to reach or exceed 90% correct sexing, whether one uses morphological traits or measurements. Uytterschaut [159] achieved accuracy between 81% and 89% accuracy on Dutch, Zulu, and Japanese test samples using a discriminant function with four measurements (glabello-occipital length, bizygomatic breadth, nasal height and nasal breadth). He concluded that although size variable is important in sexing, removing the scale can yield the same results. In one study, metric analysis found that bizygomatic breadth was the largest single trait for sex discrimination in the cranium, achieving 80% in South African Blacks [160]. The results increased to 86% discrimination when five cranial measurements were included. Recent studies on sexing South African crania have provided similar accuracy rates using traditional and 3D methods [161]. Using 20th century Americans in the Forensic Anthropology database from the University of Tennessee, correct assessment rates of 88-90% were commonly achieved [149, 162].

While much of the research has focused on multiple cranial features and measurements, some research has focused on specific regions of the cranium, in hope of providing simple, reliable sexing criteria or out of necessity for sexing fragmentary crania. For example, an analysis of the sex differences in the supraorbital margin yielded 70% discrimination based on

the gross morphology of this single indicator [163]. Occipital condyles achieved 76 % [164]. Saini [165] achieved 87% with just two measurements in the mastoid area on an Indian sample.

Regardless of the number of morphological or metric traits considered, the traditional approaches described above rely on what can be observed subjectively or physically measured on the exterior of the skull. The ability to improve estimates in sexing using images and non-traditional measurements has been suggested in a recent publication [166], wherein the authors were able to classify 100% of a modern Taiwanese sample correctly by sex (50 males and 50 females), using measurements taken from lateral radiographs. This was accomplished by concentrating on the supraorbital ridges, frontal sinuses and nuchal crests. Males were found to have greater glabella projection and larger frontal sinuses. The greater male glabella projection is common knowledge, but it appears that measuring this feature precisely increases discrimination. These results were recently replicated on a French sample, where 95.6% accuracy was achieved [167], thereby illustrating the importance of frontal sinus and glabellar projection. Bigoni [168] also achieved a 99% - 100% correct sex classification rate on a known-sex Central European sample using 3D coordinates, along with semi-landmarks quantifying curves mid-sagittal cranial shape.

Rosas and Bastir [169] carried out a geometric morphometric analysis of sexual dimorphism using coordinate data to capture differences in shape. Their results also showed the importance of the supraorbital ridges and identified sexual dimorphism in angulation of the posterior cranial base, the occipital region, and the nasopharyngeal region. Additionally, they

found three features of the mandible useful for sex diagnosis: curvature of the anterior symphysis, development of the pre-angular notch, and flexion of the ramus. According to these authors, size explained 53.7% of the total variance, and 37.3% of the variance could be attributed to the "sex-specific factor," which they linked to differences between male and female skull anatomy, not directly related to size. They also asserted that removing size in studies of cranial sex dimorphism is a way to eliminate its deceptive influence in sex discrimination.

Another geometric morphometric analysis of cranial sex dimorphism in five modern South African populations from individuals in the Dart collection discovered certain features that distinguished males from females across all populations, including features of the frontal bone and zygomatic arches [170]. They also found features unique to certain populations and advocated analyses that take population variation into account. In a further geometric morphometry study limited to indigenous South Africans, Franklin, et al. [161] identified bizygomatic breadth, forehead contour profile, the form of the supramastoid crest, alveolar prognathism, and the size of the posterior airway space as the most dimorphic features. Franklin, et al. [171] tested the comparability of their 3D coordinate data with traditional linear measurement data. They found that 3D landmark coordinates can be transformed mathematically into 2D linear measurements, thereby demonstrating the possibility of simultaneously collecting data for both types of studies with a digitizer or other instrument designed to collect coordinate data.

7.1.2 Methods

7.1.2.1 Sample and Data Acquisition

The sample for this analysis is a subset of documented crania from people with 20th century birth years from the William M. Bass Donated Skeletal Collection at the University of Tennessee's Department of Anthropology (n=222, 81 females and 141 males). The majority of the collection consists of American white individuals and is the focus of this research. The bones were packed into foam-padded boxes and CT scanned using 0.625 x 0.625 x 0.625- mm cubic voxels. The DICOM images acquired from the CT scans were then manually segmented, and surface models were generated.

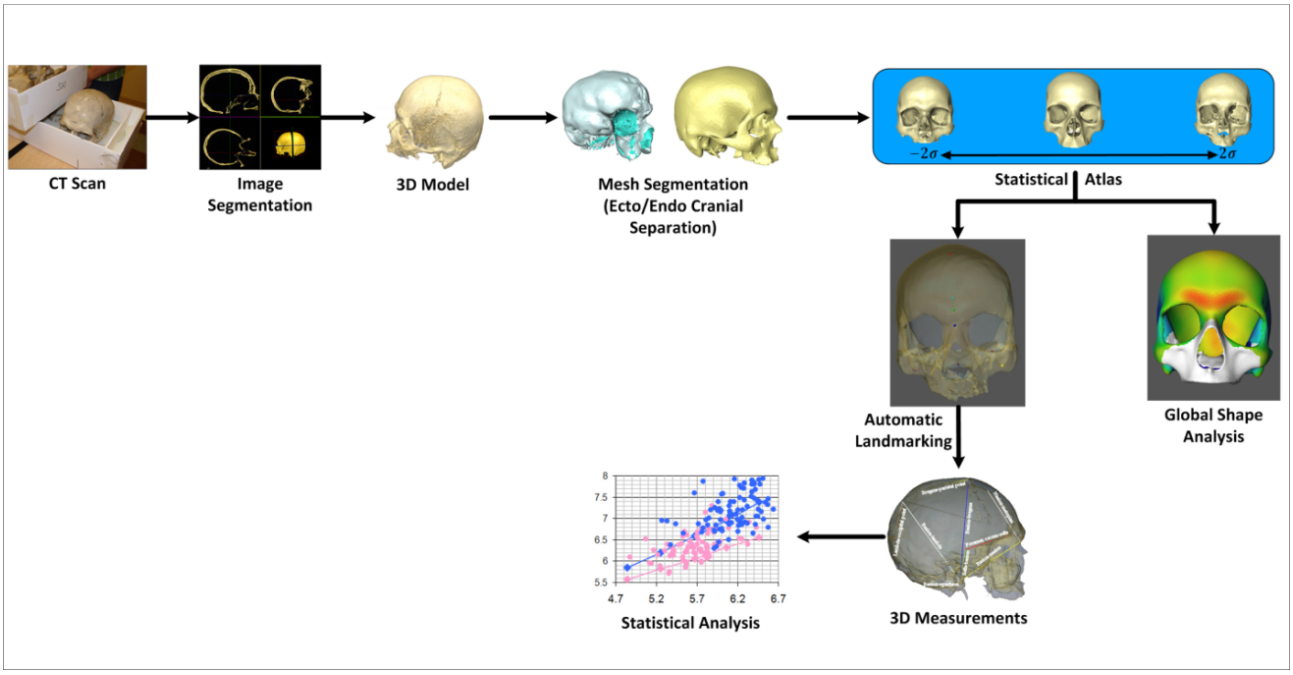


Figure 7-1 Flow chart outlining the design of the skull sexing analysis

This segmentation process has proven to be reliable with a negligible inter-observer error rate of 0.163 mm, intra-observer error of 0.105 mm, and pairwise inter-observer variability of 0.269 mm [25]. Figure 7-1 outlines the study design, starting from data scanning to statistical analysis.

7.1.2.2 Computer Automated Analyses: Global and Local

Upon adding the skull in the training dataset to the statistical atlas, two types of analyses were executed on the atlases: global and local. The global analysis examines the principal components of the SSM to pinpoint areas of significant dimorphism. This analysis is a "feature-finding" step in that it detects morphological regions of high dimorphism that can be more carefully examined in the local analysis, as landmarks defined in these highly sexually dimorphic regions possess the best potential for sex estimation. The local analysis uses endo- and ecto-cranial landmarks to compute geodesic measurements. Discriminant function analysis with stepwise variable selection was applied to these measurements to find the subset that gives the highest accuracy rates.

The 3D global analysis was used to detect areas of high size and shape dimorphism. Size dimorphism was detected by applying PCA across all crania in the atlas. The first principal component carries most of the size information, and the remaining components supply information about shape variation. In order to look at shape independent from size, all crania were first aligned and scaled to the mean model using GPA. PCA was then calculated on the normalized models using iMF software. Linear discriminant analysis (LDA) was then applied to the principal components to highlight areas of variation between sexes [25].

A set of predefined internal and external anatomical landmarks were automatically detected for the local analysis. Figure 7-2 outlines the framework for automatic landmark detection; the algorithm utilized the power of the statistical atlas to propagate the anatomical loci of the landmarks across the sample. This step was performed one time on the template mesh, and then these loci were propagated automatically for each new skull to be measured. Sets of constraints, including curvature, geometry, and search directions, were then used to detect the exact landmark in each of these loci. **Error! Not a valid bookmark self-reference.**Table 7-1 depicts the landmarks used in skull sexing and their definitions. The steps involved in landmark calculation are outlined in Figure 7-3. First, orbitale and porion were calculated and used to define the Frankfurt horizontal plane. The midsagittal plane was then defined as a plane normal to the Frankfurt plane that bisects the skull. The midsagittal contour was calculated by intersecting the midsagittal plane with the ecto- and endo-cranial models. This contour was then used to calculate landmarks one through ten. Zygion was calculated by finding the most lateral points on the zygomatic arches. Finally, mastoidale was calculated by locating the most inferior tip of each mastoid process. A set of endo- and ecto-cranial measurements was defined between these landmarks; Table 2 provides a description of each measurement.

Table 7-1 Landmarks used in skull sexing and their definitions

Landmark	Description
Basion	Most inferior posterior point in the midsagittal plane on the anterior rim of the foramen magnum
Gabella	Most anteriorly projecting point in the midsagittal plane at the lower margin of the frontal bone, which lies above the nasal root and between the superciliary arches
Inion	Most prominent point of the external occipital protuberance
Mastoidale	Lowest point of the mastoid process
Metopion	Point where the line that connects the highest points of the frontal eminences crosses the sagittal plane
Nasion	The point of intersection of the naso-frontal suture and the midsagittal plane
Opisthioncranion	Most posteriorly protruding point of the occipital bone in the midsagittal plane
Opisthion	The point at which the midsagittal plane intersects the posterior margin of the foramen magnum
Porion	Midpoint of the external auditory meatus
Sella	Midpoint of the sella turcica
Supraglabella	Most posterior point in the midsagittal plane in the supraglabellar fossa (the concavity between glabella and metopion)
Vertex	The highest point on the cranial vault in the midsagittal plane (used in lieu of bregma on account of the absence of sutures in some of the models)
Zygion	The most laterally positioned point on the zygomatic arches

Table 7-2 Measurements definitions

G-SgN	Distance between glabella and line joining supraglabella and nasion
GSg	Distance between glabella and supraglabella
GN	Distance between glabella and nasion
NSg	Distance between nasion and supraglabella
RMH	Distance between tip of right mastoid and cranial base
LMH	Distance between tip of left mastoid and cranial base
LMW	Maximum width of left mastoid
FOL	Distance between basion and opisthion (foramen magnum length)
LOBH	Left orbit height
RMW	Maximum width of right mastoid
ROBH	Right orbit height
RMS	Distance between right mastoidale and sella
RMB	Distance between right masdoidale and basion
LMS	Distance between left mastoidale and sella
LMB	Distance between left mastoidale and basion
SN	Distance between sella and nasion
BN	Distance between basion and nasion
ZYB	Distance between right and left Zygion
VN	Distance between vertex and nasion
VB	Distance between vertex and basion
SB	Distance between sella and basion
GOL	Distance between glabella and opisthocranion
GM-SN	Angle between glabella-metopion and sella-nasion
GM-BN	Angle between glabella-metopion and basion-nasion
GS-GM	Angle between glabella-sella and glabella-metopion
IOp-SN	Angle between inion-opisthocranion and sella-nasion
IO-IOp	Angle between inion-opisthion and inion-opisthocranion
GS-GN	Angle between glabella-sella and glabella-nasion
SN-SMR	Angle between sella-nasion and sella-right mastoidale
SN-SML	Angle between sella-nasion and sella-left mastoidale
IO-BN	Angle between inion-opisthion and basion-nasion
IOp-BN	Angle between inion-opisthocranion and basion-nasion
GN-GSg	Angle between glabella-nasion and glabella-supraglabella
SN-SB	Angle between sella-nasion and sella-basion
IO-PD	Angle between inion-opisthion and normal line to Frankfurt plane
IOP-PD	Angle between inion opisthocranion and normal line to Frankfurt plane
GPI	Glabella projection index (perpendicular distance from glabella to supraglabella-nasion line)*100/ (supraglabella to nasion)
VTG	Vault thickness at glabella
VTSg	Vault thickness at supraglabella
VTM	Vault thickness at metopion
VTOp	Vault thickness at opisthocranion
VTI	Vault thickness at inion
VTV	Vault thickness at vertex

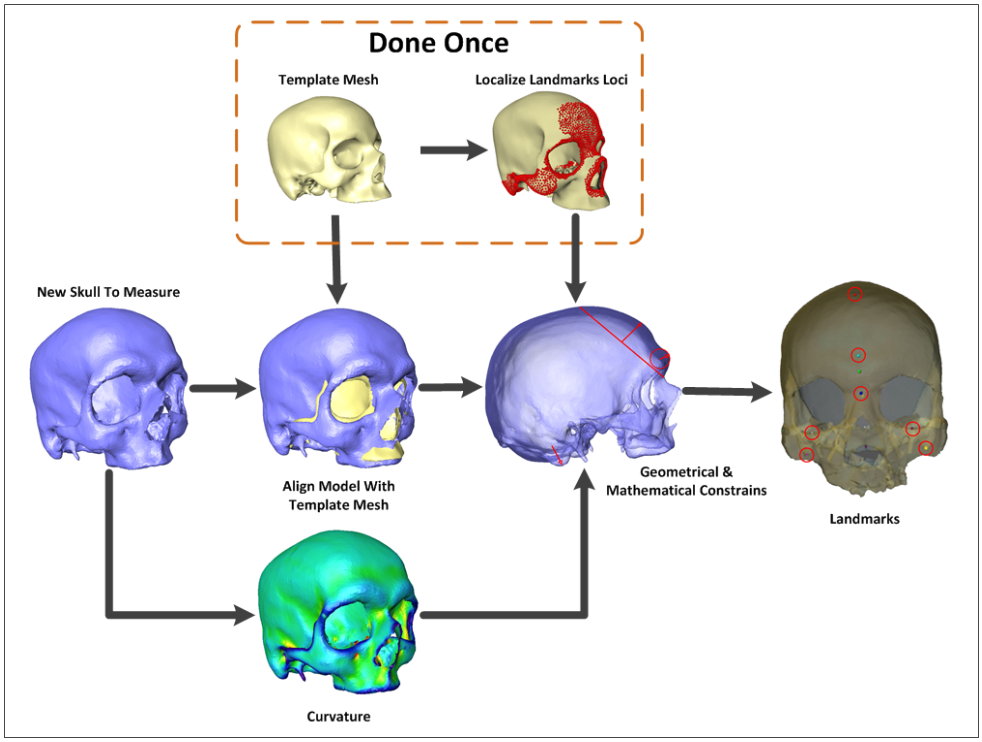


Figure 7-2 Flow chart outlining methodology of calculating automated measurements

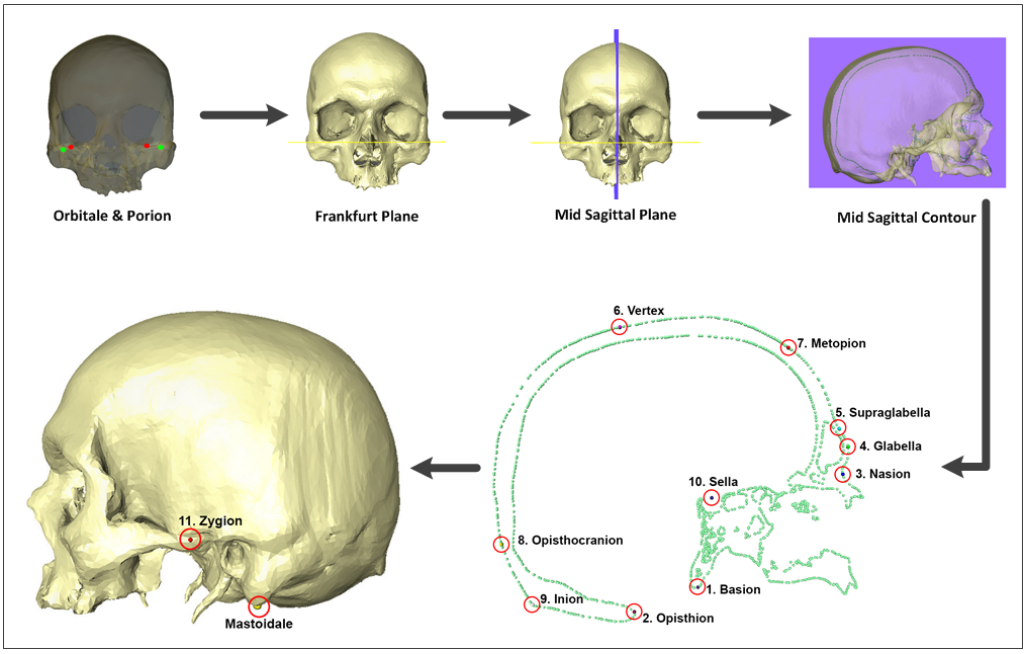


Figure 7-3 Sequence of automatic landmark calculations

7.1.2.3 Statistical Analysis and Validation

The stepwise multilinear regression was used to determine the best variables to include in the discriminant model ($p \leq 0.1$ was used as the threshold for variables to be added during the regression). The selected variables were fed to a discriminant analysis classifier, and the classification percentage for each sex and total classification rate were calculated using leave-one-out cross-validation. The mean and standard deviation were calculated for each measurement, and a chi-square goodness-of-fit test was used to test the normality of each measurement. Two sample t-tests were used to test for significant differences between the sexes for normally distributed variables (the two-sample Kolmogorov-Smirnov test was used in cases of non-normality). Due to the imbalanced sample size, two versions of the t-test were used for equal and unequal variances; the F-test was used to test for equal variance. Finally, power analysis was used to calculate the minimum sample size required to test the null hypothesis that the two populations have significantly different means ($p<.05$).

In order to validate the automatic landmarking and measurement process, the computer-automated ecto-cranial measurements were compared with measurements taken with calipers. Paired t-tests (α=.05) were used to test for significant differences between the two sets of measurements, and a percent error was calculated to examine the magnitude of the differences.

% error = (caliper measurement – bone atlas measurement) *100%bone atlas measurement

7.1.3 Results

7.1.3.1 Global Analysis

The variables loaded onto the first principal component in the non-normalized analysis are (in order of significance): glabellar region, nuchal region, cranial length, mastoid, and zygomatic (Figure 7-4). The second and third principal components captured differences in the occipital region, right zygomatic, and, to a lesser extent, left zygomatic. The fourth principal component picked up the left zygomatic and cranial breadth, and PC5 picked up the right occiput. The global analysis on the normalized crania detected similar regions of difference: cranial length, the glabellar region, the zygomatics, mastoid, and cranial breadth (Figure 7-4). Figure 7-5 illustrates the hotspots using PC1 to PC40 for size dimorphism (non-normalized: glabellar region, occipital region, mastoids, and zygomatics) and shape dimorphism (normalized: glabellar region and mastoid). Consequently, linear and angular measurements in these regions were expected to be effective discriminators.

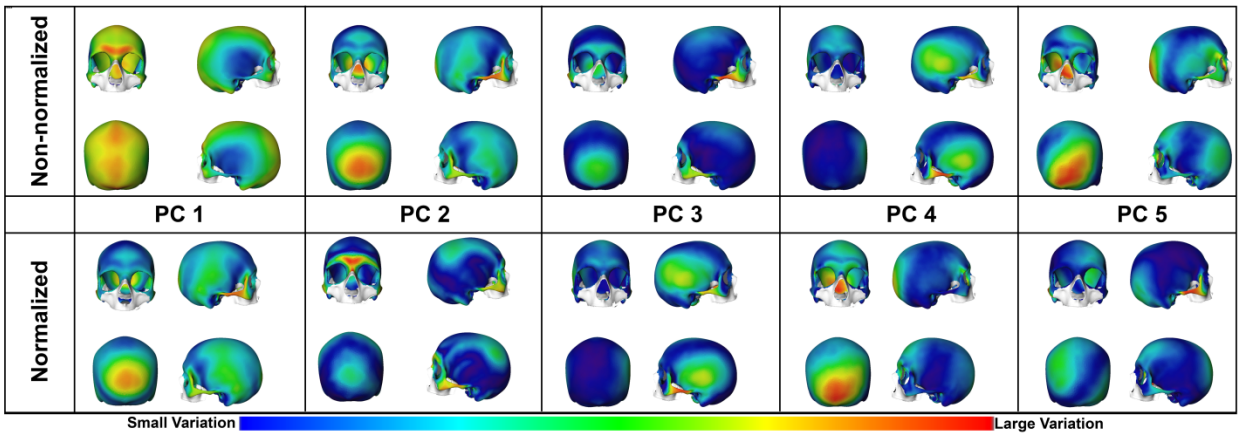


Figure 7-4 Results of global 3D surface analysis (principal components 1 through 5)

7.1.3.2 Local Analysis

Table 7-5 presents the descriptive statistics for the angular, linear, ,and vault thickness measurements, respectively. Males are significantly larger than females in all linear measurements except nasion-supraglabella (Table 7-4). Interestingly, male vaults are thicker than females at all locations except metopion (p=.01) and vertex (p=.56), so females have thicker frontal squama than males (Table 7-5). Most of the angular measurements are significantly more obtuse in females except for GM-SN, GPI (glabellar projection index), GN-GSg, and IO-BN. The first three variables largely account for the more robust and projecting glabellar region and sloping frontal bone in males. However, the more acute IO-BN in females combined with a more obtuse IO-IOp and SN-SB indicates the differences in the shape and orientation of the cranial base. Females have a larger cranial base flexion angle, as measured by SN-SB. The angles IOp-PD and IO-PD were created in order to decompose IO-IOp into anterior and posterior components and isolate whether the difference in IO-IOp was due to the larger and more projecting inion in males or to the position of opisthion (related to the position of basion and, consequently to the cranial base). IOp-PD was insignificant, but IO-PD was significant, indicating the primary difference in IO-IOp is in the anterior component, or in the orientation of opisthion, reflecting a difference in cranial base flexion between males and females.

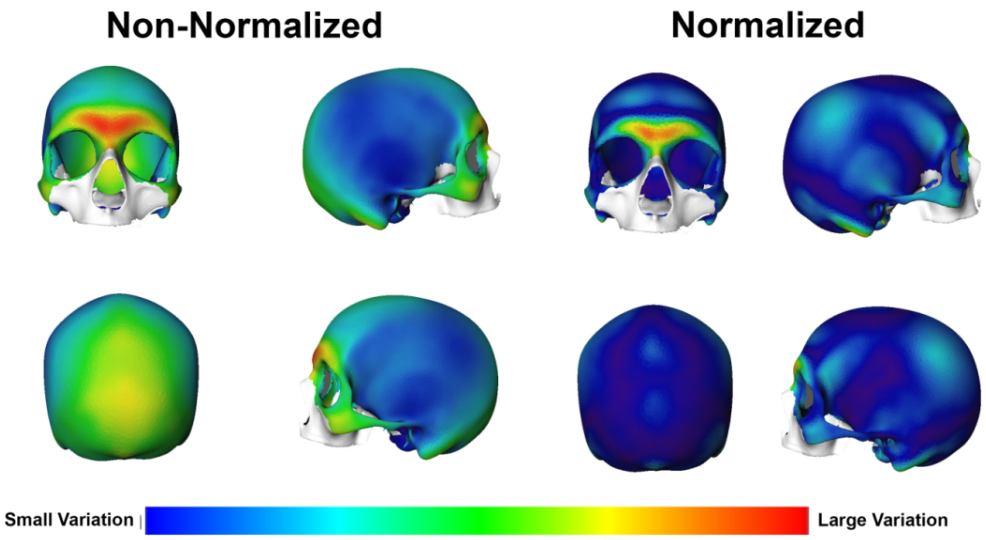


Figure 7-5 Results of global 3D surface analysis for combined principal components 1 through 40

Table 7-3 Descriptive statistics for angular measurements

	Female					Male	
	Mean	SD	t-test	F-test	Power	Mean	SD
GM-SN	107.94	3.95	0.01	0.93	79	110.22	4.00
GM-BN	95.31	3.65	0.01	0.49	131	93.62	3.92
GS-GM	84.96	4.37	0.01	0.26	18	79.87	3.92
IOp-SN*	100.93	5.71	0.93	0.42	***	100.99	5.28
IO-IOp	131.82	5.87	0.01	0.23	71	128.01	6.64
GS-GN	63.77	5.32	0.01	0.83	129	61.39	5.22
SN-SMR	120.96	4.33	0.01	<.001	114	119.15	3.22
SN-SML	120.93	3.76	0.01	0.14	70	118.79	3.26
IO-BN	125.86	6.11	0.01	0.31	101	129.14	6.78
IOp-BN*	102.32	4.87	0.44	0.86	***	102.84	4.96
GN-GSg	16.14	4.93	0.01	<.001	7	27.78	7.05
GPI	5.92	1.81	0.01	<.001	7	11.43	3.51
IOp-PD*	13.09	3.96	0.71	0.08	***	12.86	4.75
IO-PD	118.73	6.15	0.01	0.73	81	115.18	6.37
SN-SB	126.23	5.54	0.01	0.97	144	123.88	5.53

*Power > 1000

Table 7-4 Descriptive statistics for linear measurements

	Female					Male	
	Mean	SD	t-test	F-test	Power	Mean	SD
G-SgN	1.25	0.40	0.01	<.001	10	2.42	1.04
GSg	6.40	0.22	0.01	<.001	18	8.35	3.03
GN	15.24	3.82	0.01	0.03	77	13.22	3.09
NSg*	21.44	3.89	0.36	0.61	***	20.93	4.10
RMH	25.01	2.92	0.01	0.60	26	27.91	2.78
LMH	26.02	2.46	0.01	0.10	26	28.76	2.92
LMW	34.54	2.42	0.01	0.99	134	35.61	2.42
FOL	35.85	2.45	0.01	0.76	52	37.56	2.38
LOBH	36.68	2.79	0.01	0.06	178	37.86	3.37
RMW	36.70	2.39	0.03	0.63	266	37.43	2.29
ROBH	37.85	3.56	0.01	0.01	69	39.79	2.73
RMS	50.15	3.57	0.01	<.001	16	53.94	2.33
RMB	50.15	3.57	0.01	<.001	16	53.94	2.33
LMS	50.64	2.92	0.01	0.07	16	54.16	2.45
LMB	50.64	2.92	0.01	0.07	16	54.16	2.45
SN	60.72	4.44	0.01	0.39	17	66.49	4.84
BN	96.81	3.28	0.01	0.02	8	103.56	4.15
ZYB	124.20	3.58	0.01	0.05	8	131.62	4.39
VN	135.19	6.63	0.01	0.07	94	139.05	8.00
VB	136.60	4.75	0.01	0.19	25	141.86	5.43
GOL	176.99	6.81	0.01	0.53	11	187.36	6.41
SB	47.47	4.65	0.01	0.51	69	50.43	4.98

*Power > 1000

Table 7-5 Descriptive statistics for skull vault thickness measurements.

	Female					Male	
	Mean	SD	t-test	F-test	Power	Mean	SD
VTG	14.84	2.72	0.01	<.001	29	18.22	4.40
VTSg*	13.07	2.94	0.37	0.42	**	13.42	2.72
VTM	8.61	1.83	0.01	0.03	53	7.45	1.47
VTOp*	8.95	1.87	0.27	0.02	***	9.25	2.37
VTI	14.22	2.97	0.01	0.42	47	16.35	2.75
VTV*	7.54	1.21	0.56	0.13	***	7.43	1.41

*Power > 1000

7.1.3.3 Linear Discriminant Analysis

Error! Not a valid bookmark self-reference. Table 7-6 presents several of the best models obtained with leave-one-out cross-validated linear discriminant analysis and stepwise variable selection. The best model achieved 97.3% accuracy with 11 variables (note: SN-SML cannot be measured on a radiograph). The next successful model achieved a 95.5% overall classification accuracy with just eight variables, all of which were related to size differences. A model utilizing just shape variables (two angles and glabella projection index) classified 86.5% of the cross-validated sample accurately; a model with variables capturing the shape of the brow ridge (GN-GSg and G-SgN) classified 83.8% accurately. The glabella projection index alone achieved 82%, as did the basion-nasion length (cranial base length) and bizygomatic breadth (83%). With the exception of SN-SML, all of these measurements were easily obtained with calipers and/or on a lateral or anterior-posterior radiograph.

Table 7-6 Results for the linear discriminant analysis.

Model Variables	Combined	Male	Female
BN, ZYB, LMH, IO-IOp, SN-SML, VTM, GOL, VN, GSg, GPI, LMS	97.3	96.5	98.8
BN, ZYB, LMH, VTM,GOL, VN, GSg, LMS	95.5	95.0	96.3
IO-IOp, SN-SML, GPI	86.5	87.9	84.0
GN-GSg, G-SgN	83.8	87.9	76.5
GPI	82.4	84.4	79.0
ZYB	82.9	89.4	71.6
BN	82.0	86.5	74.1

7.1.3.4 Validation

Table 7-7 and , Table 7-8present the results of the validation study. Four measurements that are commonly taken with calipers were compared to the computer-automated values for those same measurements. Table 7-8 assesses the differences between caliper and computer automated measurements with a paired t-test. The null hypothesis was that the difference would be zero; the paired t-test showed significant differences from zero in all measurements except foramen magnum length. However, this measure of difference does not indicate that those differences reflect significant error, as shown in Table 7-7. The mean percent error between the caliper and atlas measurements was <2%; while there is a statistically significant bias, the value is small (< 2%) and would not normally influence results on an individual case.

Table 7-7 Measurement validation results (% error)

	ZYB	GOL	FOL	BNL
Mean % error	1.39	0.75	1.83	1.20
Median % error	1.48	0.56	2.56	0.99
Mode % error	0.00	0.00	0.00	0.00
Standard Deviation	0.81	0.66	1.98	1.04

Table 7-8 Measurement validation results (t-tests)

	ZYB		GOL		FOL		BNL	
	Caliper	*Atlas*	*Caliper*	*Atlas*	*Caliper*	*Atlas*	*Caliper*	*Atlas*
Mean	128.10	129.81	182.99	184.20	36.62	36.73	101.97	101.41
Variance	37.12	34.84	76.70	75.36	6.83	6.60	28.06	26.80
Observations	187	187	187	187	187	187	187	187
Pearson Correlation	0.98		0.99		0.89		0.96	
Hypothesized Mean Difference	0		0		0		0	
Deg. of Freedom	186		186		186		186	
t statistic	-18.07		-11.94		-1.21		5.05	
P(T<=t) one-tail	<.001		<.001		0.12		<.001	
t critical one-tail	1.65		1.65		1.65		1.65	
P(T<=t) two-tail	<.001		<.001		0.230		<.001	
t critical two-tail	1.97		1.97		1.97		1.97	

8. DIRECTIONAL ASSYMETERY

8.1 Clavicle

8.1.1 Introduction

Studies of skeletal asymmetry typically use a standard set of osteometric measurements that capture the length and robusticity of the element(s) being investigated to quantify the direction and magnitude of asymmetry. Directional asymmetry refers to significant unimodal population-level deviations from bilateral symmetry that most likely arises from lateralized behaviors[172]. This information is customarily expressed in terms of the percentage of directional asymmetry [172-175]. This method measures the direction and magnitude of asymmetry by calculating the difference between a left and right pair of measurements, standardized by the mean of the left and right measurements [%DA = ((R-L)/((R+L)/2))*100%].

These studies have elucidated several important trends regarding human skeletal asymmetry. The magnitude of asymmetry in human limb bones is greater in the upper limb than in the lower limb [175, 176]. Within the upper limb, bilateral directional asymmetry favors the right side, with diaphyseal lengths and diameters being absolutely greater in the right humerus, radius, and ulna than in the left [173, 175, 177] . However, the clavicle deviates slightly from this pattern in that the left clavicle is longer than the right [172, 174, 178]. Bilateral directional asymmetry has been interpreted frequently as the manifestation of behavioral laterality related to activity and locomotion [179-183] , as whole limb asymmetry patterns differ between species[179, 184, 185]. Other explanations focus on genetic and hormonal influences

[186], developmental differences in vascular supply to paired structures [187], and environmental stressors such as malnutrition and extreme climates[188]. Nonetheless, biomechanical stresses remain the primary explanation for limb asymmetry [181].

One way in which the asymmetrical manifestations of biomechanical stresses have been addressed is by examining entheses. Entheses, or muscle stress markers (MSMs), have a complex etiology, wherein genetics, hormones, body size and activity levels, among other factors, combine to influence their size and shape[189]. Within anthropological studies, MSMs are often associated with differences in activity patterns among human populations [190, 191] . In these papers, for example, larger MSMs have been associated with sexual dimorphism in activity type or intensity [192], as well as changes associated with age[193, 194]. Thus, asymmetry in activity should relate to size and shape asymmetry in entheses, and thus potentially provide indirect evidence that lateralized behaviors influence observed asymmetries in clavicular shape.

Biomechanically, the clavicle acts as a strut for the upper limb and serves as an attachment site for a number of back, neck, chest, and shoulder muscles and ligaments: trapezius, sternocleidomastoid, pectoralis major, deltoid, subclavius, the coracoclavicular and acromioclavicular ligaments. The complex arrangement of muscle attachments may partially explain the clavicle's distinctive shape; however, some of this explanation undoubtedly lies in its unique development [195-197]. The clavicle is the first bone to ossify and the last bone to fuse. Two primary ossification centers appear around six weeks in utero and unite to form a

single center about a week later [198]. It undergoes both intra-membranous and endo-chondral ossification during development and assumes adult form in utero. The lateral epiphysis appears and unites just prior to the second decade of life (17-19 years) [199], but the medial epiphysis fuses during the mid-to late-20s, and this process occurs over a period of roughly ten years [198].

Two of the most recent analyses of asymmetry in the human clavicle have used linear dimensions to examine the potential effects of loading and development on this bone. Mays, et al. [174] used a skeletal collection of adults and sub-adults from medieval England to address some of the complex factors that have been suggested as possible causes of clavicle asymmetry. They examined curvature (using 2D measurements from radiographs), length, robusticity, vascularization, and the morphology of muscle attachment sites and concluded that clavicle asymmetry was due most likely to laterality in mechanical loading. Auerbach [172] also found that activity patterns and loading behavior contribute significantly to clavicle asymmetry with diaphyseal breadths being more sensitive than lengths to the effects of loading. However, they add that the unique developmental pathway of the clavicle may account for the atypical pattern of asymmetry observed in this bone. Although the metrics in these studies were able to establish a consistent pattern of asymmetry, neither was capable of assessing the hypothesized factors that influenced those directional biases.

Given the complex, 3D loadings that occur in the clavicle, an alternative approach may augment these prior investigations. Recent advances in computer modeling have enabled more

detailed and sophisticated analyses of skeletal size and shape than are possible with traditional osteometrics. Mahfouz, et al. [26, 200, 201] used statistical bone atlases as a method to investigate sex and ancestry differences, as well as a means to automate bony landmark approximation and measurement calculation. A bone atlas is an average mold, or TM, that captures the primary shape variation in a skeletal element and allows for the comparison of global shape differences between groups or populations and facilitates computer-generated measurements. Three-dimensional models are constructed by segmenting a set of CT scans. Each of these models consists of tens of thousands of triangular faces and vertices that are used to align the models in the atlas and to provide standardization, normalization, and landmark correspondence across the dataset. The power of a statistical bone atlas lies in the fact that it allows for the extraction of size and/or shape information from a large sample of bones with a high degree of accuracy and precision. Furthermore, nontraditional measurements, as well as any number of novel analyses across all points of the atlas are possible, as will be demonstrated in the present analysis. Shirley's [202] investigation of sex dimorphism in clavicular morphology revealed that the statistical bone atlas is an effective tool for studying this complex bone. While 2Ds have merits for determining directional asymmetry in size and a limited interpretation of shape, 3Ds more effectively facilitate examinations of skeletal elements with complex curvatures.

8.1.2 Methods

The sample for this study is a subset of the William McCormick Clavicle Collection at the University of Tennessee. The McCormick Collection consists of clavicles from 2,694 Americans with mid- to late-20th century birth years. The collection is derived from the post-industrial East Tennessee region, so the results of this study cannot be universalized to all human groups. In this analysis, right and left clavicles from 505 individuals (285 males, 220 females) were selected using two criteria. First, only adults over 30 years of age were used to ensure complete union of the medial epiphysis. Second, only normal, non-pathological, and non-fractured bones were selected, as antemortem fractures affect bone dimensions. The clavicles were packed into foam boxes and CT scanned using 0.625 x 0.625 x 0.625-mm cubic voxels. The DICOM images acquired from the CT scans were then manually segmented, and surface models were generated.

The segmented clavicle models were added to the statistical atlas, and four different atlases were constructed: right male, right female, left male, and left female. In order to fully identify morphometric differences due to asymmetry and sexual dimorphism, a two-step feature extraction methodology was implemented as shown in Figure 8-1

This methodology facilitated two objectives essential to this analysis. (1) The method eliminates inter- and intra-observer error with automatic landmarking and computer-automated measurements. In general, computer-automated measurements guarantee 100% precision of the output measurements;

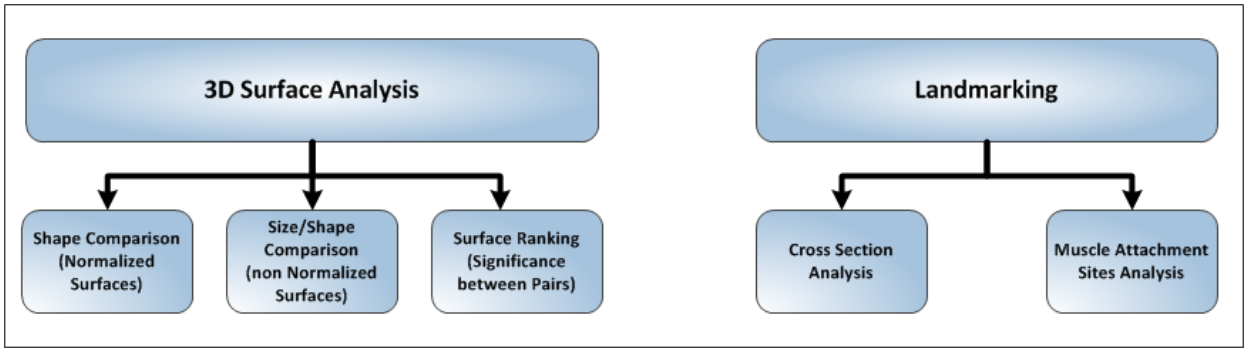


Figure 8-1 The two-step feature extraction methodology used to identify asymmetry within and between the sexes

on the other hand, they do not guarantee 100% accuracy, and this is due to the potential presence of bias or systemic error. Bias error can be detected easily and, in the case of comparative studies, performed with the same measurement system for all groups, this error will not affect the outcome, as it is constant across all groups being compared. (2) This 3D analysis permitted the evaluation of the entire bone surface for morphological differences, including important muscle and ligament attachment sites. This method expands the capacities of 2D analyses, as it allows for the examination of both intrinsic and extrinsic surface properties that may be otherwise difficult to capture, especially in the case of spatially complex bone shapes.

8.1.2.1 Landmarking and cross-sectional analyses

Landmarks were automatically calculated on each bone in the atlas. Figure 8-2 outlines the method used to calculate landmarks and extract cross-sectional data along the entire bony surface. First, the medial axis was calculated by finding the bone surface that intersects with

planes that are normal to the principal axis every 5% of the overall bounding box length (i.e. maximum length). The 5% increments begin at the lateral end of the clavicle (0%) and proceed towards the medial end (100%). Each of these planes was then rotated to find the contour that gave the minimum cross-sectional diameter. The mean of these contours represents the points of the medial axis. An iterative regression procedure was then performed to fit polylines between these points. The length of each segment and the angle between each segment were then calculated. The second step involved finding the waist contour (the contour with the smallest circumference). Area, circumference, maximum diameter, and minimum diameter were calculated for each cross-sectional contour and the waist contour. An additional measurement was calculated to estimate the precise location of the waist along the shaft of each bone.

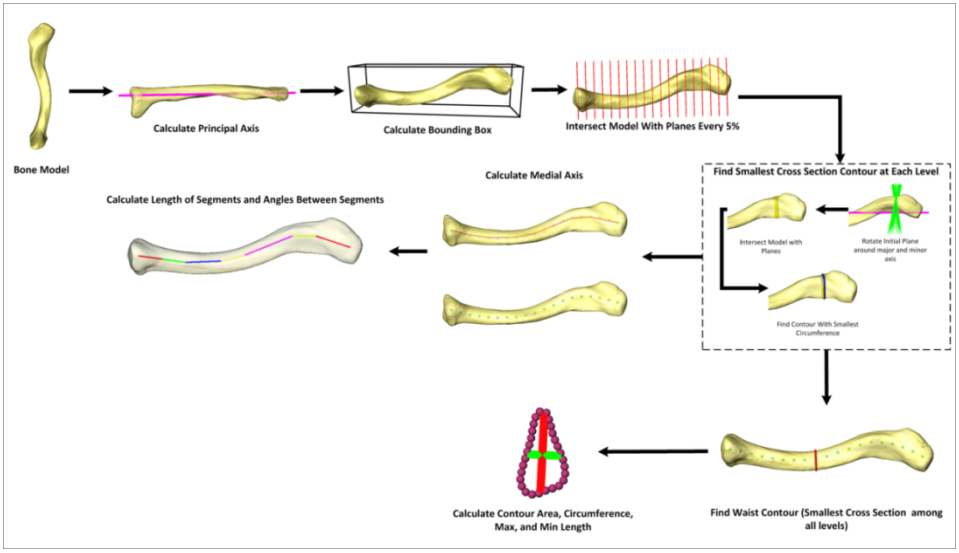


Figure 8-2 Calculating landmarks, cross-sectional contours, and the medial axis

Cross-sectional contours along specific muscle attachment sites were then identified to find more biomechanically relevant cross-sectional contours than might be offered by the 5% shaft increments. Figure 8-3 outlines the method of muscle attachment site localization and cross-sectional contour calculation at these sites. First, a mean bone for the population was calculated and used as a reference bone to localize five muscle attachment sites (trapezius, sternocleidomastoid, pectoralis major, subclavius, and deltoid). In addition, the attachment sites for the costoclavicular and conoid ligaments were mapped onto the bone atlas. Since entheses are difficult to detect on some areas of the clavicle, particularly in females, a standard anatomical text was referenced to approximate muscle and ligament attachment sites (Gray's Anatomy of the Human Body, available online at http://www.bartleby.com).

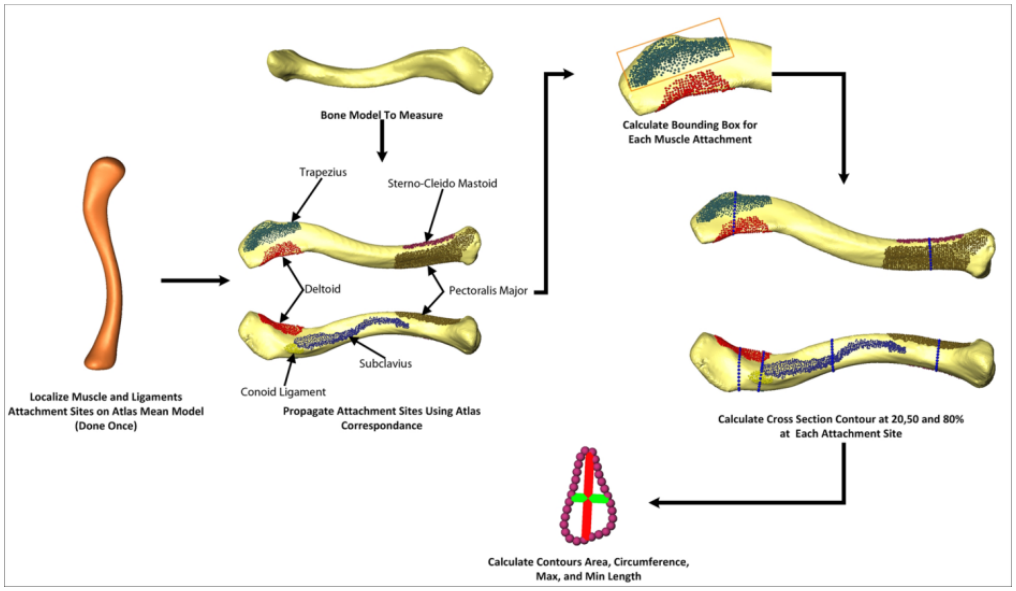


Figure 8-3 Flow chart showing the identification of the muscle attachment sites and contour calculations at these sites

These sites were then propagated across the entire sample using the statistical atlas to generate correspondence between homologous anatomical sites. Three cross-sectional contours were calculated along each muscle attachment site at 20%, 50% and 80% of the length of the bounding box of each site (i.e. the total length of the muscle attachment site). As with the 5% increment contours, area, circumference, maximum diameter, and minimum diameter were calculated for each cross-sectional contour of the muscle attachment sites.

For each measurement percent directional asymmetry (%DA), percent absolute asymmetry (%AA) and percent bias were calculated for both males and females as outlined below. Percent bias was used as a means of calculating asymmetry as a count variable. This calculation was selected as it offers a different way of expressing directional asymmetry, eliminating potential problems associated by the use of descriptive statistics in calculating %DA (a signed number and can lead to the generation of mean and standard deviation values that do not reflect the true differences between populations).

$$\%\mathrm{DA} = \frac{(\mathrm{Right}-\mathrm{Left})}{\mathrm{Average}(\mathrm{Right}+\mathrm{Left})}*100$$

$$\%\mathrm{AA} = \frac{\mathrm{Absolute\ Value}\ (\mathrm{Right}-\mathrm{Left})}{\mathrm{Average}(\mathrm{Right}+\mathrm{Left})}*100 \qquad (62)$$

$$\%\mathrm{Bias} = \frac{\mathrm{Count}(\mathrm{Right}>\mathrm{Left})}{\mathrm{Count}(\mathrm{Right})}*100$$

8.1.2.2 3D surface analysis.

Both the size and shape of a skeletal element must be considered to fully explore areas of potential asymmetry. Figure 8-4 outlines the surface analysis carried out in this study. To

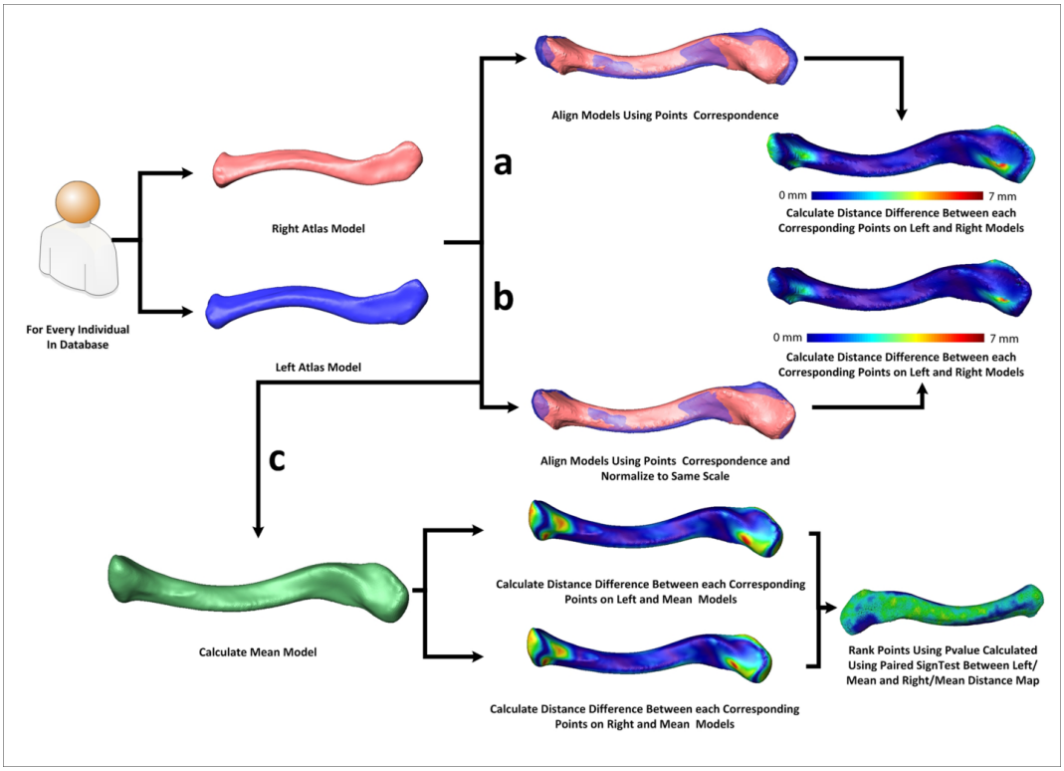


Figure 8-4 3D surface analysis performed to identify asymmetry

identify asymmetrical differences in size, left and right models for each individual were first aligned by extracting the homogenous transformation using point correspondence.

After this alignment, the distance between each homologous point pair on the left and right model was then calculated for each individual across the entire population. From these distances, the average distance, standard deviation, and RMS distance for each individual was calculated, and an average distance map for both males and females was generated.

To isolate size and examine the shape differences, right and left models were aligned and normalized to the same size using point correspondences. The same analysis described above for the un-normalized bones was performed on the normalized dataset. To identify sites

on the bone with statistically significant asymmetry, the left and right models for each individual were aligned, and the mean model of both sides was calculated. The distance between every point on the mean model and each corresponding point on both left and right models was calculated. Paired sign tests were then performed on these distances for each point across the population, giving a p-value for each point on the model, which were then used to generate a surface map showing areas of significant difference between the right and left clavicle for both sexes.

All measurements were analyzed for asymmetry differences within and between the sexes. The mean and standard deviation were calculated for each measurement, and a chi-square goodness-of-fit test was used to test for normality. Statistical significance of asymmetrical differences within each sex was calculated using the paired t-test for normally distributed variables; paired signed tests were used in cases of non-normality, as this test does not assume symmetry of the two distributions being compared. To test for significant differences between the sexes two sample t-tests were used for normally distributed variables, and two-sample Kolmogorov-Smirnov tests were used in cases of non-normality.

8.1.3 Results

8.1.3.1 Cross-sectional analyses

The results of the contour analysis at each 5% length increment are presented in Table 8-1. Overall, the left clavicle is longer than the right, and the right clavicle is more robust than the left (Figure 8-5). There were no significant differences in the location of the clavicle waist

between the left and right sides. For males, all measurements were significantly different between the left and right clavicle; however, the results of the female analysis were more variable. From 10-55%, all measurements were significantly different between the right and left clavicle except the minimum diameter of the contours. From 80-95%, there was significant asymmetry in all measurements except the maximum diameter of the contours. From these indicators, there appears to be a notable "twist" in the female clavicle near midshaft that is not evident in the male clavicle, where the significantly asymmetrical dimension changes from the maximum diameter at the lateral end to the minimum diameter at the medial end. Typically, the maximum diameter of the lateral end is in the anterior-posterior direction; the medial end is rounder and more variable, but the minimum diameter is often in the anterior-posterior direction.

Error! Reference source not found. Figure 8-6 compares the contours at 10% increments from the left and right clavicle of a typical male and female from this sample. Table 8-2 presents the results of the contour analysis at the muscle attachment sites. Again, males were significantly asymmetric (right-biased) at all locations except the maximum diameter of the contour located at the lateral portion of the trapezius insertion. Although not depicted in this table, both of the ligament attachment sites (conoid and costoclavicular) were significantly right-biased as well. The contour differences at the female muscle attachment sites followed the patterns observed in the cross-section increments. The medial muscle attachments (pectoralis

major and sternocleidomastoid) were more robust on the right side except for the maximum contour diameters.

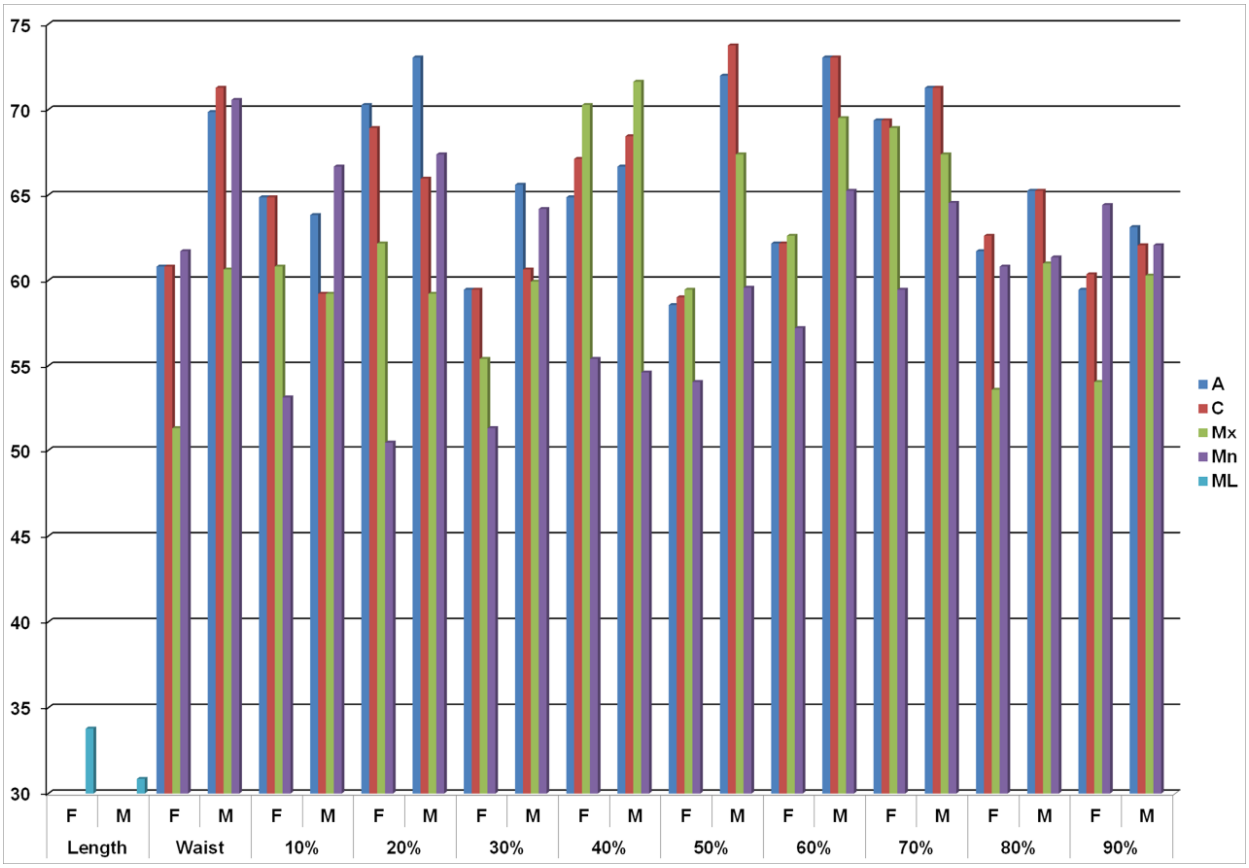


Figure 8-5 Histogram of maximum length and cross-sectional contours at 10% increments and maximum length. Asymmetry is presented as a count variable, where values >50 are right-biased and <50 are left-biased

The midshaft and lateral muscle attachment sites (subclavius, deltoid, and trapezius) were more robust on the right side except for the minimum contour diameters. Although not depicted in the table, the ligament attachments followed the same convention, wherein the contour at the costoclavicular ligament did not register as significant for the maximum diameter and the minimum contour diameter of the conoid ligament registered insignificant as well. Figure 8-7

presents the asymmetry bias in each of the measurements at muscle attachment sites. Figure 8-8 compares the contours at the 20%, 50%, and 80% increments of each muscle attachment site.

Table 8-2 exhibits some of the significant measurements where the standard deviation is greater than the mean value (e.g., waist area was 1.4% greater on the right side in males, but the standard deviation was 3%). This is due to the fact that %DA is a signed value, and because of bias in its calculation, it may not represent the true mean of the population. Using %Bias as a measure of asymmetry avoids this problem.

This is evident by examining both Table 8-2 and Figure 8-7 where some of the areas had values below 50, but in Table 8-2, these values were positive, indicating a non-significant right bias. Table 8-4 shows the measurements at the cross-section contours and the muscle attachment sites in which the magnitude of asymmetry (as reflected by absolute asymmetry) is significantly different between males and females. The magnitude of asymmetry for maximum length is significantly greater in males than in females. However, the remaining significant differences show greater magnitudes of asymmetry in females except for the contours at the deltoid origin and trapezius insertion on the lateral end, where the magnitude of asymmetry is significantly greater in males. Finally, results of the medial axis analysis are shown in Table 8-3. There are no significant differences between the lengths and angles of the segments in males, an indication that curvature asymmetry is minimal. However, females exhibit significant differences in segment angles, indicating curvature differences between the left and right clavicles.

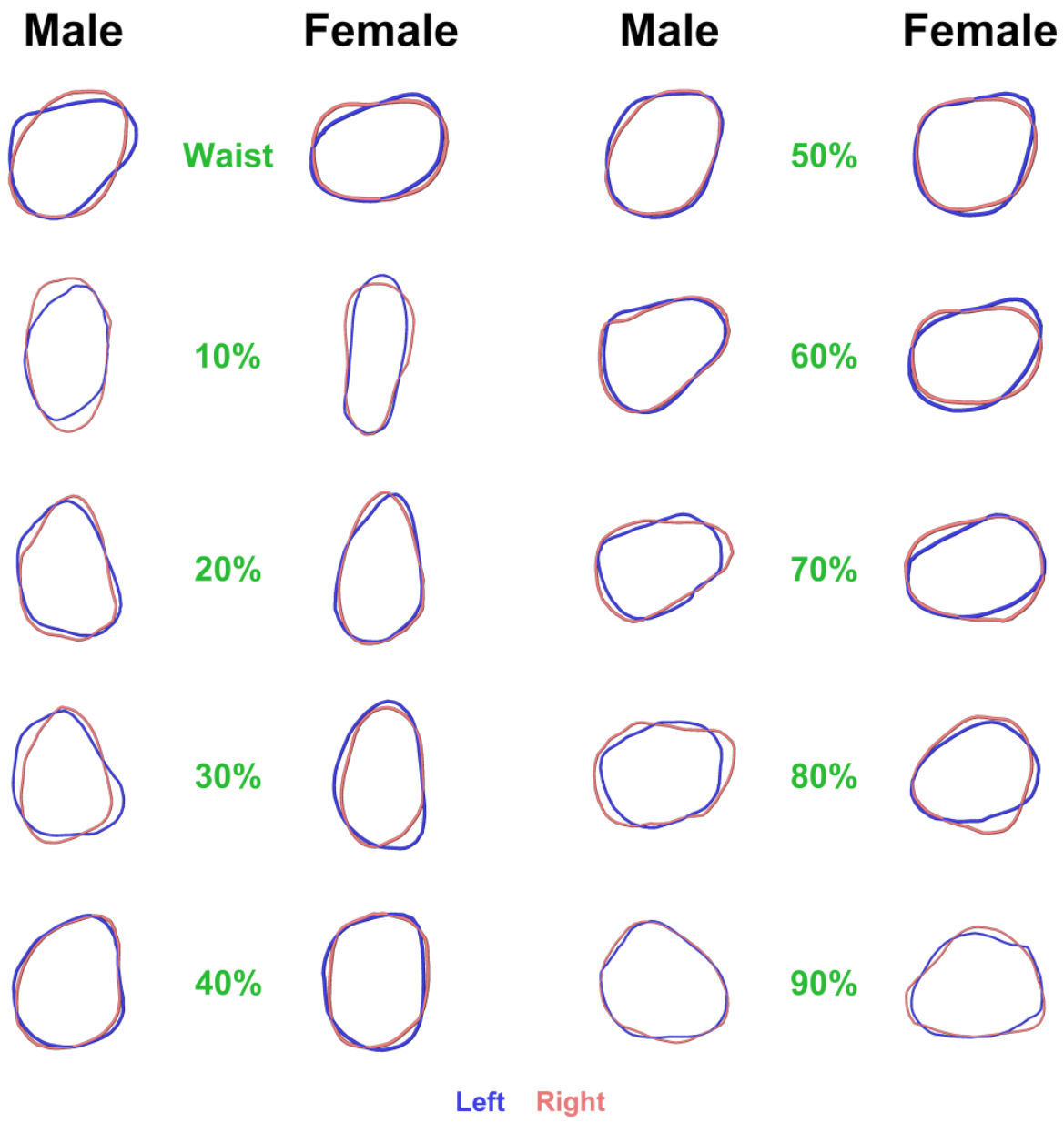


Figure 8-6 Contour differences at 10% increments, where 10% = lateral end and 90% = medial end. The vertical direction is anterior-posterior, and the horizontal direction is superior-inferior

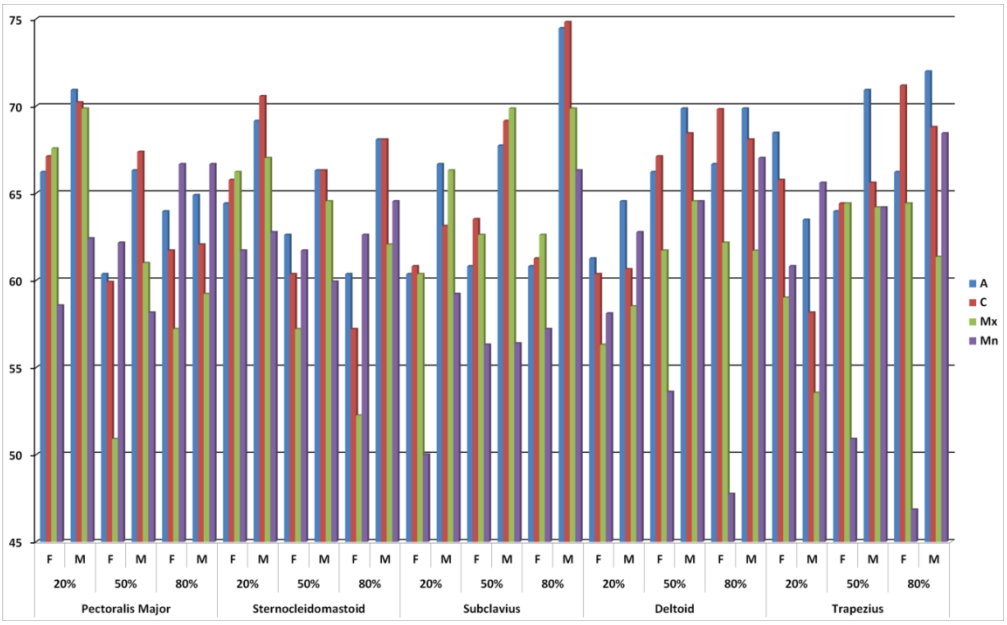


Figure 8-7 Histogram of cross-sectional contours at muscle attachment sites. Asymmetry is presented as a count variable, where values >50 are right-biased and <50 are left-biased. See Table 1 for abbreviations

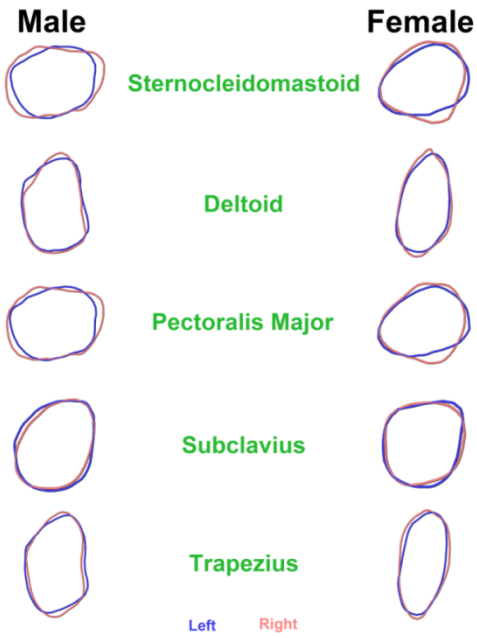


Figure 8-8 Contour differences at muscle attachment sites. The vertical direction is anterior-posterior, and the horizontal direction is superior-inferior

Table 8-1 Contour measurements at each cross-section for males (M) and females (F)

		Waist					10%				20%			
	ML	WP	A	C	Mx	Mn	A	C	Mx	Mn	A	C	Mx	Mn
Mean DA (M)	-0.3	-0.3*	1.4	0.7	0.6	0.8	1.3	0.4	0.4	0.9	1.5	0.5	0.4	1.2
SD DA (M)	0.7	3.6	3.0	1.4	2.6	1.7	3.7	2.5	2.1	2.7	3.0	1.5	2.0	2.9
AA Mean (M)	0.6	-2.7*	2.6	1.3	2.1	1.5	3.1	1.7	1.7	2.2	2.6	1.3	1.6	2.4
SD AA (M)	0.5	2.5	2.1	1.0	1.7	1.2	2.4	1.8	1.4	1.8	2.1	1.0	1.3	2.1
Mean DA (F)	-0.2	-0.2*	0.6	0.4	0.1*	0.5	1.4	0.8	0.6	0.4*	1.1	0.6	0.7	0.3*
SD DA (F)	0.6	4.1	3.4	1.6	2.8	1.9	3.6	2.2	1.9	3.3	3.0	1.5	2.0	2.9
AA Mean (F)	0.5	-3.0*	2.8	1.4	2.3*	1.6	2.7	1.5	1.5	2.4*	2.4	1.3	1.6	2.2*
AA SD (F)	0.4	2.8	2.0	1.0	1.7	1.1	2.7	1.8	1.3	2.3	2.0	1.0	1.3	1.9
			30%				40%				50%			
Mean DA (M)			1.0	0.4	0.5	0.7	1.2	0.6	0.8	0.4	1.4	0.7	0.8	0.6
SD DA (M)			3.2	1.6	2.0	2.8	3.2	1.5	1.7	2.5	3.2	1.6	1.7	2.5
AA Mean (M)			2.5	1.3	1.6	2.1	2.5	1.3	1.5	1.9	2.7	1.3	1.4	2.0
AA SD (M)			2.3	1.1	1.3	1.9	2.2	1.1	1.1	1.7	2.3	1.1	1.2	1.6
Mean DA (F)			0.6	0.3	0.4	0.0*	0.8	0.5	0.6	0.2*	0.5	0.2	0.3	0.2*
SD DA (F)			3.3	1.7	2.1	3.1	3.5	1.6	1.6	3.0	3.9	1.9	2.0	3.0
AA Mean (F)			2.5	1.3	1.7	2.3*	2.8	1.3	1.4	2.3*	3.0	1.4	1.5	2.3*
AA SD (F)			2.2	1.1	1.4	2.1	2.2	1.0	1.0	1.9	2.5	1.3	1.4	2.0
			60%				70%				75%			
Mean DA (M)			1.6	0.8	0.8	0.8	1.5	0.8	0.9	0.7	1.4	0.7	0.7	0.7
SD DA (M)			3.0	1.5	1.8	2.3	2.7	1.4	1.8	2.1	3.0	1.6	2.1	2.1
AA Mean (M)			2.6	1.3	1.5	1.9	2.4	1.2	1.6	1.7	2.4	1.3	1.7	1.7
AA SD (M)			2.2	1.1	1.3	1.5	2.0	1.0	1.3	1.5	2.4	1.3	1.7	1.7
Mean DA (F)			0.8	0.4	0.5	0.3*	1.3	0.6	0.9	0.5	1.1	0.5	0.6	0.6
SD DA (F)			3.5	1.8	2.1	2.4	3.2	1.9	2.0	2.4	3.6	1.9	2.4	2.7
AA Mean (F)			2.8	1.4	1.6	1.8*	2.8	1.5	1.8	1.8	2.9	1.5	1.9	2.1
SD AA (F)			2.3	1.2	1.4	1.6	2.1	1.3	1.3	1.6	2.4	1.3	1.6	1.8
			80%				85%				90%			
Mean DA (M)			1.3	0.7	0.6	0.6	1.4	0.7	0.7	0.7	1.0	0.5	0.3	0.6
SD DA (M)			3.4	1.9	2.6	2.3	3.3	1.9	2.5	2.3	3.3	1.8	2.3	2.2
AA Mean (M)			2.7	1.5	2.0	1.9	2.8	1.5	2.0	1.8	2.7	1.5	1.9	1.7
SD AA (M)			2.4	1.3	1.7	1.5	2.3	1.3	1.7	1.6	2.2	1.2	1.5	1.5
Mean DA (F)			0.7	0.4	0.1*	0.6	0.8	0.4*	0.1	0.8	0.9	0.4	0.3*	0.7
SD DA (F)			3.7	2.3	2.5	2.6	3.8	2.5	2.5	2.5	3.6	2.6	3.3	2.3
AA Mean (F)			2.8	1.6	1.9*	2.0	2.9	1.7*	1.9	2.0	2.8	1.7	2.1*	1.9
SD AA (F)			2.5	1.6	1.6	1.7	2.7	1.9	1.6	1.7	2.4	1.9	2.5	1.6

* Insignificant asymmetry differences (p>.05)

Table 8-2 Asymmetry of contour measurements at each muscle attachment site for males (M) and females (F). See Table 1 for abbreviations

	20%				50%				80%			
	A	C	Mx	Mn	A	C	Mx	Mn	A	C	Mx	Mn
Pectoralis Major												
Mean DA (M)	1.5	0.8	0.9	0.7	1.3	0.7	0.7	0.7	1.4	0.7	0.6	0.9
SD DA (M)	2.8	1.4	1.8	2.2	3.6	2.0	2.6	2.4	4.7	2.5	2.9	2.8
AA Mean (M)	2.4	1.2	1.6	1.8	2.9	1.6	2.1	1.9	3.7	2.0	2.2	2.2
SD AA (M)	2.1	1.1	1.3	1.5	2.6	1.4	1.8	1.6	3.3	1.7	1.9	2.0
Mean DA (F)	1.3	0.6	0.8	0.5	0.8	0.4	0.1*	0.6	1.3	0.6	0.4*	0.9
SD DA (F)	3.2	1.9	1.9	2.4	3.9	2.3	2.5	2.7	4.5	2.7	3.0	2.8
AA Mean (F)	2.7	1.5	1.8	1.9	2.9	1.6	1.9*	2.1	3.6	2.1	2.3*	2.2
SD AA (F)	2.1	1.3	1.2	1.6	2.7	1.6	1.7	1.8	3.1	1.9	1.9	2.0
Sternocleidomastoid												
Mean DA (M)	1.4	0.7	0.8	0.7	1.3	0.7	0.7	0.7	1.5	0.8	0.7	0.8
SD DA (M)	2.9	1.5	1.9	2.2	3.5	1.9	2.4	2.4	3.8	2.1	2.7	2.5
AA Mean (M)	2.4	1.2	1.6	1.8	2.7	1.5	1.9	**1.9**	3.2	1.7	2.2	2.0
SD AA (M)	2.2	1.2	1.3	1.4	2.5	1.4	1.7	1.6	2.7	1.5	1.8	1.6
Mean DA (F)	1.3	0.7	0.8	0.5	0.9	0.4	0.3	0.5	0.9	0.4	0.1*	0.8
SD DA (F)	3.2	1.8	2.1	2.5	3.7	2.1	2.5	2.7	4.1	2.5	2.7	2.6
AA Mean (F)	2.7	1.4	1.8	1.9	2.9	1.6	1.9	2.1	3.1	1.8	2.0*	2.0
SD AA (F)	2.2	1.3	1.3	1.6	2.5	1.5	1.6	1.7	2.8	1.9	1.8	1.8
Subclavius												
Mean DA (M)	1.1	0.5	0.7	0.5	1.3	0.7	0.8	0.5	1.6	0.8	0.8	0.8
SD DA (M)	3.5	1.9	2.2	2.8	3.2	1.6	1.7	2.5	3.0	1.5	1.8	2.3
AA Mean (M)	2.7	1.5	1.8	2.0	2.7	1.3	1.5	1.9	2.6	1.3	1.5	1.9
SD AA (M)	2.4	1.2	1.4	2.0	2.2	1.1	1.2	1.7	2.2	1.1	1.3	1.5
Mean DA (F)	0.6	0.3	0.5	0.1*	0.7	0.4	0.4	0.3*	0.8	0.4	0.5	0.2
SD DA (F)	3.5	2.0	2.3	3.1	3.9	1.9	1.9	3.2	3.4	1.7	2.0	2.4
AA Mean (F)	2.7	1.5	1.8	2.3*	3.1	1.5	1.4	2.4*	2.7	1.4	1.6	1.9
SD AA (F)	2.3	1.3	1.5	2.0	2.5	1.3	1.3	2.0	2.2	1.1	1.3	1.6
Deltoid												
Mean DA (M)	1.6	0.6	0.6	1.0	1.8	0.8	0.7	1.1	1.5	0.6	0.5	1.2
SD DA (M)	5.0	2.8	2.8	3.3	3.9	2.2	2.7	3.1	2.9	1.5	2.1	2.9
AA Mean (M)	4.1	2.1	2.1	2.6	3.4	1.8	2.2	2.4	2.5	1.3	1.7	2.4
SD AA (M)	3.1	1.9	1.9	2.1	2.7	1.5	1.8	2.2	2.1	1.0	1.3	2.1
Mean DA (F)	1.5	0.7	0.6	0.6	1.2	0.7	0.8	0.2*	1.1	0.6	0.7	0.1*
SD DA (F)	4.1	2.3	2.5	3.3	3.4	1.9	2.5	3.0	3.0	1.6	2.2	3.1
AA Mean (F)	3.4	1.7	1.9	2.5	2.9	1.5	2.0	2.4*	2.5	1.3	1.8	2.4*
SD AA (F)	2.8	1.6	1.7	2.1	2.2	1.3	1.7	1.9	2.0	1.1	1.5	1.9
Trapezius												
Mean DA (M)	1.4	0.4	0.2	1.5	1.9	0.9	0.9	1.0	1.5	0.6	0.5	1.2
SD DA (M)	4.5	2.7	2.6	3.7	4.2	2.4	2.6	2.9	2.9	1.5	2.1	3.0
AA Mean (M)	3.5	2.0	2.0	3.0	3.6	1.9	2.2	2.3	2.5	1.3	1.7	2.4
SD AA (M)	3.1	1.9	1.8	2.6	2.8	1.6	1.7	2.1	2.1	1.0	1.4	2.1
Mean DA (F)	1.7	0.7	0.5	1.1	1.3	0.8	0.8	0.2*	1.1	0.6	0.7	0.2*
SD DA (F)	4.3	2.6	2.6	3.5	3.6	2.2	2.4	2.9	2.9	1.5	2.1	3.0
AA Mean (F)	3.3	1.8	1.9	2.6	2.9	1.6	1.9	2.3*	2.4	1.3	1.7	2.4*
SD AA (F)	3.3	2.1	1.9	2.6	2.4	1.6	1.7	1.7	2.0	1.1	1.5	1.9

Insignificant asymmetry differences ($p>.05$).

Table 8-3 Mean, standard deviation, and p-value for average medial axis angle and length asymmetry

	Females	Males
Mean Angle Difference	3.22	3.86
SD Angle Difference	1.37	1.67
Mean Length Difference	0.39	0.43
SD Length Difference	0.23	0.22
Paired Test Angle p-value	0.01	0.36
Paired Test Length p-value	0.4	0.14

Table 8-4 Significant differences between males and females in absolute asymmetry

		Female			Male	
		Mean	**SD**	**p-value**	**Mean**	**SD**
	Max Length	0.47	0.40	0.02	0.59	0.54
Cross-Sections	**45% A**	2.97	2.36	0.02	2.61	2.20
	45% Min	2.41	2.01	0.01	1.95	1.71
	50% Min	2.29	1.96	0.03	1.96	1.62
	65% C	1.44	1.10	0.01	1.20	1.02
	65% Max	1.69	1.27	0.03	1.49	1.25
	70% A	2.76	2.13	0.01	2.37	2.01
	70% A	1.52	1.33	<0.01	1.20	1.04
	90% Min	1.86	1.55	0.03	1.65	1.53
Deltoid	**20% A**	3.39	2.79	0.01	4.14	3.15
	20% C	1.73	1.60	0.01	2.12	1.93
Pectoralis Major	**20% A**	2.69	2.15	0.03	2.38	2.09
	20% C	1.46	1.34	0.01	1.21	1.10
Subclavius	**50% A**	3.10	2.47	0.01	2.66	2.22
	50% Min	2.43	2.05	0.01	1.94	1.70
Trapezius	**50% A**	2.91	2.45	<0.01	3.56	2.84
	50% C	1.61	1.64	0.01	1.92	1.60
Sternocleidomastoid	**20% A**	2.70	2.23	0.01	2.43	2.19

8.1.3.2 3D surface analysis

Figure 8-9 in supporting information offers a visualization of the morphological differences between a left and right clavicle from an individual male and female in this study sample. The un-normalized and normalized distance maps are shown in supporting information FigureFigure 8-10 and, Figure 8-11 respectively. These maps show the average distance between homologous points on the left and right clavicles for the entire population. In this study an average RMS error of 0.01 mm was achieved for all bones as shown in supporting information Table 8-5. The un-normalized distance map shown in supporting information Figure 8-10 reflects primarily size differences. The greatest differences in this figure are in the maximum length, as reflected by the hotspots on the ends of the bone. The muscle attachment sites on the lateral end of the clavicle also show up (primarily the deltoid origin), but to a lesser extent than maximum length. The normalized distance map (Figure 8-11) reflects primarily shape differences. For males, the greatest asymmetry is at the medial end on the inferior portion of the bone in the area of the costoclavicular ligament. For females, the greatest differences are at the lateral end (deltoid origin and trapezius insertion). Additionally, an area in the midshaft registers for both sexes, although more so in males; the implications of this area will be discussed in the conclusions.

Table 8-5 RMS, mean, and standard deviation for the 3D normalized and un-normalized surface analysis

	Un-normalized					Normalized				
	RMS	Ave	SD	Max	Min	RMS	Ave	SD	Max	Min
Mean (M)	0.14	0.11	0.09	0.59	<0.0001	0.13	0.10	0.08	0.58	<0.0001
SD (M)	0.04	0.03	0.03	0.18	<0.0001	0.04	0.03	0.02	0.20	<0.0001
Mean (F)	0.11	0.09	0.07	0.46	<0.0001	0.11	0.09	0.07	0.53	<0.0001
SD (F)	0.04	0.03	0.02	0.17	<0.0001	0.04	0.03	0.03	0.31	<0.0001

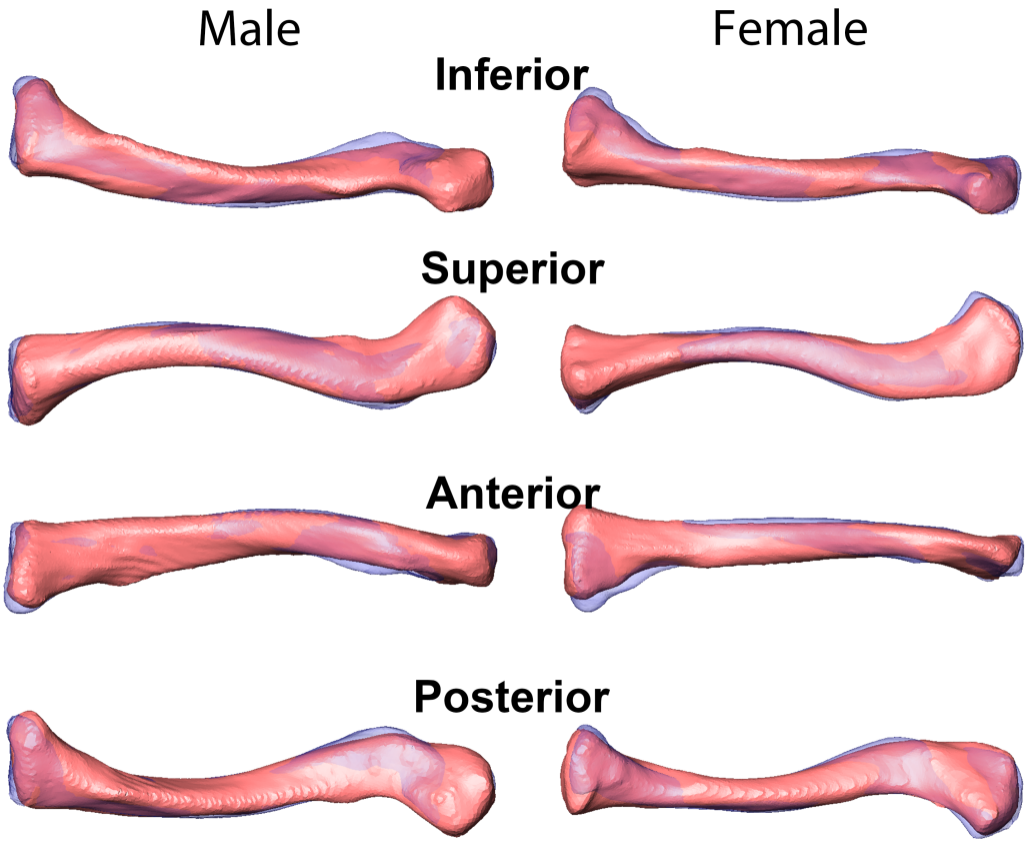


Figure 8-9 . Morphological differences between a left and right clavicle from an individual male and female in this study sample (pink=right, blue=left)

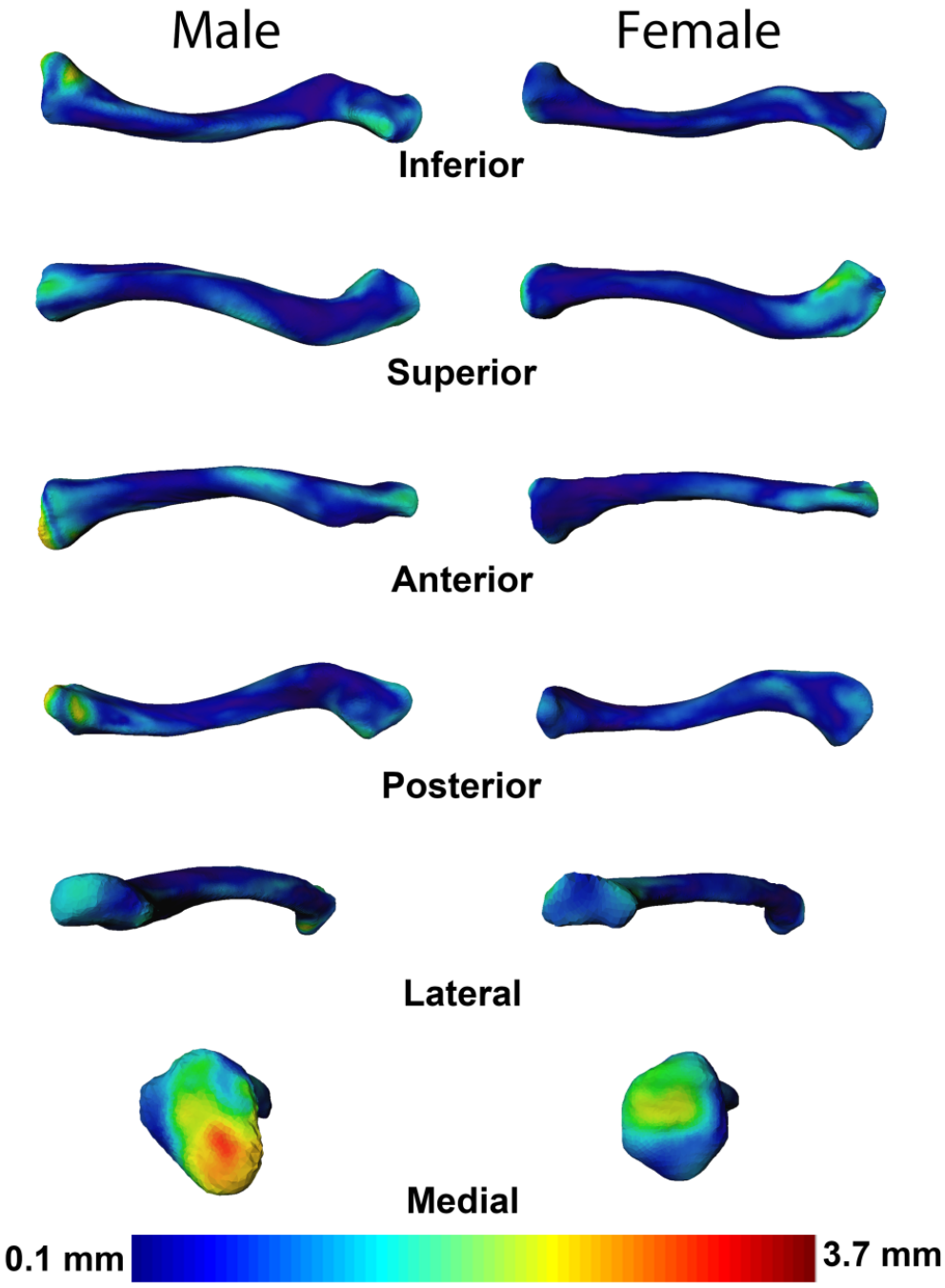


Figure 8-10 Un-normalized distance map showing the average distance between homologous points on the left and right clavicles for the entire population

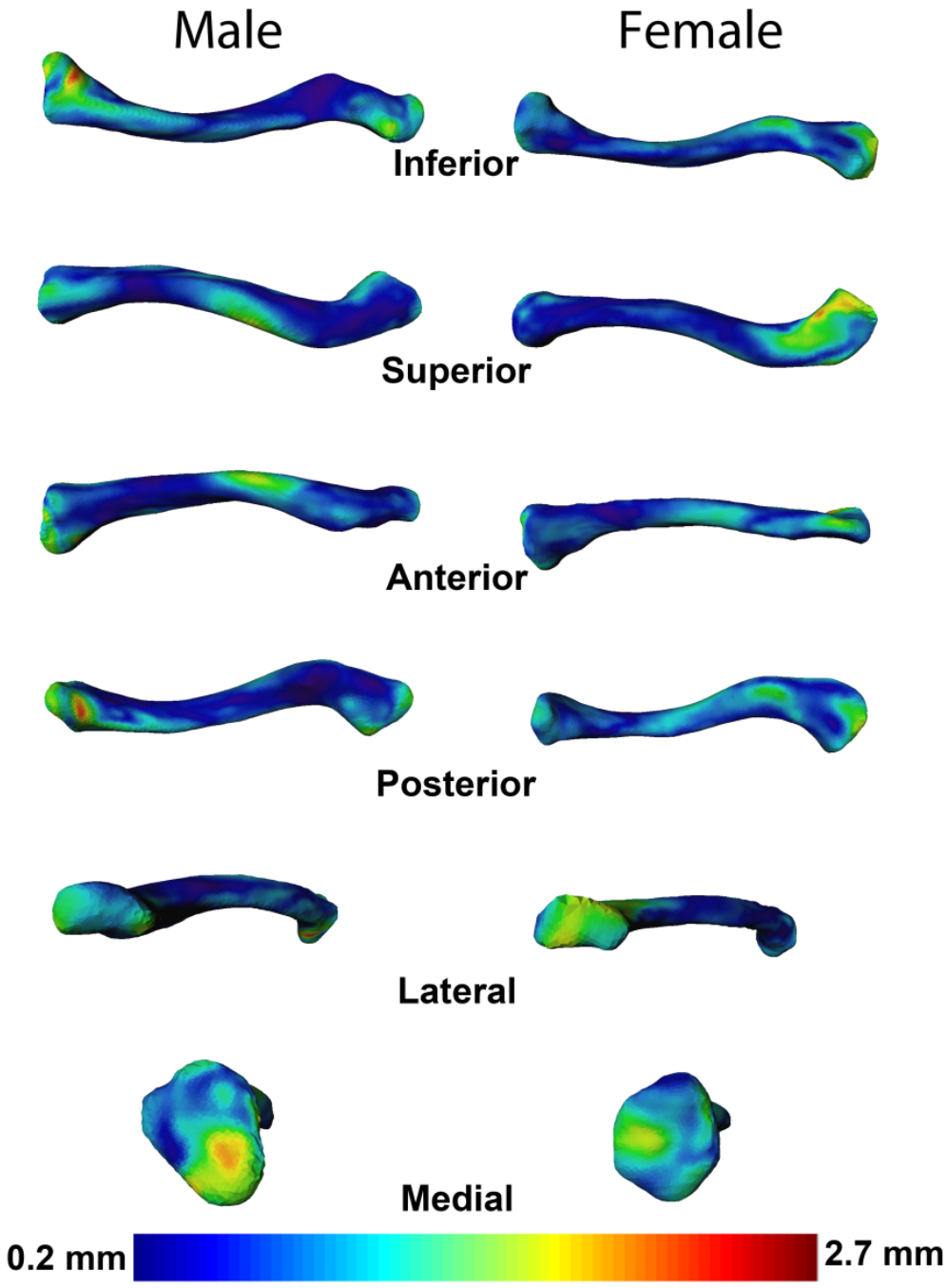


Figure 8-11 Normalized distance map showing the average distance between homologous points on the left and right clavicles for the entire population

Figure 8-12 presents the surface map showing the significant differences between the left and right clavicles based on the p-values from paired sign tests. The paired sign test was used to compare the distance between every point on a mean model and each corresponding point on the left and right models across the entire population. The most significant differences for both sexes (shown in blue) are in the lateral end (superior surface), midshaft (inferior surface), and medial end (anterior surface). The majority of these areas are muscle attachment sites (Figure 8-13). In Figure 8-13, the p-values were thresholded so that p-values >0.1 are red and p<0.1 are blue. In addition, the muscle attachment sites were superimposed onto the model to show the location of the areas of significant asymmetry in relation to these sites. The attachment sites that register as significant areas of asymmetry are pectoralis major and deltoid (anteriorly) and subclavius (inferiorly). As shown in the normalized distance maps, there is an area on the posterior midshaft that registers highly significant and, in males, a small area on the medial end. The former will be discussed below, and the latter is the attachment site for the costoclavicular ligament.

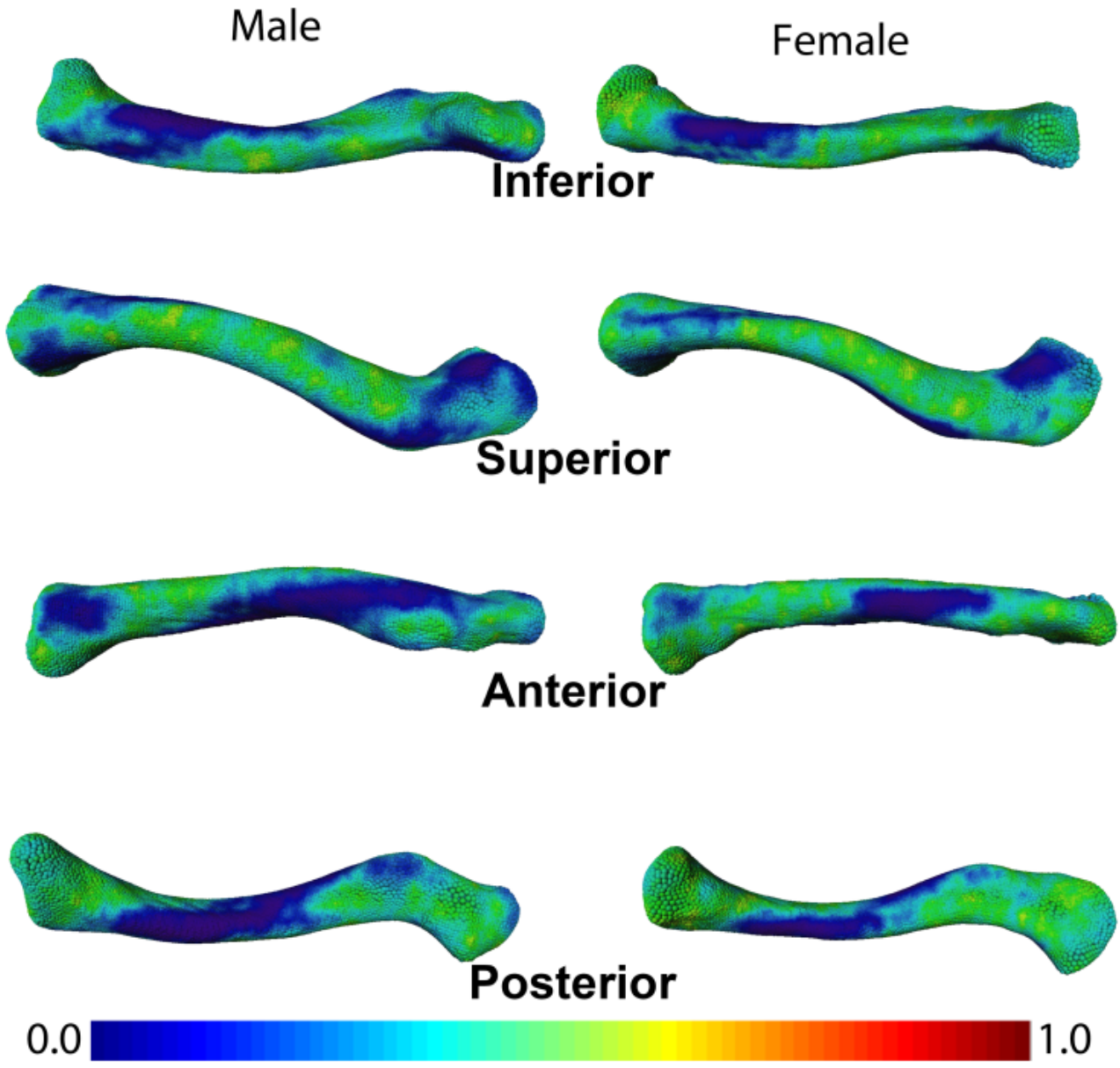


Figure 8-12 Surface map showing significant differences between the left and right clavicles based on the p-values from paired sign tests

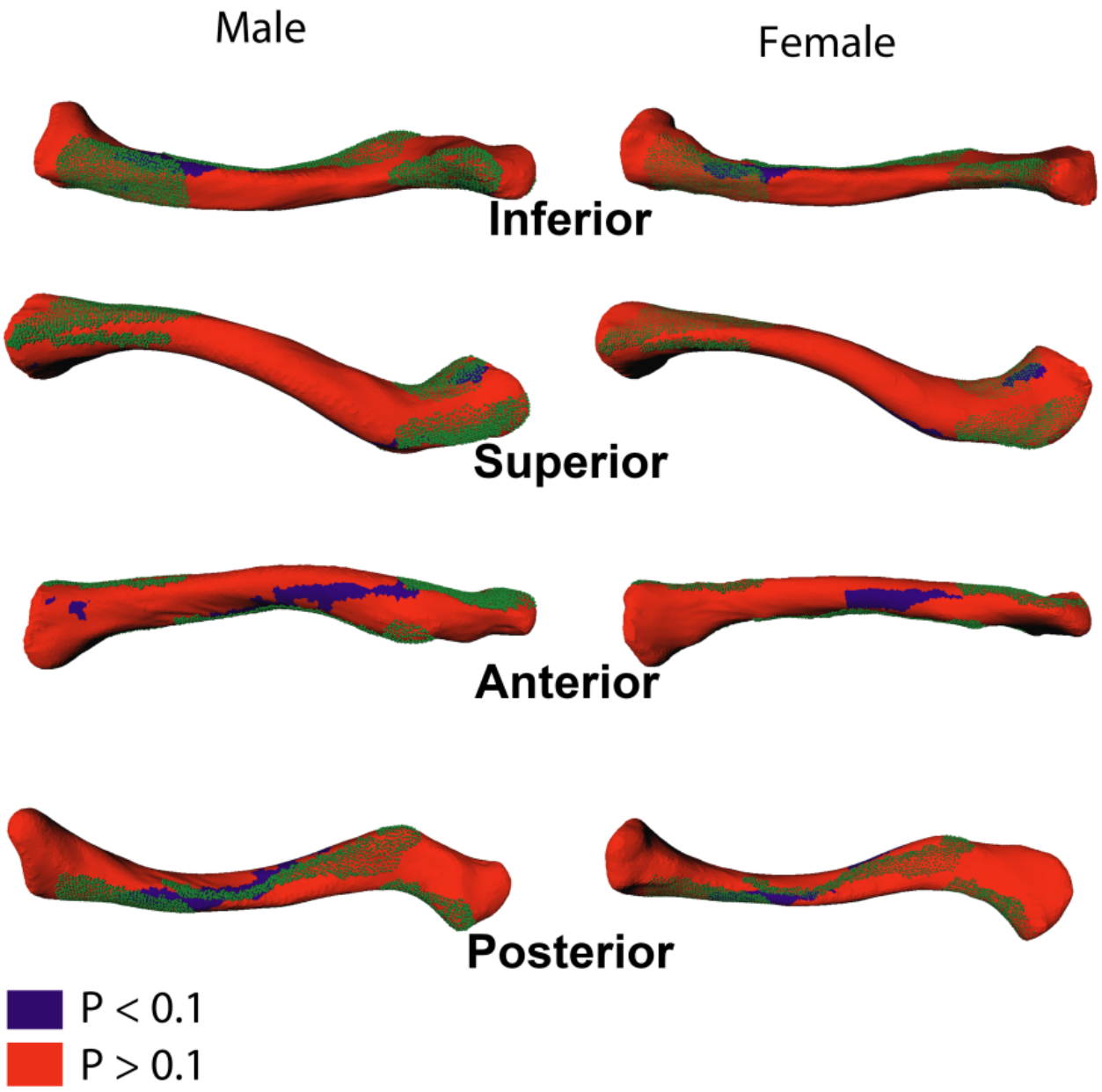


Figure 8-13 Surface map of thresholded p-values (p>0.1=red and p<0.1=blue) with superimposed muscle attachment sites (green)

9. RECONSTRUCTION OF PARTIAL OR DEFORMED ANATOMY

9.1 Introduction

Reconstruction of partial or deformed anatomy is a crucial task in many fields, including medicine, forensic anthology, paleoanthropology, and bioarcheology [203]. In forensics, the main task for forensic anthropologists is the creation of biological profiles from uncovered remains. The four primary components of the biological profile are age, sex, ancestry, and stature. This task is challenging in situations where there are only fragmentary remains, or in cases of mass disaster or commingled remains. These circumstances can be more complicated and challenging due to the presence of multiple elements from different individuals. Recent work on commingled human remains by Adams and Byrd [204] attempts to provide a series of case examples and studies of methods to address commingled remains in forensic contexts. In 2011, the Scientific Working Group for Anthropology (SWGANTH) approved draft guidelines for resolving commingled human remains. Key points of the SWGANTH guidelines target the determination of the minimum number of individuals (MNI), the assessment of the most likely number of individuals (MLNI or the Lincoln Index), and the use of scientific methods to achieve these goals. The guidelines recommend element reconstruction, visual pair matching, osteometric evaluation, and taphonomic comparisons in the assessment of MNI and the MLNI. Recent work by Herrmann [205] quantifies small fragmented remains into an Osteological Information System (OIS) using Geographic Information System (GIS) software to compute the

minimum number of elements (MNE) and MNI estimates. However, these systems are time consuming and dependent upon the observer to manually digitize each fragment into the OIS application.

In paleoanthropology and bio archeology, the use of computers for virtually reconstructing fragmentary remains is widely used [206-210], especially on the cranium [211]. Recently, Sylvester, et al. utilized statistical atlas of the femora to reconstruct AL288-1 ("Lucy") femur; the results proved to be close approximations of original reconstructions [212]. Virtual reconstruction has also opened the door to perform comparative analysis on hominid fossils by reconstructing distorted and fragmentary fossils [206, 209, 213].

In medicine, bone reconstruction is an essential task in cases where bone loss is present, due to tumors, abnormalities or trauma, especially in mandibular defects [214-216]. Bone reconstruction is also crucial in cases of pelvis defects, especially in case of pelvic discontinuity, a distinct case of bone loss associated with total hip arthroplasty (THA), where the superior aspect of the pelvis is separated from the inferior aspect [217] as shown in Figure 9-1. This complication can be seen in cases of osteolysis, infection or acute fracture [218]. Osteolysis is a caused by inflammatory reaction against particles of polyethylene over time [219]. These particles are generated as the polyethylene lining of the acetabular cup component wears. The reaction is triggered as the intra-capsular pressure forces the debris generated by wear to migrates down the medullary canal between bone-cement (or press fit interface).

Analysis in this chapter will focus on the use of SSM as a tool for reconstruction of full bone from partial anatomy. Analysis is focused on pelvis, although it can be generalized to any other bones.

9.2 Methods

The sample for this analysis is a subset of documented innominate from people with 20th century birth years from the William M. Bass Donated Skeletal Collection at the University of Tennessee's Department of Anthropology (n=94, 33 females and 61 males). The majority of the collection consists of American white individuals, and were the focus of this research. The bones were packed into foam-padded boxes and CT scanned using 0.625 x 0.625 x 0.625-mm cubic voxels. The DICOM images acquired from the CT scans were then manually segmented, and surface models were generated.

Segmented innominate were then added to the statistical atlas. In order to accurately assess the ability of SSM to reconstruct missing anatomy from partial information, the SSM was constructed using the leave-one-out method. For each output model from the atlas, this model was excluded from the training set and the remaining bones were used to create the SSM.

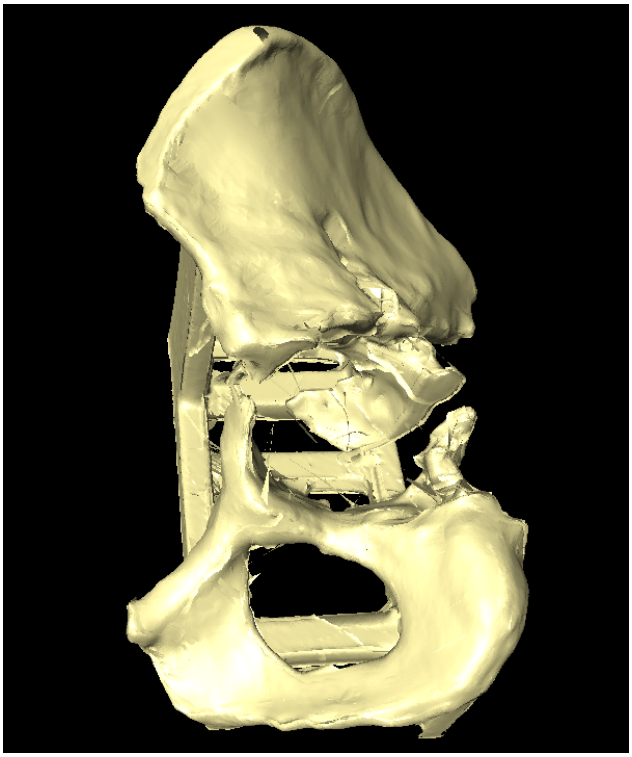


Figure 9-1 An example of pelvis discontinuity

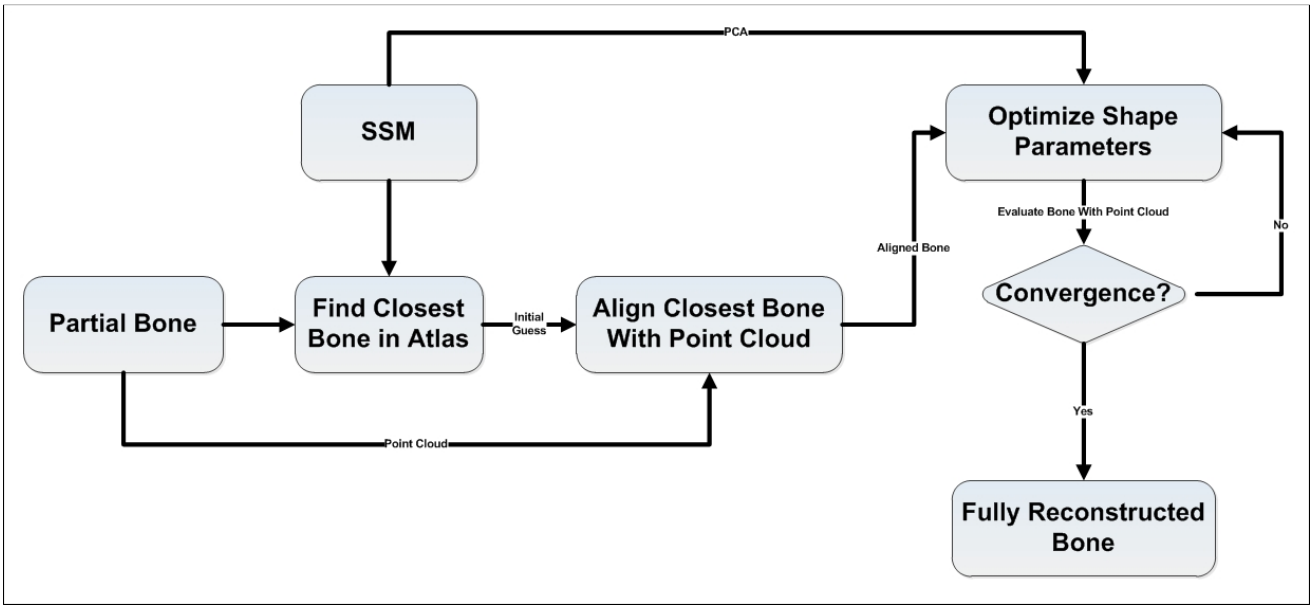


Figure 9-2 Process of reconstructing full bone from partial anatomy

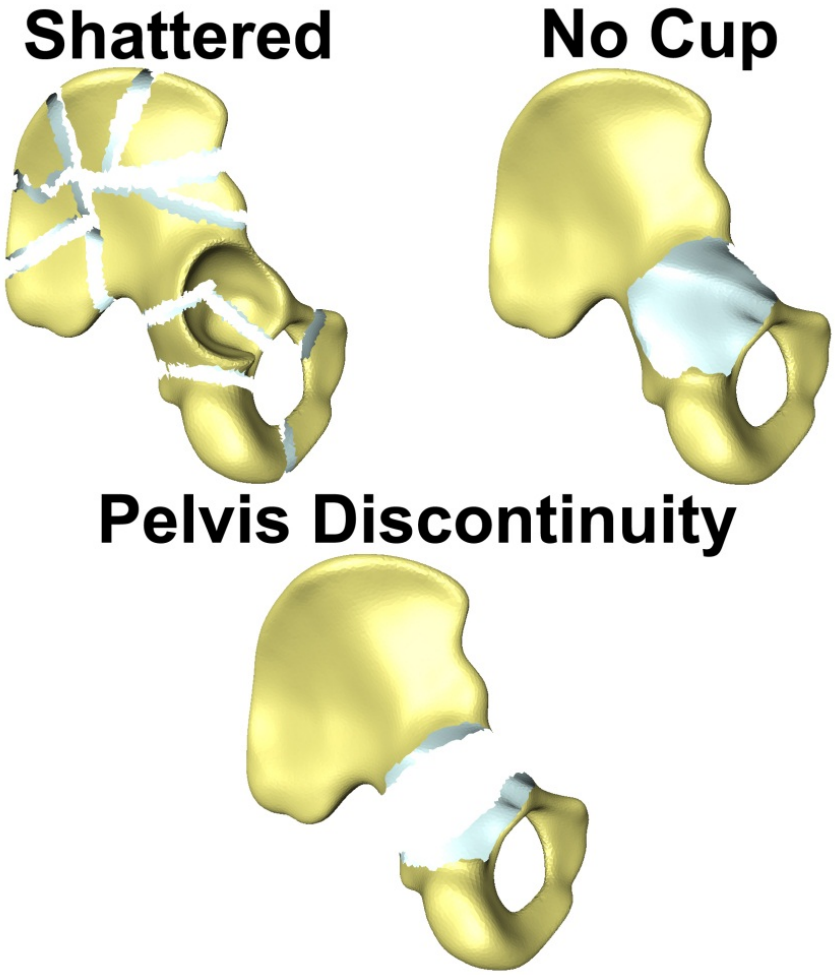


Figure 9-3 Simulating three different types of complexities

9.3 Results

Table 9-1 Descriptive statistics for the RMS error between reconstructed and original model in mm

	RMS	STD	Max
Shattered	0.54	0.35	2.91
No Cup	0.60	0.40	3.20
Discontinuity	0.61	0.41	3.29

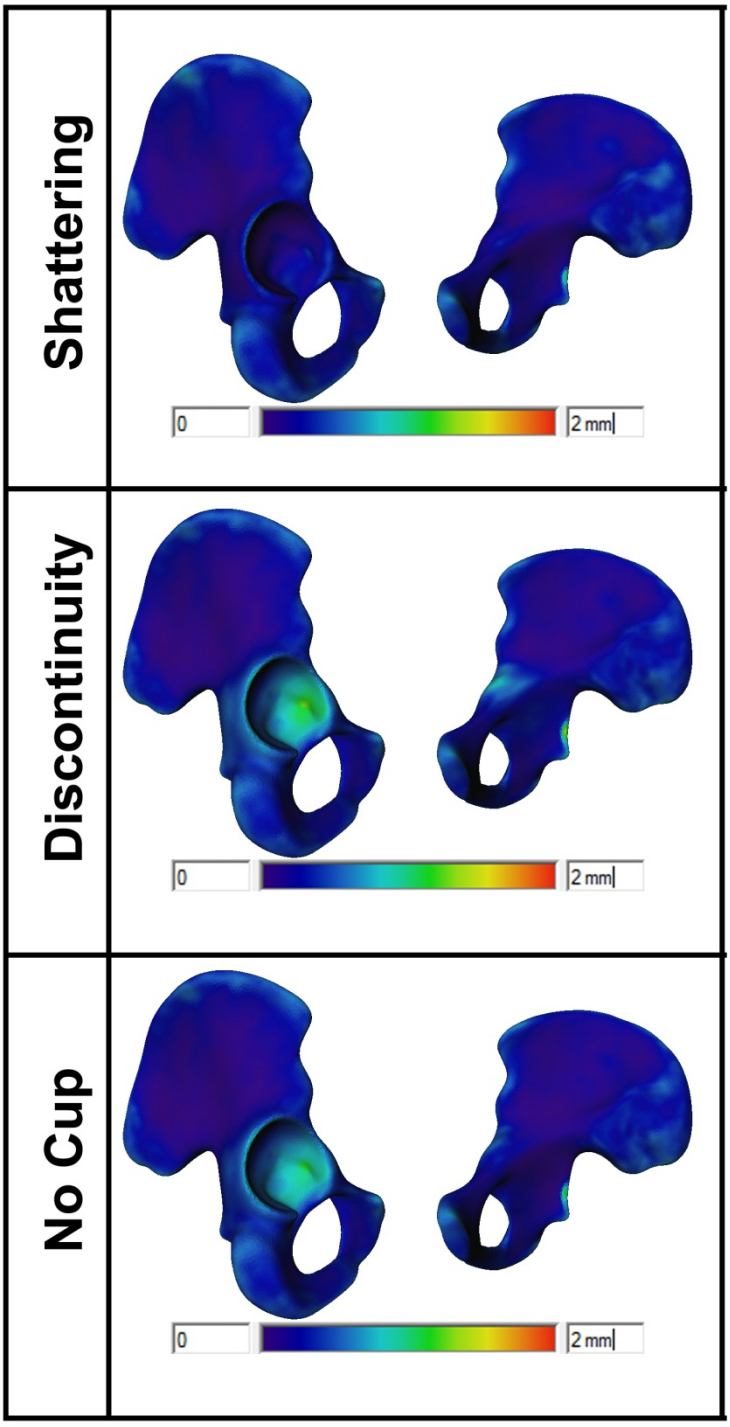


Figure 9-4 Average RMS distance map between reconstructed surface and original surface for the three complexities

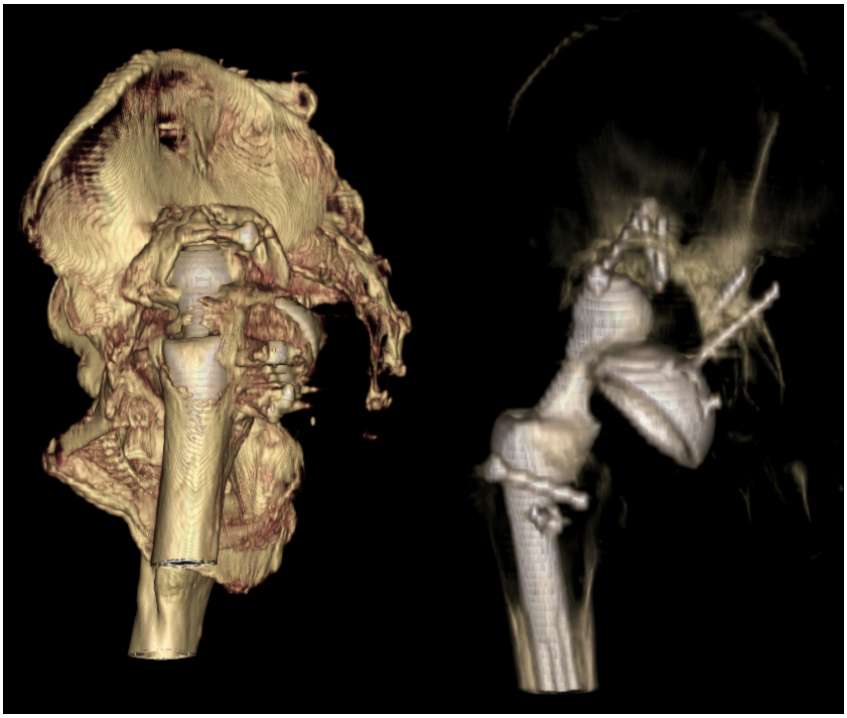


Figure 9-5 Volume render for real test patient with pelvis discontinuity

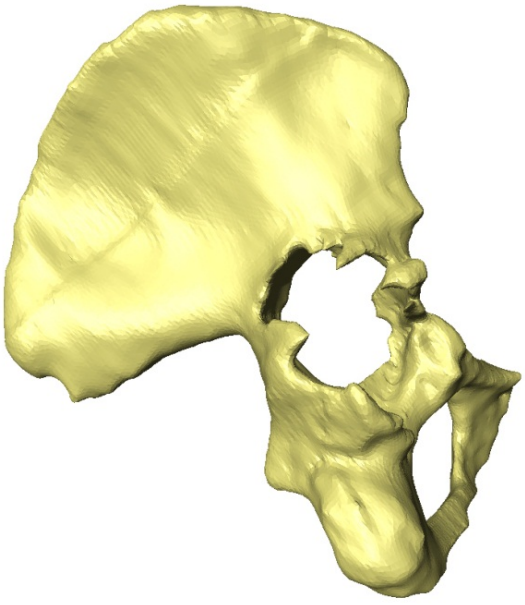


Figure 9-6 surface model for real test patient with pelvis discontinuity

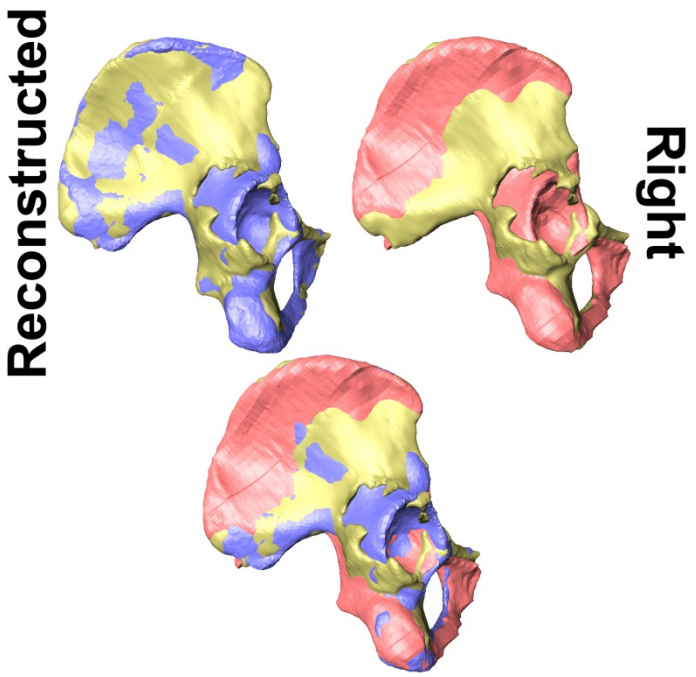


Figure 9-7 Real bone (yellow) vs. reconstructed bone (purple) and right innominate flipped

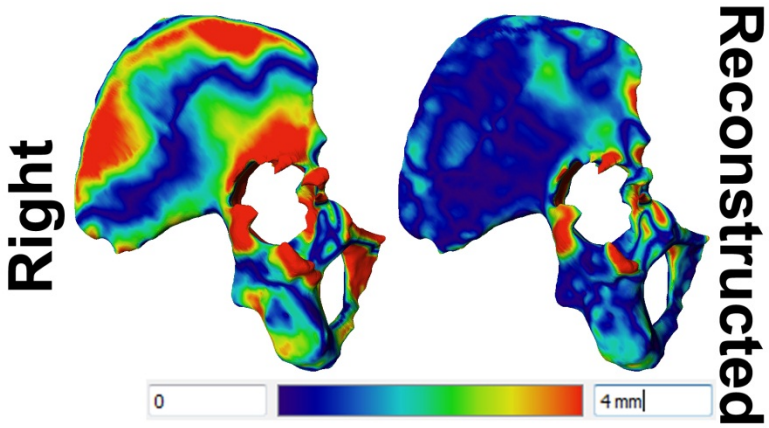


Figure 9-8 Distance map showing different between real anatomy vs. Right bone and vs. reconstructed bone

10. KINEMATIC ANALYSIS

10.1 Lumbar

The analysis in this section was funded by National Institute of Health grant number 5R01AR55882-05 entitled "Innovative Tools for in vivo Computational Prediction of Lumbar Stresses."

10.1.1 Introduction

The lumbar spine, along with the more superior spinal column, forms a complex arrangement of articulating joints which serve as the main load-bearing structure for the human musculoskeletal system. When healthy, the well-functioning lumbar architecture is capable of motion about all six degrees of freedom, permitting axial compression, flexion and extension, lateral bending and rotation, all while providing protection for delicate neural elements. Helping to facilitate these functional and protective roles is its rigid construction combined with the viscoelastic nature of the spinous ligaments and intervertebral discs coupled with the stabilizing properties imparted by the vast network of overlapping musculature. In concert, these structures help reduce impact magnitudes while increasing impact times, thereby contributing to the lumbar spine's remarkable ability to endure tremendous loads. However, when the lumbar spine is exposed to traumatic loads which occur suddenly and with large force magnitudes, the load-bearing capacities in the discs, facet joints, and soft tissue structures may begin to fail. As these occur, instances of low back pain and/or changes in the

biomechanical properties, morphologies, and dynamic characteristics of the entire lumbar spine can result, hampering the spine's function and capacity to maintain mechanical stability.

Degenerative disc disease is a large problem in the spine and while it is not the only cause, limiting or reversing the degeneration is a goal. Diagnosis of degenerative disc disease reveals disc space narrowing to be an indicator for pain [220]. This narrows the space between adjacent segments and increases the loading of the facet joint causing impingement [221]. This loss of height has been shown in multiple studies to greatly influence the kinematics.

Disc spacing is typically diagnosed using MRI in a static supine position. Research has been conducted on spinal segments using finite element analysis, and although disc space measurement is not the final outcome from this technique, stress is closely related to alteration of disc height [222]. This technique will allow for motion of the soft tissues, disc, and bones in all degrees of freedom, and models are created from CT scans taken in the supine position. This generated model has various forces applied to create the required motion from an in vitro study.

Many in vitro studies have been performed with the use of cadaveric data where the motion is simulated using a generic motion pattern and does not allow for altered motion due to pain or muscular contraction [223, 224]. Sharma, et al. studied the effect of ligament and facet (total and partial) removal and their geometry on stability of lumbar segments. The study concluded that ligaments play an important role in resisting flexion rotation and posterior

shear, whereas facets are mainly responsible for preventing large extension rotation and anterior displacement [225].

While both static and dynamic measurements can be used to analyze the disc and facets, both have limitations, one of which stems from being generated in the supine position. The use of fluoroscopy provides a non-invasive method for analyzing lumbar motion during dynamic, weight-bearing activities, and it has been proven to be a safe and effective method. Cheng, et al.[226] and Liu, et al. [227, 228] successfully utilized a 2D-to-3D registration technique with fluoroscopic video to acquire comparably accurate results without the need of markers. Using this approach, they were able to determine the 3D in vivo kinetic data in patients in an outpatient clinical setting. Likewise, they were able to calculate and compare the 3D in vivo kinetics of normal, degenerative and fused cervical spines of patients to see if surgical intervention is associated with differences in the forces generated at various levels of the spine.

On the other hand, studying morphometry of the lumbar is important from both surgical [229-232] and diagnostic [233, 234] perspectives. Most of these studies were either conducted on 2D x-rays, which do not capture the true 3D geometry, or CT slices where measurements are limited to the direction of the scan. Current literature lacks studies that utilize automated landmarking and study of the morphometry of lumbar in a full 3D sense. Employing these methods can aid in removing any intra-observer bias from manual landmarking, in addition to revealing more hidden information from true 3D analysis..

The purpose of this analysis is to utilize the statistical atlas and framework of landmark automation to investigate the relationship between disc spacing and ligament length and the affects they have on the stability of lumbar kinematics.

10.1.2 Methods

Forty-four volunteers participated in this study, all of whom were recruited from patients and staff at Vanderbilt University and the University of Tennessee. All participants in this study signed an informed consent form approved by the University of Tennessee's Institutional Review Board (IRB #7393B). Three groups consisting of ten subjects each were defined as healthy, healthy with low back pain, and degenerative. The healthy participants were asymptomatic subjects who had never been treated for low back pain and exhibited no limitation in daily activities. Furthermore, no radiological evidence of degeneration or defects were found. The healthy with low back pain group (HLBP) was healthy without radiological evidence of degeneration or defects in the lumbar spine, but symptomatic for acute low back pain (LBP). Of the subjects, eight were experiencing pain in the low back region at the time of the evaluation. The degenerative subjects were determined to have one or more of the following conditions: Schmorl's Nodes, disc bulging both with and without canal or foraminal stenosis, disc osteophyte complexes, decreased height and fluid signal in the intervertebral disc, or facet hypertrophy. The degenerations were found at a single level for six of the subjects, while the rest experienced problems at multiple levels. This degeneration was determined to not be so severe as to require surgery.

10.1.2.1 X-ray Fluoroscopy

All subjects were analyzed with a high-frequency pulsated video fluoroscopy unit and were positioned during the evaluation so the motion occurred on the sagittal plane, as shown in Figure 10-1. Each subject was asked to perform a standing flexion-extension trial and a lateral bending trial while under fluoroscopic surveillance. For both the flexion-extension and lateral bending activities, all volunteers began in a neutral standing position. For the flexion-extension activity, participants were asked to flex to the maximum without moving their hips. They were then asked to travel back through to neutral standing position and then into maximum extension. For the lateral bending activity, patients were asked to flex to their maximum left position before returning to the neutral position and continuing onto the maximum right position. The fluoroscopic video captured the participants' motions at a rate of 30 frames per second and was outputted to a camera to record the motions for future analysis.

10.1.2.2 Model Creation

CT scans of all subjects were obtained to include all lumbar vertebras (L1-L5).

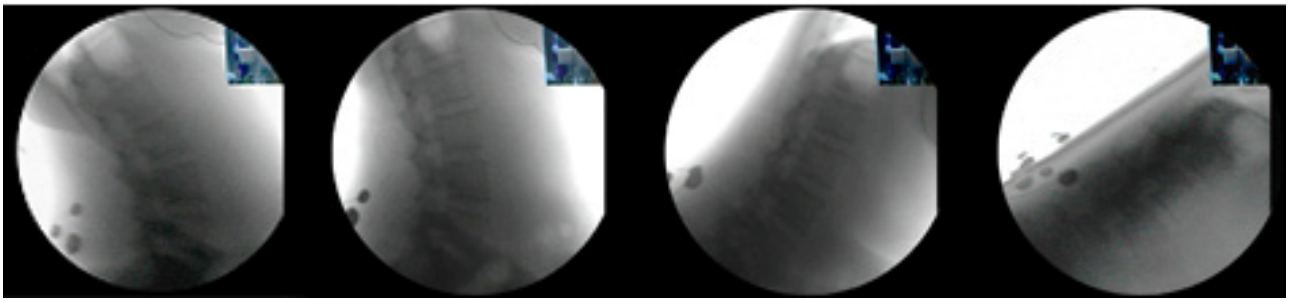


Figure 10-1 Fluoroscopic image captured during flexion-extension activity for a healthy lumbar spine captured (from left to right) at full extension, neutral, mid-flexion, and maximum flexion

Each patient's stack of scans was manually segmented by applying a thresholding filter to isolate the bone from the soft tissue. Once all slices for a patient were accurately segmented, separate 3D polygon surface models were generated for each vertebra from L5 through L1.

10.1.2.3 3D-to-2D Registration

This registration process registers the surface model of the bone to the single-plane fluoroscopic image using a direct image-to-image similarity measurement method proposed by Mahfouz, et al.[235] . The fluoroscopic video of the flexion-extension activity was broken into four single frames at maximum flexion, mid-flexion, neutral, and maximum extension positions, while the lateral bending activity contained only three frames at the maximum left position, neutral, and maximum right position.

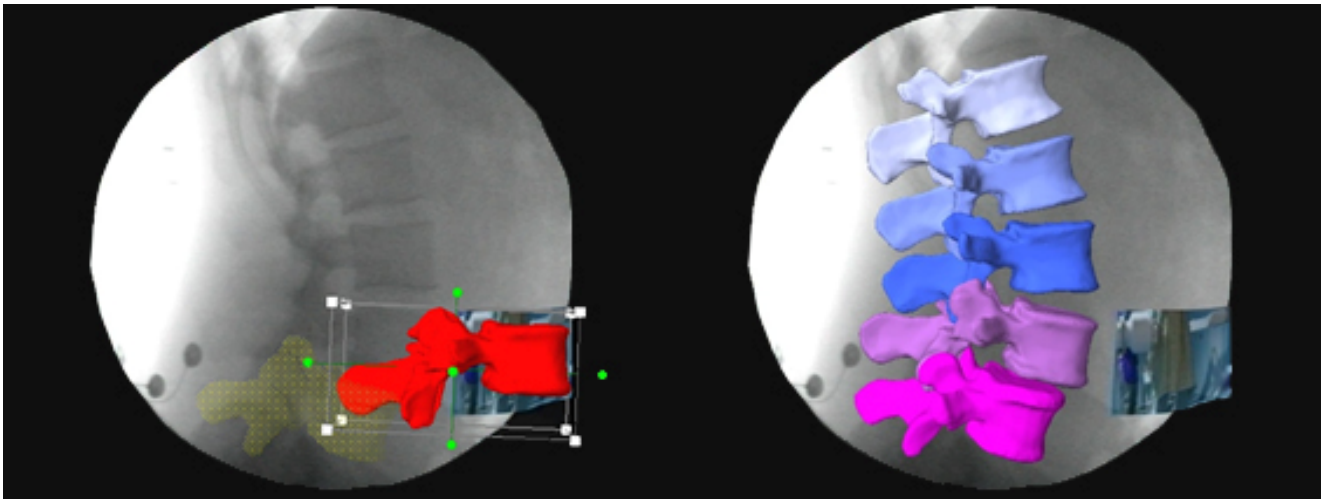


Figure 10-2 The process of overlaying: starting to fit (left) and finished spinal frame (right)

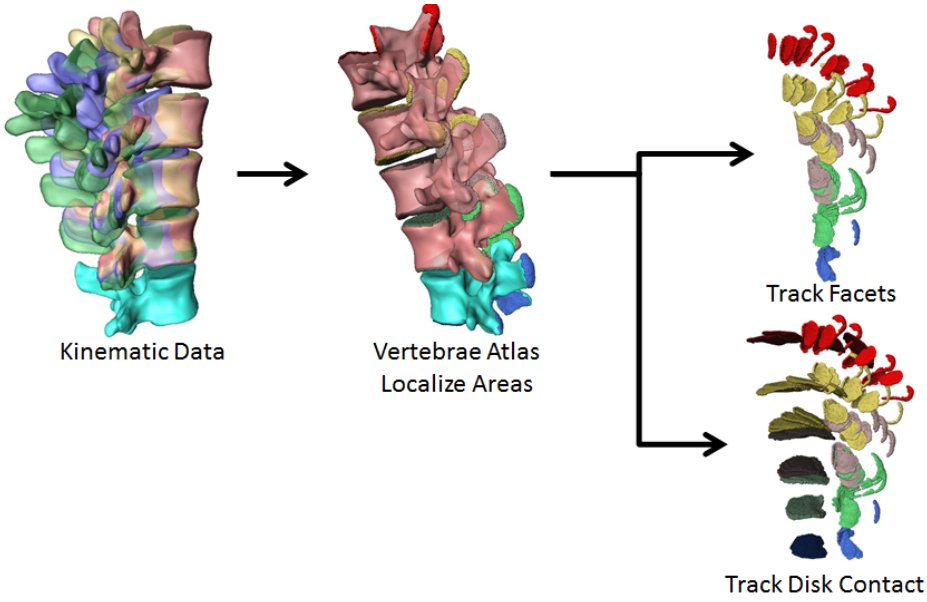


Figure 10-3 Flow chart for the analysis

The participants' individual 3D models were then manipulated within the space of each single-perspective fluoroscopic frame. Figure 2 shows a sample patient with L5 overlaid accurately, while L4 was being moved into the correct position. All vertebrae, L1-L5, were manipulated so that the silhouettes of each individual corresponding bone model best matched its counterpart within the frame, as shown in Figure 10-2.

10.1.2.4 Statistical atlas and automatic landmarking

Figure 10-3 depicts a flow chart of the automated analysis. Segmented CT bones were added to the statistical atlas. The superior and inferior contact points were identified on the TMs for each vertebra (L1-L5), as shown in Figure 10-4. These points were then propagated across all patients using atlas correspondence, and the contact areas were tracked globally.

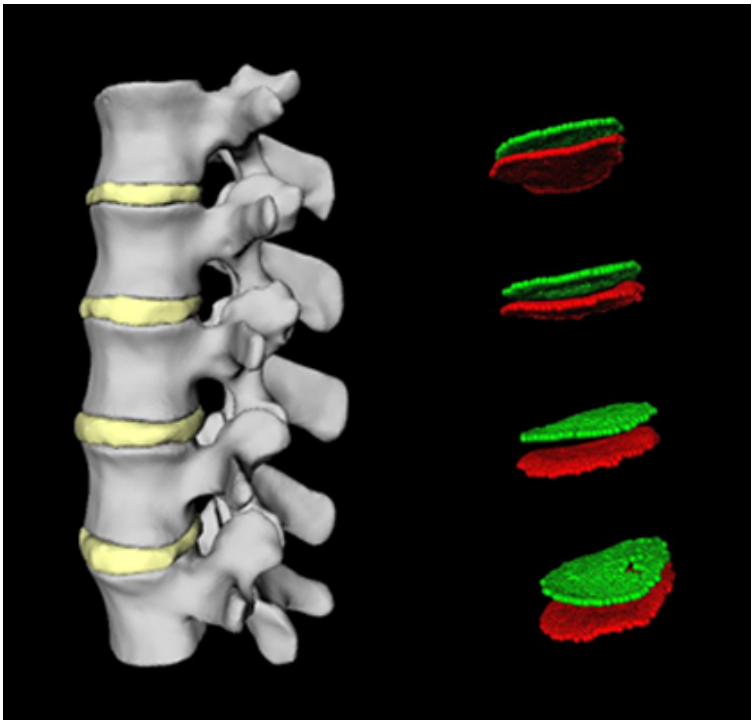


Figure 10-4 Propagation of contact points using statistical atlas

Utilizing the superior and inferior disc contact areas, each contact surface was divided into six parts (left anterior, left posterior, right anterior, right posterior, middle anterior and middle posterior), as shown in Figure 10-5. Next, an automatic algorithm was developed to calculate the supraspinous and intertransverse ligaments. Using the atlas correspondence, left and right transverse and spinous processes loci were propagated for each patient, enabling the calculation of the most prominent point for each loci, as shown in Figure 10-6. The length for each ligament was then calculated as the distance between the tip points of each neighboring vertebrae. Disc contact points and ligament lengths were then tracked through full range of motion (ROM) for each activity, see **Error! Reference source not found.**Figure 10-7.

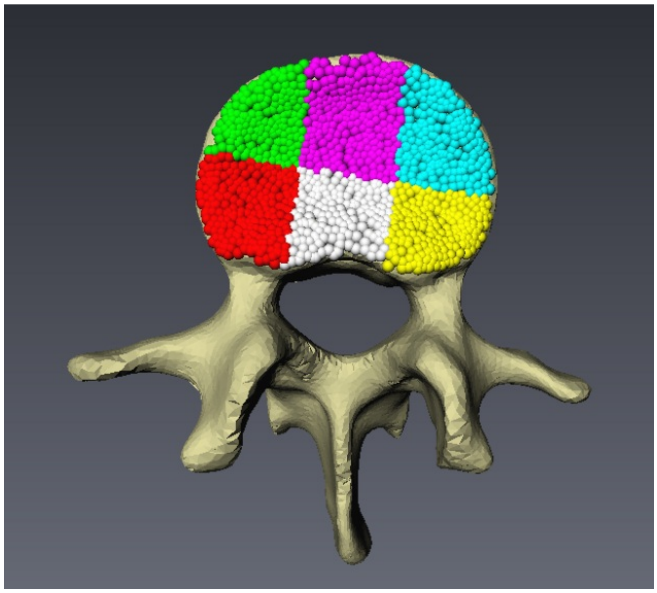


Figure 10-5 Division of the contact area on the vertebral surface into six defined parts

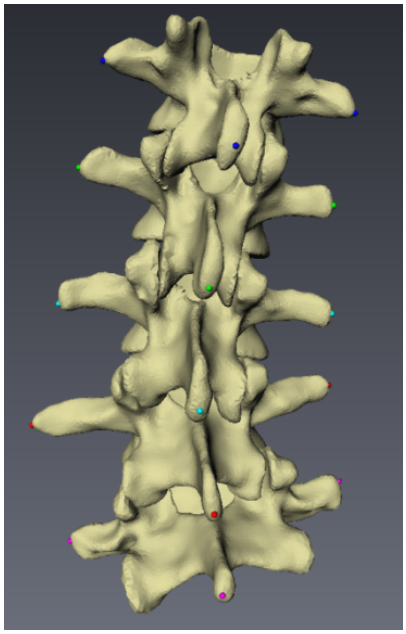


Figure 10-6 Automatic calculation of the supraspinous and intertransverse ligament attachment sites

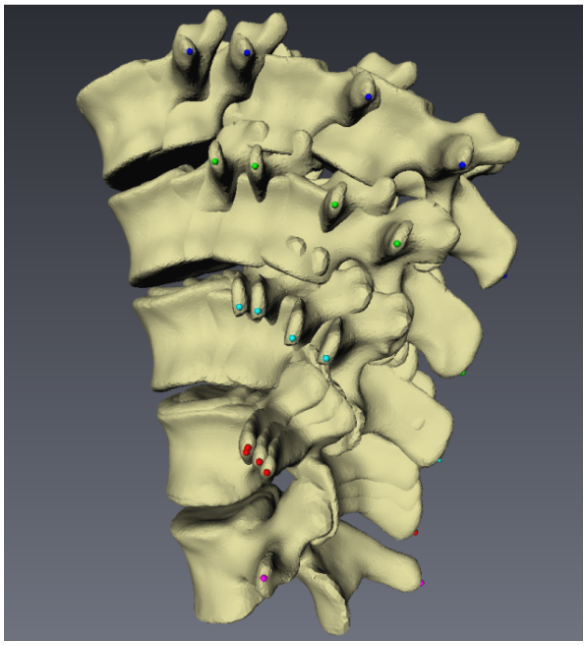


Figure 10-7 Tracking of the ligament length across the full range-of-motion during flexion-extension

10.1.3 Results

The results from the use of this tool are included in the following tables. The average overall disc spacing for each activity are listed in **Error! Not a valid bookmark self-reference.**Tables 10-1, Table 10-2, and Table 10-3. Since the force applied over an area of the intervertebral disc can induce local deformation in the disc, the disc spacing was also calculated at each of the six defined quadrants on the vertebral contact surface (Table 10-4,Table 10-5,Table 10-6Table 10-7,Table 10-8, Table 10-9). The selected ligament lengths correlated with the derived disc spacing have been included in Table 10-10, Table 10-11,Table 10-12.

Table 10-1 Average difference in disc height (mm) relative to the supine position during flexion-extension

	L1-L2	L2-L3	L3-L4	L4-L5
Healthy	4.27	3.12	2.87	4.00
Low Back Pain	3.60	4.71	4.05	3.58
Degenerative	3.29	3.12	2.70	4.22
Fusion (Pre-operative)	3.35	4.09	3.43	8.45

Table 10-2 Average difference in disc height (mm) relative to the supine position during axial rotation

	L1-L2	L2-L3	L3-L4	L4-L5
Healthy	6.60	5.64	2.98	2.03
Low Back Pain	3.42	3.56	4.09	1.77
Degenerative	2.72	5.64	3.04	1.89
Fusion (Pre-operative)	4.34	4.44	5.22	2.07

Table 10-3 Average difference in disc height (mm) relative to the supine position during lateral bending

	L1-L2	L2-L3	L3-L4	L4-L5

Healthy	6.64	5.71	3.14	2.67
Low Back Pain	3.19	2.96	3.83	2.89
Degenerative	2.60	5.71	3.23	3.18
Fusion (Pre-operative)	4.73	5.07	4.17	2.88

Table 10-4 Average difference in disc height (mm) relative to the supine position in the left anterior quadrant

	L1-L2	**L2-L3**	**L3-L4**	**L4-L5**
Healthy	3.84	3.10	3.44	5.20
Low Back Pain	3.66	4.54	4.74	4.62
Degenerative	3.46	3.10	3.09	5.53
Fusion (Pre-operative)	4.16	3.98	4.16	8.53

Table 10-5 Average difference in disc height (mm) relative to the supine position in the left posterior quadrant

	L1-L2	**L2-L3**	**L3-L4**	**L4-L5**
Healthy	4.78	3.62	3.00	5.10
Low Back Pain	3.69	5.20	4.03	4.33
Degenerative	3.47	3.62	2.76	6.04
Fusion (Pre-operative)	3.70	5.09	3.44	8.92

Table 10-6 Average difference in disc height (mm) relative to the supine position in the middle anterior quadrant

	L1-L2	**L2-L3**	**L3-L4**	**L4-L5**
Healthy	4.60	3.14	2.47	3.63
Low Back Pain	3.34	5.14	4.82	4.06
Degenerative	3.09	3.14	2.66	3.73
Fusion (Pre-operative)	3.44	4.64	3.45	7.71

Table 10-7 Average difference in disc height (mm) relative to the supine position in the middle posterior quadrant

	L1-L2	**L2-L3**	**L3-L4**	**L4-L5**
Healthy	3.85	3.66	3.01	4.11
Low Back Pain	3.46	4.66	4.61	3.74

Degenerative	3.03	3.66	2.79	3.72
Fusion (Pre-operative)	3.51	4.45	3.42	8.03

Table 10-8 Average difference in disc height (mm) relative to the supine position in the right anterior quadrant

	L1-L2	**L2-L3**	**L3-L4**	**L4-L5**
Healthy	4.98	3.20	2.44	3.61
Low Back Pain	3.66	4.82	3.91	3.86
Degenerative	3.54	3.20	2.94	3.91
Fusion (Pre-operative)	3.64	4.56	3.14	8.48

Table 10-9 Average difference in disc height (mm) relative to the supine position in the right posterior quadrant

	L1-L2	**L2-L3**	**L3-L4**	**L4-L5**
Healthy	3.90	3.11	2.90	3.81
Low Back Pain	3.34	5.27	4.82	4.29
Degenerative	3.24	3.11	2.63	4.08
Fusion (Pre-operative)	3.57	3.99	3.38	8.00

Table 10-10 Average left intertransverse ligament length (mm) relative to the supine position

	L1-L2	**L2-L3**	**L3-L4**	**L4-L5**
Healthy	9.63	8.20	8.97	8.69
Low Back Pain	9.51	11.38	11.33	10.36
Degenerative	10.44	8.20	7.89	8.45
Fusion (Pre-operative)	9.59	12.19	8.29	14.50

Table 10-11 Average right intertransverse ligament length (mm) relative to the supine position

	L1-L2	**L2-L3**	**L3-L4**	**L4-L5**
Healthy	8.61	10.54	8.74	11.52
Low Back Pain	9.24	9.90	9.68	12.59
Degenerative	8.78	10.54	8.95	10.51
Fusion (Pre-operative)	10.30	11.33	8.68	14.37

Table 10-12 Average supraspinous ligament length (mm) relative to the supine position

	L1-L2	L2-L3	L3-L4	L4-L5
Healthy	15.99	17.21	18.65	21.46
Low Back Pain	14.75	16.12	16.15	19.22
Degenerative	16.36	17.21	17.14	20.46
Fusion (Pre-operative)	15.88	15.49	16.29	16.57

In general, the disc spacing was found to correlate with ligament length. Patients having more severe degenerative disc pathologies experienced decreased disc height. Less spacing between adjacent vertebral levels, a consequence of the decreased disc heights, resulted in smaller calculated distances for ligament lengths throughout the motion path. This may allow for laxity within the ligaments and may explain the increased coupled motions observed in symptomatic and pathological subjects evaluated using 3D kinematics.

11. BONE and SOFT TISSUE THICKNESS MODELING

Mapping of soft tissue and bone thickness is an active area of research in medical and anthropology fields, among others . The main challenge in such a task is generation of accurate correspondence across a reference surface, which is then used to measure either soft tissue or bone thickness at this interface. Such analysis is a direct application to the statistical atlases. Analysis in this chapter will focus on the 3D modeling of skull vault thickness and articulating cartilage of the knee joint.

11.1 Skull Vault Thickness Modeling

11.1.1 Introduction

Studying cranial vault thickness to determine bone thickness is important in the medical field for studying its relation to age, sex and body fluid [236], as well as anthropology for studying difference between populations [237]. This chapter will cover the application of statistical atlas in knee cartilage mapping and modeling cranial vault thickness.

11.1.2 Method

The overall algorithm for modeling 3D vault thickness is outlined in Figure 11-1. Skulls were first added to the atlas, generating dense correspondence across the bone surface. Areas of interests were then localized on the template bone (Figure 11-2) and correspondence is used to propagate these areas in the whole training set. For each bone, vault thickness was calculated by computing normal distance between the ecto-cranial and endo-cranial surfaces, as shown in Figure 11-3. Three types of analysis were performed on the output thicknesses. First, descriptive

statistics were calculated to generate the average thickness and standard deviation maps. Second, PCA was performed to construct the SSM to capture this variation of thickness across the population. Next, areas of high and low variation between the populations were identified using the fisher discriminant ratio, where each vertex was given a rank (63) .

$$J(V) = \frac{\left|m_f - m_m\right|^2}{{S_m}^2 + {S_f}^2} \quad (63)$$

Where

m_f & m_m are the mean of the vault thickness at vertex V for females and males.

S_f & S_m are the variance of the vault thickness at vertex V for females and males.

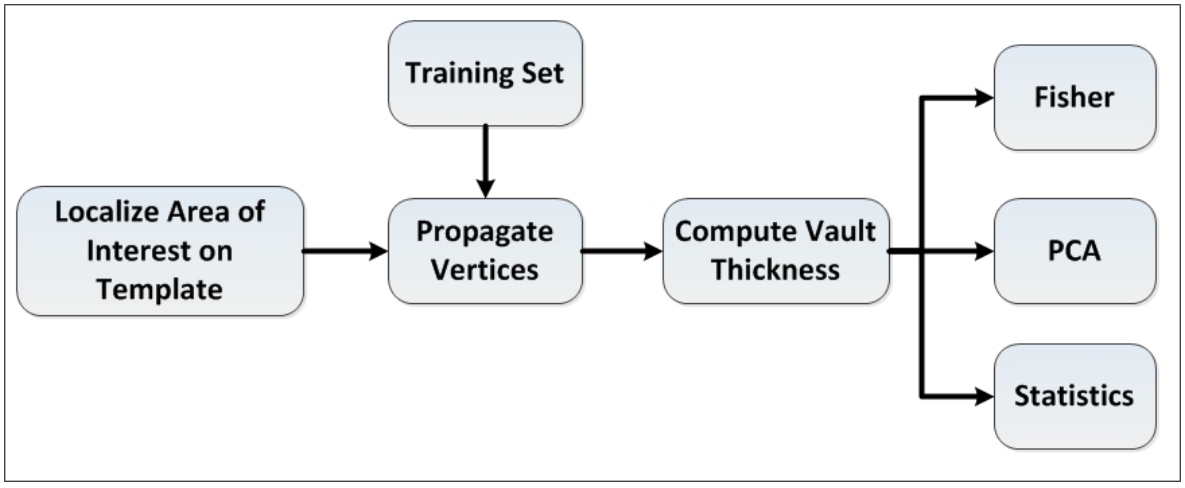


Figure 11-1 algorithm for soft tissue and bone thickness modeling

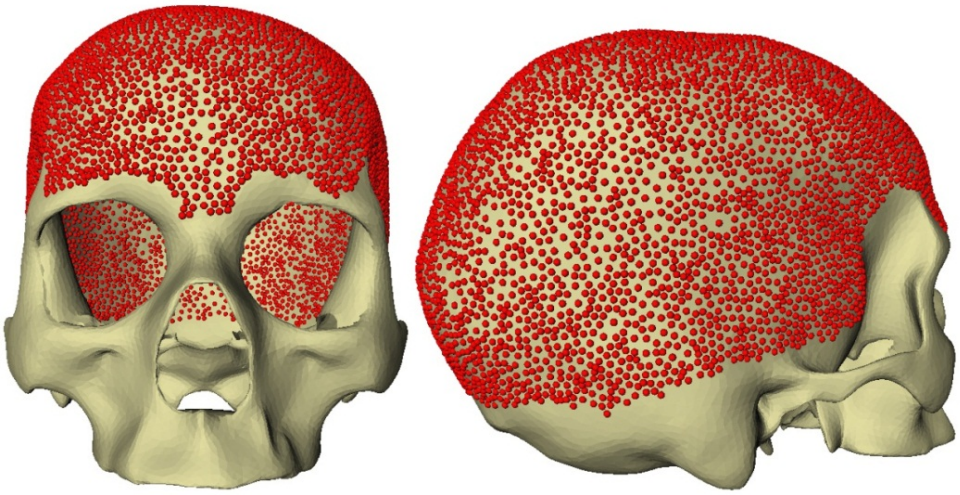


Figure 11-2 Localizing point on base mesh for vault thickness calculation

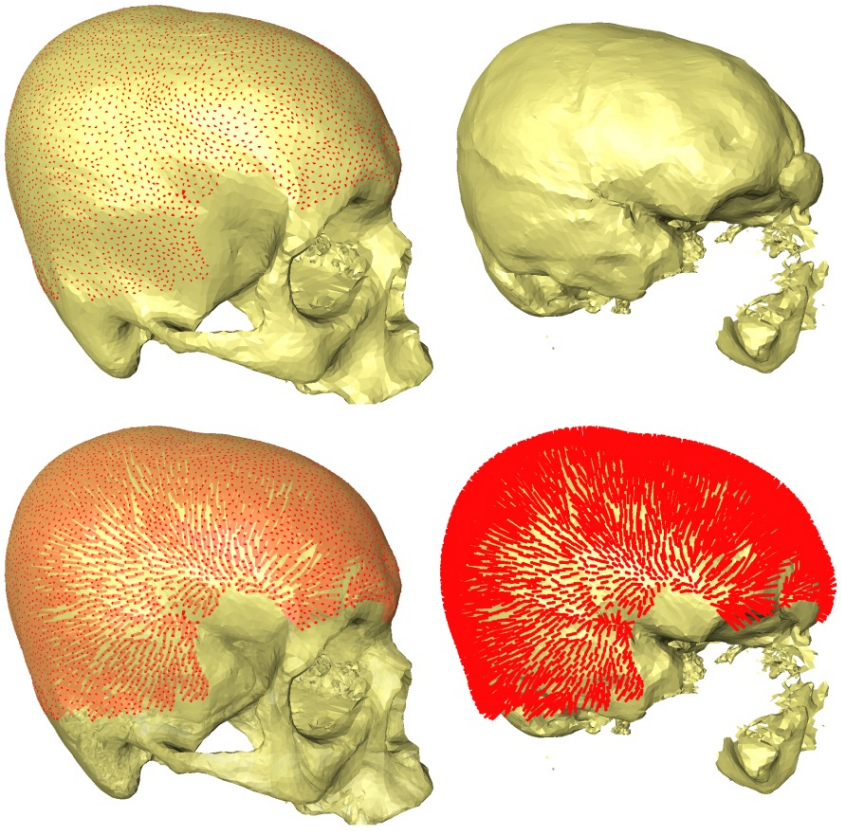


Figure 11-3 Calculation of vault thickness

11.1.3 Results

Figure 11-4 shows the average vault thickness map, where the maximum thickness was found to be 11.1 mm and minimum 2.5 mm. The standard deviation for these vertices is shown in Figure 11-5 with a minimum of 0.6 mm and maximum of 4.8 mm. The right image in Figure 11-6 outlines areas with highest and lowest variation in vault thickness between males and females; warm colors reflect areas with high variation and cold colors reflect areas with lowest variation. The left image in Figure 11-6 shows the directional bias in the vault thickness between males and females: red indicates areas where males have thicker vault and blue indicates areas where females have thicker vault.

Results of this analysis showed that the vault thickness is a sexually dimorphic feature, with females having a thicker vault than males in the frontal region and vice versa in the occipital region. This was also documented by Ishida and Dodo [238] and Ross, et al. [239] who also found that female vault thickness increases with age, and male vault thickness decreases with age. Ross, et al. also attributed the increase in female vault thickness to hyperostosis frontalis interna (HFI) [240], a condition of unknown pathogenesis with a female-to-male ratio of 100:1. Furthermore, they concluded that vault thickness in the parietal and frontal regions was not sexually dimorphic until the onset of HFI (usually around the age of 50). The average age of the females in the present study was 66.4 years, whereas the male average was 64.1 years. Consequently, the significant sex dimorphism in vault thickness of the frontal region could be due to HFI as explained by Ross, et al. [239].

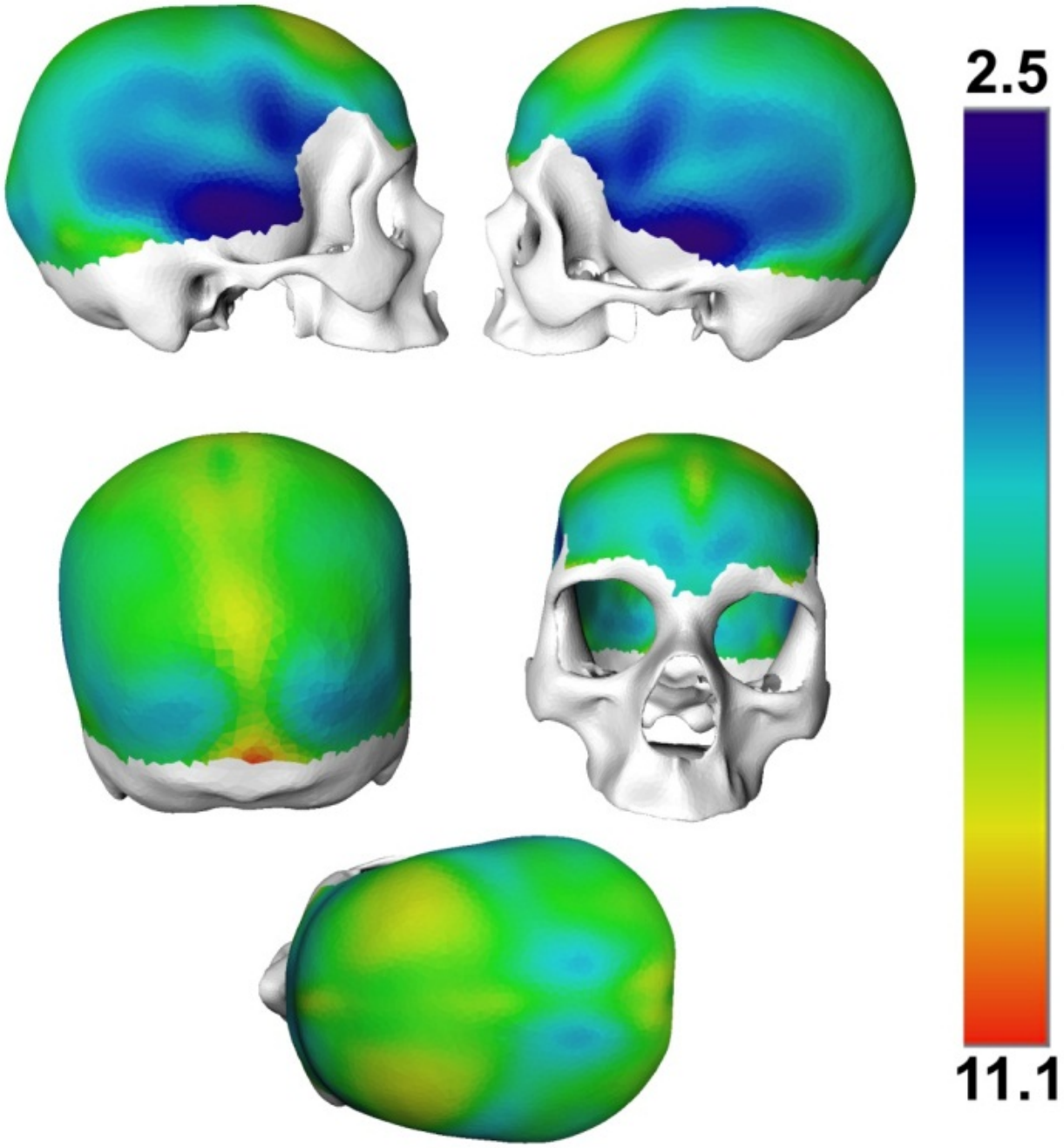


Figure 11-4 Skull vault thickness mean map (mm)

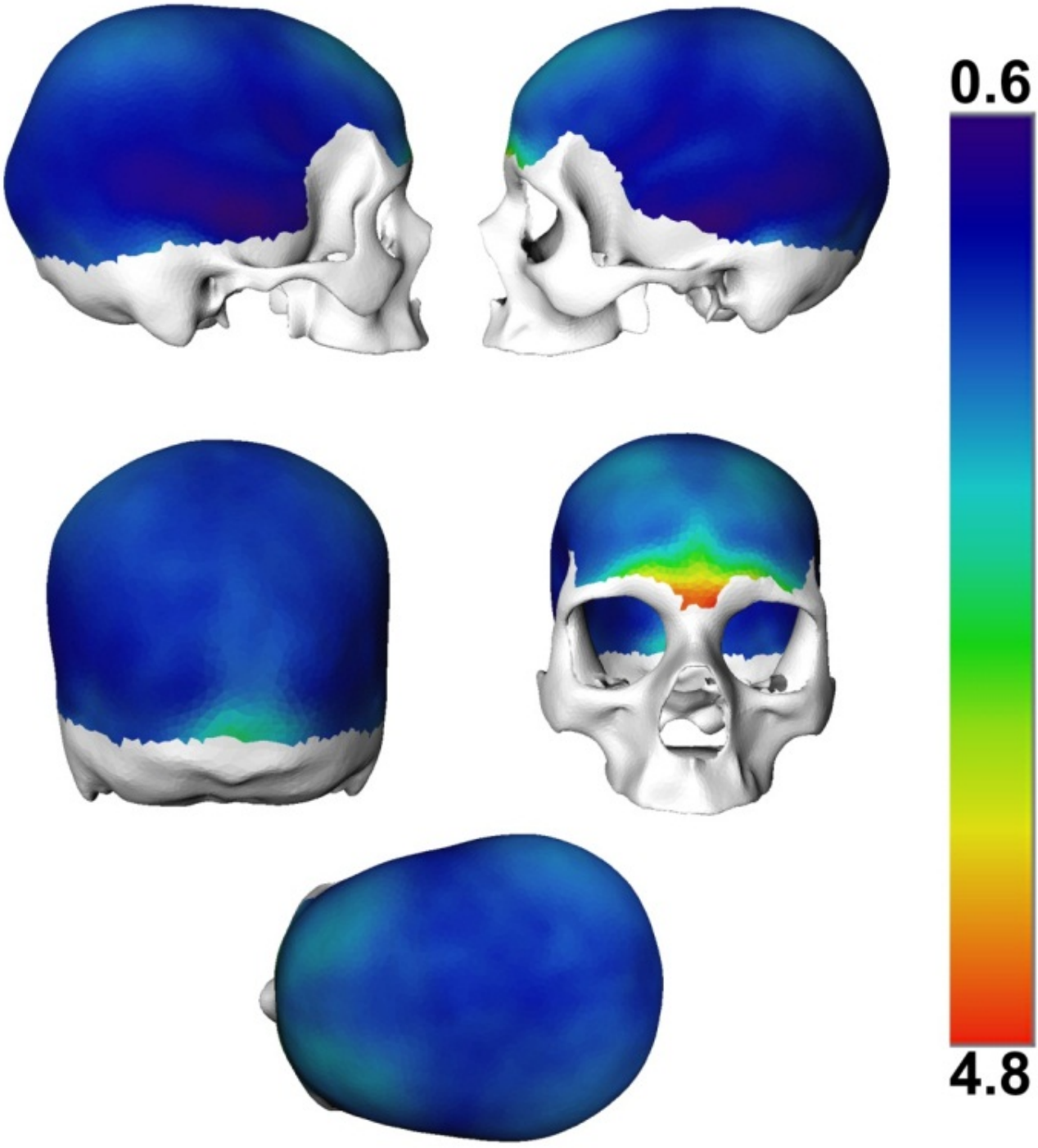


Figure 11-5 Skull vault thickness standard deviation map (mm)

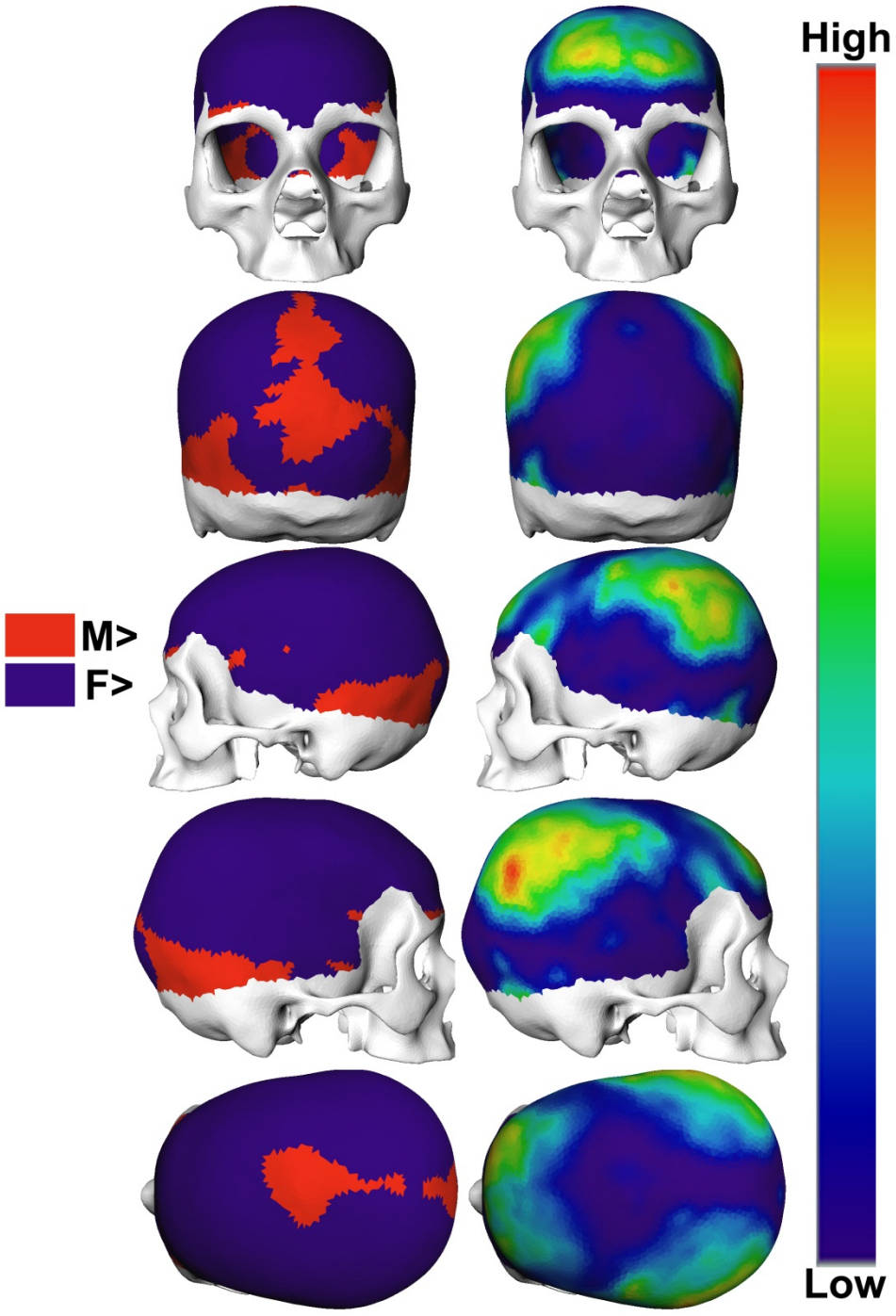


Figure 11-6 Areas of high variation (right), thickness bias (Left)

11.2 Cartilage Thickness Modeling

11.2.1 Introduction

Mapping of soft tissue and bone thickness are active areas of research in many fields, including the medical field where cartilage mapping is of great importance in studying the progress of osteoarthritis. Osteoarthritis is a disease characterized by structural change of bone, loss of articulating cartilage, and pain [241-243]. MRI is the standard imaging protocol for modeling cartilage.

11.2.2 Methods

Cartilage modeling process is a two tier process. Firstly, it involves modeling the bone cartilage interface (BCI) by identifying vertices with high probability of belonging to the BCI. The second tier is modeling the statistical distribution of the measured cartilage thickness at the identified BCI. Figure 11-7 Cartilage modeling algorithm.

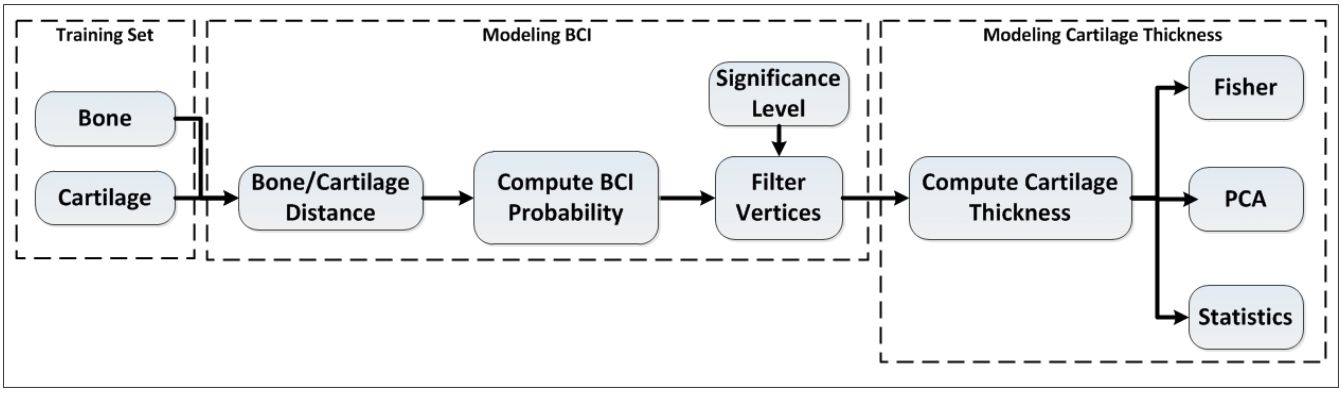


Figure 11-7 Cartilage modeling algorithm

11.2.2.1 Dataset

Thirty-seven MRIs of knee joints were used from the Osteoarthritis Initiative dataset [244]. Only normal knees were selected in this analysis (Zero OARSI atlas grade). Due to limitations in segmentation and time constraints, only male specimen were used in this analysis. MRIs were manually segmented using experts, and four surface models were generated for the femur bone and cartilage, and tibia bone and cartilage tibia. The femur and tibia bone were added to the statistical atlas to generate dense correspondence between the training sets.

11.2.2.2 Modeling BCI

The purpose of this tier is to determine the true BCI vertices on both the femur and tibia. The distance between each vertex on the femur and tibia bone to the cartilage surface was first calculated, as shown in Figure 11-8. Each vertex on the training set models were then classified as BCI or non-BCI based on a distance threshold of 3mm. The probability of each vertex, a BCI, was then computed using the number of occurrences of each vertex in the BCI. Figure 11-9 and Figure 11-10 show the histogram count and probability density estimate for the femur and the tibia, respectively. The vertices with a probability of >95% were then chosen as BCI for both the femur and tibia, as shown in Figure 11-11. Indices of these vertices were then propagated on all the training sets using the atlas correspondence. The cartilage thickness at each of these vertices was then computed by finding the normal distance between the BCI and outer cartilage surfaces. PCA was then computed along with the mean and standard deviation for both the femur and tibia.

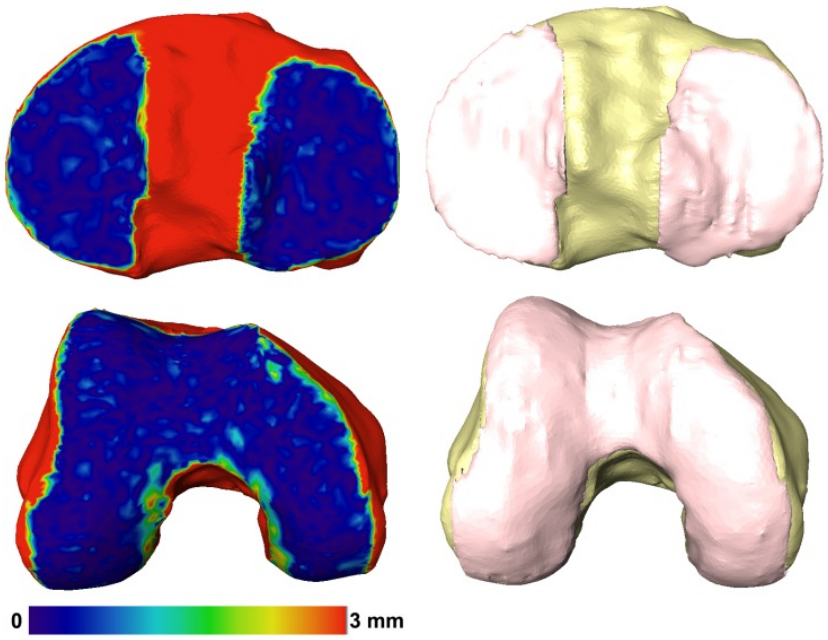


Figure 11-8 Bone cartilage distance calculation

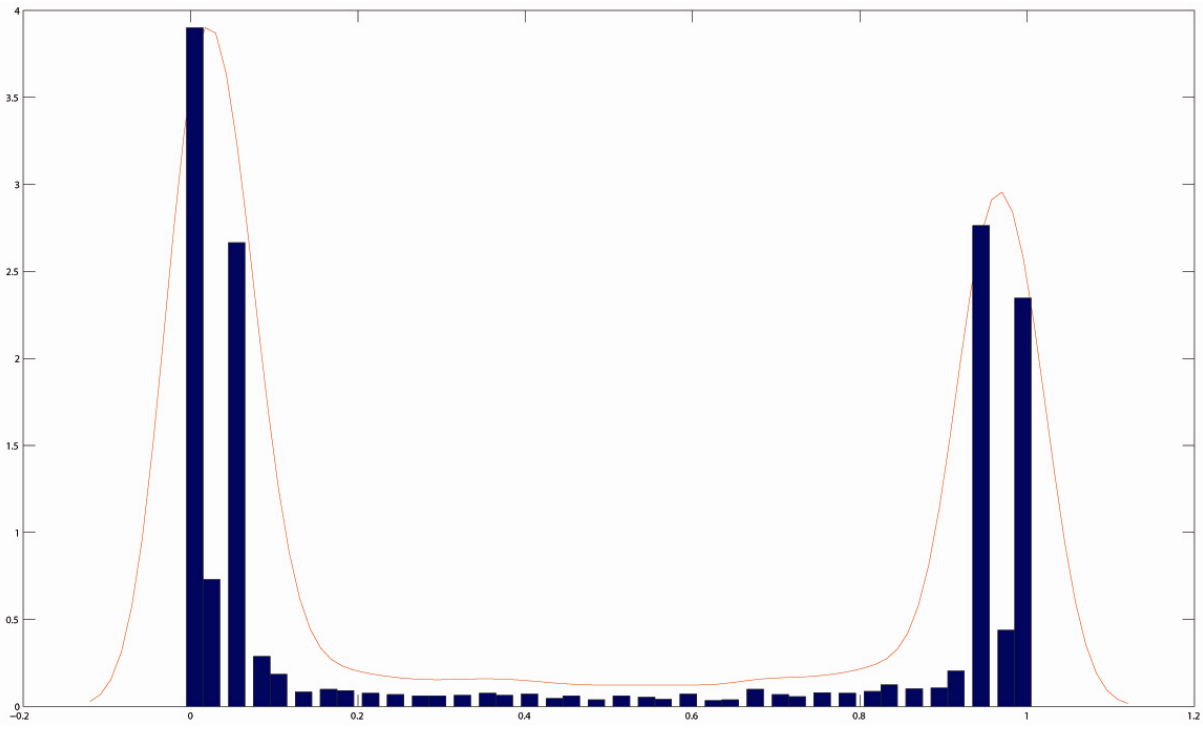


Figure 11-9 Femur vertices BCI histogram count and probability density estimate

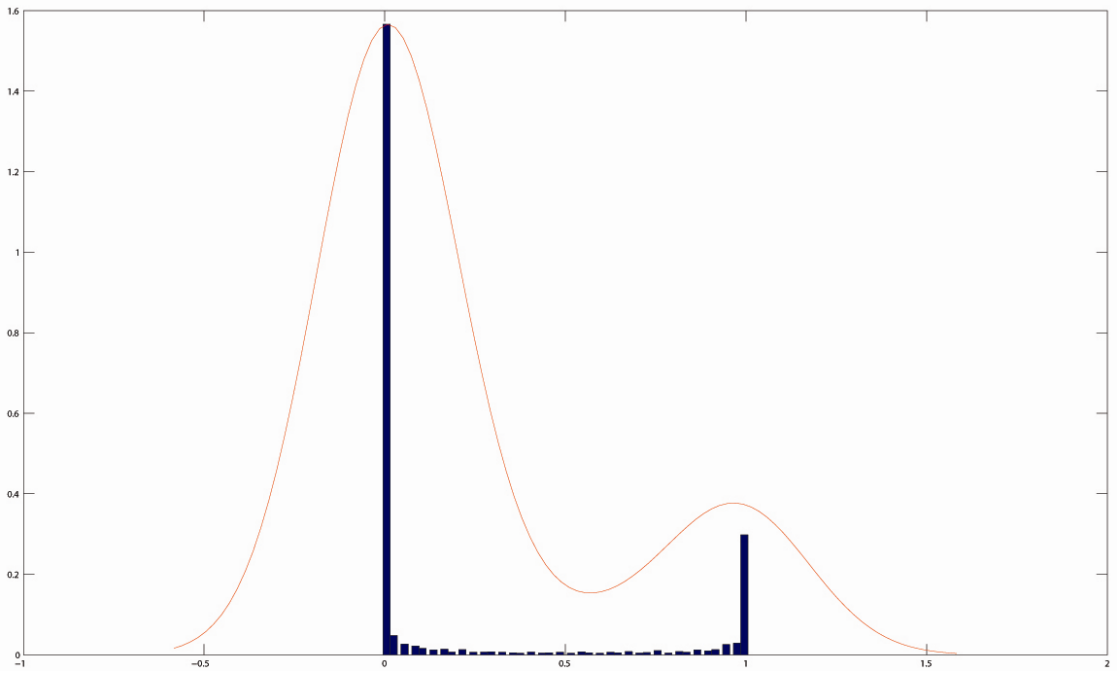


Figure 11-10 Tibia vertices BCI histogram count and probability density estimate

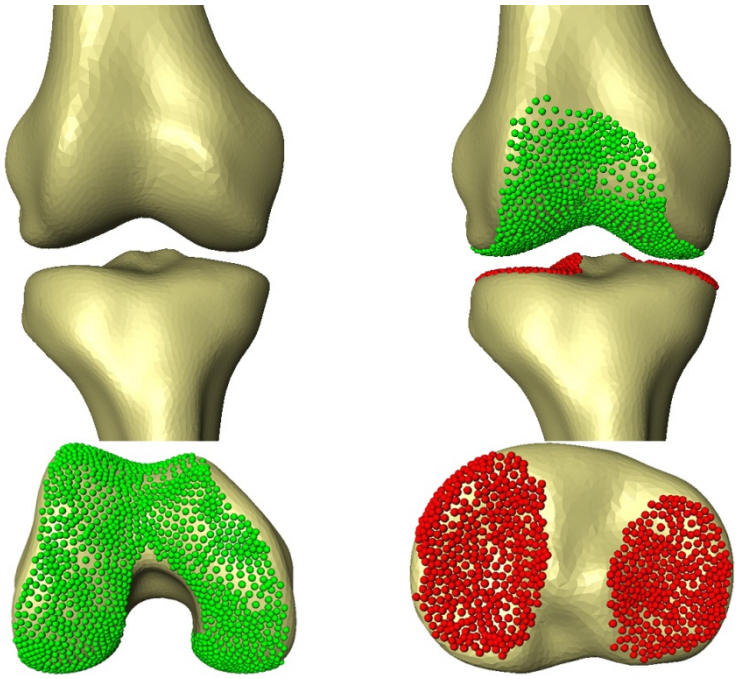


Figure 11-11 Calculated bone cartilage interface

11.2.3 Results

Figure 11-12 shows the mean and standard deviation of the cartilage thickness on the femur, which was found to be 2.5 mm with standard deviation of 1.3 mm. **Error! Not a valid bookmark self-reference.**Table 11-1 shows the descriptive statistics for the femoral and tibial cartilage. Figure 11-13 shows the mean and standard deviation map for the lateral and medial tibia cartilage. The lateral cartilage was thicker with a mean of 2.6 mm and a 1 mm standard deviation compared to 1.9 mm mean and 0.7 mm standard deviation on the medial side.

The results of this analysis showed that the anterior trochlear area of the femoral cartilage was the thickest cartilage, and these findings are similar to Koo, et al. [245] , Cohen [246] , and Gamio [243]. The medial anterior side was found to be thicker than the lateral anterior side, whereas the lateral middle was thicker than the medial middle. This coincides with results of Raynauld, et al. [247]. The Lateral tibia side had thicker cartilage compared to medial side [247].

Table 11-1 Descriptive statistics for femoral and tibial cartilage

	μ	σ	Min	Max
Femur	2.5	1.3	0.6	3.9
Tibia Lateral	2.6	1	0.6	4.7
Tibia Medial	1.9	0.7	0.2	3.7

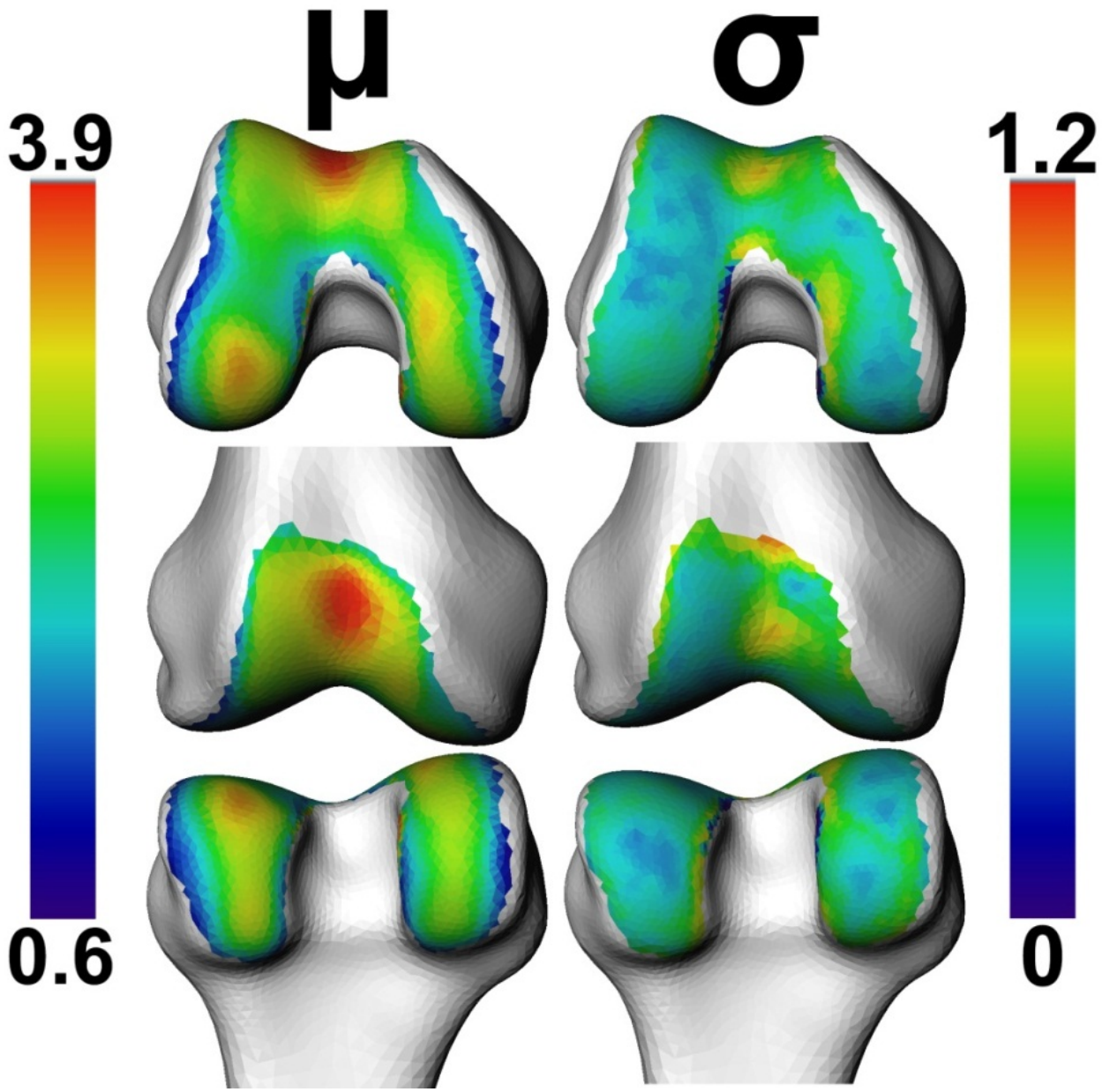


Figure 11-12 Femoral cartilage mean and stand deviation map (mm)

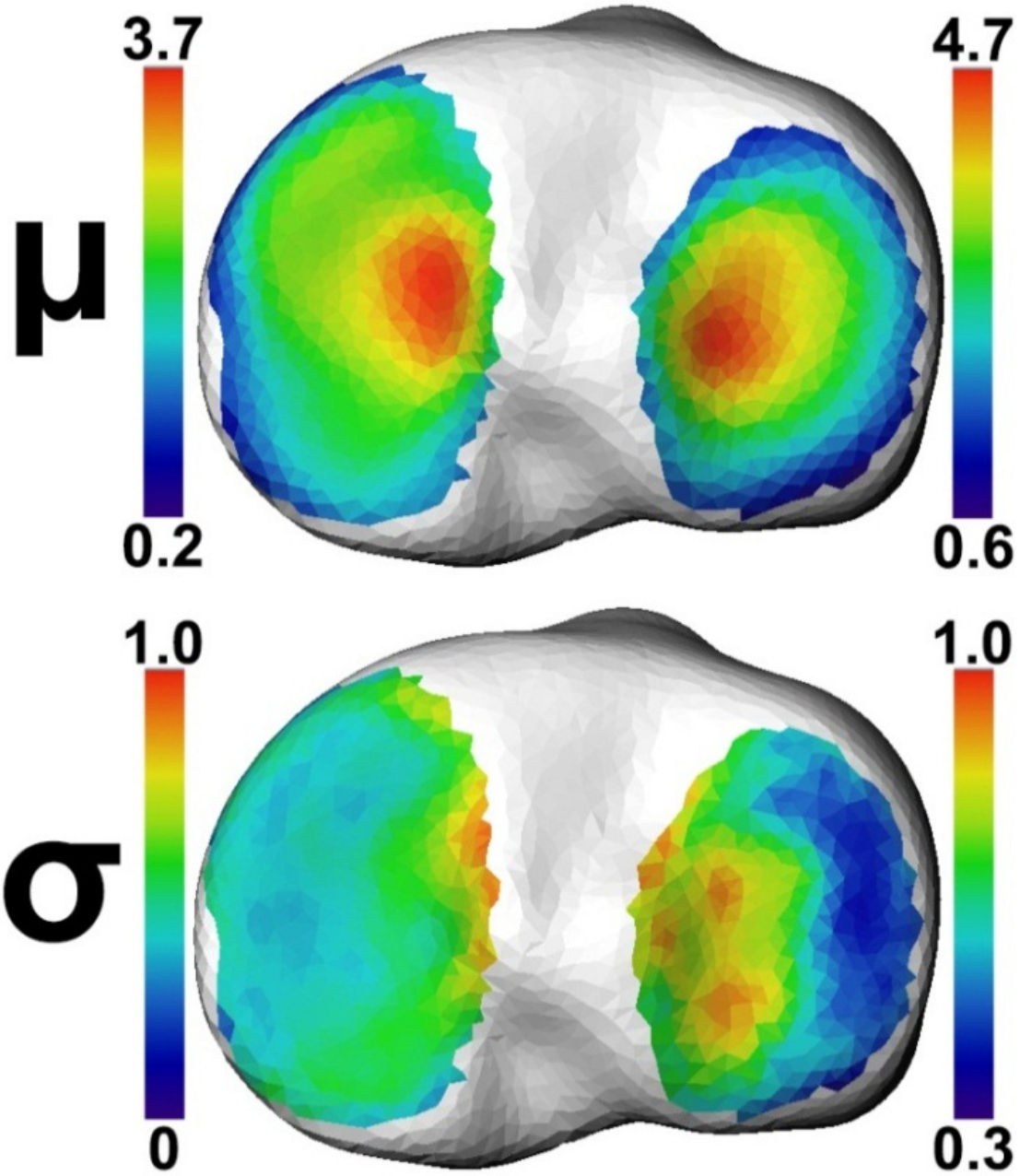


Figure 11-13 Tibial cartilage mean and stand deviation map (mm)

12. FUTURE WORK

12.1 Cartilage Prediction

MRI is the standard imaging modality for studying cartilage and generating patient-specific cartilage models. However, due to the increased cost, prolonged scanning time, and limitation of use in case of patients with metal implants, alternative imaging modalities are used, such as x-ray and CT. Unfortunately, neither x-ray nor CT reveal soft tissues or cartilage information. In such cases, a cartilage prediction model is needed to predict cartilage thickness based on the spacing between the femur and tibia. The inputs to the model are the distance between the femur and tibia at the BCI locations, patient demographic and BMI (Figure 12-1). These are used to predict the cartilage thicknesses at the BCI using a Non-Parametric Kernel Regression model. The bone distance variables comprise the input memory matrix, where the rows are the training sets used and columns are the number of BCI points. These vectors are then compared to a query input vector (with bone distances measurements at the reference points), and an Euclidean distance value is computed for each knee in the memory matrix. These distances are then converted into a weight using the Gaussian Kernel function. The prediction of the reference point cartilage thicknesses is a weighted average of the output memory matrix, where the measured cartilage thicknesses are the reference points for each knee in the model's memory. The model's memory will be augmented to best match the query's sex, ancestry, age and BMI, which can improve prediction, accuracy and decrease uncertainty.

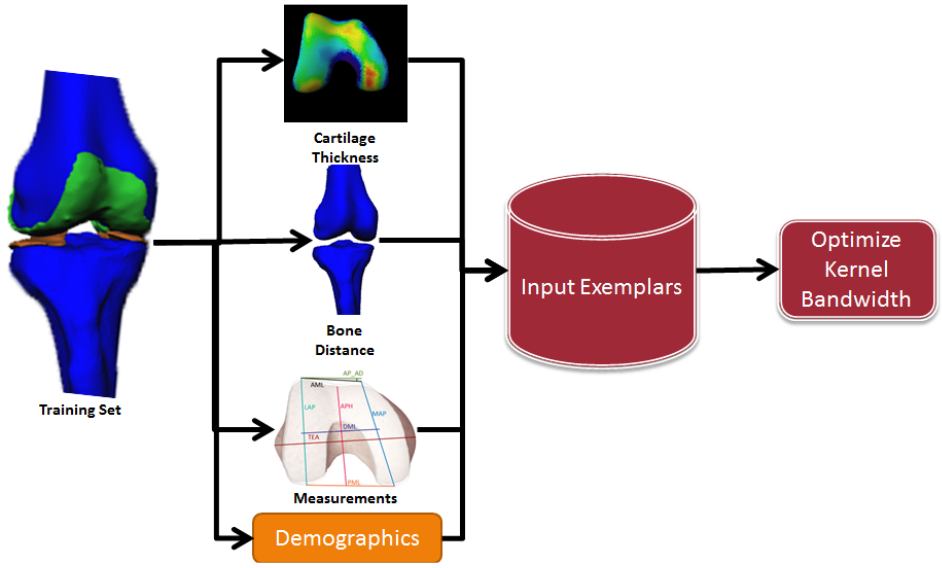


Figure 12-1 Cartilage prediction using non-parametric kernel regression

12.2 Facial Reconstruction

One application for the skull statistical atlas and the vault thickness statistical atlas is to continue to examine the correlations between the bony structure of the entire ecto-cranial surface and the soft tissue that surrounds it to find the most significant landmarks to predict soft tissue thickness. These landmarks will then be used to construct a non-parametric empirical model based on the correlations. This model will predict the facial tissue depth and reconstruct a complete 3D map of soft tissue thickness for the skull (Figure 12-2), thereby creating a soft tissue thickness atlas. This atlas will allow the capture of statistics across different ancestry, age, sex and BMI groups using principal components. These group-specific statistics will be used in interpolating the soft tissue thickness between landmarks with predicted tissue thickness. Figure 12-3 outlines a proposed framework that can be used for facial reconstruction. The

output of such a process would be a rendered virtual facial reconstruction, as shown in Figure 12-4.

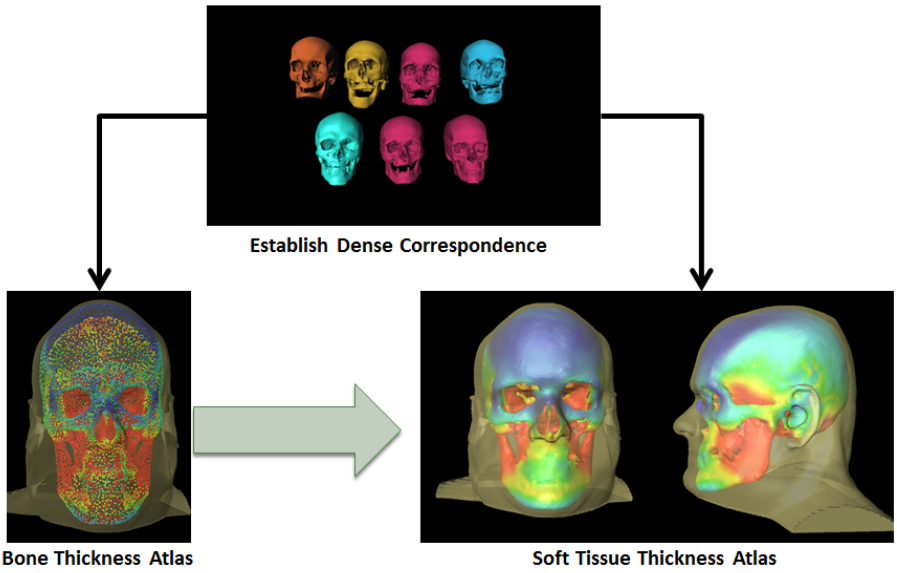


Figure 12-2 Facial reconstruction using SSM of bone and soft tissue thickness

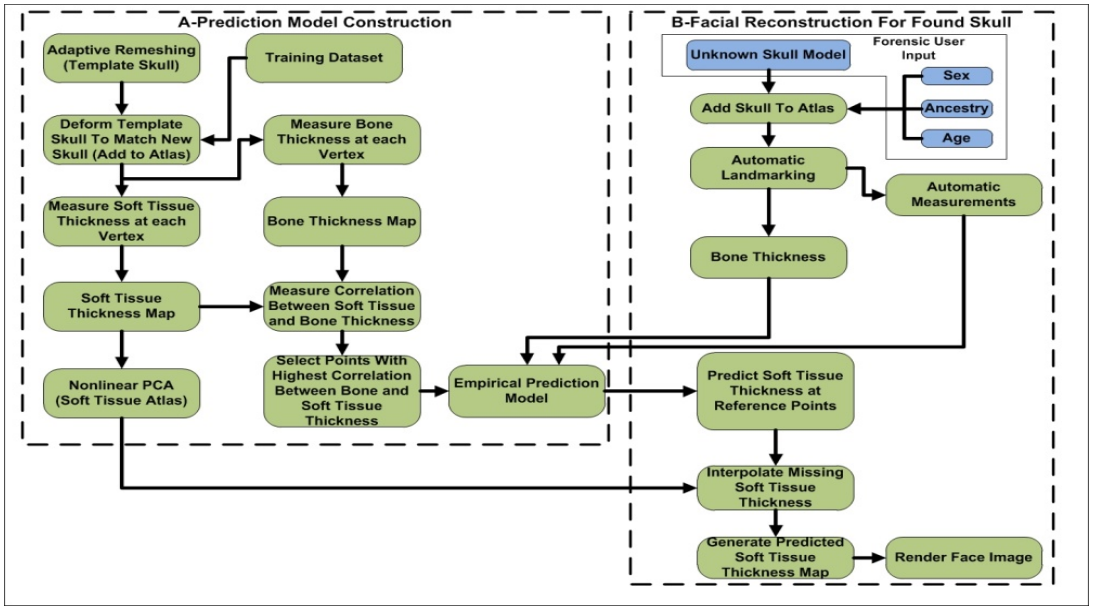


Figure 12-3 Proposed method for facial reconstruction using soft tissue and bone thickness SSM

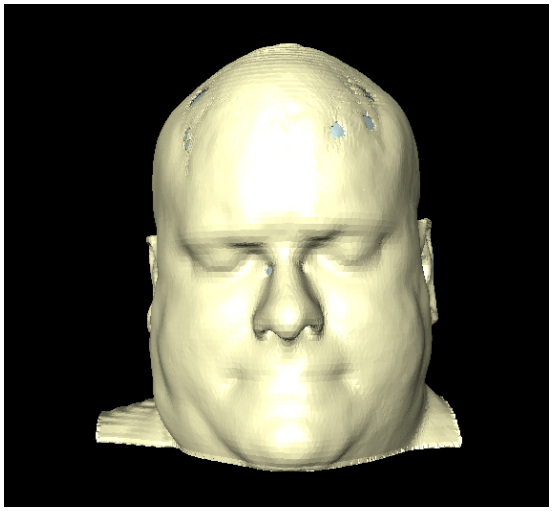


Figure 12-4 Rendered facial reconstruction

12.3 Fragmentary Remains Reconstruction

A forensic application for fragmentary remains reconstruction is the use of SSM to construct missing and deformed anatomy which can allow anthropologists to quantify and reconstruct fragmentary human skeletal remains from 3D surface files generated by CT or laser scans. First, the system will serve as an osteological case or scene management tool. All scanned skeletal remains from each scene will be reviewable within the application. Initially, the software will provide a MNE estimate of scanned material, which will allow for the determination of the MNI represented at the scene. Once the MNI is determined, the software will provide a fully reconstructed bone along with automated measurements for the user to apply to regression equations, discriminant functions, or to use with software, such as Fordisc 3.0. Such an application can be used in individual forensic casework, as well

as situations with commingled remains (e.g., mass graves or mass disaster scenarios).

Figure 12-5 shows the outline of the proposed process for fragmentary reconstruction.

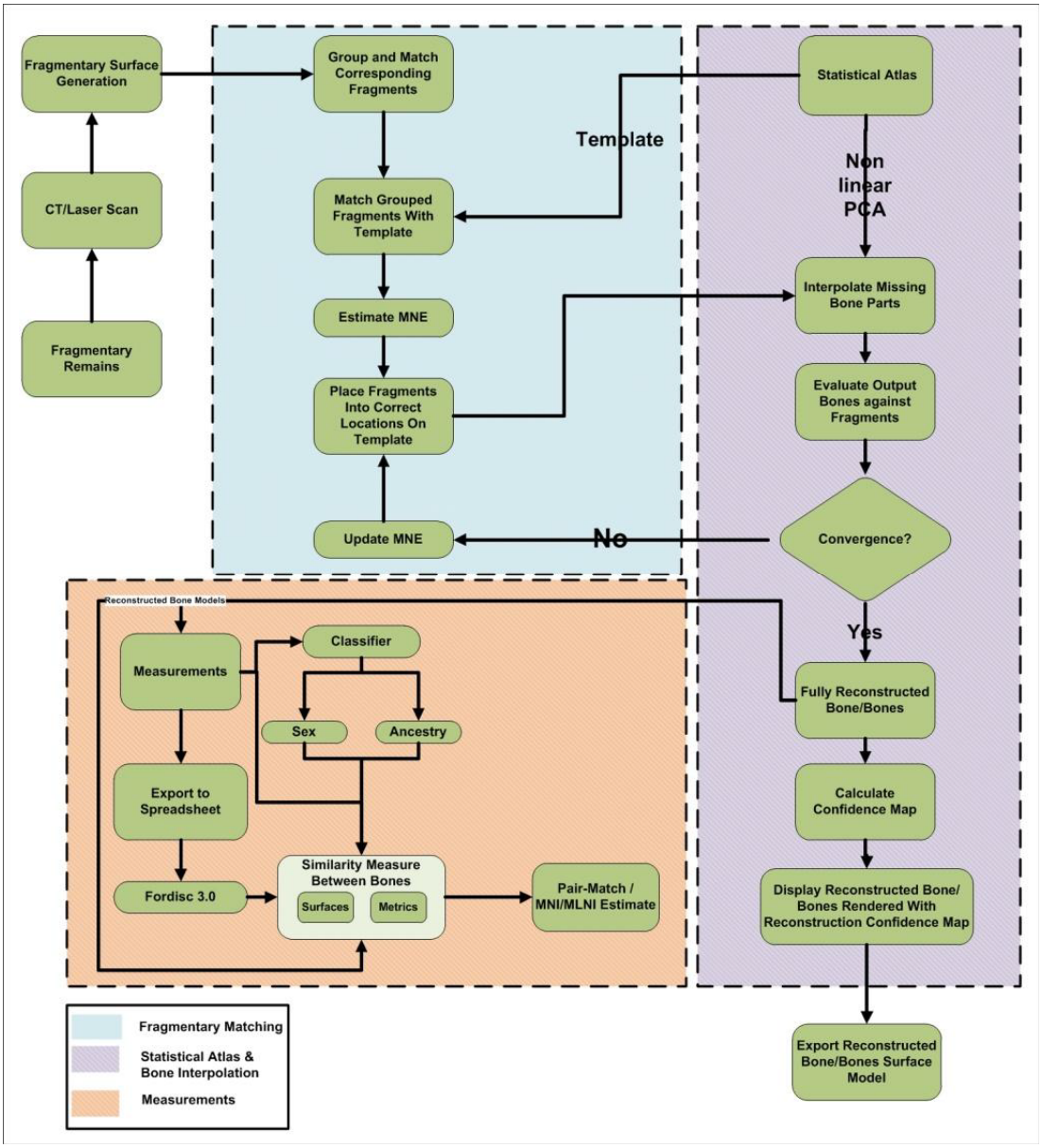


Figure 12-5 Overview of proposed method for fragmentary remain reconstruction

BIBLIOGRAPHY

[1] C. Lee, S. Huh, T. A. Ketter, and M. Unser, "Unsupervised connectivity-based thresholding segmentation of midsagittal brain MR images," *Computers in Biology and Medicine,* vol. 28, pp. 309-38, May 1998.

[2] P. Gibbs, D. L. Buckley, S. J. Blackband, and A. Horsman, "Tumour volume determination from MR images by morphological segmentation," *Physics in Medicine and Biology,* vol. 41, pp. 2437-46, Nov 1996.

[3] R. Haralick and L. Shapiro, "Image segmentation techniques," *Computer Vision, Graphics, and Image Processing,* vol. 29, pp. 100-132, 1985.

[4] S. Pohlman, K. Powell, N. Obuchowski, W. Chilcote, and S. Grundfest-Broniatowski, "Classification of breast lesions based on quantitative measures of tumor morphology," in *Engineering in Medicine and Biology Society, 1995., IEEE 17th Annual Conference*, 1995, pp. 537-538 vol.1.

[5] J. C. Bezdek, L. O. Hall, and L. P. Clarke, "Review of MR image segmentation techniques using pattern recognition," *Medical Physics,* vol. 20, pp. 1033-1048, 1993.

[6] J. C. Dunn, "A Fuzzy Relative of the ISODATA Process and Its Use in Detecting Compact Well-Separated Clusters," *Journal of Cybernetics,* vol. 3, pp. 32-57, 1973.

[7] L. Zhengrong, J. R. MacFall, and D. P. Harrington, "Parameter estimation and tissue segmentation from multispectral MR images," *Medical Imaging, IEEE Transactions on,* vol. 13, pp. 441-449, 1994.

[8] T. Lei and W. Sewchand, "Statistical approach to X-ray CT imaging and its applications in image analysis. II. A new stochastic model-based image segmentation technique for X-ray CT image," *IEEE Trans Med Imaging,* vol. 11, pp. 62-9, 1992.

[9] T. F. Cootes, C. J. Taylor, D. H. Cooper, and J. Graham, "Active Shape Models-Their Training and Application," *Computer Vision and Image Understanding,* vol. 61, pp. 38-59, 1995.

[10] N. Duta and M. Sonka, "Segmentation and interpretation of MR brain images: an improved active shape model," *IEEE Trans Med Imaging,* vol. 17, pp. 1049-62, Dec 1998.

[11] B. van Ginneken, A. F. Frangi, J. J. Staal, B. M. ter Haar Romeny, and M. A. Viergever, "Active shape model segmentation with optimal features," *IEEE Trans Med Imaging,* vol. 21, pp. 924-33, Aug 2002.

[12] M. de Bruijne, B. van Ginneken, M. A. Viergever, and W. J. Niessen, "Adapting Active Shape Models for 3D segmentation of tubular structures in medical images," *Inf Process Med Imaging,* vol. 18, pp. 136-47, Jul 2003.

[13] H. C. van Assen, M. G. Danilouchkine, M. S. Dirksen, J. H. C. Reiber, and B. P. F. Lelieveldt, "A 3-D Active Shape Model Driven by Fuzzy Inference: Application to Cardiac CT and MR," *Information Technology in Biomedicine, IEEE Transactions on,* vol. 12, pp. 595-605, 2008.

[14] C. McIntosh and G. Hamarneh, "Medial-based deformable models in nonconvex shape-spaces for medical image segmentation," *IEEE Trans Med Imaging*, vol. 31, pp. 33-50, Jan 2012.

[15] E. Berg, M. Mahfouz, C. Debrunner, and W. Hoff, "A 2D Fourier approach to deformable model segmentation of 3D medical images," *Computer Vision and Mathematical Methods in Medical and Biomedical Image Analysis*, vol. 3117, pp. 181-192, 2004.

[16] B. C. Merkl and M. R. Mahfouz, "Unsupervised Three-Dimensional Segmentation of Medical Images Using an Anatomical Bone Atlas," presented at the 12th International Conference on Biomedical Engineering, Singapore, 2005.

[17] R. Tadross and M. Mahfouz, "Intraoperative Reconstruction of Patient-Specific 3D Knee Model for Total Knee Arthroplasty," presented at the Annual Congress of the International Society for Technology in Arthroplasty, Waikoloa, HI, 2009.

[18] R. Tadross, M. Mahfouz, and R. Wasielewski, "Automatic Real-Time Reconstruction of Patient-Specific 3D Knee Modeling Using Ultrasound RF Data," presented at the 24th Annual Congress of the International Society for Technology in Arthroplasty, Bruges, Belgium, 2011.

[19] R. Tadross and M. Mahfouz, "A Novel Technique for Knee Kinematics Teaching Using A-Model Ultrasound: Simulation and Feasibility Study," presented at the 24th Annual Congress of the International Society for Technology in Arthroplasty, Bruges, Belgium, 2011.

[20] H. Lamecker, T. H. Wenckebach, and H.-C. Hege, "Atlas-based 3D-Shape Reconstruction from X-Ray Images," presented at the Proceedings of the 18th International Conference on Pattern Recognition - Volume 01, 2006.

[21] M. Mahfouz, A. Badawi, E. E. A. Fatah, M. Kuhn, and B. Merkl, "Reconstruction of 3D Patient-Specific Bone Models From Biplanar X-Ray Images Utilizing Morphometric Measurements," in *IPCV*, Las Vegas, Nevada, USA, 2006, pp. 345-349.

[22] S. Kadoury, F. Cheriet, and H. Labelle, "Personalized X-ray 3-D reconstruction of the scoliotic spine from hybrid statistical and image-based models," *IEEE Trans Med Imaging*, vol. 28, pp. 1422-35, Sep 2009.

[23] L. Humbert, T. Whitmarsh, M. D. Craene, L. M. d. R\, \#237, o. Barquero, K. Fritscher, R. Schubert, F. Eckstein, T. Link, and A. F. Frangi, "3D reconstruction of both shape and bone mineral density distribution of the femur from DXA images," presented at the Proceedings of the 2010 IEEE international conference on Biomedical imaging: from nano to Macro, Rotterdam, Netherlands, 2010.

[24] Y. Chaibi, T. Cresson, B. Aubert, J. Hausselle, P. Neyret, O. Hauger, J. A. de Guise, and W. Skalli, "Fast 3D reconstruction of the lower limb using a parametric model and statistical inferences and clinical measurements calculation from biplanar X-rays," *Computer Methods in Biomechanics and Biomedical Engineering*, vol. 15, pp. 457-466, 2012/05/01 2011.

[25] M. R. Mahfouz, B. C. Merkl, E. E. Abdel Fatah, R. Booth, and J. N. Argenson, "Automatic methods for characterization of sexual dimorphism of adult femora: distal femur," *Computer Methods in Biomechanics and Biomedical Engineering,* vol. 10, pp. 447-456, 2007/12/01 2007.

[26] M. Mahfouz, A. Badawi, B. Merkl, E. E. A. Fatah, E. Pritchard, K. Kesler, M. Moore, R. Jantz, and L. Jantz, "Patella sex determination by 3D statistical shape models and nonlinear classifiers," *Forensic Science International,* vol. 173, pp. 161-170, Dec 20 2007.

[27] M. Mahfouz, E. E. Abdel Fatah, L. S. Bowers, and G. Scuderi, "Three-dimensional morphology of the knee reveals ethnic differences," *Clin Orthop Relat Res,* vol. 470, pp. 172-85, Jan 2012.

[28] M. Mahfouz, E. Abdel Fatah, and H. ElDakhahkni, "Analysis of Variation and Automated Measurement of Adult Proximal Femora Using Sex-Specific Atlases," in *8th International Symposium on Computer Methods in Biomechanics and Biomedical Engineering*, Porto, Portugal, 2008.

[29] M. R. Mahfouz, E. E. Abdel Fatah, B. C. Merkl, and J. W. Mitchell, "Automatic and manual methodology for three-dimensional measurements of distal femoral gender differences and femoral component placement," *J Knee Surg,* vol. 22, pp. 294-304, Oct 2009.

[30] M. Moore and E. E. A. Fatah, "Body mass estimation from human femoral midshaft cross sectional area," presented at the Annual meeting of the American Association of Physical Anthropologists, Philadelphia, PA, 2007.

[31] M. Zelditch, *Geometric morphometrics for biologists : a primer*. Amsterdam; Boston: Elsevier Academic Press, 2004.

[32] D. E. Slice, "Geometric Morphometrics," *Annual Review of Anthropology,* vol. 36, pp. 261-281, 2007.

[33] I. L. Dryden and K. V. Mardia, *Statistical shape analysis*. Chichester; New York: John Wiley & Sons, 1998.

[34] F. J. Rohlf, "Morphometric Tools for Landmark Data - Geometry and Biology - Bookstein,Fl," *Journal of Classification,* vol. 10, pp. 133-136, 1993.

[35] C. Goodall, "Procrustes Methods in the Statistical-Analysis of Shape," *Journal of the Royal Statistical Society Series B-Methodological,* vol. 53, pp. 285-339, 1991.

[36] F. J. Rohlf and D. Slice, "Extensions of the Procrustes Method for the Optimal Superimposition of Landmarks," *Systematic Zoology,* vol. 39, pp. 40-59, 1990.

[37] F. Bookstein, "Thin-Plate splines and the atlas problem for biomedical images
Information Processing in Medical Imaging." vol. 511, A. Colchester and D. Hawkes, Eds., ed: Springer Berlin / Heidelberg, 1991, pp. 326-342.

[38] S. Ferson, F. J. Rohlf, and R. K. Koehn, "Measuring Shape Variation of Two-Dimensional Outlines," *Systematic Zoology,* vol. 34, pp. 59-68, 1985.

[39] F. L. Bookstein, "Landmark methods for forms without landmarks: localizing group differences in outline shape," in *Mathematical Methods in Biomedical Image Analysis, 1996., Proceedings of the Workshop on*, 1996, pp. 279-289.

[40] C. D. Good, I. S. Johnsrude, J. Ashburner, R. N. A. Henson, K. J. Friston, and R. S. J. Frackowiak, "A voxel-based morphometric study of ageing in 465 normal adult human brains," *NeuroImage,* vol. 14, pp. 21-36, Jul 2001.

[41] D. Pantazis, R. M. Leahy, T. E. Nichols, and M. Styner, "Statistical surface-based morphometry using a nonparametric approach," in *Biomedical Imaging: Nano to Macro, 2004. IEEE International Symposium on*, 2004, pp. 1283-1286 Vol. 2.

[42] M. K. Chung, K. J. Worsley, T. Paus, C. Cherif, D. L. Collins, J. N. Giedd, J. L. Rapoport, and A. C. Evanst, "A unified statistical approach to deformation-based morphometry," *NeuroImage,* vol. 14, pp. 595-606, Sep 2001.

[43] T. F. Cootes, A. Hill, C. J. Taylor, and J. Haslam, "Use of Active Shape Models for Locating Structure in Medical Images," *Image and Vision Computing,* vol. 12, pp. 355-365, Jul-Aug 1994.

[44] A. Neumann and C. Lorenz, "Statistical shape model based segmentation of medical images," *Computerized Medical Imaging and Graphics,* vol. 22, pp. 133-143, Mar-Apr 1998.

[45] A. Ericsson and J. Karlsson, "Aligning shapes by minimising the description length," *Image Analysis, Proceedings,* vol. 3540, pp. 709-718, 2005.

[46] I. T. Jolliffe, *Principal component analysis*. New York: Springer-Verlag, 1986.

[47] T. Heimann and H. P. Meinzer, "Statistical shape models for 3D medical image segmentation: A review," *Medical Image Analysis,* vol. 13, pp. 543-563, Aug 2009.

[48] G. Heitz, T. Rohlfing , and C. Maurer, "Automatic generation of shape models using nonrigid registration with a single segmented template mesh," *Proceedings 9th International Fall Workshop, Vision, Modeling and Visualization,* 2004.

[49] E. B. Dam, P. T. Fletcher, and S. M. Pizer, "Automatic shape model building based on principal geodesic analysis bootstrapping," *Med Image Anal,* vol. 12, pp. 136-51, Apr 2008.

[50] D. Rueckert, A. F. Frangi, and J. A. Schnabel, "Automatic construction of 3-D statistical deformation models of the brain using nonrigid registration," *Ieee Transactions on Medical Imaging,* vol. 22, pp. 1014-1025, Aug 2003.

[51] Y. L. Wang, M. C. Chiang, and P. M. Thompson, "Automated surface matching using mutual information applied to Riemann surface structures," *Medical Image Computing and Computer-Assisted Intervention - Miccai 2005, Pt 2,* vol. 3750, pp. 666-674, 2005.

[52] A. C. Kotcheff and C. J. Taylor, "Automatic construction of eigenshape models by direct optimization," *Med Image Anal,* vol. 2, pp. 303-14, Dec 1998.

[53] P. J. Besl and N. D. Mckay, "A Method for Registration of 3-D Shapes," *Ieee Transactions on Pattern Analysis and Machine Intelligence,* vol. 14, pp. 239-256, Feb 1992.

[54] K. Weiler, "Edge-Based Data Structures for Solid Modeling in Curved-Surface Environments," *Computer Graphics and Applications, IEEE,* vol. 5, pp. 21-40, 1985.

[55] M. Botsch, *Polygon mesh processing*. Natick, Mass.: A K Peters, 2010.
[56] A. Shamir, "A survey on mesh segmentation techniques," *Computer Graphics Forum,* vol. 27, pp. 1539-1556, Sep 2008.
[57] A. Agathos, I. Pratikakis, S. Perantonis, and N. S. Sapidis, "Protrusion-oriented 3D mesh segmentation," *Visual Computer,* vol. 26, pp. 63-81, Jan 2010.
[58] C. M. Bishop, *Pattern recognition and machine learning*. New York: Springer, 2006.
[59] T. Lindeberg, "Scale-space for discrete signals," *Pattern Analysis and Machine Intelligence, IEEE Transactions on,* vol. 12, pp. 234-254, 1990.
[60] A. P. Witkin, "Scale-space filtering," presented at the Proceedings of the Eighth international joint conference on Artificial intelligence - Volume 2, Karlsruhe, West Germany, 1983.
[61] J. J. Koenderink, "The structure of images," *Biological Cybernetics,* vol. 50, pp. 363-370, 1984.
[62] K. Mikolajczyk and C. Schmid, "A performance evaluation of local descriptors," *Pattern Analysis and Machine Intelligence, IEEE Transactions on,* vol. 27, pp. 1615-1630, 2005.
[63] D. G. Lowe, "Distinctive Image Features from Scale-Invariant Keypoints," *Int. J. Comput. Vision,* vol. 60, pp. 91-110, 2004.
[64] R. Kimmel, "Intrinsic Scale Space for Images on Surfaces: The Geodesic Curvature Flow," presented at the Proceedings of the First International Conference on Scale-Space Theory in Computer Vision, 1997.
[65] P. Yuen, F. Mokhtarian, N. Khalili, and J. Illingworth, "Curvature and torsion feature extraction from freeform 3-D meshes at multiple scales," *Iee Proceedings-Vision Image and Signal Processing,* vol. 147, pp. 454-462, Oct 2000.
[66] X. Li and I. Guskov, "Multi-scale features for approximate alignment of point-based surfaces," presented at the Proceedings of the third Eurographics symposium on Geometry processing, Vienna, Austria, 2005.
[67] H. Jing, L. Zhaoqiang, D. Ming, G. Xianfeng, and Q. Hong, "Geodesic Distance-weighted Shape Vector Image Diffusion," *Visualization and Computer Graphics, IEEE Transactions on,* vol. 14, pp. 1643-1650, 2008.
[68] R. Kimmel, "Intrinsic Scale Space for Images on Surfaces: The Geodesic Curvature Flow," *Graphical Models and Image Processing,* vol. 59, pp. 365-372, 1997.
[69] J. Novatnack and K. Nishino, "Scale-Dependent 3D Geometric Features," in *Computer Vision, 2007. ICCV 2007. IEEE 11th International Conference on*, 2007, pp. 1-8.
[70] M. Pauly, L. P. Kobbelt, and M. Gross, "Point-based multiscale surface representation," *ACM Trans. Graph.,* vol. 25, pp. 177-193, 2006.
[71] M. Pauly, R. Keiser, and M. Gross, "Multi-scale Feature Extraction on Point-Sampled Surfaces," *Computer Graphics Forum,* vol. 22, pp. 281-289, 2003.

[72] H. Laga, H. Takahashi, and M. Nakajima, "Scale-space processing of point-sampled geometry for efficient 3D object segmentation," in *Cyberworlds, 2004 International Conference on*, 2004, pp. 377-383.

[73] G. Zou, J. Hua, Z. Lai, X. Gu, and M. Dong, "Intrinsic geometric scale space by shape diffusion," *IEEE Trans Vis Comput Graph,* vol. 15, pp. 1193-200, Nov-Dec 2009.

[74] G. Taubin, "A signal processing approach to fair surface design," presented at the Proceedings of the 22nd annual conference on Computer graphics and interactive techniques, 1995.

[75] D. D. Hoffman and M. Singh, "Salience of visual parts," *Cognition,* vol. 63, pp. 29-78, Apr 1997.

[76] K. L. Boyer, R. Srikantiah, and P. J. Flynn, "Saliency sequential surface organization for free-form object recognition," *Comput. Vis. Image Underst.,* vol. 88, pp. 152-188, 2002.

[77] R. Osada, T. Funkhouser, B. Chazelle, and D. Dobkin, "Shape distributions," *ACM Trans. Graph.,* vol. 21, pp. 807-832, 2002.

[78] S. Mahmoudi and M. Daoudi, "3D models retrieval by using characteristic views," in *Pattern Recognition, 2002. Proceedings. 16th International Conference on*, 2002, pp. 457-460 vol.2.

[79] T. F. Ansary, J.-P. Vandeborre, S. Mahmoudi, and M. Daoudi, "A Bayesian Framework for 3D Models Retrieval Based on Characteristic Views," presented at the Proceedings of the 3D Data Processing, Visualization, and Transmission, 2nd International Symposium, 2004.

[80] M. Ankerst, G. Kastenm\, \#252, ller, H.-P. Kriegel, and T. Seidl, "3D Shape Histograms for Similarity Search and Classification in Spatial Databases," presented at the Proceedings of the 6th International Symposium on Advances in Spatial Databases, 1999.

[81] P. H. Todd and R. J. Y. McLeod, "Numerical estimation of the curvature of surfaces," *Comput. Aided Des.,* vol. 18, pp. 33-37, 1986.

[82] D. S. Meek and D. J. Walton, "On surface normal and Gaussian curvature approximations given data sampled from a smooth surface," *Computer Aided Geometric Design,* vol. 17, pp. 521-543, 2000.

[83] P. Lancaster and K. S□alkauskas, *Curve and surface fitting: an introduction*: Academic Press, 1986.

[84] F. Cazals and M. Pouget, "Estimating differential quantities using polynomial fitting of osculating jets," presented at the Proceedings of the 2003 Eurographics/ACM SIGGRAPH symposium on Geometry processing, Aachen, Germany, 2003.

[85] R. Martin, "Estimation of principal curvatures from range " *International Journal of Shape Modeling,* vol. 4, pp. 99-109, 1998.

[86] H. Akima, "On estimating partial derivatives for bivariate interpolation of scattered data," *Rocky Mountain Journal of Mathematics,* vol. 14, pp. 41-52, 1984.

[87] J. L. Brown, "Vertex based data dependent triangulations," *Computer Aided Geometric Design*, vol. 8, pp. 239-251, 1991.

[88] L. A. Shirman, C. H. S, #233, and quin, "Local surface interpolation with Bézier patches," *Comput. Aided Geom. Des.*, vol. 4, pp. 279-295, 1987.

[89] H. Gouraud, "Continuous Shading of Curved Surfaces," *Computers, IEEE Transactions on*, vol. C-20, pp. 623-629, 1971.

[90] G. Taubin, "Estimating the tensor of curvature of a surface from a polyhedral approximation," presented at the Proceedings of the Fifth International Conference on Computer Vision, 1995.

[91] N. Dyn, K. Hormann, S.-J. Kim, and D. Levin, "Optimizing 3D triangulations using discrete curvature analysis," in *Mathematical Methods for Curves and Surfaces*, ed: Vanderbilt University, 2001, pp. 135-146.

[92] S.-J. Kim, C.-H. Kim, and D. Levin, "Surface simplification using a discrete curvature norm," *Computers & Graphics*, vol. 26, pp. 657-663, 2002.

[93] T. Surazhsky, E. Magid, O. Soldea, G. Elber, and E. Rivlin, "A comparison of Gaussian and mean curvatures estimation methods on triangular meshes," in *Robotics and Automation, 2003. Proceedings. ICRA '03. IEEE International Conference on*, 2003, pp. 1021-1026 vol.1.

[94] D. Liu and G. Xu, "Angle deficit approximation of Gaussian curvature and its convergence over quadrilateral meshes," *Computer-Aided Design*, vol. 39, pp. 506-517, 2007.

[95] K. Watanabe and A. G. Belyaev, "Detection of Salient Curvature Features on Polygonal Surfaces," *Computer Graphics Forum*, vol. 20, pp. 385-392, 2001.

[96] A. Willis and B. Zhou, " Ridge Walking for 3D Surface Segmentation," presented at the ifth International Symposium on 3D Data Processing, Visualization and Transmission (3DPVT), Paris, France, 2010.

[97] D. Eberly, *Ridges in Image and Data Analysis*: Springer, 1996.

[98] P. W. Hallinan, *Two- and three-dimensional patterns of the face*: A.K. Peters, 1999.

[99] X. Pennec, N. Ayache, and J.-P. Thirion, "Landmark-based registration using features identified through differential geometry," in *Handbook of medical imaging*, N. B. Isaac, Ed., ed: Academic Press, Inc., 2000, pp. 499-513.

[100] Y. Ohtake, A. Belyaev, and H.-P. Seidel, "Ridge-valley lines on meshes via implicit surface fitting," *ACM Trans. Graph.*, vol. 23, pp. 609-612, 2004.

[101] J. J. Koenderink and A. J. Vandoorn, "Surface Shape and Curvature Scales," *Image and Vision Computing*, vol. 10, pp. 557-564, Oct 1992.

[102] F. Cazals, J.-C. Faugere, M. Pouget, and F. Rouillier, "The implicit structure of ridges of a smooth parametric surface," *Comput. Aided Geom. Des.*, vol. 23, pp. 582-598, 2006.

[103] P. Yan and K. W. Bowyer, "Biometric Recognition Using 3D Ear Shape," *IEEE Trans. Pattern Anal. Mach. Intell.*, vol. 29, pp. 1297-1308, 2007.

[104] F. Pighin, R. Szeliski, and D. H. Salesin, "Resynthesizing facial animation through 3D model-based tracking," in *Computer Vision, 1999. The Proceedings of the Seventh IEEE International Conference on*, 1999, pp. 143-150 vol.1.

[105] L. Armesto, J. Minguez, and L. Montesano, "A generalization of the metric-based Iterative Closest Point technique for 3D scan matching," in *Robotics and Automation (ICRA), 2010 IEEE International Conference on*, 2010, pp. 1367-1372.

[106] G. C. Sharp, S. W. Lee, and D. K. Wehe, "ICP registration using invariant features," *Pattern Analysis and Machine Intelligence, IEEE Transactions on,* vol. 24, pp. 90-102, 2002.

[107] O. Benedens, "Robust Watermarking and Affine Registration of 3D Meshes," presented at the Revised Papers from the 5th International Workshop on Information Hiding, 2003.

[108] P. Cachier, J.-F. Mangin, X. Pennec, D. Rivi\, \#232, re, D. Papadopoulos-Orfanos, J. R\, \#233, gis, and N. Ayache, "Multisubject Non-rigid Registration of Brain MRI Using Intensity and Geometric Features," presented at the Proceedings of the 4th International Conference on Medical Image Computing and Computer-Assisted Intervention, 2001.

[109] D. M. Cash, M. I. Miga, S. C. Glasgow, B. M. Dawant, L. W. Clements, Z. Cao, R. L. Galloway, and W. C. Chapman, "Concepts and preliminary data toward the realization of image-guided liver surgery," *J Gastrointest Surg,* vol. 11, pp. 844-59, Jul 2007.

[110] L. Maier-Hein, A. M. Franz, T. R. d. Santos, M. Schmidt, M. Fangerau, H.-P. Meinzer, and J. M. Fitzpatrick, "Convergent Iterative Closest-Point Algorithm to Accomodate Anisotropic and Inhomogenous Localization Error," *IEEE Trans. Pattern Anal. Mach. Intell.,* vol. 34, pp. 1520-1532, 2012.

[111] J. Zhu, S. Du, Z. Yuan, Y. Liu, and L. Ma, "Robust affine iterative closest point algorithm with bidirectional distance," *Computer Vision, IET,* vol. 6, pp. 252-261, 2012.

[112] D. Shaoyi, Z. Nanning, M. Gaofeng, and Y. Zejian, "Affine Registration of Point Sets Using ICP and ICA," *Signal Processing Letters, IEEE,* vol. 15, pp. 689-692, 2008.

[113] R. Horaud, F. Forbes, M. Yguel, G. Dewaele, and Z. Jian, "Rigid and Articulated Point Registration with Expectation Conditional Maximization," *Pattern Analysis and Machine Intelligence, IEEE Transactions on,* vol. 33, pp. 587-602, 2011.

[114] J. Feldmar, G. Malandain, J. Declerck, and N. Ayache, "Extension of the ICP algorithm to non-rigid intensity-based registration of 3D volumes," in *Mathematical Methods in Biomedical Image Analysis, 1996., Proceedings of the Workshop on*, 1996, pp. 84-93.

[115] G. C. Sharp, S. W. Lee, and D. K. Wehe, "Maximum-Likelihood Registration of Range Images with Missing Data," *IEEE Trans. Pattern Anal. Mach. Intell.,* vol. 30, pp. 120-130, 2008.

[116] B. Horn, "Closed-form solution of absolute orientation using unit quaternions," *Journal of the Optical Society of America. A,* vol. 4, pp. 629-642, 1987.

[117] P. J. Besl and N. D. McKay, "A Method for Registration of 3-D Shapes," *IEEE Trans. Pattern Anal. Mach. Intell.,* vol. 14, pp. 239-256, 1992.

[118] S. Rusinkiewicz and M. Levoy, "Efficient variants of the ICP algorithm," in *3-D Digital Imaging and Modeling, 2001. Proceedings. Third International Conference on*, 2001, pp. 145-152.

[119] G. Turk and M. Levoy, "Zippered polygon meshes from range images," presented at the Proceedings of the 21st annual conference on Computer graphics and interactive techniques, 1994.

[120] T. Masuda, K. Sakaue, and N. Yokoya, "Registration and integration of multiple range images for 3-D model construction," in *Pattern Recognition, 1996., Proceedings of the 13th International Conference on*, 1996, pp. 879-883 vol.1.

[121] J. Feldmar and N. Ayache, "Rigid, affine and locally affine registration of free-form surfaces," *Int. J. Comput. Vision,* vol. 18, pp. 99-119, 1996.

[122] K. Pulli, "Multiview registration for large data sets," in *3-D Digital Imaging and Modeling, 1999. Proceedings. Second International Conference on*, 1999, pp. 160-168.

[123] S. Granger and X. Pennec, "Multi-scale EM-ICP: A Fast and Robust Approach for Surface Registration," in *Computer Vision — ECCV 2002*. vol. 2353, A. Heyden, G. Sparr, M. Nielsen, and P. Johansen, Eds., ed: Springer Berlin / Heidelberg, 2006, pp. 69-73.

[124] G. Godin, M. Rioux, and R. Baribeau, "{Three-dimensional registration using range and intensity information}," in *{Proceedings of the SPIE: Videometrics III}*, 1994, pp. 279-290.

[125] K. S. Arun, T. S. Huang, and S. D. Blostein, "Least-Squares Fitting of Two 3-D Point Sets," *Pattern Analysis and Machine Intelligence, IEEE Transactions on,* vol. PAMI-9, pp. 698-700, 1987.

[126] M. W. Walker, L. Shao, and R. A. Volz, "Estimating 3-D location parameters using dual number quaternions," *CVGIP: Image Underst.,* vol. 54, pp. 358-367, 1991.

[127] B. Horn, H. Hilden, and S. Negahdaripour, "Closed-form solution of absolute orientation using orthonormal matrices," *Journal of the Optical Society of America A: Optics, Image Science, and Vision,* vol. 5, 1988.

[128] C. Chu-Song, H. Yi-Ping, and C. Jen-Bo, "A fast automatic method for registration of partially-overlapping range images," in *Computer Vision, 1998. Sixth International Conference on*, 1998, pp. 242-248.

[129] M. de Berg, v. Krefeld, and O. Schwarzkopf, *Computational Geometry: Algorithms and Applications*: Springer, 2000.

[130] J. L. Bentley, "Multidimensional binary search trees used for associative searching," *Commun. ACM,* vol. 18, pp. 509-517, 1975.

[131] I. Wald and V. Havran, "On building fast kd-Trees for Ray Tracing, and on doing that in O(N log N)," in *Interactive Ray Tracing 2006, IEEE Symposium on*, 2006, pp. 61-69.

[132] J. H. Friedman, J. L. Bentley, and R. A. Finkel, "An Algorithm for Finding Best Matches in Logarithmic Expected Time," *ACM Trans. Math. Softw.,* vol. 3, pp. 209-226, 1977.

[133] S. Maneewongvatana and D. Mount, "It's Okay to Be Skinny, If Your Friends Are Fat," in *Center for Geometric Computing 4th Annual Workshop on Computational Geometry*, 1999.

[134] J. Elseberg, S. Magnenat, R. Siegwart, and A. Nüchter, "Comparison of nearest-neighbor-search strategies and implementations for efficient shape registration," *Journal of Software Engineering for Robotics (JOSER),* vol. 3, pp. 2-12, 2012.

[135] A. Shmukler and A. Fischer, "Verification of 3D freeform parts by registration of multiscale shape descriptors," *The International Journal of Advanced Manufacturing Technology,* vol. 49, pp. 1093-1106, 2010.

[136] M. Sofka, Y. Gehua, and C. V. Stewart, "Simultaneous Covariance Driven Correspondence (CDC) and Transformation Estimation in the Expectation Maximization Framework," in *Computer Vision and Pattern Recognition, 2007. CVPR '07. IEEE Conference on*, 2007, pp. 1-8.

[137] C. Dorai and A. K. Jain, "COSMOS-A Representation Scheme for 3D Free-Form Objects," *IEEE Trans. Pattern Anal. Mach. Intell.,* vol. 19, pp. 1115-1130, 1997.

[138] M. Styner, K. Rajamani, L.-P. Nolte, G. Zsemlye, G. Székely, C. Taylor, and R. Davies, "Evaluation of 3D Correspondence Methods for Model Building

Information Processing in Medical Imaging." vol. 2732, C. Taylor and J. Noble, Eds., ed: Springer Berlin / Heidelberg, 2003, pp. 63-75.

[139] A. Ericsson and J. Karlsson, "Measures for Benchmarking of Automatic Correspondence Algorithms," *Journal of Mathematical Imaging and Vision,* vol. 28, pp. 225-241, 2007.

[140] H. Lamecker, M. Seebass, H. Hege, and P. Deuflhard, "A 3D statistical shape model of the pelvic bone for segmentation," in *Medical Imaging 2004: Image Processing*, San Diego, CA, USA, 2004, pp. 1341-1351.

[141] S. Meller and W. Kalender, "Building a statistical shape model of the pelvis," *CARS 2004 - Computer Assisted Radiology and Surgery. Proceedings of the 18th International Congress and Exhibition,* vol. 1268, pp. 561-566, 2004.

[142] P. Paysan, M. L, #252, thi, T. Albrecht, A. Lerch, B. Amberg, F. Santini, and T. Vetter, "Face Reconstruction from Skull Shapes and Physical Attributes," presented at the Proceedings of the 31st DAGM Symposium on Pattern Recognition, Jena, Germany, 2009.

[143] F. Yokota, T. Okada, M. Takao, N. Sugano, Y. Tada, and Y. Sato, "Automated Segmentation of the Femur and Pelvis from 3D CT Data of Diseased Hip Using Hierarchical Statistical Shape Model of Joint Structure," presented at the Proceedings of the 12th International Conference on Medical Image Computing and Computer-Assisted Intervention: Part II, London, UK, 2009.

[144] M. Styner, K. Rajamani, L.-P. Nolte, G. Zsemlye, G. Székely, C. Taylor, and R. Davies, "Evaluation of 3D Correspondence Methods for Model Building," in *Information Processing in Medical Imaging*. vol. 2732, C. Taylor and J. Noble, Eds., ed: Springer Berlin / Heidelberg, 2003, pp. 63-75.

[145] T. F. Cootes, C. J. Taylor, D. H. Cooper, and J. Graham, "Active shape models\—their training and application," *Comput. Vis. Image Underst.,* vol. 61, pp. 38-59, 1995.
[146] F. Bookstein, *Morphometric tools for landmark data : geometry and biology*: Cambridge University Press, 1997.
[147] D. Mohamed Mahfouz Ph, B. Emam ElHak Abdel Fatah, M. Lyndsay Smith Bowers, and M. D. Giles Scuderi, "Three-dimensional Morphology of the Knee Reveals Ethnic Differences," vol. 0, pp. 1-14, 0001.
[148] R. L. Jantz and M. Mahfouz, "Improving Sex Estimation from Crania using 3-dimensional CT Scans," ed: National Institue of Justice, 2008.
[149] D. A. Komar and J. E. Buikstra, *Forensic anthropology: contemporary theory and practice*: Oxford University Press, 2007.
[150] T. D. Stewart, *Essentials of forensic anthropology : especially as developed in the United States* Springfield, IL: C.C. Thomas, 1979.
[151] W. M. Krogman and Y. İşcan, *The human skeleton in forensic medicine*: C.C. Thomas, 1986.
[152] B. Williams and T. Rogers, "Evaluating the accuracy and precision of cranial morphological traits for sex determination," *J Forensic Sci,* vol. 51, pp. 729-735, 2006.
[153] L. Konigsberg and S. Hens, "Use of ordinal categorical variables in skeletal assessment of sex from the cranium," *Am J Phys Anthropol,* vol. 107, pp. 97-112, 1998.
[154] P. Walker, "Sexing skulls using discriminant function analysis of visually assessed traits," *Am J Phys Anthropol,* vol. 136, pp. 39-50, 2008.
[155] N. R. Shirley and R. L. Jantz, "Spheno-occipital synchondrosis fusion in modern Americans," *J Forensic Sci,* vol. 56, pp. 580-5, May 2011.
[156] H. M. Garvin and C. B. Ruff, "Sexual dimorphism in skeletal browridge and chin morphologies determined using a new quantitative method," *American Journal of Physical Anthropology,* vol. 147, pp. 661-670, 2012.
[157] F. Ramsthaler, M. Kettner, A. Gehl, and M. A. Verhoff, "Digital forensic osteology: Morphological sexing of skeletal remains using volume-rendered cranial CT scans," *Forensic Science International,* vol. 195, pp. 148-152, 2010.
[158] E. Giles and O. Elliot, "Sex determination by discriminant function analysis of crania," *Am J Phys Anthropol,* vol. 21, pp. 53-68, 1963.
[159] H. Uytterschaut, "Sexual dimorphism in human skulls. A comparison of sexual dimorphism in different populations," *Hum Evol,* vol. 1, pp. 243-250, 1986.
[160] M. Steyn and M. Y. İşcan, "Sexual dimorphism in the crania and mandibles of South African whites," *Forensic Science International,* vol. 98, pp. 9-16, 1998.
[161] D. Franklin, L. Freedman, N. Milne, and C. E. Oxnard, "A geometric morphometric study of sexual dimorphism in the crania of indigenous southern Africans," *South African Journal of Science,* vol. 102, pp. 229-238, 2006.

[162] D. France, "Observational and metric analysis of sex in the skeleton," in *Forensic Osteology*, K. Reichs, Ed., ed Springfield, IL: Charles C. Thomas, 1998, pp. 163-186.
[163] M. Graw, A. Czarnetzki, and H.-T. Haffner, "The form of the supraorbital margin as a criterion in identification of sex from the skull: Investigations based on modern human skulls," *American Journal of Physical Anthropology,* vol. 108, pp. 91-96, 1999.
[164] R. Gapert, S. Black, and J. Last, "Sex determination from the occipital condyle: Discriminant function analysis in an Eighteenth and Nineteenth Century British sample," *American Journal of Physical Anthropology,* vol. 138, pp. 384-394, 2009.
[165] V. Saini, R. Srivastava, R. K. Rai, S. N. Shamal, T. B. Singh, and S. K. Tripathi, "Sex Estimation from the Mastoid Process Among North Indians*," *Journal of Forensic Sciences,* vol. 57, pp. 434-439, 2012.
[166] T. Hsiao, H. Chang, and K. Liu, "Sex determination by discriminant function analysis of lateral radiographic cephalometry," *J Forensic Sci,* vol. 41, pp. 792-795, 1996.
[167] S. A. Veyre-Goulet, C. Mercier, O. Robin, and C. Guérin, "Recent Human Sexual Dimorphism Study Using Cephalometric Plots on Lateral Teleradiography and Discriminant Function Analysis," *Journal of Forensic Sciences,* vol. 53, pp. 786-789, 2008.
[168] L. Bigoni, J. Velemínská, and J. Brůžek, "Three-dimensional geometric morphometric analysis of cranio-facial sexual dimorphism in a Central European sample of known sex," *HOMO - Journal of Comparative Human Biology,* vol. 61, pp. 16-32, 2010.
[169] A. Rosas and M. Bastir, "Thin-plate spline analysis of allometry and sexual dimorphism in the human craniofacial complex," *American Journal of Physical Anthropology,* vol. 117, pp. 236-245, 2002.
[170] D. Franklin, N. Milne, and L. Freedman, "A geometric morphometric study of cranial sexual dimorphism in selected indigenous populations of South Africa," *Am J Phys Anthropol,* vol. 123, p. 96, 2004.
[171] D. Franklin, L. Freedman, and N. Milne, "Sexual dimorphism and discriminant function sexing in indigenous South African crania," *Homo,* vol. 55, pp. 213-218, 2005.
[172] B. M. Auerbach and M. H. Raxter, "Patterns of clavicular bilateral asymmetry in relation to the humerus: variation among humans," *Journal of Human Evolution,* vol. 54, pp. 663-674, May 2008.
[173] J. Steele and S. Mays, "Handedness and Directional Asymmetry in the Long Bones of the Human Upper-limb," *International Journal of Osteoarchaeology,* vol. 5, pp. 39-49, Mar 1995.
[174] S. Mays, J. Steele, and M. Ford, "Directional asymmetry in the human clavicle," *International Journal of Osteoarchaeology,* vol. 9, pp. 18-28, Jan-Feb 1999.
[175] B. M. Auerbach and C. B. Ruff, "Limb bone bilateral asymmetry: variability and commonality among modern humans," *Journal of Human Evolution,* vol. 50, pp. 203-218, 2006.

[176] M. Kujanova, L. Bigoni, J. Veleminska, and P. Veleminsky, "Limb bones asymmetry and stress in Medieval and recent populations of Central Europe," *International Journal of Osteoarchaeology,* vol. 18, pp. 476-491, Sep-Oct 2008.

[177] A. H. Schultz, "Proportions, variability and asymmetries of the long bones of the limbs and clavicles in man and apes," *Hum Biol,* vol. 9, pp. 281-328, 1937.

[178] F. G. Parsons, "On the proportions and characteristics of the modern English clavicle," *Journal of Anatomy,* vol. 51, pp. 71-93, Oct 1916.

[179] H. H. Jones, J. D. Priest, W. C. Hayes, C. C. Tichenor, and D. A. Nagel, "Humeral hypertrophy in response to exercise," *J Bone Joint Surg,* vol. 59, pp. 204-8, 1977.

[180] C. B. Ruff and H. H. Jones, "Bilateral asymmetry in cortical bone of the humerus and tibia-sex and age factors," *Hum Biol,* vol. 53, pp. 69-86, 1981.

[181] C. B. Ruff, "Biomechanical analyses of archaeological human skeletons," in *Biological Anthropology of the Human Skeleton*, M. A. a. S. Katzenburg, S.R., Ed., ed New York: Wiley-Liss, 2000.

[182] C. N. Shaw and J. T. Stock, "Habitual throwing and swimming correspond with upper limb diaphyseal strength and shape in modern human athletes," *Am J Phys Anthropol,* vol. 140, pp. 160-72, 2009.

[183] D. Marchi and C. N. Shaw, "Variation in fibular robusticity reflects variation in mobility patterns," *J Hum Evol,* vol. 61, pp. 609-16, 2011.

[184] L. A. Sarringhaus, J. T. Stock, L. F. Marchant, and W. C. McGrew, "Bilateral asymmetry in the limb bones of the chimpanzee (Pan troglodytes)," *American Journal of Physical Anthropology,* vol. 128, pp. 840-845, 2005.

[185] J. T. Stock, T. Davies, L. Sarringhaus, and C. N. Shaw, "Three dimensional quantification of upper limb bilateral asymmetry among modern humans and great apes," *American Journal of Physical Anthropology,* vol. 147, pp. 278-279, 2012.

[186] R. C. Helmkamp and D. Falk, "Age- and sex-associated variations in the directional asymmetry of Rhesus macaque forelimb bones," *American Journal of Physical Anthropology,* vol. 83, pp. 211-18, 1990.

[187] G. von Bonin, "Anatomical asymmetries of the cerebral hemispheres," in *Interhemispheric Relations and Cerebral Dominance*, V. B. Mount-castle, Ed., ed Baltimore: Johns Hopkins Press, 1962.

[188] L. M. Schell, F. E. Johnston, D. R. Smith, and A. M. Paolone, "Directional asymmetry of body dimensions among white adolescents," *American Journal of Physical Anthropology,* pp. 317-22, 1985.

[189] S. H. Schlecht, "Understanding Entheses: Bridging the Gap Between Clinical and Anthropological Perspectives," *The Anatomical Record: Advances in Integrative Anatomy and Evolutionary Biology,* vol. 295, pp. 1239-1251, 2012.

[190] D. E. Hawkey and C. F. Merbs, "Activity-induced musculoskeletal stress markers (MSM) and subsistence strategy changes among ancient Hudson Bay Eskimos," *International Journal of Osteoarchaeology,* vol. 5, pp. 324-338, 1995.
[191] E. Weiss, "Understanding muscle markers: lower limbs," *Am J Phys Anthropol,* vol. 125, pp. 232-8, Nov 2004.
[192] V. Eshed, A. Gopher, E. Galili, and I. Hershkovitz, "Musculoskeletal stress markers in Natufian hunter-gatherers and Neolithic farmers in the Levant: the upper limb," *Am J Phys Anthropol,* vol. 123, pp. 303-15, Apr 2004.
[193] C. A. Wilczak, "Consideration of sexual dimorphism, age, and asymmetry in quantitative measurements of muscle insertion sites," *International Journal of Osteoarchaeology,* vol. 8, pp. 311-325, 1998.
[194] E. Weiss, "Muscle markers revisited: activity pattern reconstruction with controls in a central California Amerind population," *Am J Phys Anthropol,* vol. 133, pp. 931-40, Jul 2007.
[195] A. E. Ljunggren, "Clavicular function," *Acta Orthop Scand,* vol. 50, pp. 261-8, Jun 1979.
[196] J.-L. Voisin, "Evolution de la morphologie claviculaire au sein du genre Homo. Consequences architecturales et fonctionnelles sur la ceinture scapulaire," *L'Anthropologie,* vol. 105, pp. 449-468, 2001.
[197] J.-L. Voisin, "Clavicle, a neglected bone: Morphology and relation to arm movements and shoulder architecture in primates," *The Anatomical Record Part A: Discoveries in Molecular, Cellular, and Evolutionary Biology,* vol. 288A, pp. 944-953, 2006.
[198] L. Scheuer and S. Black, *Developmental juvenile osteology*, 1st ed. New York: Academic Press, 2000.
[199] T. Todd and J. D'Errico, "The clavicular epiphyses," *Am J Anat,* vol. 41, pp. 25-50, 1928.
[200] P. M. Mahfouz, B. E. E. A. Fatah, M. L. S. Bowers, and M. G. Scuderi, "Three-dimensional Morphology of the Knee Reveals Ethnic Differences," *Clinical Orthopaedics and Related Research®,* vol. 470, pp. 172-185, January 1, 0001.
[201] M. R. Mahfouz, B. C. Merkl, E. E. Fatah, R. Booth, and J. N. Argenson, "Automatic methods for characterization of sexual dimorphism of adult femora: distal femur," *Comput Methods Biomech Biomed Engin,* vol. 10, pp. 447-56, 2007.
[202] N. R. Shirley, "Age and sex estimation from the human clavicle: an investigation of traditional and novel methods," Ph.D., Anthropology, University of Tennessee, Knoxville, 2009.
[203] S. Benazzi, E. Stansfield, O. Kullmer, L. Fiorenza, and G. Gruppioni, "Geometric morphometric methods for bone reconstruction: the mandibular condylar process of Pico della Mirandola," *Anat Rec (Hoboken),* vol. 292, pp. 1088-97, Aug 2009.
[204] B. J. Adams and J. E. Byrd, *Recovery, Analysis, and Identification of Commingled Human Remains*: Humana Press, 2008.

[205] N. P. Herrmann and J. B. Devlin, "Assessment of Commingled Human Remains Using a GIS-Based Approach
Recovery, Analysis, and Identification of Commingled Human Remains," B. J. Adams and J. E. Byrd, Eds., ed: Humana Press, 2008, pp. 257-269.
[206] M. S. Ponce De León and C. P. E. Zollikofer, "New evidence from Le Moustier 1: Computer-assisted reconstruction and morphometry of the skull," *The Anatomical Record,* vol. 254, pp. 474-489, 1999.
[207] W. Recheis, G. W. Weber, K. Schäfer, R. Knapp, H. Seidler, and D. zur Nedden, "Virtual reality and anthropology," *European Journal of Radiology,* vol. 31, pp. 88-96, 1999.
[208] G. W. Weber, "Virtual anthropology (VA): A call for Glasnost in paleoanthropology," *The Anatomical Record,* vol. 265, pp. 193-201, 2001.
[209] S. Neubauer, P. Gunz, P. Mitteroecker, and G. W. Weber, "Three-dimensional digital imaging of the partial Australopithecus africanus endocranium MLD 37/38," *Can Assoc Radiol J,* vol. 55, pp. 271-8, Oct 2004.
[210] L. Ulhaas, "27 Computer-Based Reconstruction: Technical Aspects and Applications
Handbook of Paleoanthropology," W. Henke and I. Tattersall, Eds., ed: Springer Berlin Heidelberg, 2007, pp. 787-813.
[211] C. P. Zollikofer, M. S. Ponce de Leon, D. E. Lieberman, F. Guy, D. Pilbeam, A. Likius, H. T. Mackaye, P. Vignaud, and M. Brunet, "Virtual cranial reconstruction of Sahelanthropus tchadensis," *Nature,* vol. 434, pp. 755-9, Apr 7 2005.
[212] A. D. Sylvester, B. C. Merkl, and M. R. Mahfouz, "Assessing A.L. 288-1 femur length using computer-aided three-dimensional reconstruction," *Journal of Human Evolution,* vol. 55, pp. 665-671, 2008.
[213] G. P, M. P, B. FL, and W. GW, "Computeraided reconstruction of incomplete human crania using statistical and geometrical estimation methods," in *Enter the past: computer applications and quantitative methods in archaeology*, ed: Oxford: Archaeopress, 2004, pp. 92–94.
[214] R. P. Mehta and D. G. Deschler, "Mandibular reconstruction in 2004: an analysis of different techniques," *Curr Opin Otolaryngol Head Neck Surg,* vol. 12, pp. 288-93, Aug 2004.
[215] C. W. Young, M. A. Pogrel, and B. L. Schmidt, "Quality of life in patients undergoing segmental mandibular resection and staged reconstruction with nonvascularized bone grafts," *J Oral Maxillofac Surg,* vol. 65, pp. 706-12, Apr 2007.
[216] M. J. Madsen, C. A. McDaniel, and R. H. Haug, "A Biomechanical Evaluation of Plating Techniques Used for Reconstructing Mandibular Symphysis/Parasymphysis Fractures," *Journal of Oral and Maxillofacial Surgery,* vol. 66, pp. 2012-2019, 2008.
[217] D. J. Berry, D. G. Lewallen, A. D. Hanssen, and M. E. Cabanela, "Pelvic Discontinuity in Revision Total Hip Arthroplasty*," *The Journal of Bone & Joint Surgery,* vol. 81, pp. 1692-1702, 1999.

[218] M. Taunton, T. Fehring, P. Edwards, T. Bernasek, G. Holt, and M. Christie, "Pelvic Discontinuity Treated With Custom Triflange Component: A Reliable Option," *Clinical Orthopaedics and Related Research®,* vol. 470, pp. 428-434, 2012.

[219] S. Agarwal, "Osteolysis—basic science, incidence and diagnosis," *Current Orthopaedics,* vol. 18, pp. 220-231, 2004.

[220] E. I. T. de Schepper, J. Damen, J. B. J. van Meurs, A. Z. Ginai, M. Popham, A. Hofman, B. W. Koes, and S. M. Bierma-Zeinstra, "The Association Between Lumbar Disc Degeneration and Low Back Pain: The Influence of Age, Gender, and Individual Radiographic Features," *Spine (Phila Pa 1976),* vol. 35, pp. 531-536 10.1097/BRS.0b013e3181aa5b33, 2010.

[221] R. B. Dunlop, M. A. Adams, and W. C. Hutton, "Disc space narrowing and the lumbar facet joints," *J Bone Joint Surg Br,* vol. 66, pp. 706-10, Nov 1984.

[222] I. Kingma, J. H. van Dieën, K. Nicolay, J. J. Maat, and H. Weinans, "Monitoring water content in deforming intervertebral disc tissue by finite element analysis of MRI data," *Magnetic Resonance in Medicine,* vol. 44, pp. 650-654, 2000.

[223] R. E. Gay, B. Ilharreborde, K. D. Zhao, L. J. Berglund, G. Bronfort, and K.-N. An, "Stress in lumbar intervertebral discs during distraction: a cadaveric study," *The Spine Journal,* vol. 8, pp. 982-990, 2008.

[224] J. N. Grauer, A. Biyani, A. Faizan, A. Kiapour, K. Sairyo, A. Ivanov, N. A. Ebraheim, T. C. Patel, and V. K. Goel, "Biomechanics of two-level Charité artificial disc placement in comparison to fusion plus single-level disc placement combination," *The Spine Journal,* vol. 6, pp. 659-666, 2006.

[225] M. Sharma, N. A. Langrana, and J. Rodriguez, "Role of ligaments and facets in lumbar spinal stability," *Spine (Phila Pa 1976),* vol. 20, pp. 887-900, Apr 15 1995.

[226] J. S. Cheng, F. Liu, R. D. Komistek, M. R. Mahfouz, A. Sharma, and D. Glaser, "Comparison of cervical spine kinematics using a fluoroscopic model for adjacent segment degeneration," *Journal of Neurosurgery: Spine,* vol. 7, pp. 509-513, 2007.

[227] F. Liu, J. Cheng, R. D. Komistek, M. R. Mahfouz, and A. Sharma, "In vivo evaluation of dynamic characteristics of the normal, fused, and disc replacement cervical spines," *Spine (Phila Pa 1976),* vol. 32, pp. 2578-84, Nov 1 2007.

[228] F. Liu, J. S. Cheng, R. D. Komistek, and M. R. Mahfouz, "Normal, fused, and degenerative cervical spines: a comparative study of three-dimensional in vivo kinetics," *J Bone Joint Surg Am,* vol. 90 Suppl 4, pp. 85-9, Nov 2008.

[229] H. S. Karabekir, N. Gocmen-Mas, M. Edizer, T. Ertekin, C. Yazici, and D. Atamturk, "Lumbar vertebra morphometry and stereological assesment of intervertebral space volumetry: a methodological study," *Ann Anat,* vol. 193, pp. 231-6, May 2011.

[230] J. M. Olsewski, E. H. Simmons, F. C. Kallen, F. C. Mendel, C. M. Severin, and D. L. Berens, "Morphometry of the lumbar spine: anatomical perspectives related to transpedicular fixation," *J Bone Joint Surg Am,* vol. 72, pp. 541-9, Apr 1990.

[231] A. Wolf, M. Shoham, S. Michael, and R. Moshe, "Morphometric study of the human lumbar spine for operation-workspace specifications," *Spine (Phila Pa 1976),* vol. 26, pp. 2472-7, Nov 15 2001.

[232] M. H. Krag, D. L. Weaver, B. D. Beynnon, and L. D. Haugh, "Morphometry of the thoracic and lumbar spine related to transpedicular screw placement for surgical spinal fixation," *Spine (Phila Pa 1976),* vol. 13, pp. 27-32, Jan 1988.

[233] S. Eisenstein, "The morphometry and pathological anatomy of the lumbar spine in South African negroes and caucasoids with specific reference to spinal stenosis," *Journal of Bone & Joint Surgery, British Volume,* vol. 59-B, pp. 173-180, May 1, 1977 1977.

[234] J. J. P. Vanschaik, H. Verbiest, and F. D. J. Vanschaik, "Morphometry of Lower Lumbar Vertebrae as Seen on Ct Scans - Newly Recognized Characteristics," *American Journal of Roentgenology,* vol. 145, pp. 327-335, 1985.

[235] M. R. Mahfouz, W. A. Hoff, R. D. Komistek, and D. A. Dennis, "A robust method for registration of three-dimensional knee implant models to two-dimensional fluoroscopy images," *Medical Imaging, IEEE Transactions on,* vol. 22, pp. 1561-1574, 2003.

[236] N. Lynnerup, J. G. Astrup, and B. Sejrsen, "Thickness of the human cranial diploe in relation to age, sex and general body build," *Head Face Med,* vol. 1, p. 13, 2005.

[237] T. Brown, S. K. Pinkerton, and W. Lambert, "Thickness of the Cranial Vault in Australian Aboriginals," *Archaeology & Physical Anthropology in Oceania,* vol. 14, pp. 54-71, 1979.

[238] H. Ishida and Y. Dodo, "Cranial thickness of modern and neolithic populations in Japan," *Hum Biol,* vol. 62, pp. 389-401, Jun 1990.

[239] A. H. Ross, R. L. Jantz, and W. F. McCormick, "Cranial thickness in American females and males," *Journal of Forensic Sciences,* vol. 43, pp. 267-72, Mar 1998.

[240] R. She and J. Szakacs, "Hyperostosis frontalis interna: case report and review of literature," *Ann Clin Lab Sci,* vol. 34, pp. 206-8, Spring 2004.

[241] T. G. Williams, A. P. Holmes, J. C. Waterton, R. A. Maciewicz, C. E. Hutchinson, R. J. Moots, A. F. Nash, and C. J. Taylor, "Anatomically corresponded regional analysis of cartilage in asymptomatic and osteoarthritic knees by statistical shape modelling of the bone," *IEEE Trans Med Imaging,* vol. 29, pp. 1541-59, Aug 2010.

[242] F. Agnesi, K. K. Amrami, C. A. Frigo, and K. R. Kaufman, "Comparison of cartilage thickness with radiologic grade of knee osteoarthritis," *Skeletal Radiol,* vol. 37, pp. 639-43, Jul 2008.

[243] J. Carballido-Gamio, J. S. Bauer, R. Stahl, K. Y. Lee, S. Krause, T. M. Link, and S. Majumdar, "Inter-subject comparison of MRI knee cartilage thickness," *Med Image Anal,* vol. 12, pp. 120-35, Apr 2008.

[244] F. Eckstein, W. Wirth, and M. C. Nevitt, "Recent advances in osteoarthritis imaging-the Osteoarthritis Initiative," *Nat Rev Rheumatol,* vol. 8, pp. 622-30, Oct 2012.

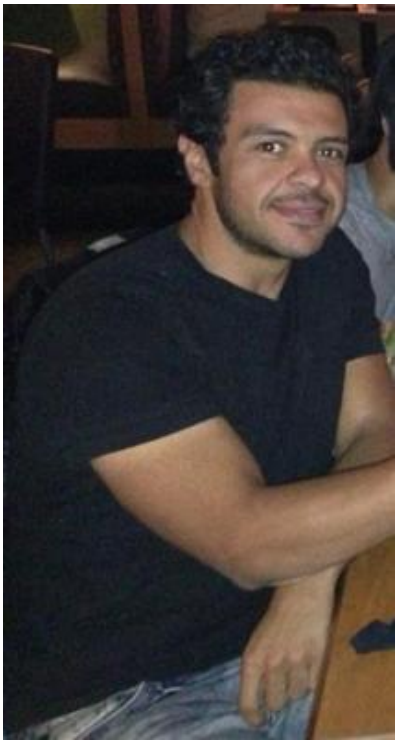
[245] S. Koo, E. J. Alexander, G. E. Gold, N. Giori, and T. P.Andriacchi, "Morphology and Thickness in Tibia and Femoral Cartilage at the Knee Influenced by The Mechanics of

Walking," presented at the Summer Bioengineering Conference, Sonesta Beach Resort in Key Biscayne, Florida, 2003.

[246] Z. A. Cohen, D. M. McCarthy, S. D. Kwak, P. Legrand, F. Fogarasi, E. J. Ciaccio, and G. A. Ateshian, "Knee cartilage topography, thickness, and contact areas from MRI: in-vitro calibration and in-vivo measurements," *Osteoarthritis Cartilage,* vol. 7, pp. 95-109, Jan 1999.

[247] J. P. Raynauld, C. Kauffmann, G. Beaudoin, M. J. Berthiaume, J. A. de Guise, D. A. Bloch, F. Camacho, B. Godbout, R. D. Altman, M. Hochberg, J. M. Meyer, G. Cline, J. P. Pelletier, and J. Martel-Pelletier, "Reliability of a quantification imaging system using magnetic resonance images to measure cartilage thickness and volume in human normal and osteoarthritic knees," *Osteoarthritis and Cartilage,* vol. 11, pp. 351-360, 2003.

VITA



Emam ElHak Abdel Fatah was born in Cairo, Egypt, in 1980. He received the B.S. degree in biomedical and system engineering from the Cairo University, Cairo, Egypt, in 2002. Just upon graduation, he worked as a research and development engineer in IBE Tech. in Cairo, Egypt where he was involved in the development of 3D and 4D ultrasound solutions. In 2003, he joined IBM Egypt as part of the development team of IBM WBI department. He received the Ph.D. degree in biomedical engineering from the University of Tennessee, Knoxville, TN, in 2012. He has published and presented at numerous journals and international conferences in the fields of biomedical engineering, clinical orthopedics, and anthropology. His current research interests include medical imaging, pattern recognition, computer vision, statistical and mathematical modeling of anatomical structures, physical and forensic anthropology.